A Metrological Atomic Force Microscope

by

Andrew John Stein

B.S., Mechanical Engineering (2000)
Cornell University

Submitted to the Department of Mechanical Engineering
in partial fulfillment of the requirements for the degree of

Master of Science

at the

MASSACHUSETTS INSTITUTE OF TECHNOLOGY

September 2002

Author . . . .
Department of Mechanical Engineering
August 26, 2002

Certified by . . . .
David L. Trumper
Associate Professor of Mechanical Engineering
Thesis Supervisor

Accepted by . . . .
Ain A. Sonin
Chairman, Department Committee on Graduate Students

A Metrological Atomic Force Microscope

by

Andrew John Stein

Submitted to the Department of Mechanical Engineering
on August 26, 2002, in partial fulfillment of the
requirements for the degree of
Master of Science

Abstract

This thesis describes the design, fabrication, and testing of a metrological atomic force microscope (AFM). This design serves as a prototype for a similar system that will later be integrated with the Sub-Atomic Measuring Machine (SAMM) under development in collaboration with the University of North Carolina at Charlotte. The microscope uses a piezoelectric tube scanner with a quartz tuning fork proximity sensor to image three-dimensional sample topographies. The probe position is measured with a set of capacitance sensors, aligned so as to minimize Abbe offset error, for direct measurement of probe tip displacements.

A PC-based digital control system provides closed-loop control of the lateral scanning and axial height regulation actions of the probe assembly. The lateral scanning system, which dictates the probe's motion in directions parallel to the sample plane, has measured -3 dB closed-loop bandwidths of 189 Hz and 191 Hz in the X and Y directions, respectively. Meanwhile, the axial height regulator, which adjusts the length of the tube scanner to control for a constant gap between the probe tip and the sample surface, has demonstrated a -3 dB closed-loop bandwidth of as high as 184 Hz.

The metrological AFM is operational and has been used to collect several images of sample surfaces. Images taken of a silicon calibration grating indicate that the microscope can easily resolve 100 nm-scale step changes in height. However, several errors are observed in the image data. Possible reasons for these errors are discussed, and ideas for follow-on work are suggested.

Thesis Supervisor: David L. Trumper
Title: Associate Professor of Mechanical Engineering

Acknowledgments

I wish to thank a number of people for their help during this project. I am particularly grateful to have had the opportunity to work with my advisor, Professor David Trumper. I am constantly amazed by the depth and breadth of his knowledge about seemingly all things mechanical and electrical. His creativity and enthusiasm had a tremendous positive influence on the work described in this thesis. He has taught me a great deal about electronics, feedback control, and precision engineering in general. He also provided the extra push I needed to perform at my best.

Additionally, this research benefited greatly from the input of Professor Robert Hocken, who is the Director of the Center for Precision Metrology at the University of North Carolina at Charlotte (UNCC). I thank him for providing his substantial insight several times over the course of the project and for lending the high-voltage amplifier used extensively in our experiments.

Also at UNCC, Professor Patrick Moyer offered his expertise on the tuning fork proximity sensor incorporated in both our microscope heads. Dr. Chunhai Wang was quite generous in his assistance, as well, particularly in making the optical fiber tips used with the metrological AFM.

Several other people deserve credit for their contributions to this research. Professor Martin Culpepper, from MIT's Mechanical Engineering Department, provided valuable assistance during the design of the metrological AFM's kinematic coupling. Gerry Wentworth and Mark Belanger were both incredibly helpful and patient whenever I made a visit to the LMP machine shop. Roy Mallory and Al Hamilton, from ADE Technologies, offered their assistance in determining how best to integrate capacitance sensors in the metrological AFM head. David Otten, who is taking over where I am leaving off, saved me a great deal of time and frustration with his suggestions during the initial testing of the microscope. I wish him much future success with the project.

During my two years working in the Precision Motion Control Lab, I have had the great pleasure of working in the company of many talented and thoughtful grad-

uate students. I received much valuable advice and instruction from Richard Montesanti, who was always willing and able to discuss all matters of precision engineering. Marten Byl was another source of informed suggestions and creative ideas. I could always count on Katherine Lilienkamp to give a well thought-out reply to any question I might bring her way. I was fortunate to be able to tap Xiaodong Lu's impressive knowledge of electrical and mechanical engineering concepts. Joseph Cattell was also a great help many times over the course of my research. I additionally benefitted from several technical discussions with Vijay Shilpiekandula. During my first year at MIT, I had the good fortune of knowing Amar Kendale, Marsette Vona, and Dr. Michael Liebman — as well as visiting scientist Tsuyoshi Sato — who all contributed some excellent work to the lab.

While I worked on my research, my life was made easier by David Rodriguera and Margaret Beucler, who both helped streamline the purchasing process and generally kept all sorts of MIT-related affairs in order.

Finally, the last two years would have been much more of a struggle, if not for the support of my family and friends. I am particularly thankful to Timothy Coker, Joseph Caprario, Philip Tang, James Celestino, and all of my former softball teammates. Most of all, my parents and two sisters have been a much needed source of love, support, and inspiration, for which I am deeply grateful.

This research was funded by the National Science Foundation, under grant number DMI-9820126. The author received additional support from an MIT Presidential Fellowship.

For Mom, Dad, Mara, and Karen

Contents

List of Figures

List of Tables

Chapter 1

Introduction

1.1 Project Summary

This thesis presents the development of a metrological atomic force microscope (AFM). This prototype is the foundation for a future version that will be integrated in the Sub-Atomic Measuring Machine (SAMM) — a high-accuracy precision positioning stage located at the University of North Carolina at Charlotte (UNCC) [19, 16].

Figure 1-1 shows a three-dimensional model of our metrological AFM, with the housing transparent to reveal the inner components. A piezoelectric tube scanner extends downward from the top of the housing. Six capacitance sensors are clamped inside the housing and measure the position of a cone-shaped target mounted on the tube's free end. By controlling the voltages applied to four electrodes on the piezo tube's outer surface with respect to an electrode on its inner surface, we command three degree-of-freedom motion of the cone. The AFM's probe-sample proximity sensor protrudes from the bottom of the cone. This sensor is based on the quartz tuning fork from a watch crystal, with a tapered optical fiber glued to one side (Figure 1-2). The tuning fork is electrically driven at a frequency slightly (about 1 Hz) below its first mechanical resonance, which generally lies between 32.1 kHz

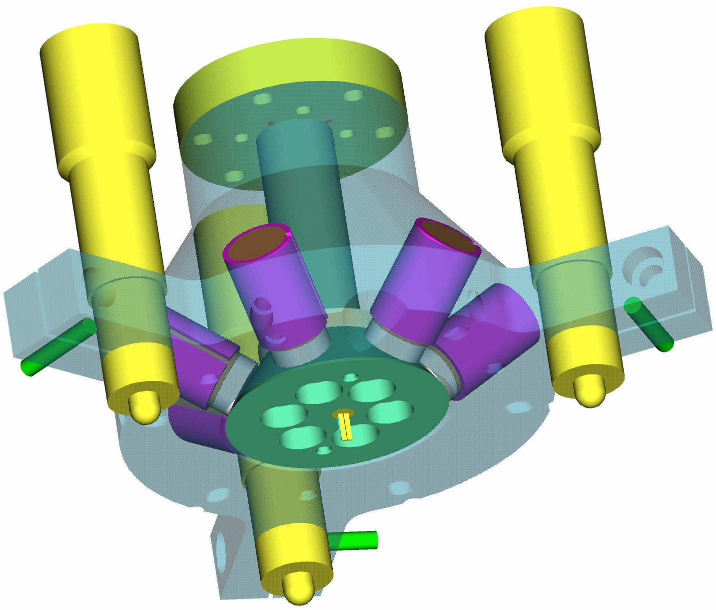

Figure 1-1: Three-dimensional model of the metrological AFM head. The housing is transparent, to allow a view of the inner components. A piezoelectric tube scanner extends downward from the top of the housing. Six cylindrical capacitance sensors arrayed around the base of the head measure the displacement of the cone-shaped target on the tube scanner's free end. The sensors' measurement axes intersect at the tip of a tapered optical fiber, which is mounted to the tuning fork seen protruding from the bottom of the cone.

and 32.6 kHz, depending on the size of the fiber and the amount of glue applied. With the fiber tip operating within tens of nanometers of the sample surface, the AC current flowing through the fork becomes sensitive to nanometer-scale changes in the probe-sample separation.

While the AFM scans closed-loop in the lateral directions — using X and Y values measured by the capacitance sensors for feedback — the controller of the tube scanner adjusts the tube's length to maintain a constant signal from the proximity sensor, resulting in a constant tip-sample separation. The trajectory of the probe tip thereby follows the contours of the sample surface. To accurately measure the tip motion,

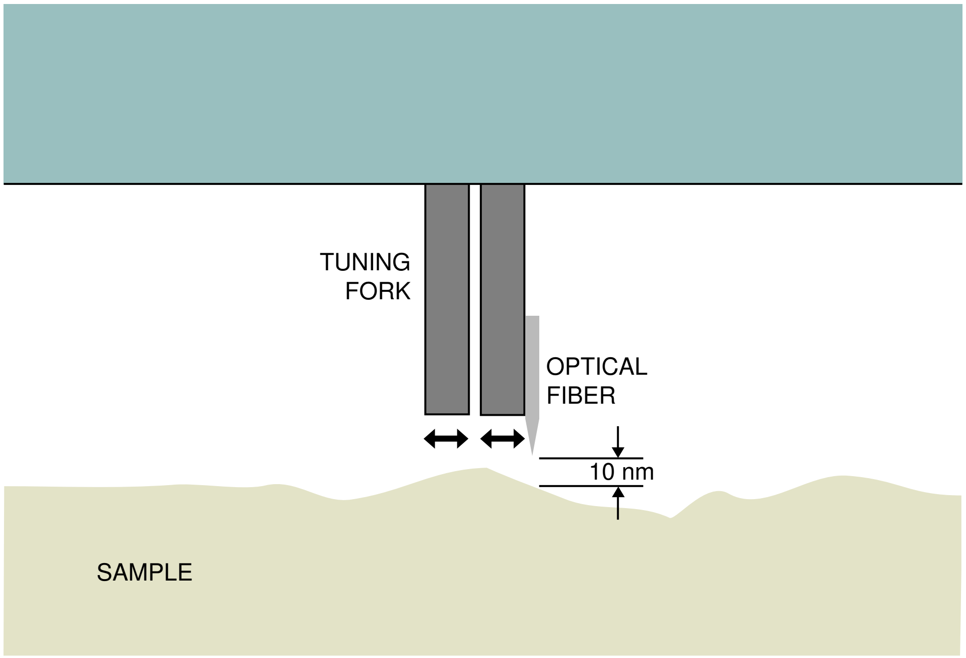

Figure 1-2: Schematic drawing of tuning fork sensor. A tapered optical fiber is bonded to one of the tines on a quartz tuning fork crystal. When the fork is electrically excited near its resonance and the tip is brought within tens of nanometers of the sample surface, the tuning fork's dynamics become sensitive to nanometer-scale changes in the gap size.

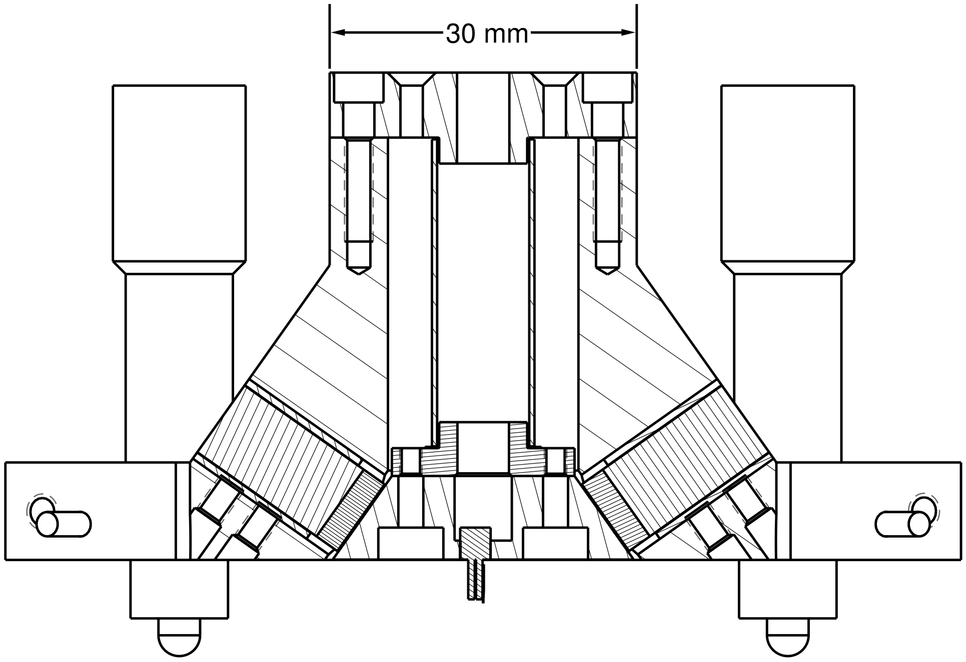

Figure 1-3: Cross-section of the metrological AFM head. As shown in this drawing, the AFM's capacitance sensors are aligned with their measurement axes meeting at a single point. We nominally eliminate Abbe offset from measurements of the probe's displacement by locating the probe tip at the axes' point of intersection. The indicated head diameter dimension at the top of the drawing shows the size of the head.

and therefore the sample topography, we align the capacitance sensors' measurement axes such that they intersect at a single point, coincident with the probe tip. This novel configuration, shown in Figure 1-3, minimizes Abbe offsets of the measurement axes with respect to the tip.

We have built and tested the AFM described above. The assembled AFM head mounted on its base plate is shown in Figure 1-4. This microscope can scan sample regions of an area of approximately 10 μm x 10 μm, with maximum peak-to-peak height variation of about 1 μm. This system has demonstrated -3 dB closed-loop bandwidths of 189 Hz and 191 Hz in the X and Y axes, respectively, and of up to 184 Hz for the probe's axial following action.

With this system, we have successfully acquired image data from, for example, a squarewave silicon grating with a calibrated 104.5 nm step height and a 3000 nm

Figure 1-4: The metrological AFM head mounted on its base plate. Extension springs preload a kinematic coupling between balls at the ends of the coarse-approach micrometers and grooves in the plate. The small microscope shown in the lower-left corner of the picture is used to visually monitor the probe's position during coarse approach of the head.

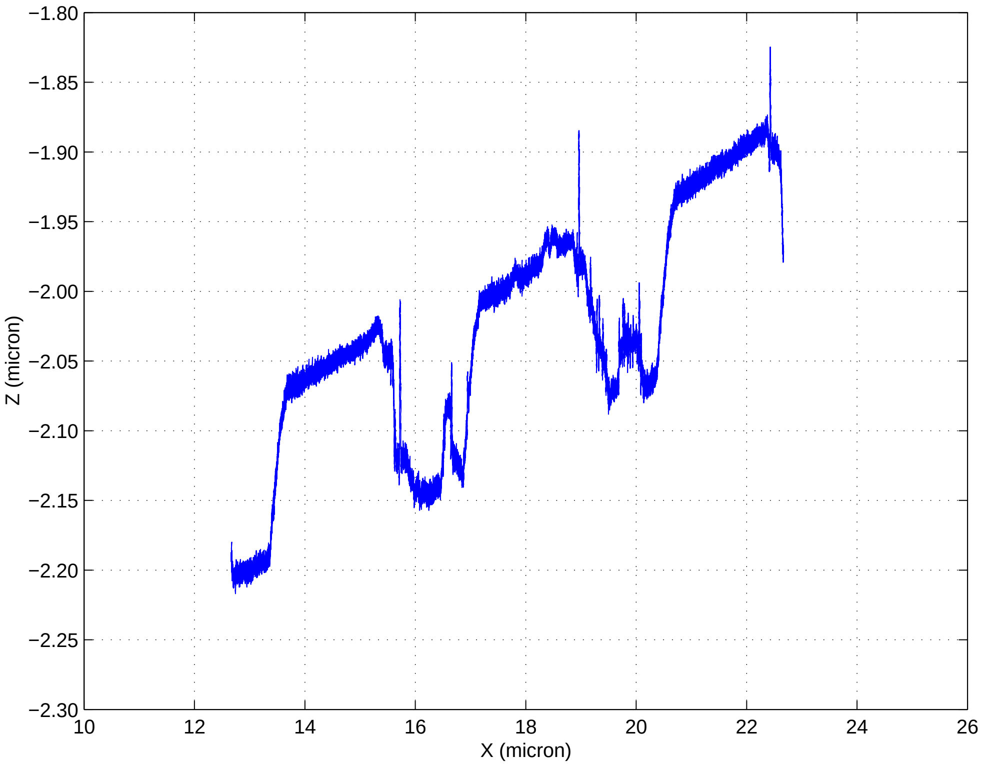

Figure 1-5: Linescan taken of a squarewave grating with 104.5 nm peak-to-peak amplitude and 3000 nm pitch. Three ridges are clearly detected by the AFM. However, the data also contains some image errors.

pitch (manufactured by MikroMasch[1]). Figure 1-5 shows data from a linescan of this grating. As seen in the figure, the AFM has successfully detected the grating features, although there are also clearly some significant image errors. These errors include large vertical spikes at the falling (right) edges and two unexpected bumps between the ridges. The causes of these errors may be related to either a blunt tip or dirt buildup. The data also indicates step height and pitch values which are significantly larger than those of the actual grating. This error likely results from the AFM's position sensors not being well calibrated for the small, curved target surface used in the head.

The microscope has also been used to take three-dimensional scans of the grating

---

[1] See Appendix B.

surface. The image shown in Figure 1-6 represents the best demonstration, to date, of the metrological AFM's imaging capabilities. The data was acquired by David Otten, and the plot was generated with the assistance of Katherine Lilienkamp. The scan generally looks quite good, except for several small spikes observed at various points along the scan trajectory, where the probe tip loses tracking of the surface. The reason for the loss of tracking has not yet been determined, but may be the result of a defect in the probe tip's geometry. In this image, the measured surface features again appear larger than their actual size, likely because the sensors are not properly calibrated for their target. Additionally, several large bumps are visible on the grating surface. We believe these bumps correspond to specks of dirt that have collected on the surface over time.

1.2 Thesis Overview

The remainder of this chapter presents the context of and motivation for the metrological AFM project, and includes a brief history of atomic force microscopy. In Chapter 2, we describe the development of an open-loop prototype AFM, which we built to gain familiarity with several components of our AFM design, particularly the piezoelectric tube scanner and the tuning fork proximity sensor. Chapter 3 details the mechanical design of the metrological AFM. Chapter 4 explains the integration of the probe position data collected from the microscope's capacitance sensors. Chapter 5 covers the PC-based digital controllers implemented with the imager. Chapter 6 describes the results achieved and presents some of the images captured with the AFM. Finally, in Chapter 7, we discuss the lessons learned from this research and offer some suggestions for future work.

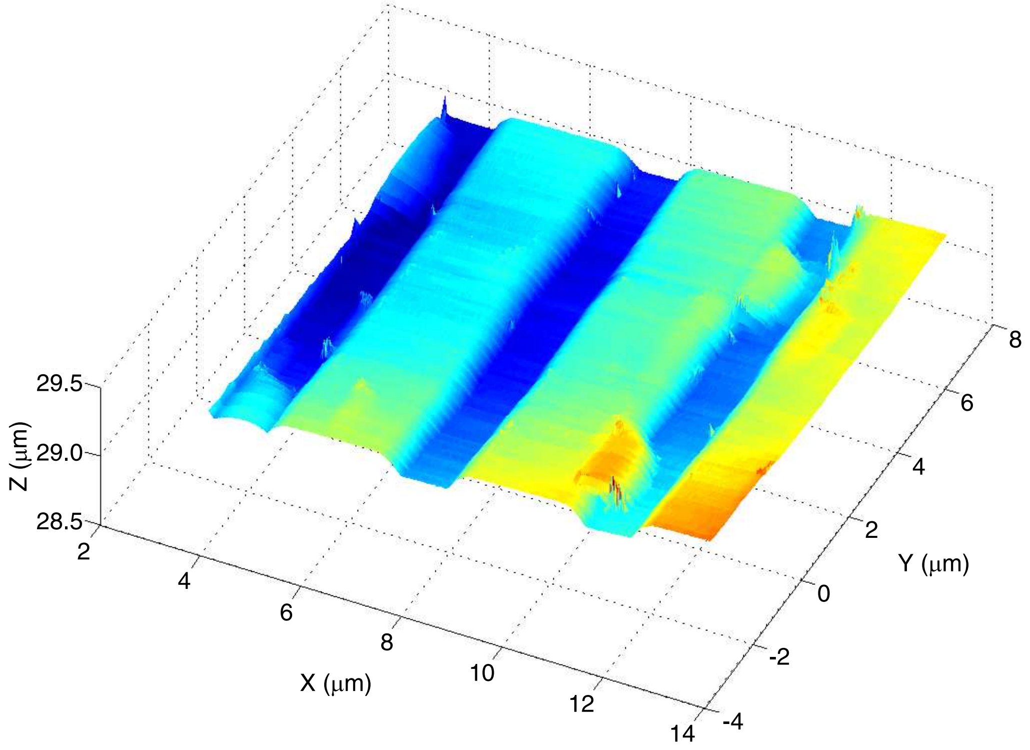

Figure 1-6: Three-dimensional image of a squarewave grating surface taken with the metrological AFM head. The grating has a calibrated step height of 104.5 nm and a pitch of 3000 nm. The image data was acquired by David Otten, and the plot was generated with assistance from Katherine Lilienkamp. Several bumps are observed on the grating surface, which are believed to be small accumulations of dirt.

1.3 Background

1.3.1 Atomic Force Microscopy

Scanning probe microscopy (SPM) originated with the invention of the Topografiner by Young [43] in 1972. This device measured the voltage of a field emitter probe [42] operated at constant current and brought close to a conducting surface while piezoelectric actuators laterally scanned the tip, to produce an image of the surface topography. Though Young presented some intriguing results, this approach to high-resolution imaging did not provoke much research interest until Binnig and Rohrer [4] demonstrated atomic resolution with their scanning tunneling microscope (STM) in 1982. The significance of the SPM was recognized with the awarding of the Nobel Prize in Physics in 1986 to these two researchers for their work with the STM. In the same year, Binnig [3] introduced the atomic force microscope.[2]

Whereas conventional far-field optical microscopes collect electromagnetic radiation in parallel to produce an image of a sample, an SPM instead relies on serial collection of its image data at discrete points throughout the sample plane. Though there now exists a wide variety of SPM types, they share the same basic mode of operation: a sharp probe raster scans over the surface of the sample,[3] while sensing some form of probe-sample interaction. Without reliance on far-field electromagnetic waves for detecting surface features, SPMs circumvent the issue of diffraction, which limits the spatial resolution of conventional optical microscopes to about 200 nm. SPMs have demonstrated resolutions down to the atomic scale (i.e., on the order of 0.1 nm). The ability to image to such fine detail is important for the semiconductor industry, biology, material science, and a host of other fields [39].

To understand the AFM's place in the SPM family, it is instructive to first study the operating principles of the scanning tunneling microscope. The following de-

---

[2] Sometimes referred to as the scanning force microscope (SFM).

[3] Conversely, the sample is sometimes scanned beneath the probe.

scription is a summary of these principles. For a more thorough explanation, refer to [7].

An STM operates by measuring the electron tunneling current[4] between a conducting probe tip and a conducting sample surface to sense the proximity of the probe to the sample, while a piezoelectric actuator[5] scans the tip over the surface. The typical probe-to-sample gap is on the order of 0.5-5 nm. With a constant voltage difference applied between tip and sample, the tunneling current decays exponentially with increasing tip-sample gap size. As the tip scans laterally over the sample plane, a feedback loop adjusts the tip's height to maintain the current at a constant value. Since, on a given sample material, constant current means constant tip-sample separation, the tip traces the sample topography. In the most common approach, an image is produced by relating the piezoelectric actuator's drive voltages to the displacement of the probe tip.

Since the STM's tunneling current is exponentially related to the probe's height above the sample, the majority of the current flows through the atom on the tip closest to the sample surface — effectively providing an atomically sharp probe. Thus, the STM provides the highest resolution of all the SPM types. However, the requirement that the sample surface be conductive severely limits the STM's usefulness. For example, biological samples often must be coated with a conducting layer before being scanned by an STM, a process that can obscure important surface features. Primarily for this reason, the AFM — which does not require any special surface treatment and can be operated in a variety of media — has assumed a preferred role in many applications requiring high-resolution imaging [32].

Atomic force microscopy utilizes a wide variety of imaging modes which have been developed since the introduction of the first AFM. In one of the more common designs, a laser-based optical detector measures the deflection of a silicon cantilever, where

---

[4] Typically, on the order of a few nanoamps.

[5] In some cases, multiple piezoelectric actuators are used to provide the scanning motion.

the deflection is related to the probe-sample gap size. In this configuration, shown schematically in Figure 1-7, a photodiode detector collects laser light reflected off the back of the cantilever. A piezoelectric actuator scans the cantilever tip over the sample to produce a topographic map of the surface. One may operate this type of AFM in contact mode, where the tip is essentially dragged over the sample topography, while the scanner adjusts its height to maintain a constant cantilever deflection. An alternative is to operate in the 'tapping' mode, in which the cantilever oscillates at or near its resonant frequency, while its tip lightly pecks the surface of the sample. Here, the scanner moves up or down to keep some averaged measure[6] of the deflection fixed. In another common mode — non-contact AFM — the cantilever again oscillates near resonance, but without touching tip to sample. In this mode, the scanner attempts to maintain either a constant amplitude or frequency of oscillation [10], where the van der Waals forces [40] between tip and sample result in measurable changes in the cantilever dynamics as a function of the probe's proximity to the surface.

In 1995, Karrai and Grober [28] introduced an alternative mechanism for tip-sample distance control, using a miniature quartz tuning fork taken from a watch crystal with a sharp tip glued to the outside of one tine. For the sensor's original configuration, they mechanically excited the fork's resonance with a piezoelectric tube, with the tip vibrating parallel to the sample plane. In this arrangement, with the tip positioned tens of nanometers above the surface, the fork sensor's output signal — the voltage between two electrical contacts on the fork synchronously detected with a lock-in amplifier — is sensitive to small changes in the probe-sample separation. In later work, Karrai and Grober [29] presented a minor, but important, modification, by removing the mechanical dither from the sensor subsystem. Here, a small sinusoidal voltage is applied directly to the tuning fork electrode pair, and synchronous detection of the current drawn by the fork provides the feedback signal to the gap regulator.

---

[6] e.g. the root-mean-square (RMS) value

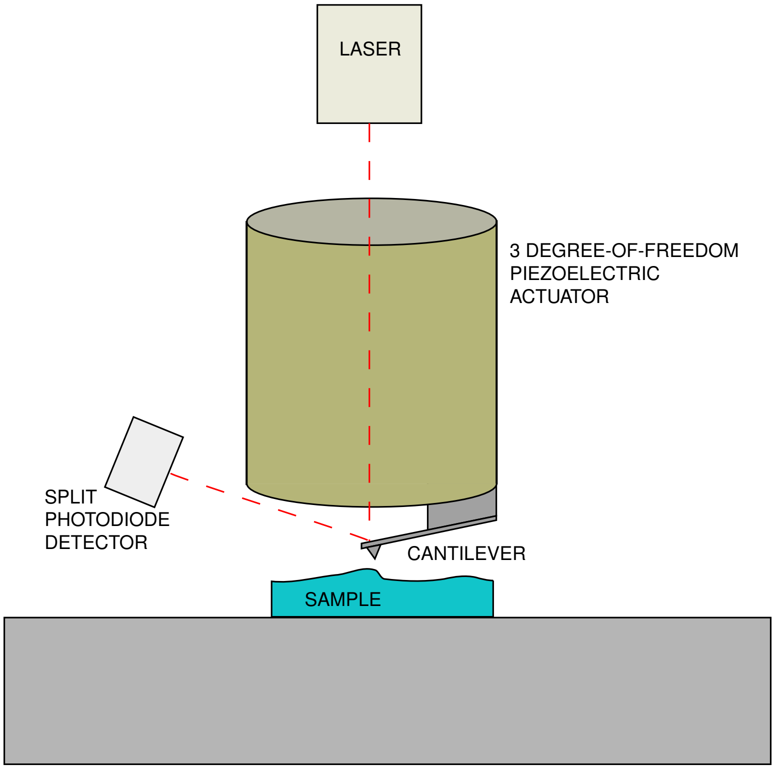

Figure 1-7: Schematic drawing of a canitilever-based AFM head. This drawing is adapted from a Digital Instruments 'Scanning Probe Microscopy Training Notebook' [10].

Thus the piezo scanner no longer needs to provide vibration to the tuning fork. This decoupling of sensor and scanner simplifies the overall closed-loop control strategy. Further, the use of the tuning fork proximity sensor allows for a less complex and more compact AFM head design than can be attained using the cantilever-with-optical detector scheme.

Karrai and Grober initially developed the tuning fork sensor for use in a near-field scanning optical microscope (NSOM) [34], another member of the SPM family. Two groups oversaw much of the early development of NSOM technology: one at the same lab in Zurich that gave birth to the STM [12]; the other at Cornell University [23]. As the name suggests, this form of microscopy uses visible light to detect features on the sample surface. However, an NSOM is capable of resolving at better than the diffraction limit. NSOMs break through this limit by placing a small aperture very close to the sample surface, where the aperture diameter and tip-sample gap size are both less than the wavelength of the probe radiation. The NSOM collects image data by using the aperture as the source and/or the collector of the radiation, while scanning the aperture over the sample. To maintain the desired probe-sample separation, NSOMs generally also employ some form of proximity sensing, such as the tuning fork sensor described above. In these designs, one may acquire both topographic and optical image data in a single scan.

Though SPM designs are quite varied, they almost exclusively use some form of piezoelectric actuation to produce their scanning motion. This approach is preferred, since piezoelectric materials can provide smooth motion with exceptionally fine resolution. With a sufficiently low-noise voltage drive, these actuators are capable of positioning resolution on the sub-atomic scale. After its introduction in 1986 [5], the piezoelectric tube scanner soon became the most common three degree-of-freedom scanning device. Though generally accepted as the best choice for this application, piezoelectric actuators do have significant nonidealities in the relationship between applied voltage and tip displacement. Nonlinearities, hysteresis, creep, and aging can all introduce errors in the image data when voltage is assumed to be directly proportional to displacement, as is the case in the open-loop design frequently used in commercial AFMs [10].

A number of groups have investigated means for removing such nonlinear artifacts from SPM image data. Newcomb and Flinn [33] found that the displacement of a piezoelectric actuator is more nearly linearly related to applied charge than to applied voltage and suggested a charge control method for more precise open-loop motions. In other work, Kaizuka [27] presented the capacitor insertion method for achieving better linearity in voltage-controlled displacements. However, neither approach meets the needs of high-precision metrological applications. Jørgensen [25] describes several techniques for post-processing the image data from open-loop SPMs, again to reduce the effects of scanner nonlinearities. While some improvements can be made, none of these methods directly address the source of the errors, so they can have only limited effect.

By integrating metrology with SPMs, several groups have demonstrated significant improvements in imaging accuracy. Researchers at PTB [26] have produced an STM mounted on a closed-loop X-Y scanning stage. The stage is equipped with capacitance sensors — aligned for minimal Abbe offset — to provide feedback and image data. A single degree-of-freedom piezoelectric actuator controls vertical motion of the probe tip, while a capacitance gauge measures its displacement. All three sensors are calibrated in situ, using laser interferometry.

Similar work at the National Institute of Standards and Technology (NIST) [11] has focused on the development of a calibrated AFM (C-AFM). This device uses a set of laser interferometers to measure the lateral scanning motion of a flexure X-Y stage, while a Z-axis piezoelectric actuator adjusts the probe height. Similar to PTB's metrological STM, the C-AFM employs an integrated capacitance sensor to measure the Z displacement.

1.3.2 The Sub-Atomic Measuring Machine

The research described in this thesis forms part of the Sub-Atomic Measuring Machine (SAMM) project. The SAMM project aims to advance the state-of-the-art in precision motion control to the extent that macroscopic objects may be measured on the sub-atomic scale — a goal of particular consequence to the semiconductor industry.

The Angstrom Stage

The SAMM project has its roots in the Angstrom Stage [20], a six degree-of-freedom stage that used magnetic suspension to control motion with 0.05 nm RMS positioning noise over a travel of 100 μm in X, Y, and Z. The platen was floated in an oil bath, both to provide a well-damped system and to reduce the current drawn by the actuators in maintaining the platen position. The platen's position and orientation were measured using capacitance gauges. With the sensors sufficiently narrow-banded and amplified, the stage could achieve atomic-scale stability for short periods of time. A commercial scanning tunneling microscope was mounted to the stage's frame and was successfully used to image the surface of a graphite sample with atomic resolution.

The Long-Range Scanning Stage

The Long-Range Scanning (LORS) Stage, principally designed by Michael Holmes in his doctoral thesis [18], adapts several fundamental design principles from the Angstrom Stage to provide six degree-of-freedom precision motion over a significantly larger workspace than its predecessor. With the magnetic bearings replaced by maglev linear motors to position the oil-floated platen, this stage is designed to meet 0.1 nm resolution, 1 nm repeatability, and 10 nm accuracy specifications over a 25 mm x 25 mm x 0.1 mm positioning range.

Figure 1-8 shows the stage's principal mechanical components. A set of four linear motor stator windings are fixed to the bottom of the aluminum machine frame. This position allows for no moving wires and for relatively easy dissipation of heat. A corresponding set of permanent magnet arrays are located underneath the platen, directly above the stators. Each motor/magnet set is capable of lateral and vertical force control. The set of motors is thus capable of regulating position in six degrees of freedom. A Zerodur reference block is mounted to the top of the platen, via a set of flexures. This block provides the reference surfaces for the stage's capacitive and interferometric position sensors. During imaging, a sample sits within a kinematically-mounted sample holder, in a recessed section of the reference block. The active measurement portion of the capacitance probes and the laser interferometers are mounted on a Zerodur metrology head, which is kinematically mounted to the top of the machine frame. The Zerodur metrology head contains three laser interferometers for lateral position measurements (X, Y, and yaw) and three capacitance probes for vertical position measurements (Z, roll, and pitch). The metrology head also includes a notch and a set of grooves, for installing a kinematically-mounted SPM head.

The SAMM

The Sub-Atomic Measuring Machine [16] represents a continued development of the LORS Stage, in an effort to achieve the full promise of the LORS design. To date, this system has demonstrated measurements of sub-nanometer resolution, 1 nm repeatability, and on the order of 30 nm accuracy, utilizing a metrological microscope designed by Dr. Robert Hocken and Dr. Chunhai Wang.

One of the initial goals of the LORS project was the characterization of the stage's error motions from STM measurements. However, experiments indicated that the original STM head was not sufficiently accurate for this purpose. The desired measurements have since been obtained using Wang and Hocken's optical microscope. In

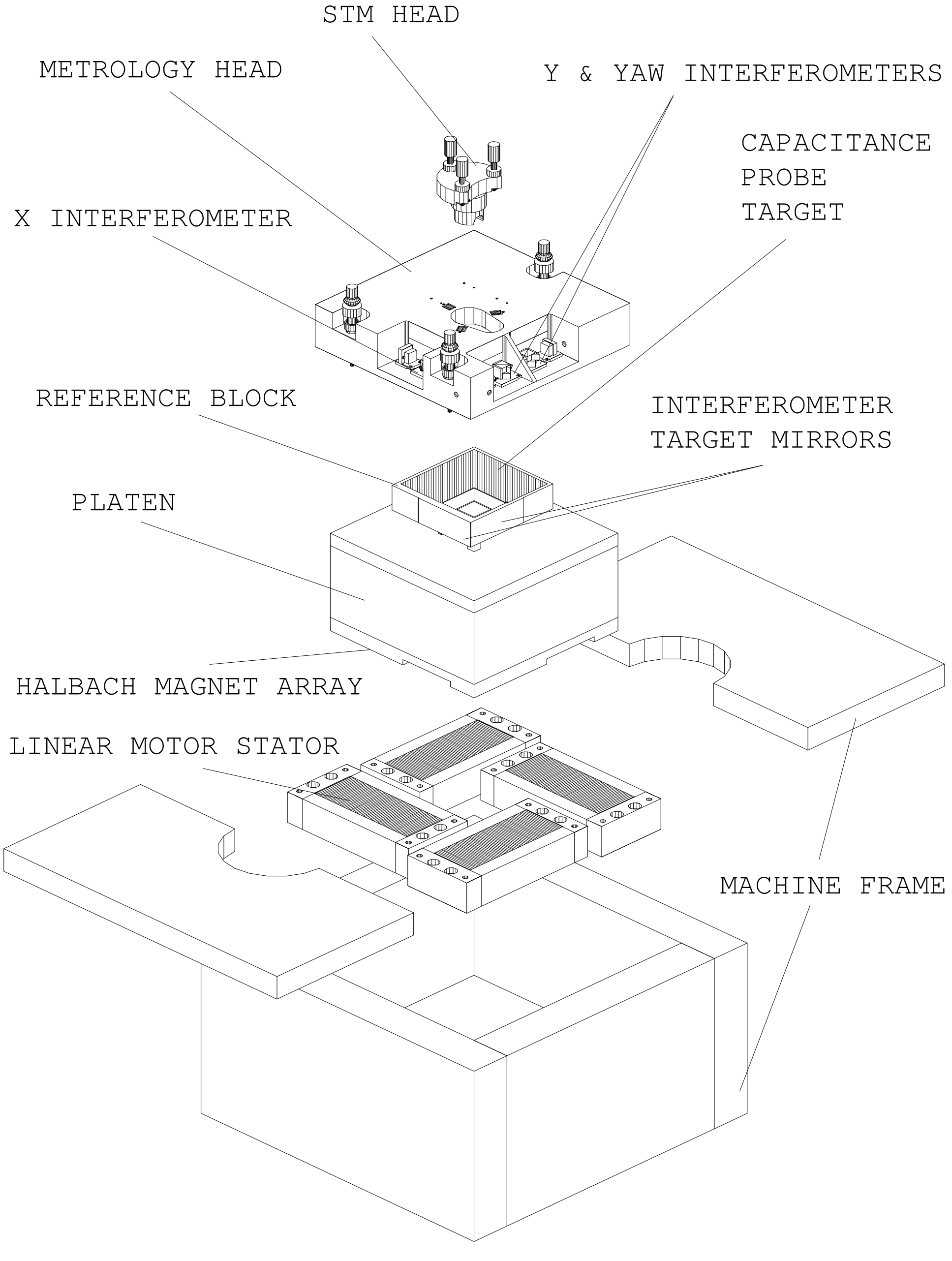

Figure 1-8: Exploded view of the LORS Stage. This drawing is taken from Michael Holmes' doctoral thesis [18].

the future, the SAMM Stage will be equipped with a metrological AFM head, which will replace the commercial STM used during initial testing of the LORS Stage, and whose performance can be compared with the optical microscope results of Wang and Hocken. The metrological AFM described in this thesis serves as a prototype for this upcoming SAMM AFM. The combined system will provide a mechanism for imaging sub-atomic features over scans of macroscopic extent.

Chapter 2

Open-Loop Prototype AFM

As the first significant step in this thesis research, we developed an open-loop prototype AFM that incorporates several of the components that were later implemented in the metrological AFM. This chapter details the prototype's development.

Section 2.1 begins with a description of the AFM's key actuation and sensing elements and discusses the reasons for abandoning our initial plans to integrate closed-loop metrology with the microscope head. Section 2.2 then discusses the prototype AFM's two primary electrical systems: the high-voltage amplifier which drives the piezoelectric tube scanner, and the tuning fork sensor measurement circuit. With the microscope's mechanical and electrical elements in place, we implemented an integral controller to close the loop on the axial height regulation system, as detailed in section 2.3. Section 2.4 presents image data collected with the prototype AFM, which appears to demonstrate basic functioning of the imaging system. Finally, section 2.5 wraps up the chapter by reviewing some of the observations made during the microscope's development. Overall, the prototype AFM provided valuable hands-on experience, while illuminating several issues which later would be important for the successful design and instrumentation of the metrological AFM.

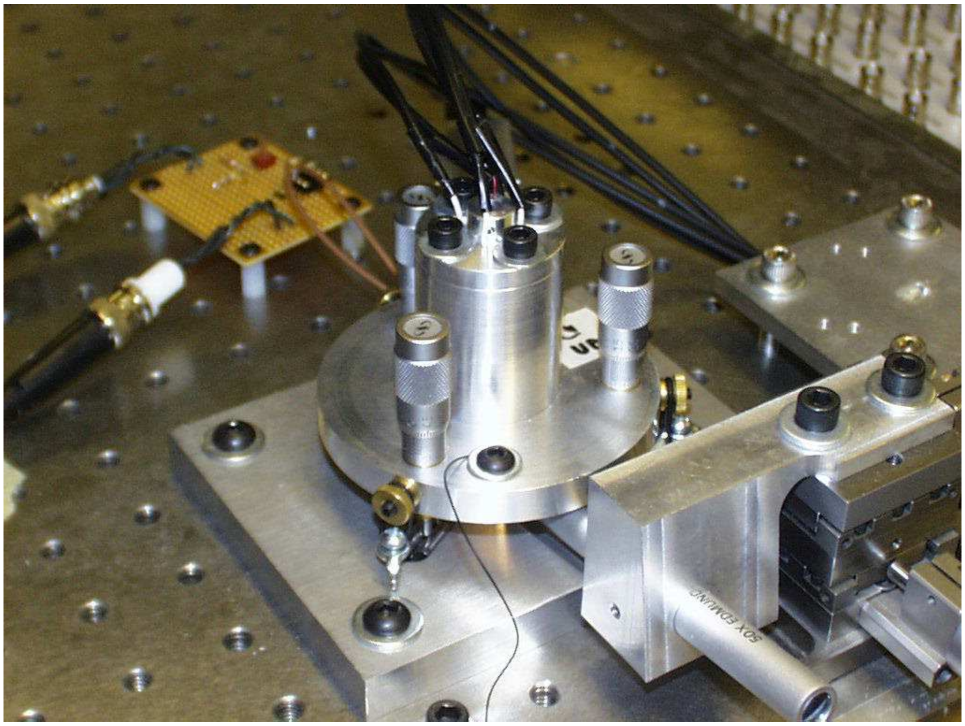

Figure 2-1: The open-loop prototype AFM head.

2.1 Mechanical Design

The assembled open-loop prototype AFM head is shown in Figure 2-1. The microscope uses a piezoelectric tube scanner to provide three degree-of-freedom motion of the probe tip. The tip is attached to a quartz tuning fork, whose output is a function of the probe-sample gap size. We originally designed the AFM head to incorporate a set of inductive sensors to directly measure the displacement of the microscope's scanner assembly, but later found that these sensors would not work simultaneously on a single target due to interference effects.

The remainder of this section explains how the tube scanner and tuning fork proximity sensor are employed in the prototype AFM — in a manner similar to their eventual implementation in the metrological AFM. The discussion then turns to the inductive position sensors, the initial plan for their implementation, and the reasons why interference prevented their use as planned. Remaining details of the

Density	7.80 g/cm^3
Dielectric Constant, ε_{33}	2400
Mechanical Q	120
Curie Temperature	250°C
d_{31}	-220×10^{-12} m/V
d_{33}	450×10^{-12} m/V
Elastic Constant, s^e_{11}	15.0×10^{-12} m/V
Coercitive Field	620 V/mm

Table 2.1: Material properties for PIC 151.

microscope's mechanical design are presented at the end of the section.

2.1.1 Piezoelectric Tube Scanner

As mentioned in section 1.3.1, the piezoelectric tube scanner is the most common scanning mechanism in SPM designs, primarily because of its simplicity, compact size, high stiffness, and ability to provide positioning resolution on the sub-atomic scale. Figure 2-2 shows a drawing of one of these tube scanners. The thin-walled cylinder is a monolithic piezoelectric ceramic. The entire inner surface of the tube is covered with an electrode material. The outer surface is covered with a set of 'quartered' electrodes, in four evenly spaced patches which run the length of the tube. In both prototypes used in this thesis, we use a Physik Instrumente (PI) PT-130.24 tube scanner.[1] This scanner has an outer diameter of 10.00 mm, an inner diameter of 9.00 mm, and a length of 30.0 mm.[2] We believe the tubes are made of PIC 151 material.[3]

Here, we describe some basic practical aspects of a piezo tube scanner's operation.

---

[1] Company information listed in Appendix B, under Polytec PI, Inc.

[2] These dimensions are the nominal values listed on the manufacturer's website.

[3] The manufacturer lists three different materials used in their tube scanners. Based on the observed relationship between the driving voltage and the resulting displacement of the metrological AFM's scanner assembly, we believe that its tube scanner was made from PIC 151. The values of the other two ceramics' material properties generally differ from those of PIC 151 by a factor of two or less, so the values listed here should be representative of the true material properties, even if the tube is in fact made from one of the other ceramics.

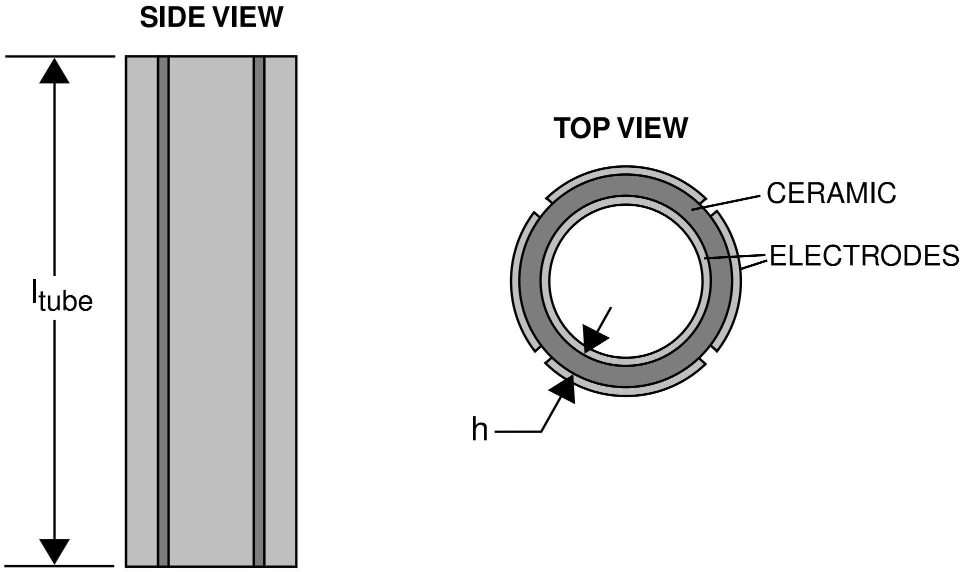

Figure 2-2: Drawing of the piezoelectric tube scanner. The thin-walled ceramic tube has an electrode covering its inner surface and four electrodes running length-wise along its outer surface.

A much more detailed and comprehensive treatment of the behavior of piezoelectric materials may be found in [22].

When an electric field is applied to the tube's ceramic, the tube deforms. The quartered electrode configuration allows us to individually control the field present in the tube's four quadrants. With reference to Figure 2-3, when all four outer electrodes are held at a common voltage, V_{axial}, while the inner electrode is grounded, the tube's length changes according to

$$\Delta l_{tube} = \frac{d_{31} l_{tube} V_{axial}}{h}, \tag{2.1}$$

as presented in [9]. Here, l_{tube} is the nominal length of the tube, Δl_{tube} is the change in length, d_{31} is one of the ceramic's piezoelectric coefficients, and h is the tube's wall thickness.

Figure 2-4 shows the voltage condition used to move the probe tip laterally. A differential voltage pair, $+V_{lateral}$ and $-V_{lateral}$, is applied to an opposing pair of outer

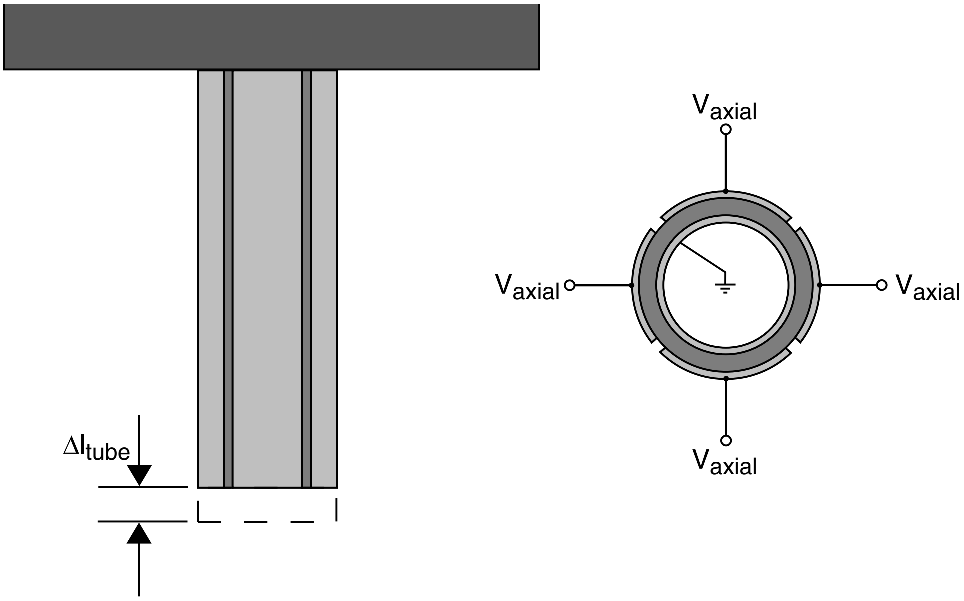

Figure 2-3: Sketch of the voltage condition used to axially displace the free end of the piezoelectric tube scanner.

electrodes, while the other two outer electrodes and the inner electrode are all held at ground potential. With the differential voltage drive, one of the driven quadrants extends, while the other one contracts, resulting in a net bending effect. From basic geometry (Figure 2-5), the tip's lateral displacement is

$$\begin{aligned}\Delta x_{tip} &= \Delta x_{tube} + l_{tip}\sin\theta \\ &\approx \Delta x_{tube} + l_{tip}\theta,\end{aligned} \tag{2.2}$$

where Δx_{tube} is the lateral displacement of the tube's free end, l_{tip} is the distance from the bottom of the tube to the probe tip, and θ is the (small) angle between the tangent to the tube at its free end and the vertical axis. This angle is related to the tube's radius of curvature, R, according to

$$\theta = \frac{l_{tube}}{R}. \tag{2.3}$$

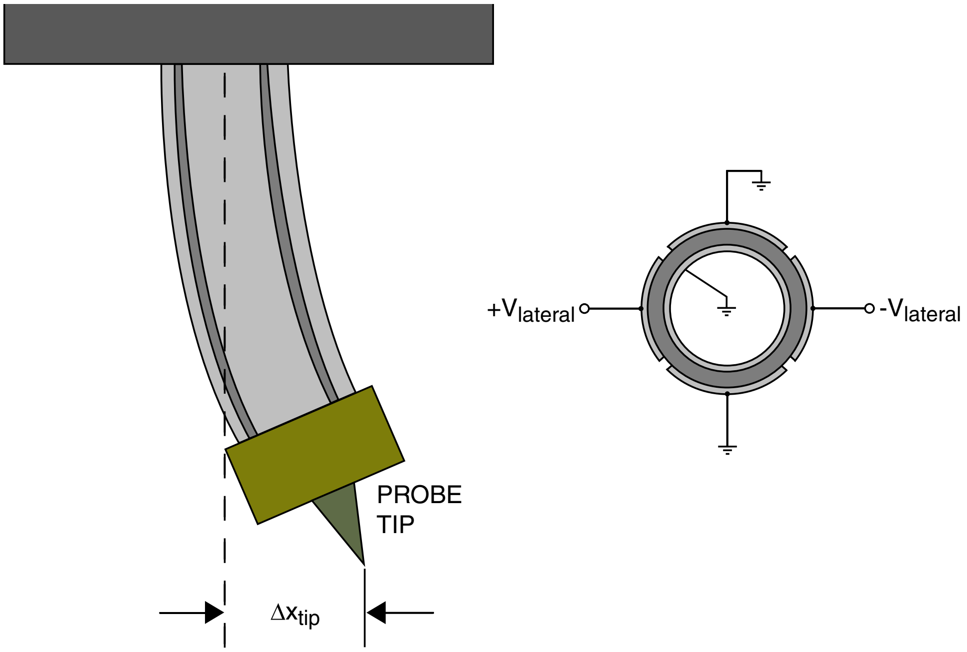

Figure 2-4: Sketch of the voltage condition used to laterally displace the free end of the piezoelectric tube scanner.

Again from the tube's geometry,

$$\begin{aligned}\Delta x_{tube} &= (1-\cos\theta)\,R \\ &\approx \frac{R\theta^2}{2},\end{aligned} \tag{2.4}$$

where the approximation is valid under the assumption that θ is small, which is valid for the small tip motions involved. Substituting equations (2.3) and (2.4) into equation (2.2),

$$\Delta x_{tip} \approx \left(\frac{l_{tube}}{2} + l_{tip}\right)\frac{l_{tube}}{R}. \tag{2.5}$$

An expression for R is presented in [9],

$$R = \frac{\pi D h}{4\sqrt{2}d_{31}V_{lateral}}, \tag{2.6}$$

where D is the tube's average diameter.

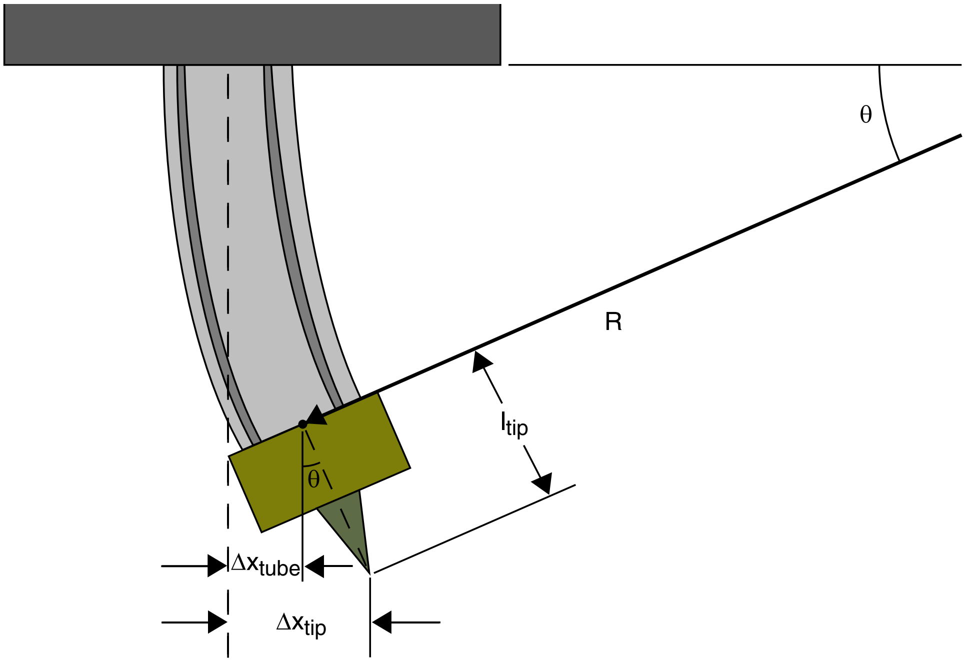

Figure 2-5: Geometry for the lateral displacement condition. Not drawn to scale.

Full three degree-of-freedom motion of the probe tip may be commanded by simply superimposing the lateral displacement voltage condition for both pairs of opposing electrodes with the axial displacement voltage condition. A multi-channel high-voltage amplifier, described in section 2.2.1, provides the desired drive levels to the tube. According to the manufacturer, the outer electrodes of the PT-130.24 tube should not be driven more than 100 V below or 500 V above the inner electrode potential, to prevent depolarization of the ceramic. The high-voltage amplifier, however, is set to output between -100 V and +100 V to each of the four outer electrodes, while the inner electrode is nominally held at 0 V. Therefore, the amplifier is the limiting factor for the tube's maximum displacement, resulting in a total vertical range of about $\pm 1.3\ \mu$m and a total lateral range at the end of the tube of about $\pm 3.8\ \mu$m. Actually, the given value for the vertical range assumes zero displacement in the lateral plane, and the lateral range value assumes zero axial displacement. When $V_{axial} \neq 0$ V, for example, the magnitude of the maximum differential voltage that the amplifier can supply to one opposing pair of outer electrodes is $|V_{lateral}|_{max} = 100\text{ V}-|V_{axial}|$. Likewise, if $|V_{lateral}| \neq 0$ V for either or both of the lateral degrees of freedom, then the range of the axial degree of freedom is correspondingly reduced.

We used the calibration fixture shown in Figure 2-7 to measure the open-loop axial displacement of the prototype AFM's tube scanner as a function of V_{axial}. In this setup, a Kaman Instrumentation[4] inductive sensor measures the position of a flat aluminum target clamped to the end of the scanner. The prototype AFM head was inverted to allow the sensor easier access to the target. An adjustable DC power supply provided the same reference input to all four of the high-voltage amplifier's outer electrode channels, while the input to the inner electrode channel was grounded (Figure 2-6). The sensor output signal was fed to a Tektronix AM 502 differential amplifier, with the gain set at 200. Figure 2-8 shows the resulting calibration data for positive increasing and decreasing values of V_{axial}. The plot clearly demonstrates the tube's nonlinear and hysteretic behavior. The average slope of the best fit lines through the two sets of data is

$$\frac{\Delta l_{tube}}{V_{axial}} \approx 22\text{ nm/V}. \tag{2.7}$$

Measurements were also taken of the tube scanner's resonant frequencies, which were significantly affected by the additional mass of the endpiece described in section 2.1.4. Using an inductive sensor to measure the lateral deflection of a target mounted to the base of the tube while the amplifier excited oscillatory lateral motion, we observed a resonant peak at about 800 Hz. The calibration fixture mentioned above was later utilized to measure the scanner's open-loop frequency response, for commanded axial motion. This data indicates the scanner assembly's first axial mode occurs at approximately 3 kHz.

---

[4] See Appendix B.

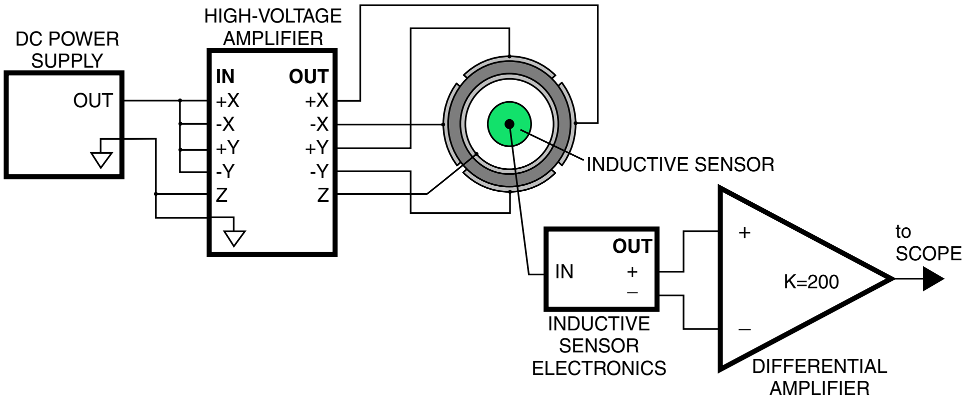

Figure 2-6: Circuit used to acquire the tube scanner axial calibration data.

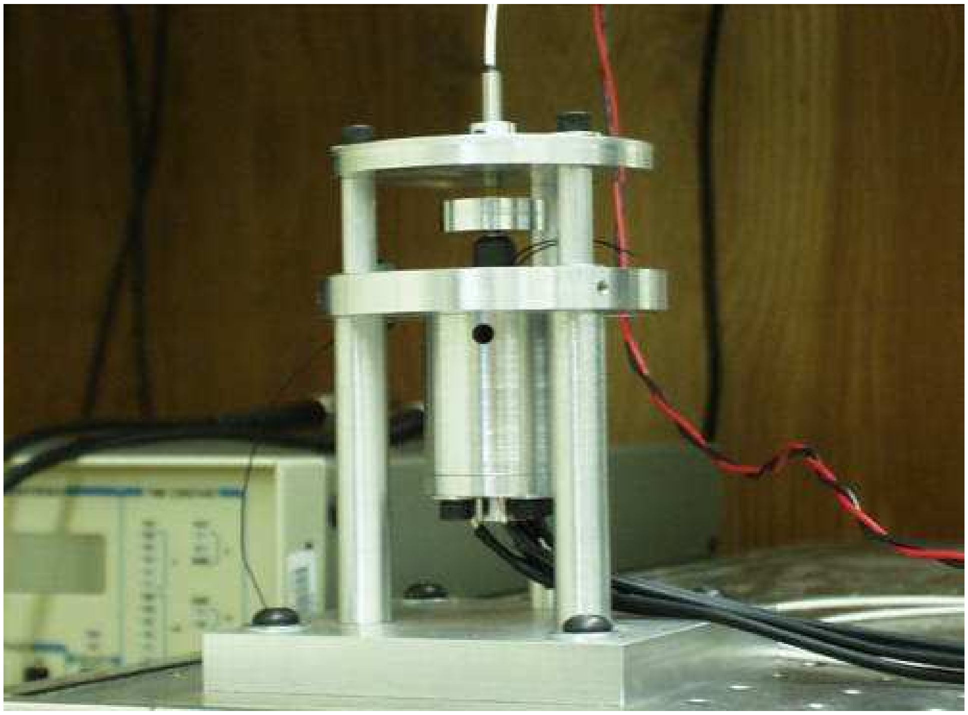

Figure 2-7: Calibration fixture used to measure the axial displacement of the prototype AFM's piezoelectric tube scanner.

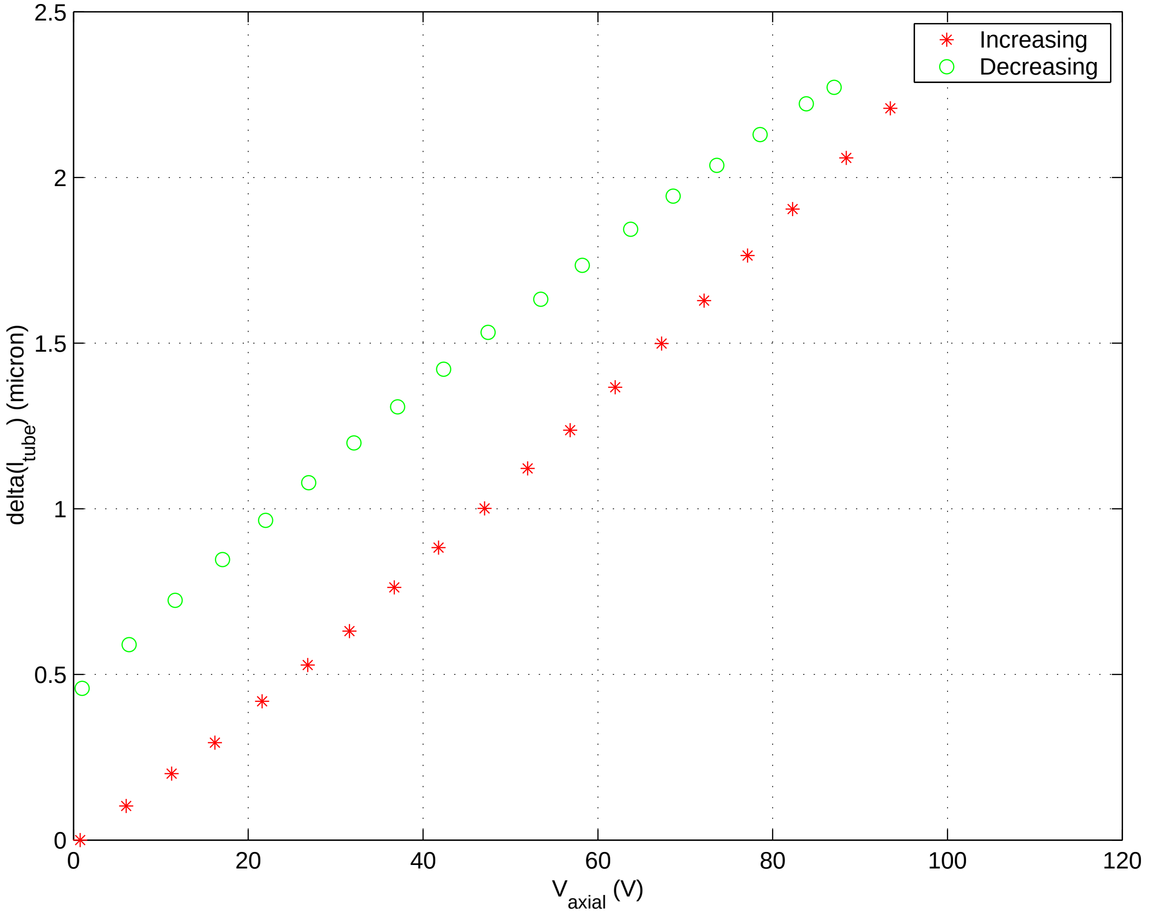

Figure 2-8: Calibration data, which demonstrates the nonlinear and hysteretic behavior of the piezoelectric tube scanner. From this data, an approximate calibration constant of 22 nm/V is determined.

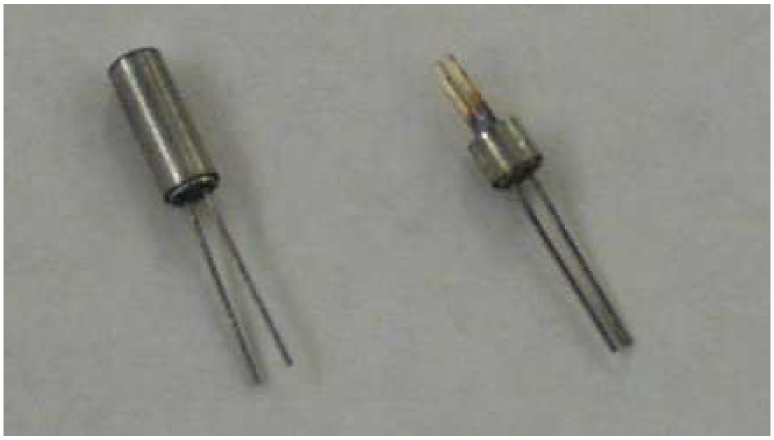

Figure 2-9: A pair of tuning forks. On the left, a fork in its original packaging. On the right, an exposed fork crystal, after the top of the can has been cut away.

2.1.2 Quartz Tuning Fork Sensor

A quartz tuning fork gauges proximity from the probe tip to the sample surface, in a manner similar to that described in [29]. These forks usually serve as timing crystals in digital watches and are available in bulk quantities at low prices (about 20 cents each). All of the proximity sensors described in this thesis are based on ECS-3X8 crystals from ECS, Inc.[5] As shown in Figure 2-9, the fork comes packaged inside a small metal can. Using a technique taught to us by Dr. Patrick Moyer, we remove the top of the can with a laser diode can opener — a Thorlabs[6] WR1 — to expose the crystal. The tool's rollers had to be moved slightly from their original position, to provide a balanced grip on the tuning fork can during the cut. This modification simply consists of unscrewing the threaded rods on which the rollers are mounted, such that the cutting wheel lines up with the rollers' surfaces.

An electrode pattern covers the front and back surfaces of the fork. A sinusoidally-varying voltage applied between the two leads connected to these electrodes excites a mechanical vibration of the tines. The amplitude of this vibration peaks in the vicinity of the fork's first mechanical resonance, which generally lies between 32.1 kHz

---

[5] See Appendix B.

[6] See Appendix B.

and 32.6 kHz, depending on how much mass is added during the tuning fork sensor assembly process. We use the oscillating crystal for shear mode proximity sensing. In this mode, the fork is oriented so that its tines vibrate parallel to the sample surface (Figure 2-10). A sharp tip protruding beyond the end of one of the tines is brought very close to the surface, within about 10 nm. When the probe comes within this range, interatomic forces between the sample surface and the end of the tip begin to have a measurable effect on the fork's dynamics. As the tip comes closer to the sample, the fork's amplitude of oscillation decreases; as the tip retracts from the sample, its amplitude increases. Since the fork is piezoelectric, changes in the fork's mechanical behavior are reflected in its electrical properties — under constant amplitude voltage drive, the magnitude of the current flowing through the tuning fork decreases as the probe moves closer to the surface and increases as the probe moves further away. This relationship between the current's magnitude and the probe-sample gap size allows us to use the measured current to close the loop on axial height regulation of the probe. The circuit described in section 2.2.2 provides the desired measurement, while the controller described in section 2.3 acts on the circuit's output to make the necessary adjustments to the probe's height.

A tapered optical fiber acts as the proximity sensor's sharp tip. The tips are made using a heating-and-pulling method similar to the one described in [2], but with a laser providing the source of heat instead of a Pt-Ir filament. We cut a strand of fiber, strip away a few inches of cladding near its midpoint, then clamp the fiber's two ends inside a commercial fiber puller. The puller's user-programmable microprocessor controls the rest of the tip-making process: a focused laser beam heats a spot on the stripped section of the fiber and melts the glass, while the two ends of the fiber are pulled apart. This method can produce tapers with tip radii smaller than 100 nm.

The tip is cut off the end of the fiber, then bonded to the side of one of the fork's tines with a drop of cyanoacrylate glue. A pair of positioning stages are used to con-

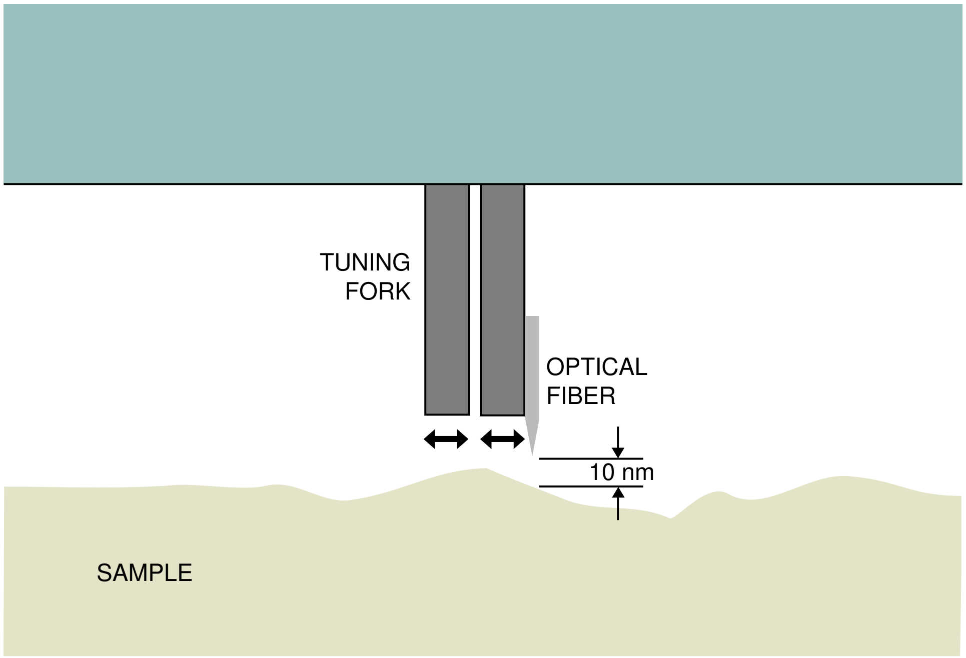

Figure 2-10: Drawing of the quartz tuning fork sensor, with a sharp tip glued to the side of the fork. We electrically excite the fork slightly below its first mechanical resonance, which produces the desired vibration of the tip. Not drawn to scale.

trol the relative position of the tip and the fork during this delicate assembly process. After the fork-fiber unit is secured in the AFM head, a sinusoidal voltage is applied to the fork's electrodes at a frequency slightly below its first mechanical resonance, generally somewhere between 32.1 kHz and 32.6 kHz. Operating at this frequency reduces the fork's sensitivity to thermal fluctuations, as compared to operating precisely on the resonant peak. As a result of the added mass of the fiber and glue, the resonance occurs several hundred Hertz below its original value of 32.768 kHz.[7] During our literature review, we found no analytical expression relating the tip's amplitude of oscillation to the fork's geometry and drive level. However, based on representative values found in [29] and [15], the ratio of the tip oscillation amplitude, $|x_{fork}(t)|$, to

---

[7] This frequency is a power of two: $32768 = 2^{15}$.

the fork's drive voltage amplitude, $|V_{fork}(t)|$, appears to be approximately

$$\frac{|x_{fork}(t)|}{|V_{fork}(t)|} \approx 0.1 \text{ nm/mV} \tag{2.8}$$

in the vicinity of resonance, for the ECS-3X8 forks we used. While testing the open-loop prototype AFM, we generally set $|V_{fork}(t)| \approx 100$ mV, corresponding to $|x_{fork}(t)| \approx 10$ nm.

The circuit shown in Figure 2-11 was used to measure the tuning fork's frequency response for four separate conditions: 1) with the metal can fully intact, 2) with the top of the can removed, 3) with the top of the can removed and a fiber glued to one tine, and 4) with the top of the can removed and fibers glued to both tines. In this circuit, a function generator drives the tuning fork with a sinusoidal voltage. A voltage divider, with 10 MΩ and 1.1 MΩ resistors, provides an input-output gain of $\frac{1}{10}$ to attenuate the function generator's output and prevent overdriving the crystal. The resistance values were picked such that the resulting Thévenin equivalent resistance equals 1 MΩ, which turns out to be much too large, as detailed below. The current flowing through the tuning fork is synchronously detected with a lock-in amplifier — an instrument that plays a key role in the tuning fork sensor measurement and which is described briefly in section 2.2.2. The magnitude R, and phase ϕ, of the current were manually recorded from the lock-in readings, as the function generator's frequency was incrementally increased. The results are shown in Figure 2-12, where only the points around the fork's resonance are included.

The data provides important insight into the tuning fork sensor's behavior. All four responses have the same general shape — the current exhibits a sharp resonance, which is followed a few Hertz later by a sharp anti-resonance. However, these curves differ in both their resonant frequencies and their Q-factors. For example, the fork's Q decreases when the top of the can is removed. This change possibly indicates that

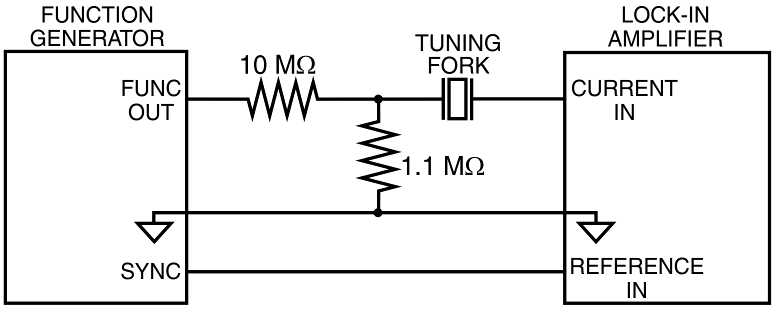

Figure 2-11: The circuit used to measure the frequency response of the quartz tuning fork sensor.

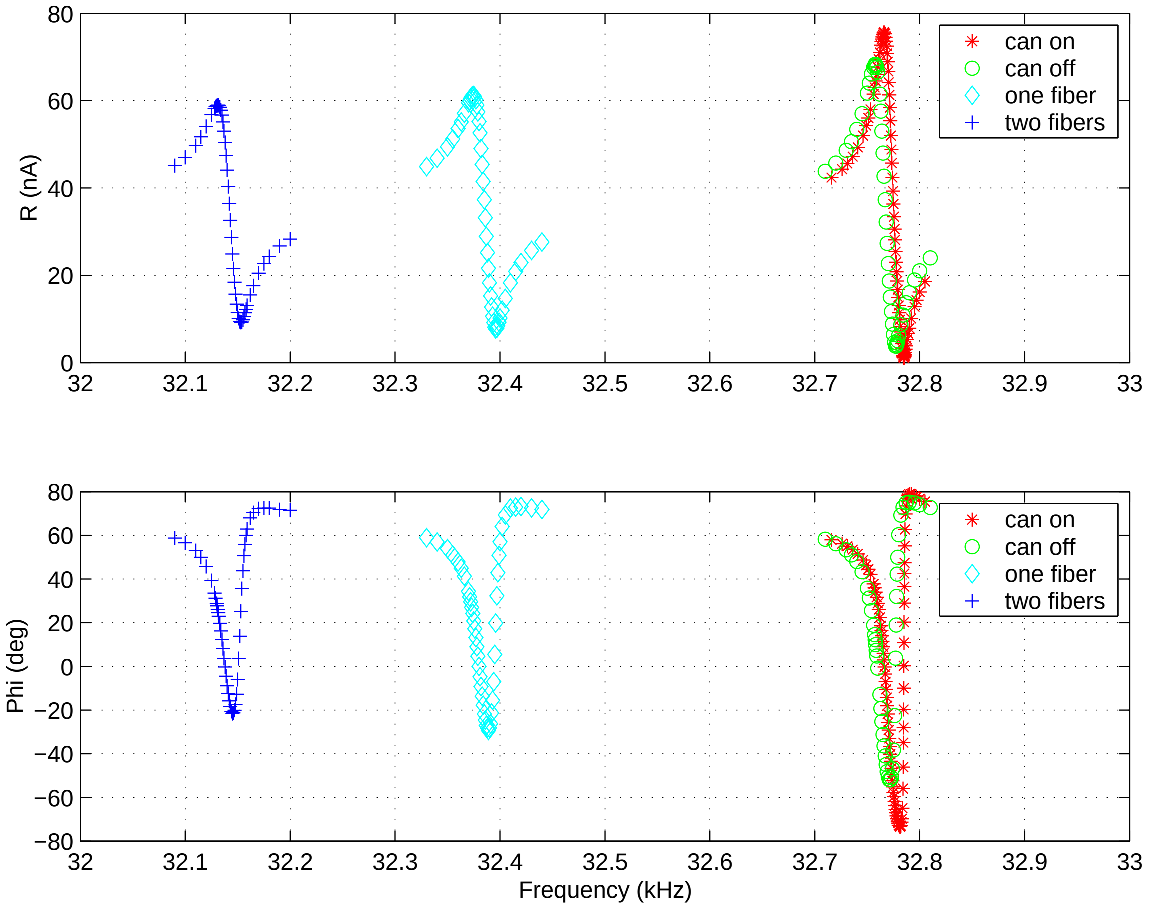

Figure 2-12: The frequency response of the tuning fork current, as measured with the circuit shown in Figure 2-11. The top graph shows the response magnitude R in units of nA, as a function of frequency. The bottom chart shows the associated phase. This data was taken with a signal generator drive voltage amplitude of 1.0 V, corresponding to a tuning fork drive voltage of approximately 100 mV.

the interior of the can is initially evacuated and that the loss of vacuum dampens the resonant peak. When a fiber is glued to the crystal, the Q drops again and the resonant frequency decreases by several hundred Hertz. The lowering of the resonant frequency results from the additional mass of the fiber and glue, while the reduction in Q is due to the additional losses in the glue joints and to breaking of the fork's symmetry.

The fourth set of data represents an attempt to use the technique described in [41], where an extra mass is added to the unused side of the tuning fork crystal to counterbalance the mass of the tip. The referenced article demonstrates a significant increase in Q using this balancing mass. However, we were not able to reproduce their results, perhaps because the two masses used in our experiment were not precisely matched. Since we were able to achieve a fairly high Q with just the single fiber glued to the fork, we did not spend much time pursuing this dual fiber approach.

As mentioned earlier, the circuit shown in Figure 2-11 is somewhat flawed. Since the voltage divider's resistors are so large — 10 MΩ and 1.1 MΩ — the circuit is much more sensitive to stray capacitance than is necessary. This unmodelled capacitance provides a relatively low-impedance path to ground, as compared to the resistors' impedances and considering the relatively high frequency of the drive voltage — over 32 kHz. In fact, the voltage divider's resistors could be made smaller by a factor of about 10,000 without drawing too much current from the function generator. We reconfigured the measurement circuit with smaller resistors for later tests with the open-loop prototype AFM, but did not remeasure the tuning fork's frequency response after doing so. Nevertheless, the data shown in Figure 2-12 should be a qualitatively accurate representation of the fork's true behavior.

2.1.3 Probe Position Sensors

We originally planned for the prototype AFM to incorporate closed-loop metrology, using three inductive sensors to directly measure the three-dimensional trajectory of a brass block mounted to the end of the piezoelectric tube scanner. For an explanation of the operating principles behind inductive sensors, as well as a discussion of several practical considerations related to their usage, refer to [6].

An inductive sensor works by generating a time-varying magnetic field from a coil on the sensor's face. When the sensor comes close to the surface of a conductive material, the time-varying magnetic field causes eddy currents to form in the material. The strength of the eddy currents varies as a function of the sensor-target gap, resulting in a measurable change in the sensor coil's impedance. The sensor's electronics detect the impedance variation and thereby develops an output voltage which, to first order, is linearly dependent on the gap size.

The drawing in Figure 2-13 shows the prototype AFM with the planned sensor configuration. One sensor would be aligned along the axis of the tube scanner and would measure the vertical displacement of a flat target surface located inside the tube. The other two sensors would be mounted in a plane perpendicular to the tube's axis and aimed at the block's cylindrical target surface, to provide measurements of the scanner assembly's lateral motion.

During testing of the axial displacement sensor, the sensor's output was found to be insensitive to the tube scanner's motion. A simple experiment led to this conclusion: with the sensor mounted in the AFM head, we applied a small axial force to the end of the tube. Based on the tube's stiffness, the magnitude of this force should have been enough to result in a relatively large change in the sensor's output. However, the measured signal barely registered any change at all.

Apparently, the sensor cannot operate properly within the tube's inner electrode, which resulted in eddy currents being generated within the tube itself. In support of

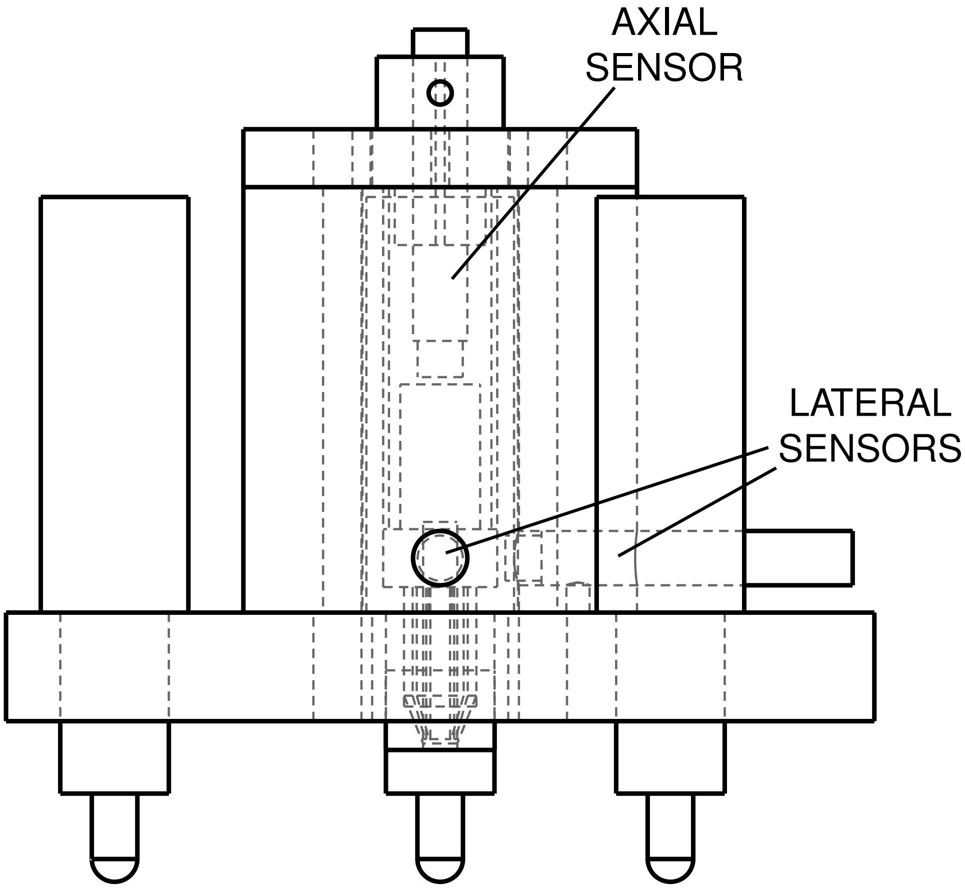

Figure 2-13: Drawing of the prototype AFM head with inductive sensors. Tests revealed several problems with this metrology design; chief among these is interference between the three probes. Additionally, the axial sensor does not operate properly within the conductive inner surface of the tube scanner.

this view, the sensor's output changed significantly as a function of depth inside the tube, even while the target surface was clearly beyond the sensor's range. We tried to reduce the unwanted eddy currents by scraping vertical lines into the electrode, thereby attempting to break the eddy-current path in the electrode, but this effort did not measurably improve the sensitivity.

The two lateral position measurements were also problematic. While running only one of these sensors, we found it was satisfactorily sensitive to the tube's lateral motion. However, with both sensors active, a large 5 Hz signal component dominated the sensors' output. This problem resulted from the two sensors operating from separate oscillators with slightly different frequencies. When the sensor faces were brought close to one another inside the AFM head, cross-talk between the two coils resulted in a low-frequency beat effect. With such large-amplitude, low-frequency noise, we were unable to measure the DC component of the tube scanner's lateral position, rendering the sensors unusable.

Though we believe we understood the problems that we faced during initial testing of the prototype AFM's inductive sensors, we decided not to devote too much time trying to resolve them. We instead removed the sensors from the head and shifted our focus to proving out the functionality of the open-loop system.

2.1.4 Design Details

The open-loop prototype AFM's scanner assembly is shown in Figure 2-14. The piezoelectric tube scanner mounts to a nub on the bottom of an aluminum disk. A Delrin ring sandwiched between the tube and the nub insulates the aluminum from the tube's electrodes. A two-part epoxy holds the joint together.

The mechanism used for holding the tuning fork sensor is mounted at the opposite end of the tube. The photo in Figure 2-15 is an exploded view of this assembly. A nub on the top of the brass endpiece slips inside the bottom end of the tube scanner,

Figure 2-14: The open-loop prototype AFM's scanner assembly. A piezoelectric tube scanner mounts to the bottom of the housing cap. The tuning fork sensor mounting mechanism is located on the other end of the tube. The fork is held in a collet taken from a Dremel tool. This picture also shows the back end of the axial displacement sensor, which was eventually removed from the AFM head.

again with a Delrin ring providing insulation and with two-part epoxy solidifying the joint. A collet mechanism clamps the tuning fork can at the bottom of the endpiece. We adapted this design from a Dremel[8] rotary tool, since a quick test with our lab's Dremel indicated that the tuning fork can fits nicely inside its standard 1/8" diameter collet. The dimensions of the brass endpiece were made similar to those of the collet receptacle at the end of the Dremel tool's spindle, so we could directly use the Dremel's collet and collet nut. To mount the fork, we slide the can inside the collet, insert the collet into the hole in the bottom of the endpiece, and — careful not to damage the fork or the fiber tip — slip the collet nut over the endpiece's male threads. As the nut is tightened onto the endpiece, the collet squeezes against the can and firmly holds it in place. A hole in the side of the endpiece provides an exit route for the wires connecting the tuning fork leads to the proximity sensor measurement circuit.

Figure 2-16 shows the assembled open-loop prototype AFM head. The scanner assembly fits inside a hole in the center of the AFM housing body and is bolted into place. An aluminum disk with a diameter large enough to fit a set of three micrometer heads bolts to the bottom of the housing body. The micrometers are used for coarse height adjustment of the probe tip's height and are clamped to the disk with set screws. Balls at the ends of the micrometer spindles sit in grooves formed between pairs of steel dowel pins, which are epoxied inside notches in the aluminum base plate (Figure 2-17). Rubber O-rings preload this kinematic coupling. A small 50x-magnification microscope mounted off the side of the AFM head provides a close-up view of the probe tip. This coarse approach viewer allows us to quickly move the tip close to the surface, without accidentally crashing it into the base plate.

---

[8] See Appendix B.

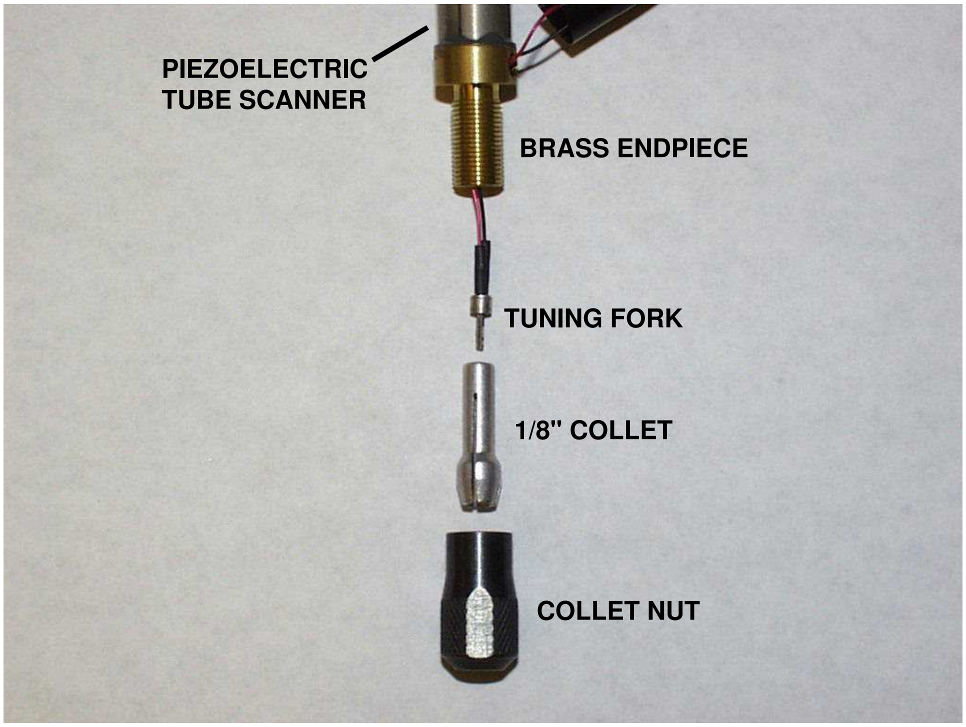

Figure 2-15: The collet mechanism used to clamp the tuning fork sensor to the scanner assembly. We designed the brass endpiece so we could directly use the collet and nut from a Dremel rotary tool set.

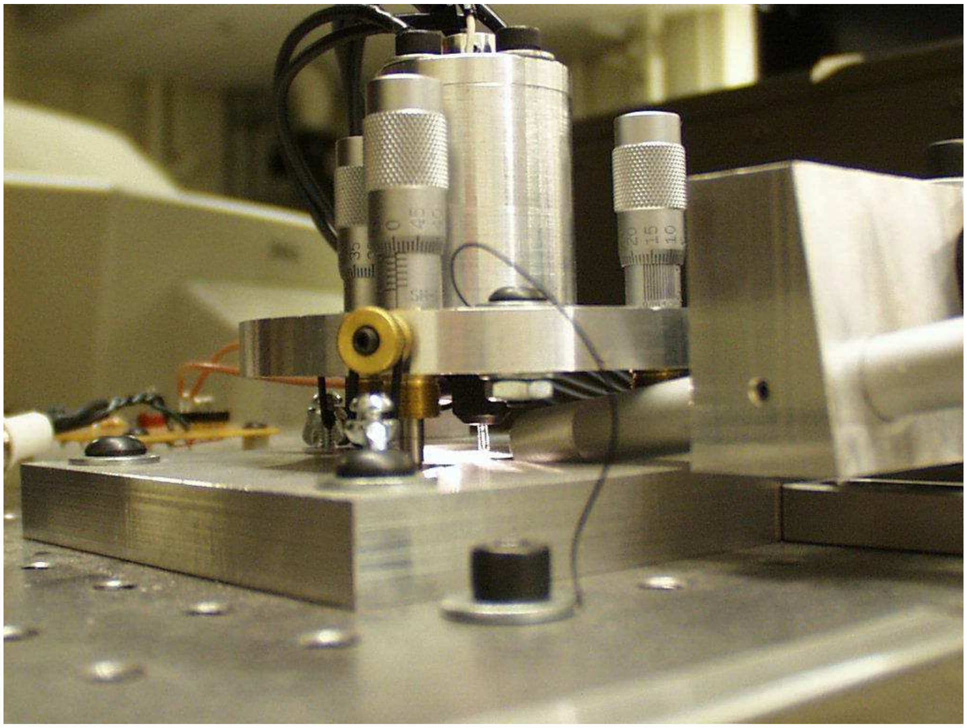

Figure 2-16: The assembled prototype AFM head. In this photograph, the quartz tuning fork can be seen protruding from the bottom of the collet nut.

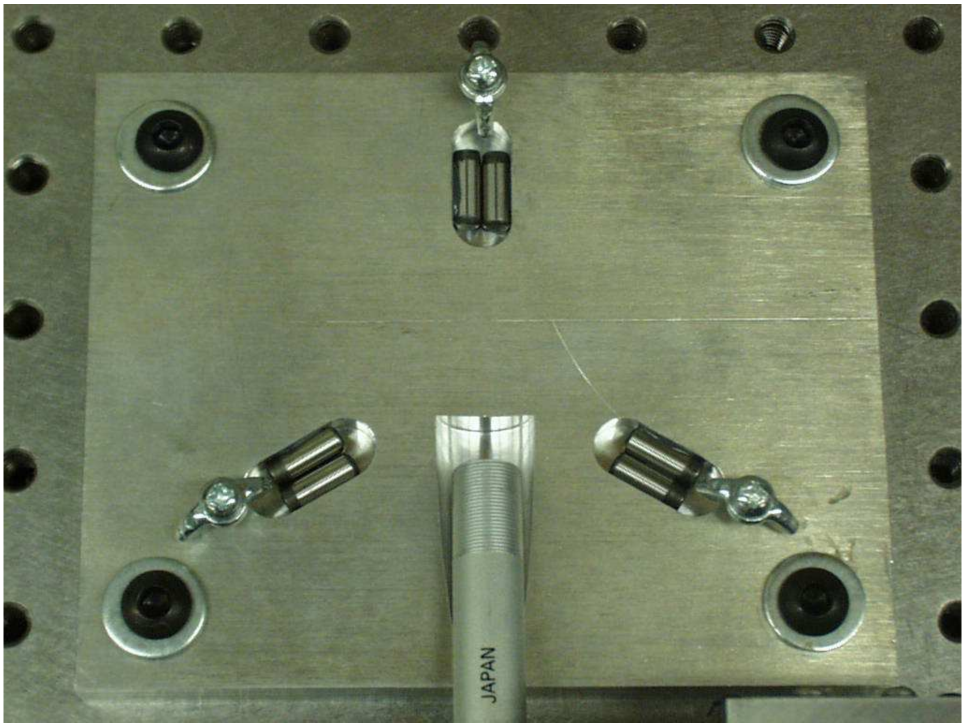

Figure 2-17: The base plate used with the open-loop prototype AFM head. Pairs of dowel pins epoxied to the plate act as grooves in a kinematic coupling between the AFM head and the plate. A small optical microscope fits within a groove cut into the plate and provides a means for visually monitoring the probe's height during coarse approach.

2.2 Electrical Design

Two electrical systems play important roles for the operation of the open-loop prototype AFM: a high-voltage amplifier drives the piezoelectric tube scanner, and a lock-in amplifier measures the current flowing through the tuning fork sensor, as driven by a signal generator. These systems are explained here.

2.2.1 High-Voltage Amplifier

The piezoelectric tube scanner requires a relatively large voltage drive to produce micron-scale deflections. For both of the AFM heads mentioned in this text, the drive signals are supplied by a five-channel high-voltage amplifier. This amplifier was originally developed by Brian Boudreau for his research on near-field infrared scanning microscopy [8] at UNC-Charlotte, as part of his studies toward a doctorate from Michigan Technological University. We modified its circuits so the voltage on each of the tube's five electrodes could be adjusted independently. Figures 2-18 and 2-19 show the circuit diagrams for one of the four identical outer electrode channels and for the inner electrode channel, respectively. In both cases, the input-output gain equals 10. Since the digital-to-analog channels providing the amplifier inputs (see sections 2.3 and 5.1 for more details on the controller board's input/output channels) have ±10 V limits, the tube electrode voltages are then commanded to a ±100 V limit. However, the amplifier power supply provides ±200 V to the op-amps, so we are only using about half of the amplifier's maximum range. Safety concerns were the initial motivation for setting this limit, though we clearly could have later increased the gain to achieve the amplifier's full range, had we wanted to.

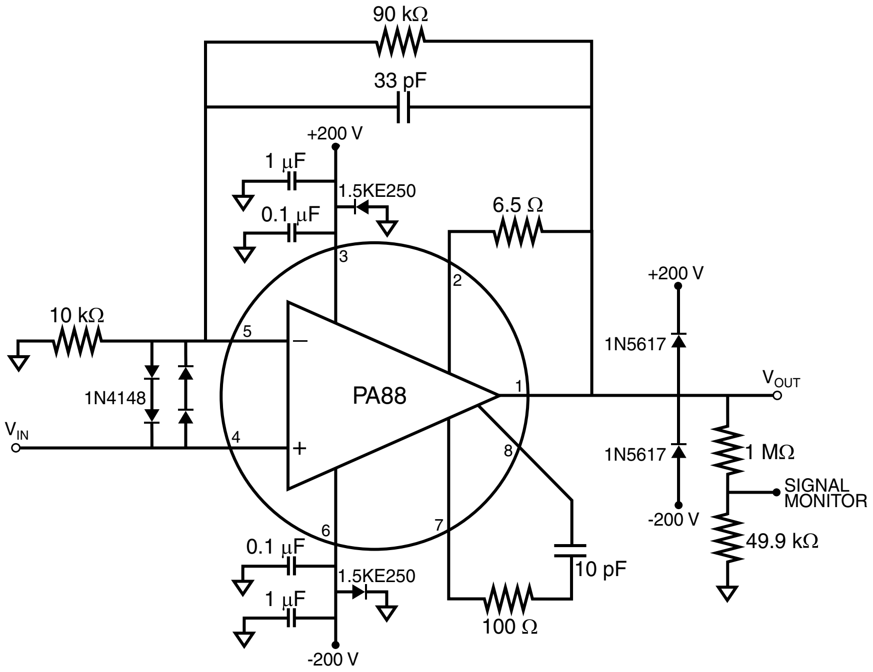

Figure 2-18: The circuit used for all four of the high-voltage amplifier's outer electrode channels. The input-output gain equals 10.

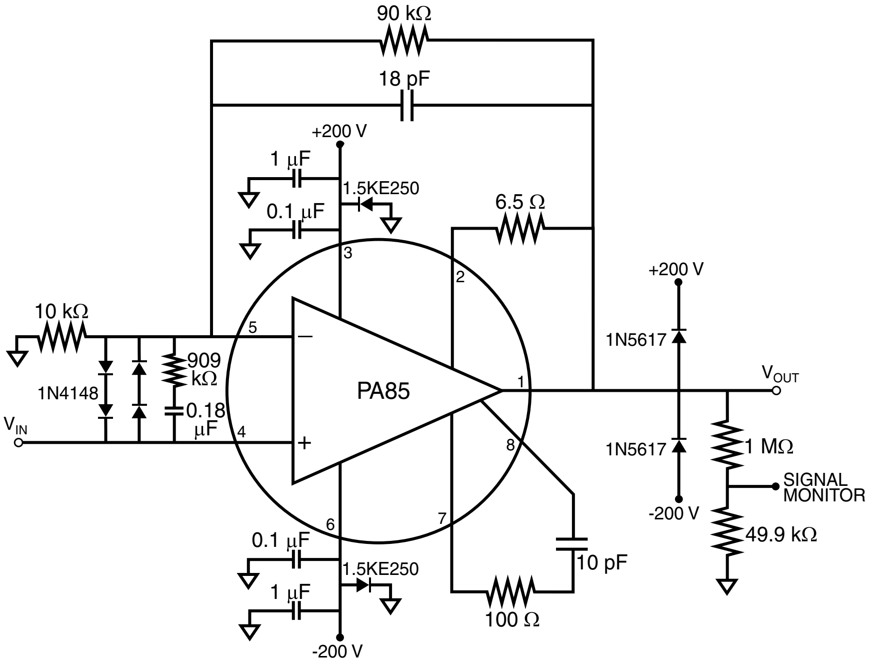

Figure 2-19: The circuit used for the high-voltage amplifier's inner electrode channel. The input-output gain equals 10.

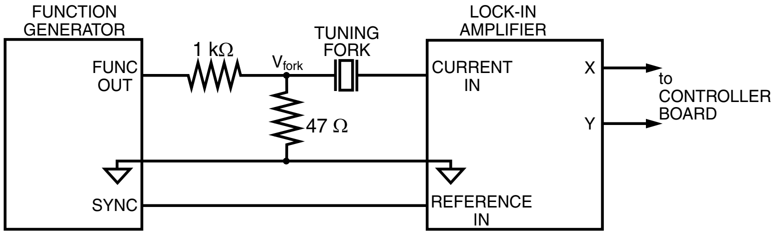

Figure 2-20: Circuit used with the open-loop prototype AFM to measure the tuning fork sensor's signal. Note the lowered resistance values relative to the circuit shown in Figure 2-11.

2.2.2 Tuning Fork Sensor Measurement

In section 2.1.2, we noted that the magnitude of the current flowing through the tuning fork sensor is a sensitive measure of the probe-sample separation. This section describes the method used to exploit this effect to provide the AFM's control system with a signal that is a function of the gap size.

Figure 2-20 shows the electrical circuit used with the open-loop prototype AFM to produce the tuning fork sensor's output signal. A function generator feeds a sinusoidally-varying voltage to one of the tuning fork electrodes, via a voltage divider. The divider attenuates the function generator's output to prevent overdriving the fork's mechanical oscillations. During tests with the prototype hardware, $|V_{fork}(t)|$ was generally maintained at about 100 mV. Based on equation (2.8), this drive level corresponds to a mechanical amplitude at the end of the fork of roughly 10 nm.

The current flowing through the tuning fork is synchronously detected with a Stanford Research Systems[9] model SR530 lock-in amplifier. The lock-in measurement technique is described in [21]. A brief explanation follows.

Lock-in amplifiers are used to measure very small AC signals. As configured for the circuit in Figure 2-20, the lock-in measures the current flowing through the fork, converts the current to a voltage signal, then feeds this voltage to a pair of analog multipliers, where it is multiplied by two reference signals at the same frequency

---

[9] See Appendix B.

as the signal generator output. The two reference signals have a 90° relative phase difference. Each of the multiplier outputs passes through a low-pass filter, which results in a pair of output voltages — one proportional to the in-phase component X of the current at the reference frequency, and the other proportional to the quadrature-phase component Y of the current at the reference frequency. These components are related to the magnitude R, and phase ϕ, of the current according to

$$R = \sqrt{X^2 + Y^2}, \tag{2.9}$$

and

$$\phi = \tan^{-1}\left(\frac{Y}{X}\right). \tag{2.10}$$

The SR530 uses a microprocessor to compute R and ϕ from the analog X and Y signals. However, the R and ϕ outputs have an update rate of only about 300 Hz. This rate is far too slow for the controller we wish to implement, so we instead use X and Y as inputs to the AFM's PC-based digital control system, then program the controller to compute R itself. The digital control system is mentioned briefly in section 2.3 and described in more detail in section 5.1.

Figure 2-22 shows measured frequency response data for the lock-in amplifier, as collected using the circuit shown in Figure 2-21. For this measurement, a Hewlett-Packard (HP) 35665A dynamic signal analyzer (DSA) provides a low-frequency amplitude-modulating (AM) input to a function generator set at a fixed frequency of 32 kHz. The function generator drives a resistive load, and the resulting current flow is detected by the lock-in. To complete the measurement loop, the lock-in's Y signal is fed to the DSA's Channel 2 input. The Bode magnitude plot rolls off at 160 Hz with a slope of about -20 dB/dec. These dynamics seem consistent with our selection of the lock-in's 1 ms time-constant low-pass filter, which follows each of the analog multipliers.

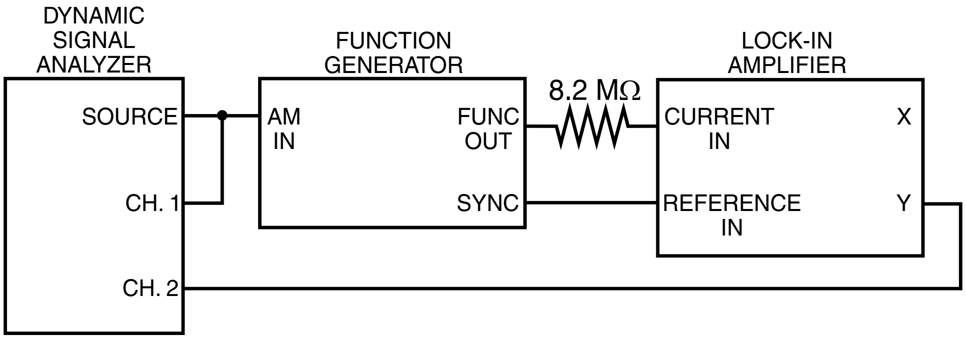

Figure 2-21: Drawing of the circuit used to measure the lock-in amplifier's frequency response.

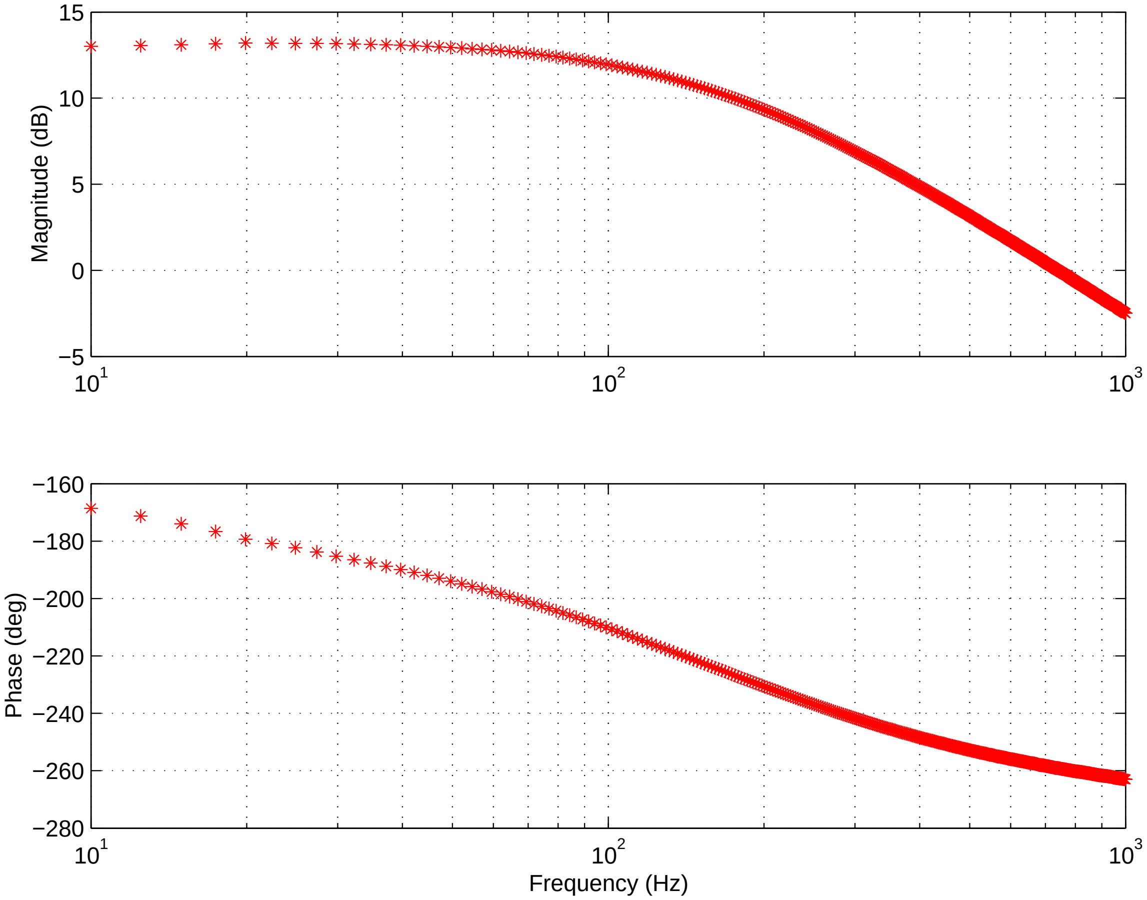

Figure 2-22: The measured lock-in amplifier frequency response data. As shown in the circuit diagram of Figure 2-21, the input signal is the amplitude-modulating input to a function generator set for a 32 kHz sine wave, and the output signal is the lock-in's Y output.

When we first tried measuring the tuning fork signal, we used a twisted pair of unshielded wires to couple the fork leads to the rest of the measurement circuit. However, after adding these wires, we noticed a dramatic decrease in the sharpness of the fork's resonance. We later realized that the relatively large capacitance between the two wires accounted for a majority of the current flowing into the lock-in, essentially shunting the tuning fork's dynamics out of the measurement. To fix this problem, the twisted pair was replaced with two coaxial cables, which resulted in a much sharper resonance. Figure 2-23 shows the circuit drawings corresponding to (a) the original, flawed tuning fork wiring and (b) the revised layout.

2.3 Control System

The X and Y outputs from the tuning fork sensor measurement circuit are fed to two 16-bit analog-to-digital conversion channels in the prototype AFM's PC-based digital control system, which runs off a dSPACE[10] DS1103 controller board. The associated hardware and software are described in section 5.1, but the details are omitted from the present discussion.

Figure 2-24 shows the block diagram for the prototype AFM's closed-loop axial height regulation system, which adjusts the common outer electrode voltage, V_{axial}, to lengthen or shorten the piezoelectric tube scanner according to the desired probe-sample separation. During each 100 μs sampling period, the value of the magnitude R is computed from the lock-in X and Y, with the result compared to the controller's set point. The corresponding error signal is multiplied by a gain K, and then fed into an integrator. A 14-bit digital-to-analog converter takes the integrator's output and produces an analog voltage from it, which is tied to the input of all four of the high-voltage amplifier's outer electrode channels.

The initial decision to use an integral controller was primarily motivated by its

---

[10] See Appendix B.

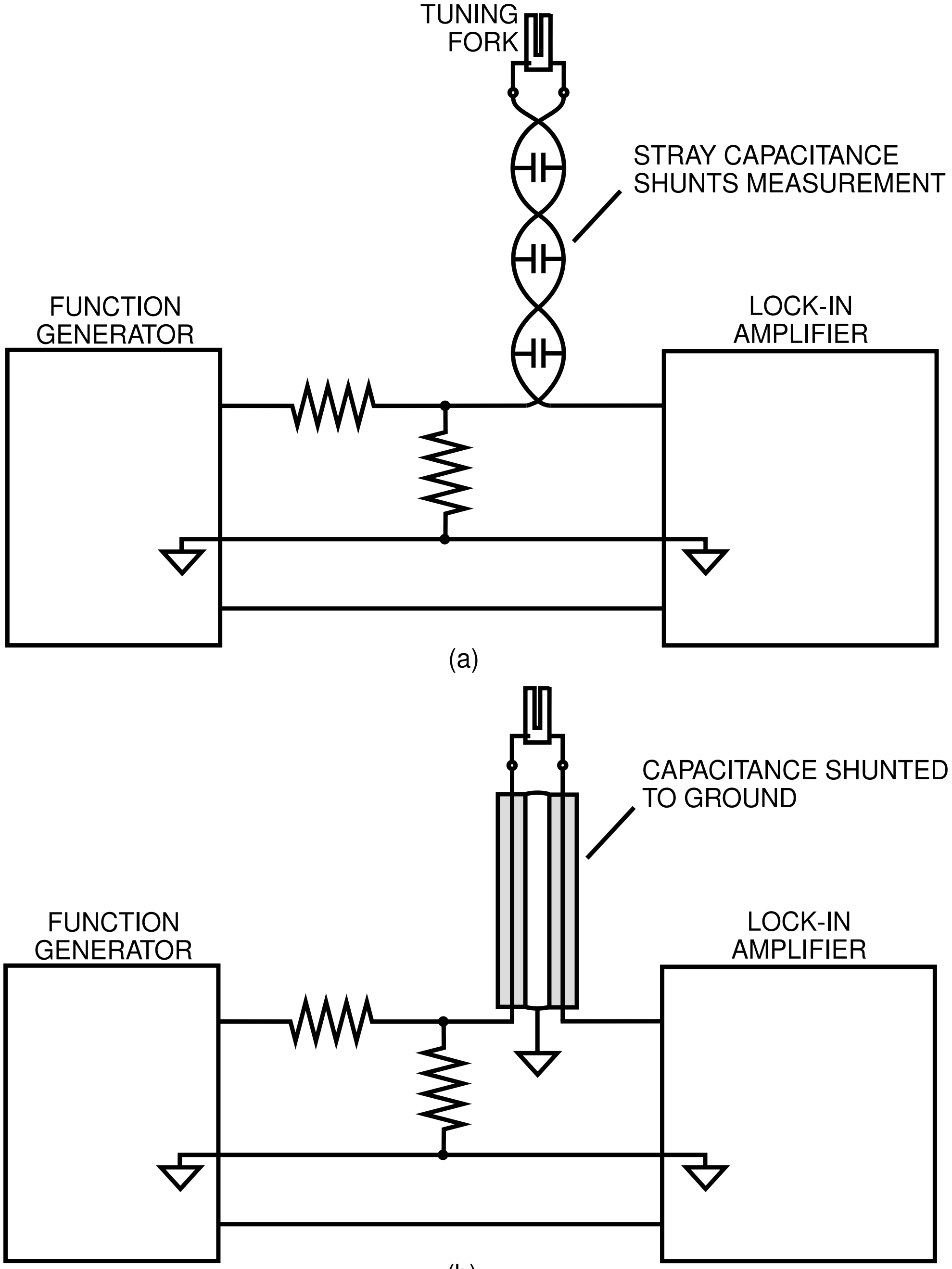

(a)

(b)

Figure 2-23: (a) Circuit originally used to measure the current flow through the tuning fork. Here, a twisted pair of unshielded wires couples the fork's electrodes to the rest of the circuit. The resulting stray capacitance shunts the measurement. (b) The revised circuit layout. A pair of coaxial cables now couples the fork to the rest of the circuit, resulting in a much sharper measured resonance.

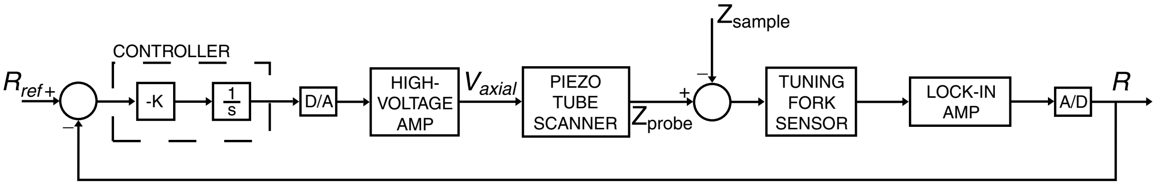

Figure 2-24: Block diagram for the prototype AFM's closed-loop axial height regulation system. Pure integral control is used.

ease of implementation. Earlier attempts to measure the open-loop frequency response from the amplifier input to the tuning fork sensor output indicated that the plant's phase was high enough to stabilize the system using this control strategy. Representative open-loop frequency response data is shown in Figure 2-25. This data was collected with the dSPACE board providing analog Channel 1 and Channel 2 signals to the HP DSA.[11] The system begins with a phase of 180° at low frequencies, since a positive change in V_{axial} causes a negative change in R. The magnitude response rolls-off at frequencies above approximately 10 Hz. This behavior appears to result from the tuning fork's high Q-factor, as discussed in [15], [13], and [1]. When a high-Q resonator is disturbed, it rings with a relatively long settling time, proportional to Q. This effect thereby limits the tuning fork's open-loop response at high frequencies.

Nevertheless, the system is still controllable. Figure 2-26 shows measured closed-loop frequency response data, again taken with the HP DSA interfaced with an integral controller running off the dSPACE controller board. From this data, the system has demonstrated a relatively low -3 dB closed-loop bandwidth of 7 Hz. The large resonant peak indicates an undesirably small phase margin of about 18°. Clearly, we would not want to try to increase the closed-loop bandwidth much above this value by using a higher controller gain, for fear of destabilizing the loop.

---

[11] This measurement can be more easily accomplished using the dSPACE-based DSA mentioned in section 5.2.1.

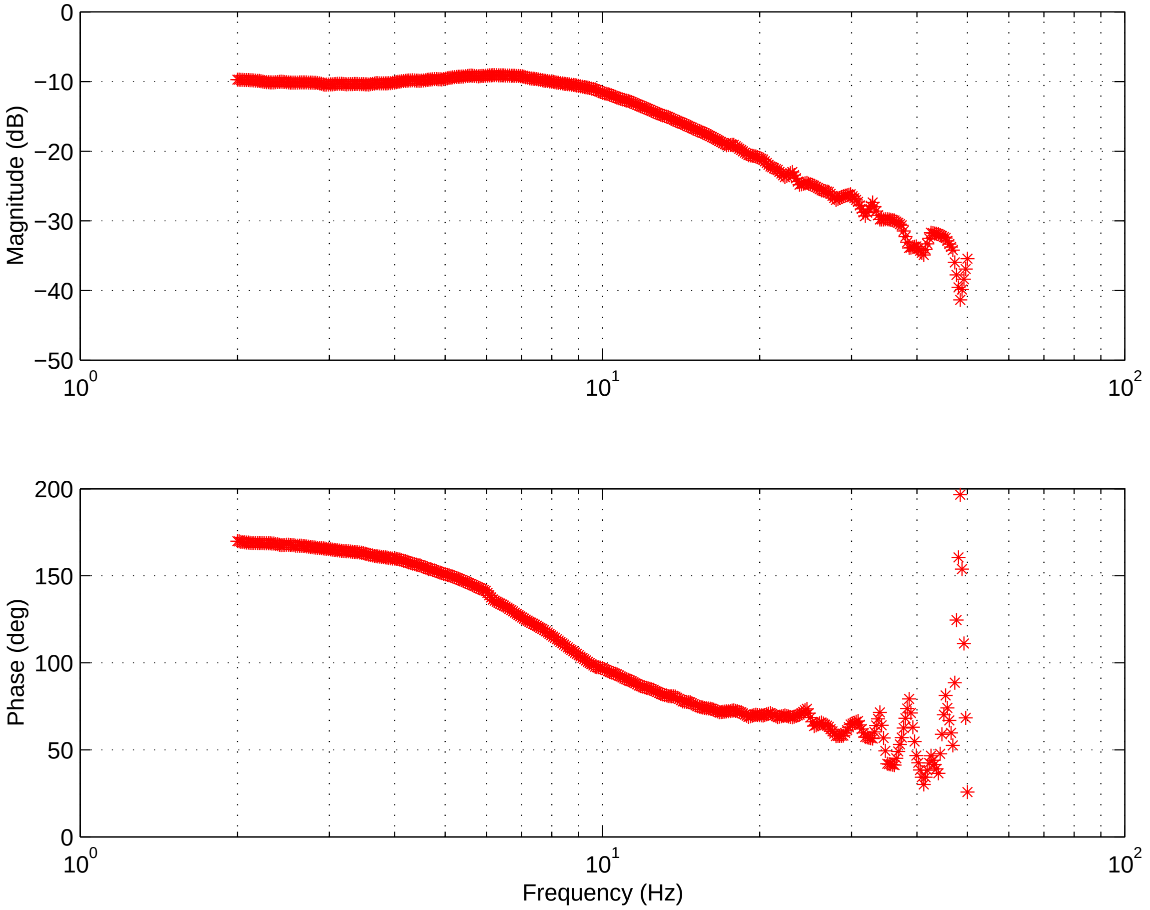

Figure 2-25: Open-loop frequency response data measured for the prototype AFM's axial height regulation system.

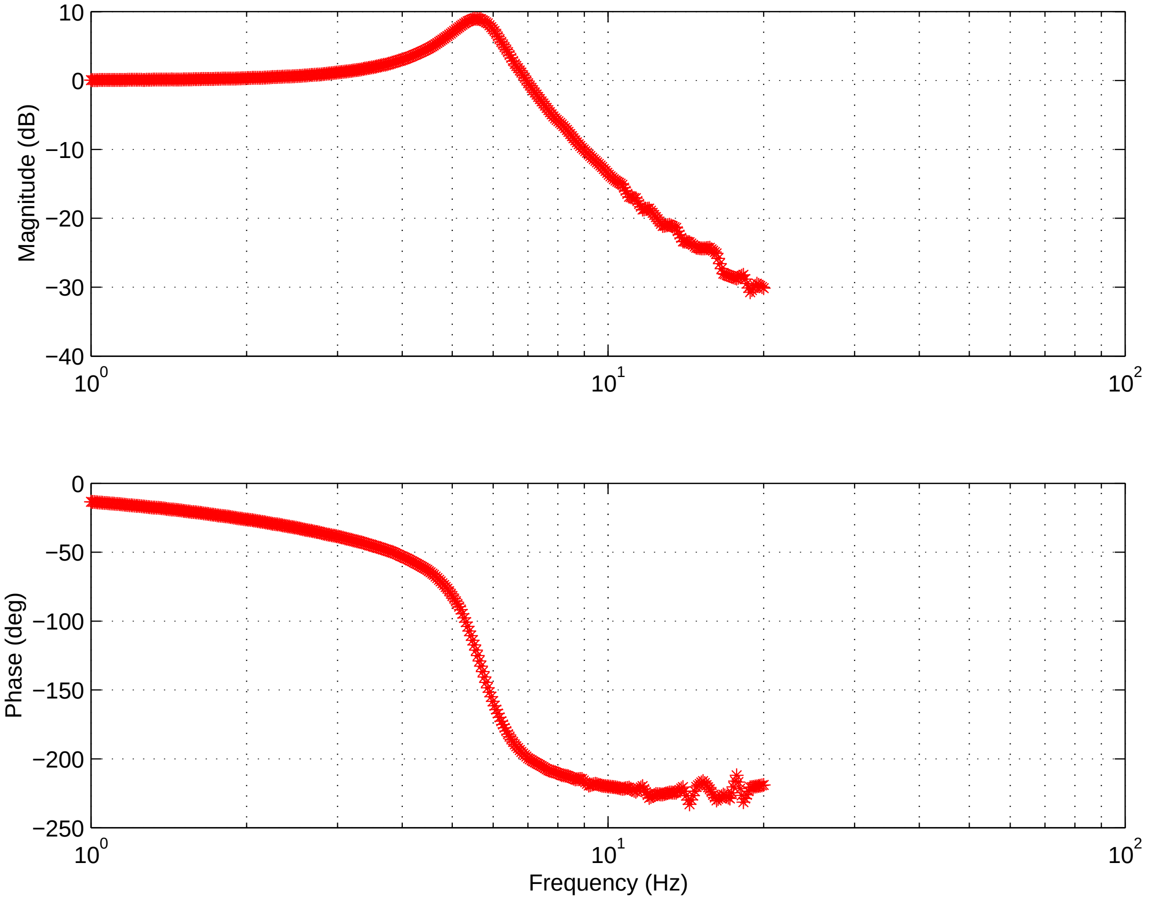

Figure 2-26: Closed-loop frequency response data measured for the prototype AFM's axial height regulation system, for a pure integral controller. The measured -3 dB closed-loop bandwidth is 7 Hz.

2.4 Results

Using an integral controller similar to the one described in the previous section, we collected a few three-dimensional images with the open-loop prototype AFM. The data plotted in Figure 2-27 provides strong evidence that this system performed properly. For this image, the tuning fork sensor was engaged on a nominally flat surface on the side of a steel razor blade,[12] then scanned sinusoidally in one lateral axis — the fast-scan axis — and at a constant-speed in the other — the slow-scan axis. The total scan time was 10 minutes. The plotted Z trajectory is computed from the commanded V_{axial} signal, based on the calibration constant given in equation (2.7). However, since we did not calibrate the scanner assembly's lateral displacement, we instead use equations (2.5) and (2.6) to provide a rough estimate of the probe's actual position in X and Y. The resulting image indicates that the probe tip successfully tracked the changing surface profile, since adjacent scan lines follow the same contour shape.

A discontinuous change in the probe's Z position is observed in one of the scan lines. However, the surface contours before and after the shift look essentially identical. The measured discontinuity is therefore likely the result of a mechanical disturbance which forced the blade to move slightly, instead of an actual abrupt change in the surface topography.

2.5 Conclusions

The development of the open-loop prototype AFM provided us valuable experience with the piezoelectric tube scanner and quartz tuning fork sensor, as well as their associated electronics. We additionally learned that the inductive sensors were improperly configured for use in our original design. These sensors apparently lose much

---

[12] During these tests, we did not have any samples with high spatial frequencies available, so all of our images are of nominally flat surfaces.

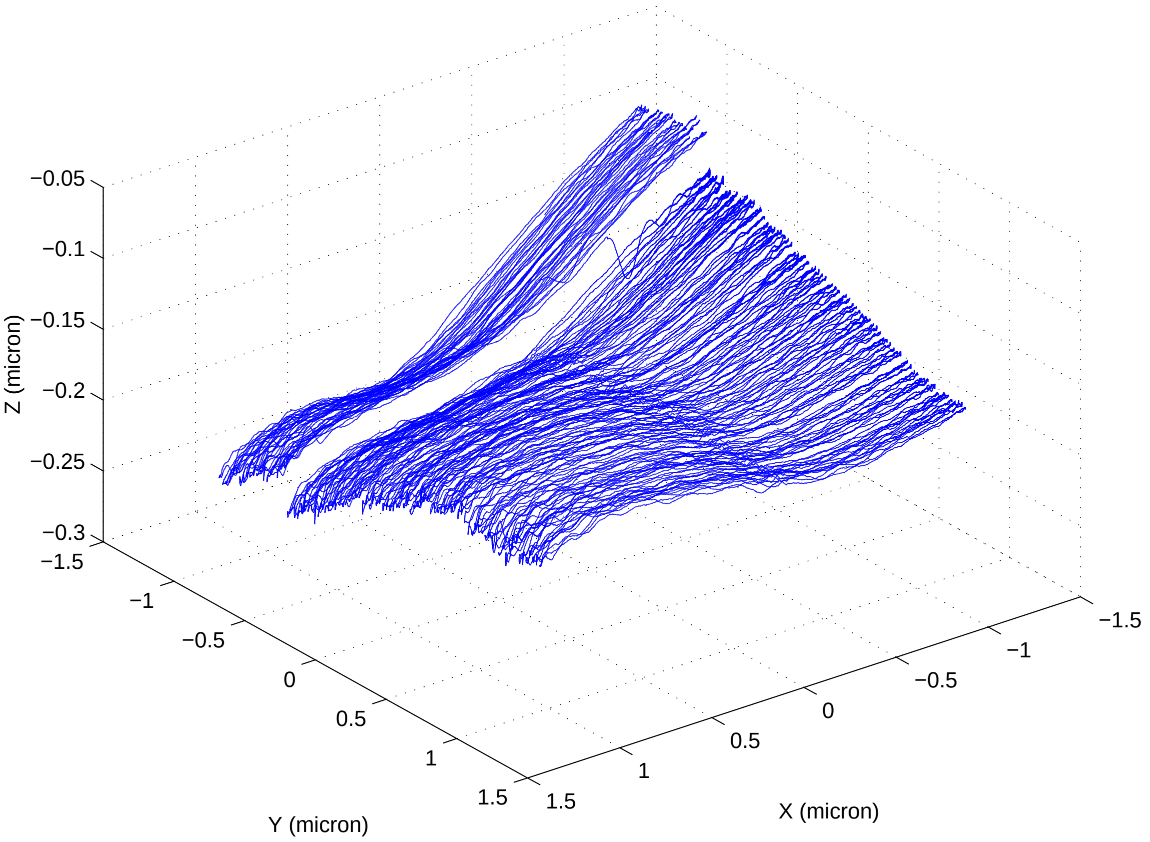

Figure 2-27: Three-dimensional image of the surface of a razor blade, acquired with the open-loop prototype AFM.

of their sensitivity when surrounded by conductive material and are also susceptible to low-frequency beats when brought within close proximity of one another.

We learned a number of other useful lessons during the design, fabrication, and testing of the AFM. The original attempt to use an unshielded twisted pair to connect the tuning fork leads to the measurement circuit led to an unacceptably low Q, as a result of the relatively large capacitive feedthrough between the two wires. Replacing these wires with coaxial cables largely solved this problem.

We also found that the fixture used for gluing the fiber tips to the tuning forks was fairly unreliable. The main problem here was our use of pliers to manually transfer the tips to the fixture, which resulted in an unacceptably high number of lost fibers.

Based on Figure 2-27, the prototype AFM demonstrated three-dimensional imaging capabilities. We build upon this success in the development of the metrological AFM, which is described next.

Chapter 3

The Metrological AFM — Mechanical Design

This chapter describes the development of the mechanical design of the metrological atomic force microscope, which is shown in the photograph in Figure 3-1. Section 3.1 presents a discussion of the early conceptualization for the AFM head. Section 3.2 then fills in some key details of the selected design. Section 3.3 describes several auxiliary features of the completed system that assist in the proper functioning of the assembled microscope. Finally, section 3.4 summarizes the most important aspects of the AFM's mechanical design.

3.1 Conceptualization

We initiated the design of the metrological atomic force microscope by brainstorming a number of alternative concepts for its general form. This section details the progression from preliminary sketches to a single fleshed-out model for the actual microscope. Several key considerations that helped shape the final design are described here. The discussion then focuses on the form, placement, and alignment of the microscope's capacitance sensors, design issues which played a significant role in

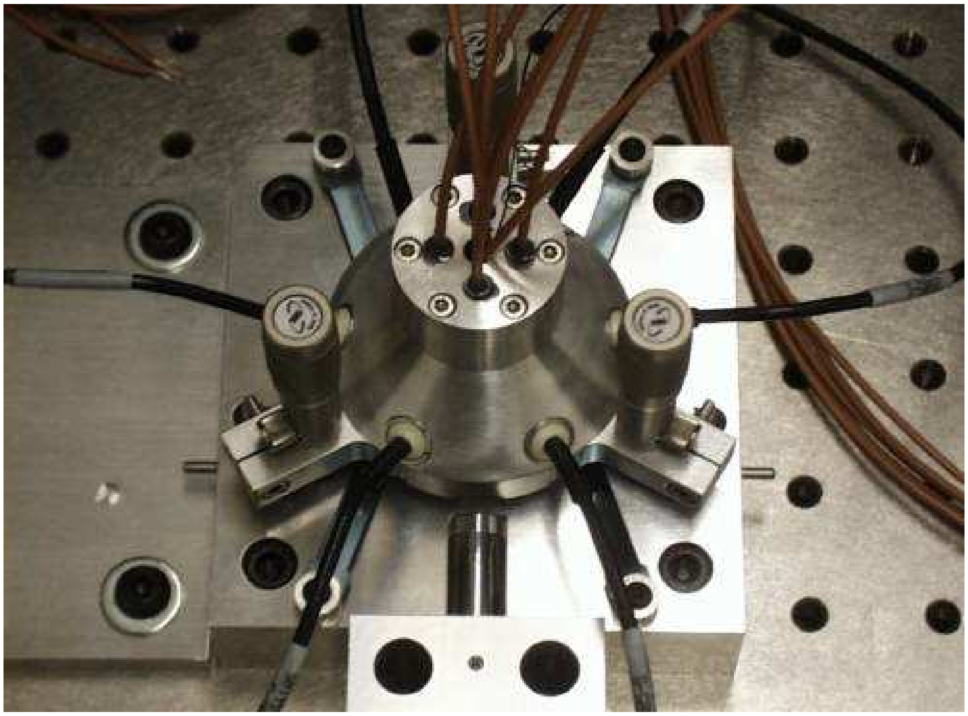

Figure 3-1: The metrological AFM.

the optimization of the microscope's accuracy. Finally, details are presented on the conceptual development of the sensors' target.

3.1.1 Design Considerations

In approaching the open-ended problem of designing a metrological atomic force microscope, it was necessary to define a number of performance measures and practical constraints for use in differentiating the relative merits of the various designs.

In designing our metrological AFM, we primarily aimed to prove out a number of concepts for optimizing the microscope's accuracy. This goal substantially motivated the decision to integrate metrology in the AFM. It also led to a sensor topology that minimizes Abbe offset, which is a potentially significant source of measurement error.

However, since this metrological AFM serves as a prototype for an upcoming SAMM AFM, we have not taken all of the steps necessary to fully optimize its performance. This approach is particularly evident in the frequent use of aluminum, a material with a fairly high coefficient of thermal expansion, but which can be purchased and machined at relatively low cost. Similar tradeoffs occur several times throughout the design process. As a result of these tradeoffs, we sacrifice the ability to demonstrate accuracy at the sub-10 nm level, an eventual requirement of the SAMM AFM, in return for a relatively rapid prototype/test cycle.

3.1.2 Probe Position Sensors

For the metrological AFM, we decided to use capacitance sensors to measure the probe's displacement. These sensors can provide the desired accuracy, are relatively simple to use, and are more robust with respect to stray fields than the inductive sensors mentioned in section 2.1.3. A good explanation of the basic operating principles for capacitance sensors may be found in [37].

Figure 3-2 shows a simplified drawing of one of these sensors. Here, the sensor's face is assumed to be flat, though this need not be the case. Two electrodes cover the face: a sense electrode and a guard electrode. Both electrodes are driven with identical voltage waveforms. The sensor's electronics transduce displacement from changes in the capacitance between the sense electrode and the target surface, which is inversely proportional to the sensor-target gap size. The guard electrode serves two important purposes. Firstly, it reduces the sense electrode's sensitivity to stray capacitance. Secondly, it forces the electric field between the sense electrode and the target surface to be uniform, since this field sees no discontinuous edges.

Sensor Configuration

During early discussions of the microscope's form, we examined several designs for mounting the sensors. One such approach is the 'Cartesian' alignment shown in Figure 3-3. The main advantage of this layout is its relatively simple target geometry.

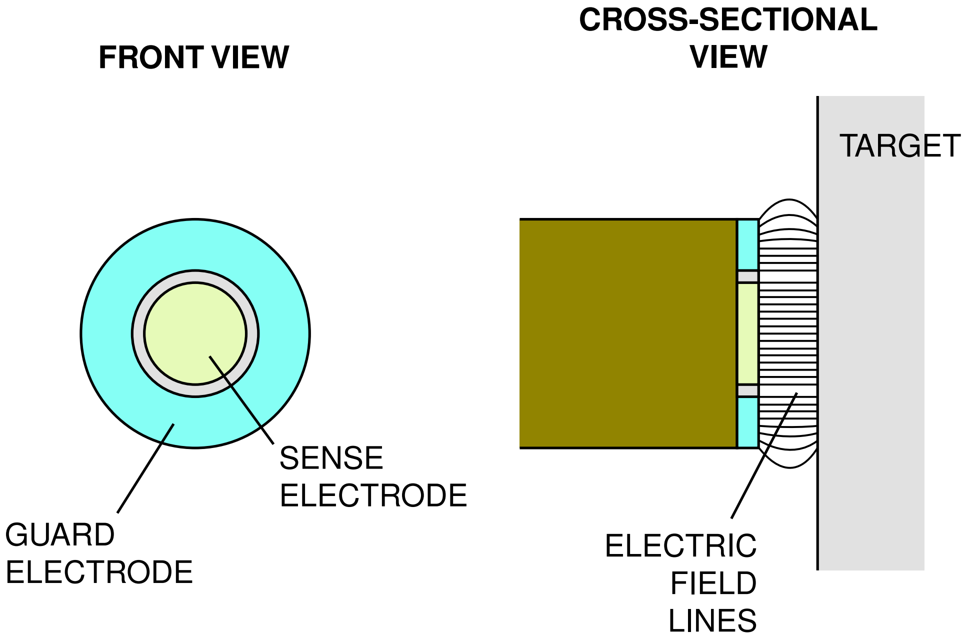

Figure 3-2: Schematic drawing of a capacitance sensor. The sense electrode is located in the center of the sensor's face and is surrounded by a guard electrode. As seen in the cross-sectional view, the presence of the guard electrode results in a uniform electric field from the sense electrode to the target surface.

However, we ultimately decided not to pursue this design because of the large Abbe offset error that results, for measurements of the probe tip's lateral displacement.

Abbe offset is the distance from a measurement axis to the point being measured. Figure 3-4 shows a simplified model of the Cartesian sensor alignment, where the Abbe offset from one of the lateral sensors to the probe tip is labelled as l_{Abbe}. It is important that this distance be minimized, since the angle at the end of the tube scanner can be significant relative to the nanometer displacements being measured. In Figure 3-5, the piezoelectric tube scanner is shown in the bent condition — corresponding to a lateral probe displacement. Using equations 2.5 and 2.3, the approximate value of the angle of the tube at its free end, θ, is given by

$$\theta \approx \frac{\Delta x_{tip}}{l_{tube}/2 + l_{tip}}. \tag{3.1}$$

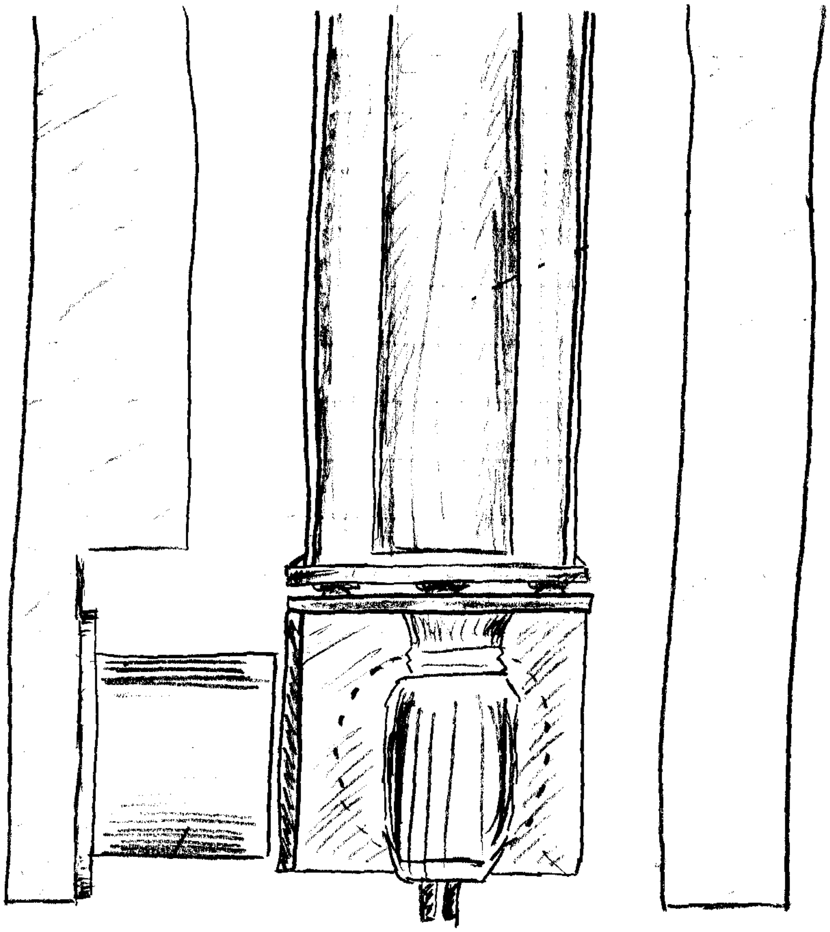

Figure 3-3: Sketch of the Cartesian sensor layout. This sensor topology introduces a large Abbe offset error into measurements of the probe tip's lateral displacement.

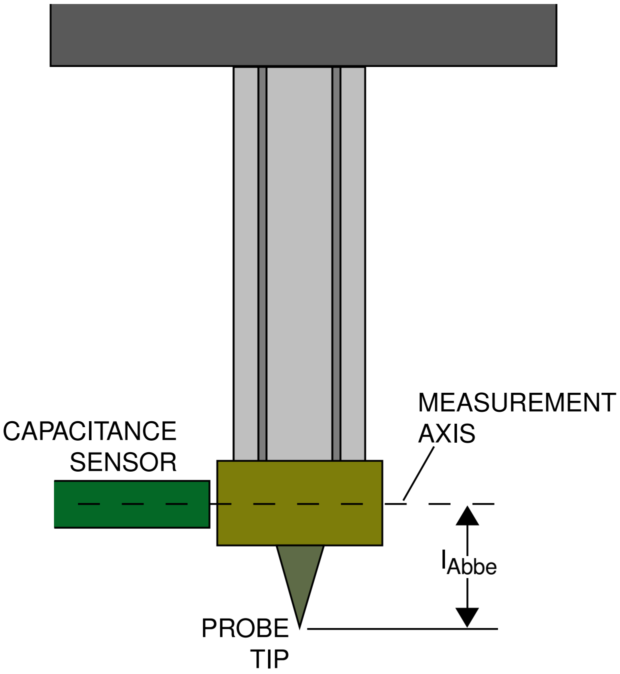

Figure 3-4: The scanner assembly, with the piezoelectric tube in its relaxed state. The distance from the capacitance sensor's measurement axis to the probe tip is the Abbe offset, l_{Abbe}.

Using a representative value of $l_{tip} = 15$ mm, the angle needed for a lateral displacement of $\Delta x_{tip} = 10$ μm is $\theta \approx 3.3 \times 10^{-4}$ rad. Then, for a representative Abbe offset of $l_{Abbe} = 8$ mm, the resulting Abbe offset error — the additional distance that the tip moves which is not measured by the sensor — is $\Delta x_{Abbe} = l_{Abbe} \sin\theta = 2.6$ μm. Clearly, the Abbe offset error can become significant for this sensor topology.

There are two distinct approaches for removing the effect of Abbe offset from the recorded image data. One way is to post-process the data, using an algorithm to approximate the actual sample topography. For example, one could calculate the expected curvature of the tube scanner based on the sensor data, then compute the theoretical incremental displacement of the probe tip with respect to the sensor target's position using the approximate angle at the tube's base. While this approach can result in improved accuracy in the image data, it still provides only an indirect means for measuring the sample topography.

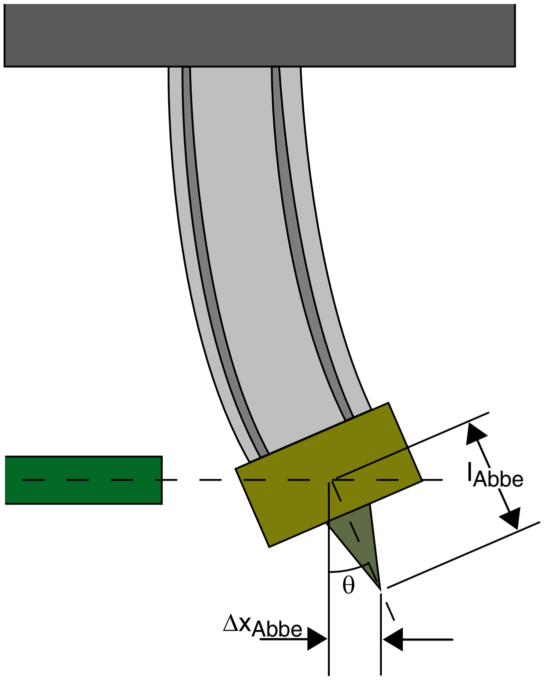

Figure 3-5: The scanner assembly, with the piezoelectric tube scanner bent to produce a lateral displacement of the probe tip. For representative dimensions, a displacement of $\Delta x_{tip} = 10$ μm results in an Abbe offset error of $\Delta x_{Abbe} = 2.6$ μm.

A more elegant approach to this problem is described schematically in Figure 3-6. Drawing inspiration from the work of Ruijl [36] and Schellekens [24] — which in both cases involve the design of small, high-precision coordinate measuring machines — we decided to employ a purely mechanical solution, in which the axes of the sensors[1] are aligned such that they all intersect at a point coincident with the probe tip. In this way, Abbe offset has been nominally eliminated.[2] Therefore, in the absence of other error sources, the AFM position sensor data translates directly to tip position, without need for post-processing corrections.

For optimal resolution in the sensors' position measurements, the three measurement axes are aligned in a mutually orthogonal configuration. This geometry gives an angle, θ, from each measurement axis to the vertical axis of 54.7°, with 120° sep-

---

[1] More precisely, the sensors' 'measurement axes.' See section 4.1 for an explanation of this term.

[2] There will be, however, some finite Abbe offset introduced from machining and alignment tolerances.

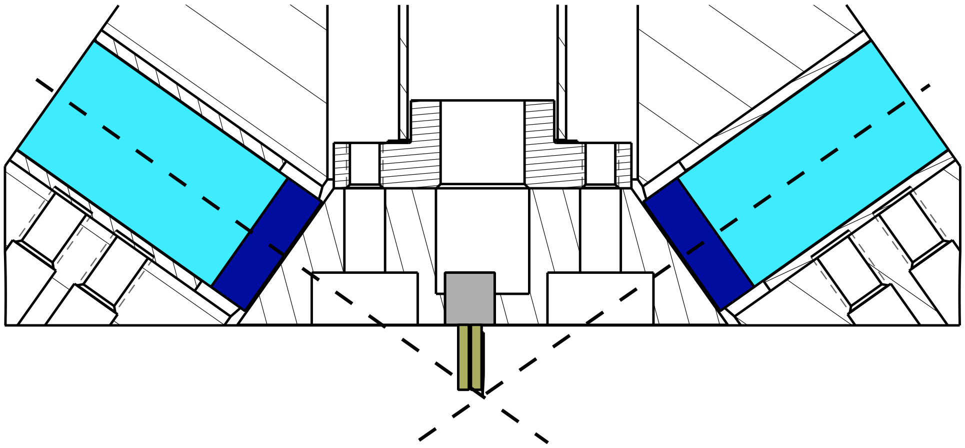

Figure 3-6: Cross-section of the selected sensor configuration. Visible is a pair of opposing sensors with measurement axes intersecting at a point coincident with the probe tip.

arating the projections of the three axes in the horizontal plane. Said another way, the faces of the probes, taken in a set of three, lie on three mutually orthogonal faces of a cube.

Sensor Form Factor

Having decided on the alignment of the sensors' measurement axes, we next needed to select the sensors' form factor. A number of possibilities were explored, with the final choice allowing for 1) a housing design that is both inexpensive and relatively simple to fabricate, and 2) a sensor mounting scheme that is robust and easy to implement.

Button Sensors We initially planned to use a set of custom-made 'button sensors,' which were donated to us by ADE Technologies.[3] When investigating this option, we were working toward integrating the AFM head in the SAMM stage, a goal which was eventually set aside for a future project. Designing the AFM head to fit within the SAMM's relatively small SPM notch would have severely limited the length of the sensors that could have been used, a consideration that made the 6.4 mm-long

---

[3] See Appendix B.

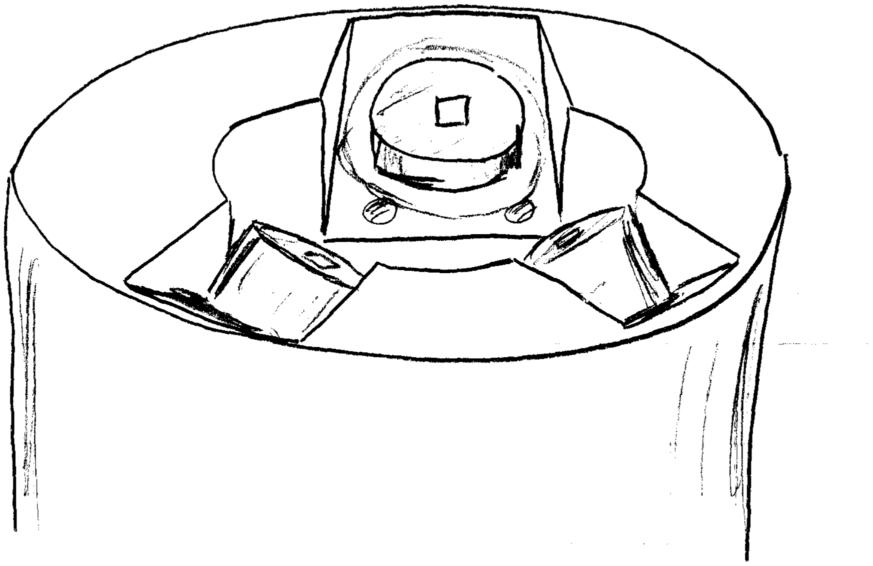

Figure 3-7: Conceptual sketch of the button sensors mounted in the AFM housing. The resulting housing geometry would have been too difficult and costly to machine.

button sensors an attractive choice. However, after the decision to design the AFM head as part of a free-standing prototype system, the button sensors' compact size was no longer an advantage. On the other hand, the difficulty of packaging the sensors within the head was a critical disadvantage of this design. Specifically, the sensor shell was part of the driven guard and therefore had to be electrically isolated from the AFM housing. To meet this requirement, a dielectric substrate — such as a quartz disk — would need to be affixed to the back of the shell. Then, the other side of the substrate would be used as a mounting surface when placing the sensor in the head. Figure 3-7 suggests what the resulting housing geometry might have looked like. We were concerned that such a design would have been too difficult and costly to fabricate. Machining the head's mounting surfaces, with the necessary tolerances on orthogonality and flatness, likely would have required much more effort — at higher cost — than would have been needed for the options mentioned below.

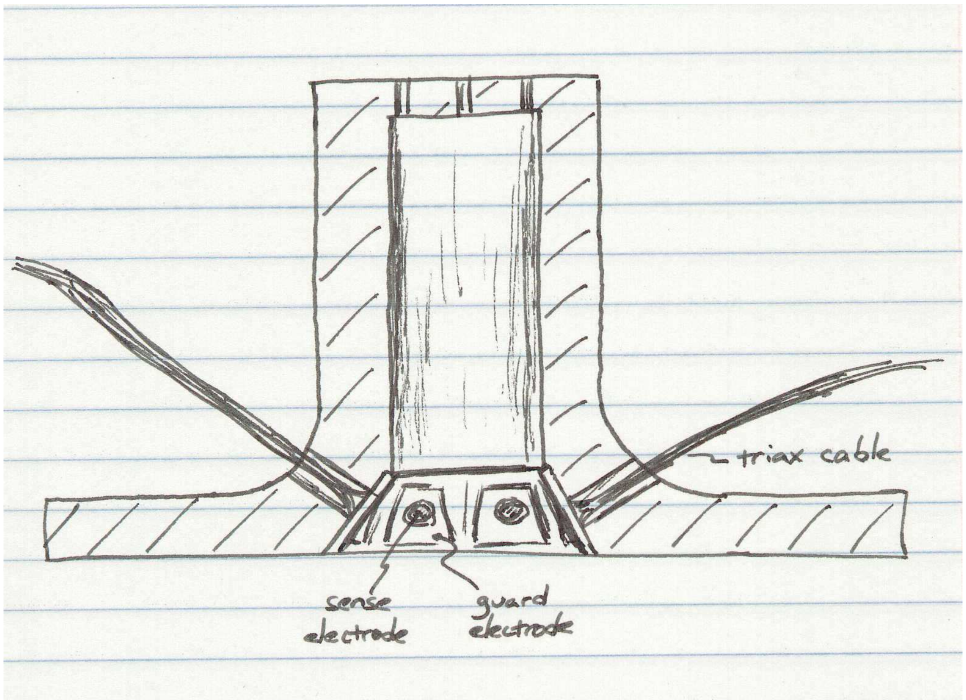

Figure 3-8: Sketch of the cross-section of an AFM head with circuit board sensors.

Circuit Board Sensors Another option would have allowed for greater ease of fabrication. Figure 3-8 shows a conceptual sketch of an AFM with a set of sense and guard electrode patterns cut into a thin strip of multi-layered circuit board. The strip has been bent into the shape of a cone, then affixed to a mating surface on the underside of the housing. With this design, the AFM head has a set of very thin capacitance sensors permanently mounted inside its housing.

This configuration has two key advantages over the button sensor concept. Firstly, it avoids the most difficult fabrication challenge involved in making the head shown in Figure 3-7. Instead of milling a set of orthogonal flats for mounting the sensors, this design would only require that a conic cavity be machined into the bottom of the housing, a task easily accomplished with a lathe. The circuit board's inherent compactness serves as the other main benefit. We would likely have used either three- or four-layer board, with total thickness on the order of 1 mm, making it significantly thinner than the button sensors.

However, this design also suffers from serious drawbacks. Making low-noise capacitance gauges requires great care, particularly in providing proper guarding of the sense electrode's signal. Additionally, we were worried about possible difficulties in wiring the sensors' triax cables to the back of the circuit board — a common failure point for this type of design.

'Long' Cylindrical Probes Having explored the options described above, we finally selected a set of commercially available capacitance sensors with cylindrical bodies (Figure 3-9), which could be clamped directly to the housing. Like the button sensors, the selected probes (model number 2805-S) were available from ADE Technologies, eliminating the development process required for the circuit board sensor idea. Additionally, these probes can be mounted relatively easily, unlike the button sensors. Since the main portion of the 2805-S sensor's body is not coupled to the driven guard, it does not need to be isolated from the AFM housing. Instead, it can be simply slipped into a mating hole in the housing and clamped into place.

Table 3.1.2 shows the performance specifications for the 2805-S sensor when used in conjunction with ADE's Model 3800 gaging electronics. We chose to use these sensors with a 100 μm total range, which is large enough to allow us to zero the sensor's position by hand, but is not too much larger than the stroke of the PZT tube scanner, thereby allowing a relatively large signal-to-noise ratio.

3.1.3 Target Design

Several options were also considered for the tube scanner's endpiece, which serves as the target for the metrological AFM's capacitance sensors. Early in the design process, we decided to use a removable endpiece design. This approach allows for the replacement of a broken (or otherwise sub-optimal) tuning fork sensor with a new one

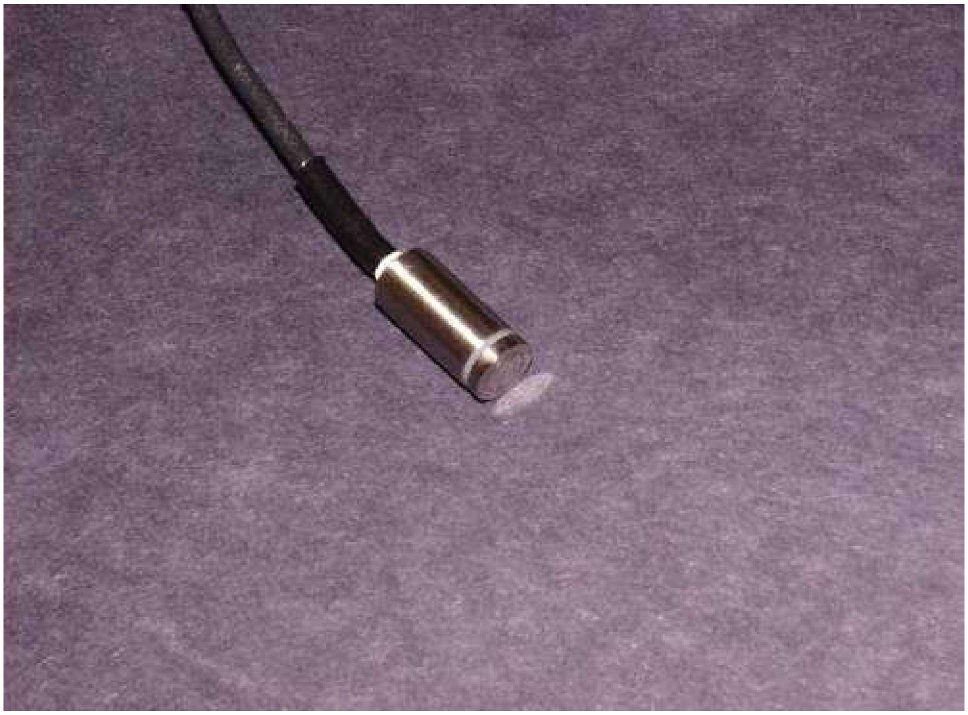

Figure 3-9: The capacitance sensor used in the metrological AFM.

Range	±50 μm
Output Voltage	±10 V
Bandwidth	1 kHz
Noise	0.27 mV RMS (1.4 nm RMS)
Linearity	±32.60 nm
Accuracy	±32.79 nm

Table 3.1: The performance specifications quoted by ADE Technologies for the 2805-S sensors and 3800 gaging electronics used with the metrological AFM head. The values given for the noise, linearity, and accuracy are averages for the AFM's six sensors.

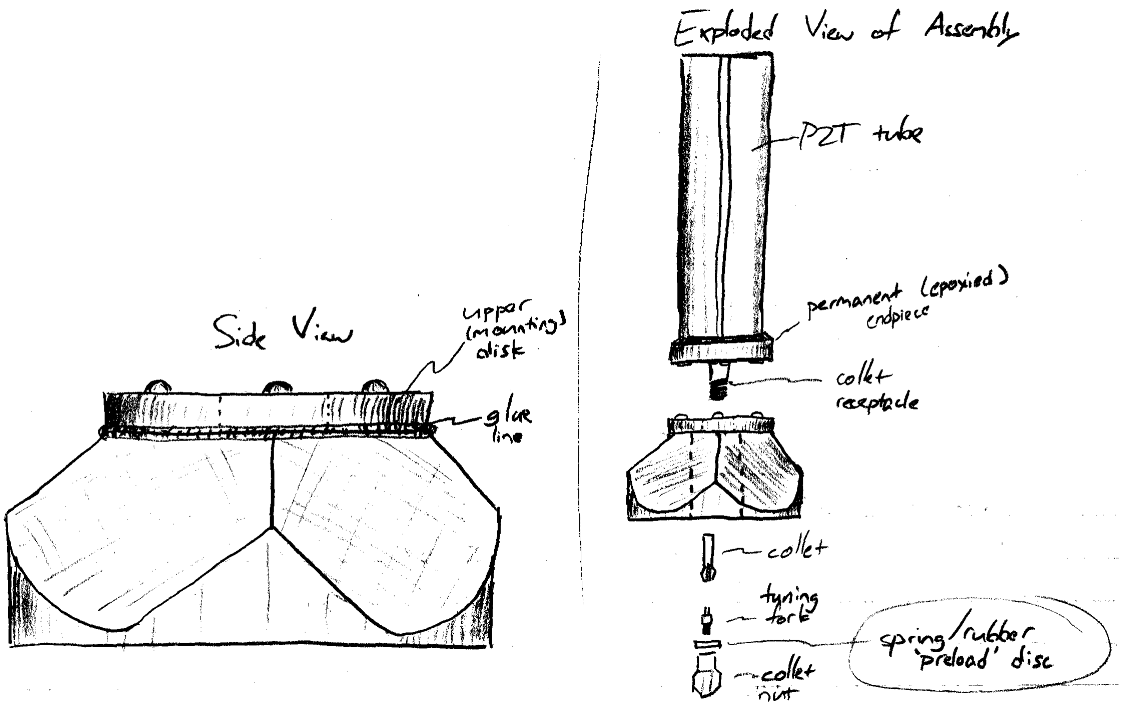

Figure 3-10: Sketch of a candidate design for the scanner assembly, with a removable corner cube target.

using a much less complicated fixturing process than would be required if the target were permanently mounted to the rest of the AFM.

Next, we brainstormed a number of options for the actual target shape. The sketches in Figures 3-10 and 3-11 represent a couple of early candidate designs. In both cases, the targets would be highly-orthogonal, flat surfaces.

The first of these designs would be based on a corner cube retroreflector — a common optical element that already has the desired geometrical characteristics. We would cut off material from the top of this glass block, epoxy a metal plate to the exposed flat, and tighten the assembled unit to the bottom of a mounting plate permanently fixed to the end of the tube scanner.[4] The three flats of the corner cube

---

[4] This sketch includes a kinematic coupling between the removable block and the permanent mounting plate. To avoid the large stresses and strains that result from contact between such small balls and grooves, however, this mounting method is replaced with simple planar contact in later designs.

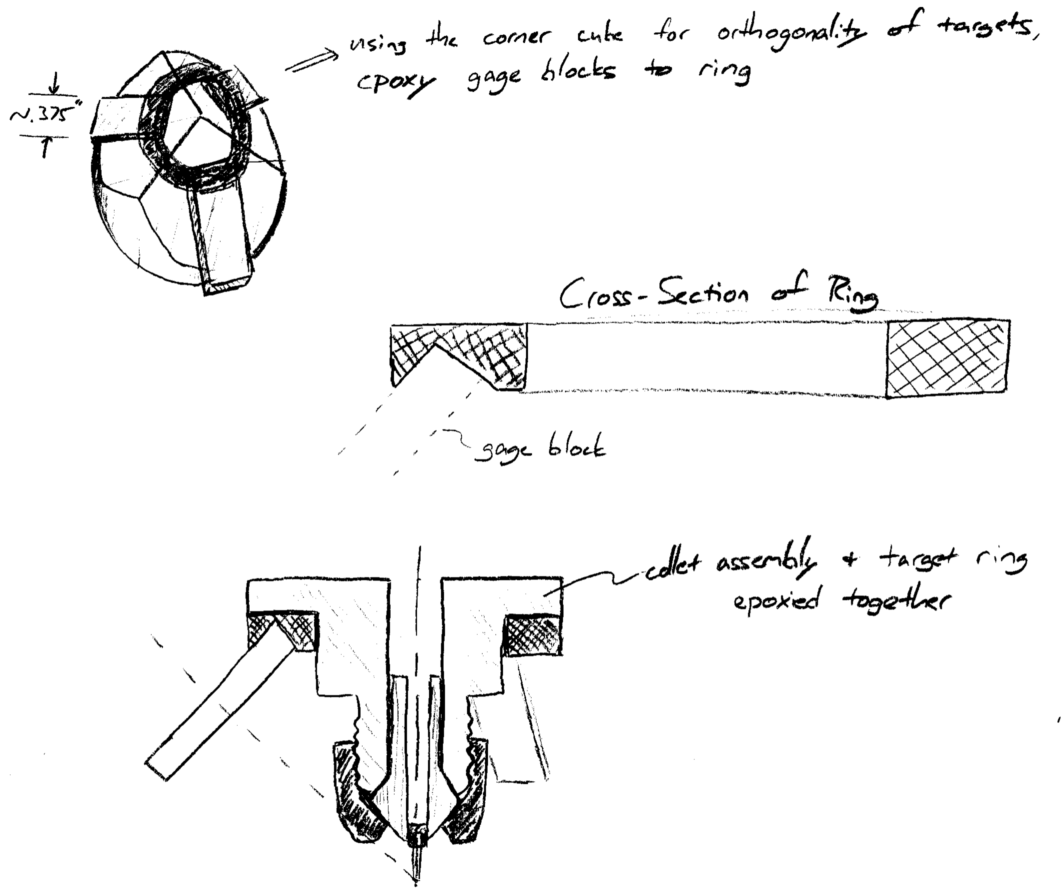

Figure 3-11: A target endpiece using gauge blocks for flats.

would be metalized, to provide the conductive targets required by the capacitance gauges. We later decided against using this design, primarily due to the difficulty of machining glass and concerns that residual stresses left from the original manufacturing process would cause unwanted distortions of the target surfaces upon removal of any additional material.

Figure 3-11 shows a sketch of a similarly conceived target endpiece. The design utilizes a set of rectangular steel gauge blocks, aligned with respect to a corner cube to insure orthogonality, then fixed in a ring assembly with some epoxy. This design was removed from contention, due to concerns that the assembled targets would not be suitably stable and rigid.

We next considered making the target endpiece entirely 'from scratch,' using an easily machined material (e.g. aluminum). This approach would provide greater flexibility in the size and shape of the designed part. However, making our own part with the orthogonality and flatness of a corner cube is a very difficult task. Instead, we considered designs that would both be more forgiving with respect to alignment errors and require relatively simple machining operations. A conceptual sketch of the final selection is shown in Figure 3-12. This drawing is an exploded view of a scanner assembly with a simple conic endpiece. The idea for this part geometry originated during discussion of the circuit board sensor idea, in which the conic sensor configuration naturally suggests a conic target. The cone's continuous outer surface serves as a target for the full set of capacitance sensors. This part is relatively easy to machine to fairly strict tolerances. Also, because of its axial symmetry, angular alignment about the axis of the scanner tube is no longer a concern, which leads to relaxed constraints on the assembly and remounting processes. However, these advantages come at the cost of measurement nonlinearities introduced by the target's curvature. Fortunately, this effect should be small enough not to significantly impact the AFM's performance. In any case, for the final installation in the SAMM, the probes in the microscope head will be calibrated in situ against the laser interferometer sensors of the SAMM stage.

3.2 Design Details

After deciding on the general shape and function of the metrological AFM's parts, we worked through the AFM's detailed design. This section touches on specific features of the housing and endpiece assembly. Appendix A contains details of the design in mechanical drawings of the associated parts.

3.2.1 Housing

The housing is a two-piece assembly — a removable housing cap (Figure 3-13) mounts to the top of the housing body (Figures 3-14 and 3-15). The top end of the piezoelectric tube scanner epoxies to a mating nub on the bottom of the housing cap. A set of thin Mylar strips are used as standoffs between the cap's conductive surface and the tube's electrodes, both axially and radially, to avoid short circuits. Before mounting the tube, coaxial cables are soldered to its five electrodes. The outer electrode cables individually pass through holes in the cap, where they are epoxied in place to reduce stressing of the fragile soldered joints. The inner electrode cable passes through a larger hole in the center of the cap, along with the target ground wire and the tuning fork coaxial cables. A drawing of the housing cap is shown in Figure A-1 of Appendix A.

The housing cap bolts to the top of the housing body, with the piezoelectric tube passing through the body's central bore. The bore is only slightly larger than the diameter of the mounting endpiece, in part to provide shielding of the capacitance sensors from the electric fields generated by the tube scanner's electrodes. Also, as seen in Figure 3-15, a total of six holes have been drilled into the body for mounting

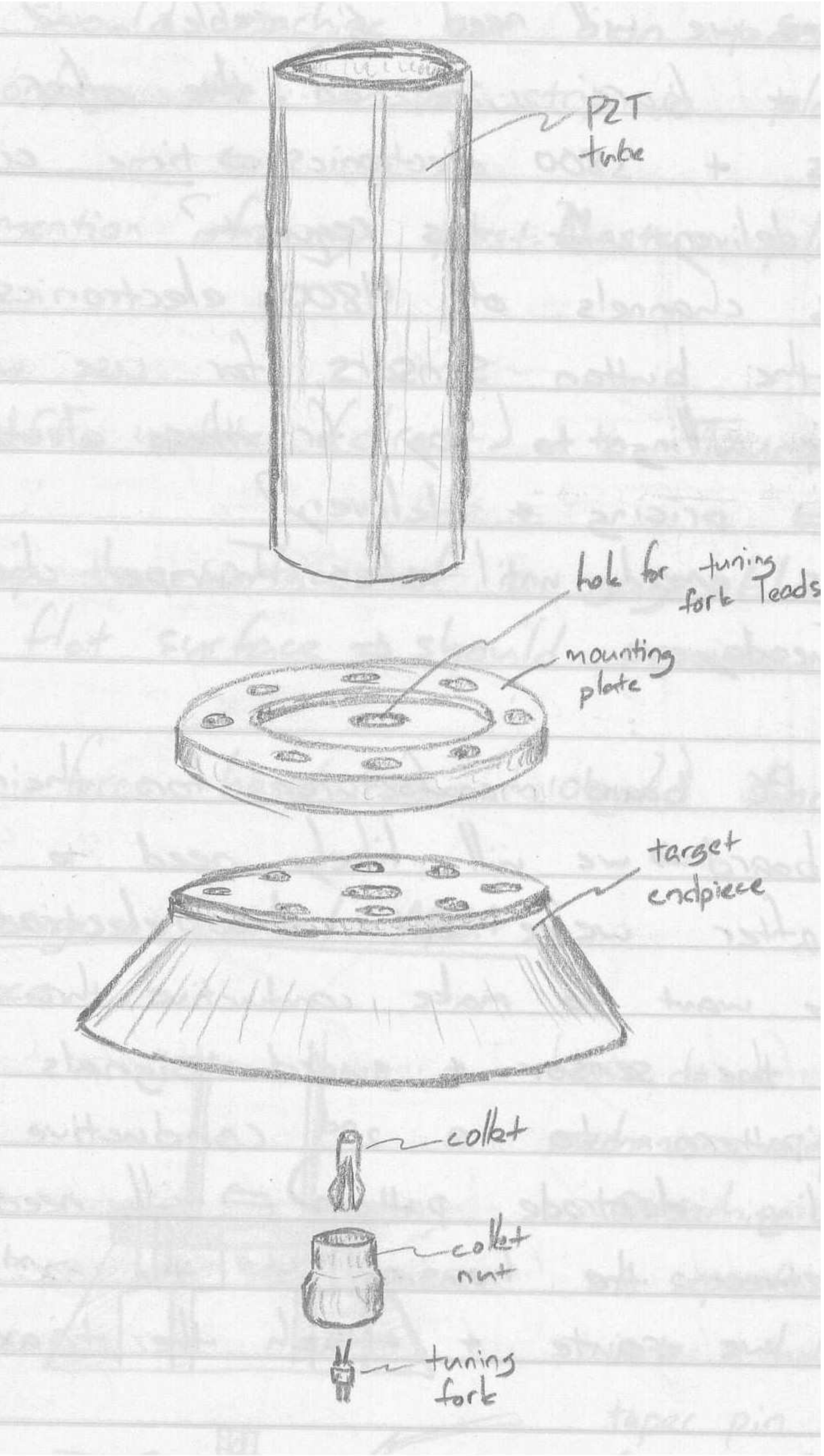

Figure 3-12: Sketch of the conical target endpiece concept. This design was implemented in the metrological AFM.

Figure 3-13: The housing cap.

Figure 3-14: The housing body — isometric view.

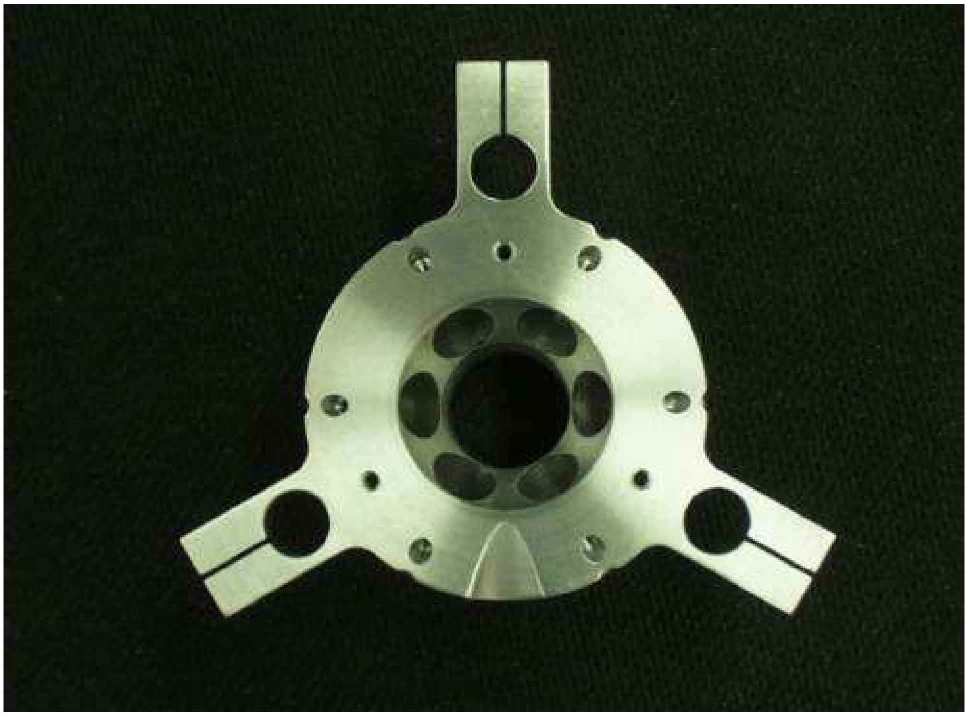

Figure 3-15: The housing body — bottom view.

the sensors. We decided to add the extra three holes to afford ourselves greater flexibility with the microscope's metrology. In normal operation, three probes are sufficient to measure the three degree-of-freedom motion of the target. However, follow-on work with the microscope may show that using all six sensors results in more accurate image data. In the body's underside, a conic cavity provides clearance for the cone-shaped target. Three legs extend from the side of the housing body, which serve as clamps for coarse-approach micrometer heads. Figures A-2 through A-10 of Appendix A contain the nine sheets of the mechanical drawing for the housing body.

In choosing a material for the AFM housing, we weighed considerations of thermal drift, cost, and machinability. We finally settled on 6061-T6 aluminum, though it has a much higher coefficient of thermal expansion than either Invar or Zerodur — two materials frequently employed in precision machine applications. Here, we considered the ultimate goal of this project: to develop fundamental design strategies for future use in a metrological AFM integrated with the SAMM. For such a prototype, the measured accuracy is not of absolute importance. As a result, the much lower cost and more rapid turnaround of machining aluminum dictated the material choice.

Sensor Mount

When the housing body was dimensioned, the diameter of the sensor holes were left slightly oversized. This feature allows a thin-walled aluminum sleeve to slide between the sensor and the inside of the hole, with a pair of soft-tipped set screws used to clamp the sleeve-sensor unit firmly inside the housing. This mounting scheme avoids the large stress concentrations, and the resulting distortions, that would arise if the set screws were tightened directly against the sensor body. Further, the sleeves provide a standoff distance between the driven probe tip and the housing, to avoid loading or shorting out the guard drive. Figure 3-16 shows a photograph of a sleeve lined up with one of the sensors. In Appendix A, Figure A-11 shows the mechanical drawing for the sleeve. The sleeves were anodized, to minimize surface wear.

3.2.2 Endpiece Assembly

As previously mentioned, we decided to implement a removable endpiece assembly, with a cone-shaped target mounted to a small disk permanently attached to the tube scanner's free end. By minimizing the total endpiece mass, the scanner assembly's resonant frequencies may be maintained at relatively high values, thereby allowing sufficiently fast controller bandwidths. Proper low-noise operation of the capacitance sensors also requires a low impedance path be made from the target surface to the common of the sensor electronics. Another important design consideration is the ease with which the target endpiece can be removed, handled, and remounted. The entire scanner assembly — consisting of the housing lid, piezoelectric tube scanner, mounting endpiece, and target endpiece — is displayed in Figure 3-17.

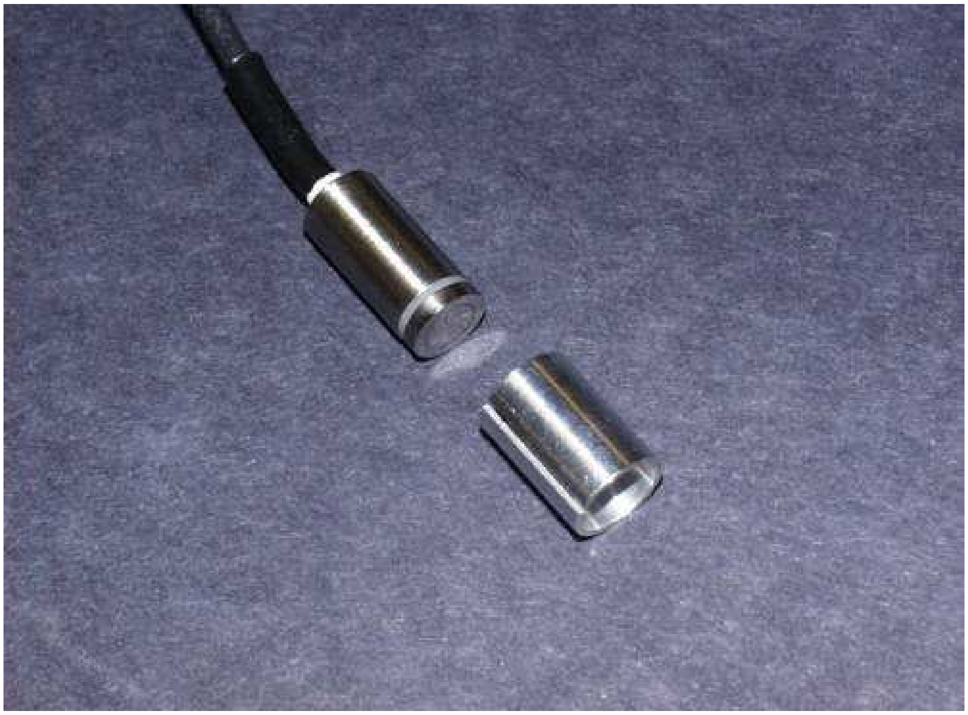

Figure 3-16: A sensor sleeve, next to one of the capacitance sensors.

Figure 3-17: The assembled scanner assembly — housing lid, piezoelectric tube scanner, mounting endpiece, and target endpiece.

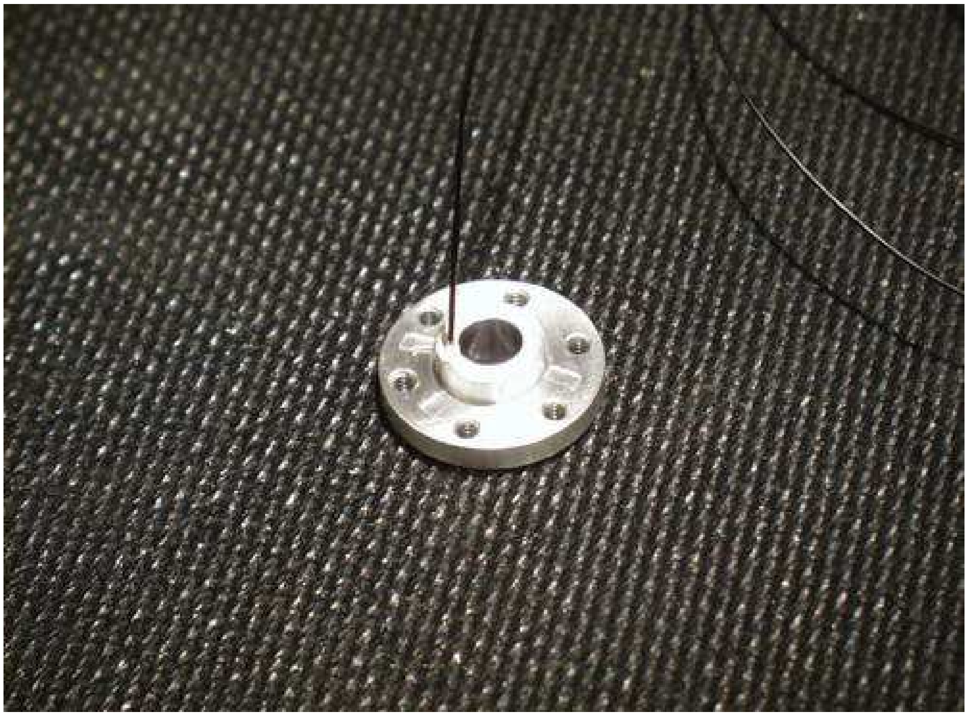

Figure 3-18: The mounting endpiece, with the Mylar standoffs and target ground wire.

Mounting Endpiece

As shown in Figure 3-18, the mounting endpiece is simply an aluminum disk with a small nub on one side. During assembly of the AFM, the bottom end of the tube scanner slips over this nub and epoxy solidifies the joint, with Mylar standoffs again used to prevent short circuits. Cyanoacrylate glue is applied beforehand to bond the Mylar strips to the top surface of the disk and to the side of the disk's nub, thereby providing insulating axial and radial standoffs, respectively. Figure A-12 of Appendix A shows the mechanical drawing for the mounting endpiece.

A strand of 30 AWG wire provides the necessary conductive path from the endpiece assembly to the capacitance sensor electronics. One end of the wire is inserted in a small hole in the mounting endpiece's nub, with silver-filled epoxy[5] making the desired mechanical and electrical connection. The other end of this wire is connected to a

---

[5] a.k.a. cold solder

post on the back of one of the sensor boards.

Target Endpiece

The target endpiece contains several important features. As suggested by the sketch in Figure 3-12, we initially considered integrating a collet-based tuning fork holder, similar to the one used in the open-loop prototype. However, the additional mass and complexity introduced by this mechanism encouraged us to explore other options. In the chosen design, the tuning fork can is glued to the inside of a hole in the bottom of the endpiece. This simple approach results in a mechanical connection with the desired stiffness and strength, without any extra parts. When a mounted tuning fork sensor needs to be removed, the cyanoacrylate bond is softened with a few drops of solvent, then the can is knocked out of the hole with a hammer, using the implement shown in Figure 3-19. Multiple conical endpieces have been fabricated to allow the preparation and replacement of probes without affecting the probe operating in the AFM head itself. A two-sheet mechanical drawing of the target endpiece is shown in Figures A-13 and A-14 of Appendix A.

To reduce the size — and, therefore, the total mass — of the endpiece assembly, small screws (#2-56) are used for bolting the target and mounting endpieces together. A Belleville washer is placed under each screw head, to allow better control of the preload force. The total mass of the endpieces and mounting hardware is estimated at 12 g.

For a piezoelectric tube scanner of fixed geometry and material properties — thus with an assumed constant stiffness — the following equations relate the mass mounted at the free end, m, to the axial mode frequency, ω_{axial}, and the bending mode frequency, $\omega_{bending}$:

$$m^{1/2}\omega_{axial} = \text{constant}, \tag{3.2}$$

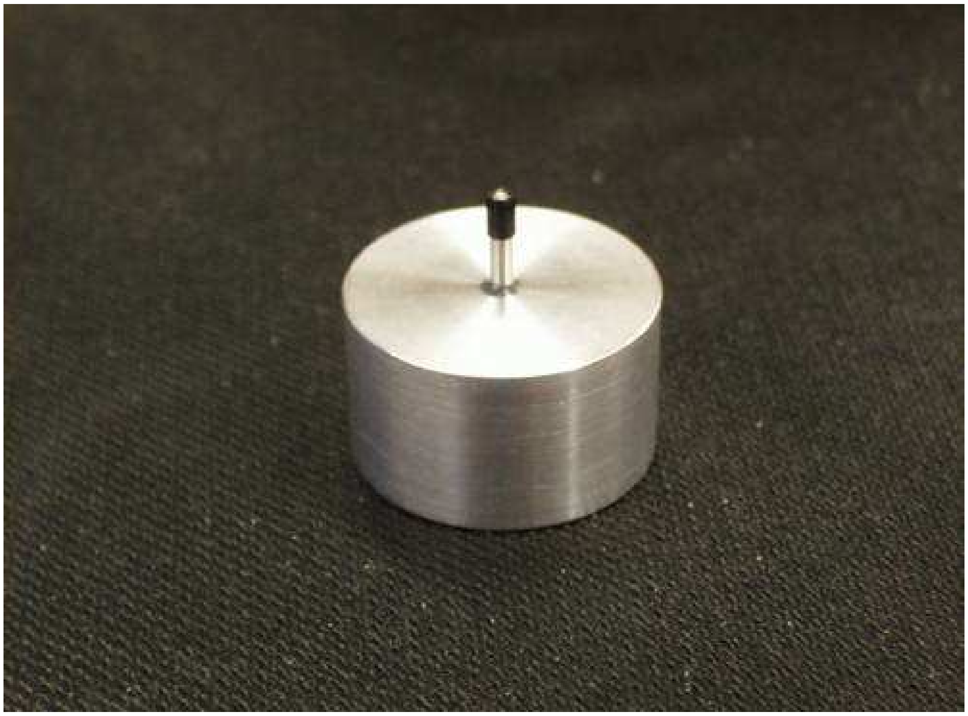

Figure 3-19: Implement used to hammer old tuning fork sensors out of the target endpiece.

$$m^{1/2}\omega_{bending} = \text{constant}, \tag{3.3}$$

based on work presented by Taylor [38]. From earlier measurements of the bending and axial mode frequencies of the open-loop prototype AFM's scanner assembly (see section 2.1.1), and from an approximation of the prototype's endpiece mass, we estimated that $\omega_{axial} \approx 3.3$ kHz and $\omega_{bending} \approx 870$ Hz for the metrological AFM. Both these values are sufficiently high to allow for relatively high closed-loop bandwidths when feedback control is introduced.

A pair of shallow, tapped holes are also included in the bottom of the target endpiece, for a pair of long bolts. We lightly screw the bolts into the holes and use them as temporary handles, when the target needs to be moved to or from the AFM proper.

3.3 Auxiliary Features

This section describes the features designed into the metrological AFM's auxiliary hardware — the parts that are not directly included in the AFM head, but that still serve an important role in the microscope's functioning. This hardware includes the assembly fixtures, kinematic mount, sample mount, and coarse approach viewer.

3.3.1 Assembly Fixtures

Our success in optimizing the accuracy of the metrological AFM depends in large part on our ability to precisely assemble its parts. This section details the fixtures made to help ensure proper alignment and assembly.

Alignment Endpiece

The primary concern in thinking about the initial assembly of the metrological AFM involves our ability to position the target endpiece such that the nominal probe tip position[6] coincides with the intersection of the capacitance sensors' measurement axes. The special alignment endpiece shown in Figure 3-20 helps to achieve this goal. The corresponding mechanical drawing is shown in Figure A-15 of Appendix A.

To begin the assembly process, the fixed endpiece is bolted to the top of the alignment endpiece, with a dowel pin slipped through the two center holes (of equal diameter) to ensure adequate centricity. Epoxy is then applied to the top of the fixed endpiece, and the piezoelectric tube scanner is slid over the endpiece's nub, with the Mylar shims acting as both radial and axial standoffs between the mating surfaces. Next, we bolt the alignment endpiece to the bottom of the housing body, making small adjustments in the relative position of the two parts until their outer surfaces feel flush — in the process, centering the fixed endpiece with respect to the housing.

---

[6] The actual probe tip position will also depend on the accuracy of the tuning fork and fiber tip assembly steps, addressed later in this section.

Figure 3-20: The alignment endpiece used during initial assembly of the metrological AFM.

Finally, the housing cap's nub, covered with epoxy and several strips of Mylar, is aligned with the top of the tube scanner and bolted to the housing — again, with centricity gauged by touch. The assembly is set aside until the epoxy cures (Figure 3-21).

Before the alignment endpiece is removed, its conic surface is used as the zero displacement reference during initial positioning of the capacitance sensors. Having set the dimensions of this surface nominally equal[7] to the corresponding dimensions on the target endpiece allows us to simply slide each sensor into the housing until its output reads zero volts. The readings from the mounted sensors are later monitored when centering the target endpiece, again with the goal of achieving roughly zero output from each.[8]

---

[7] Assuming perfect tolerancing of the target and alignment endpieces during fabrication.

[8] As it turned out, the actual dimensions of the endpieces were sufficiently dissimilar that the sensors needed to be re-zeroed upon initial mounting of the target.

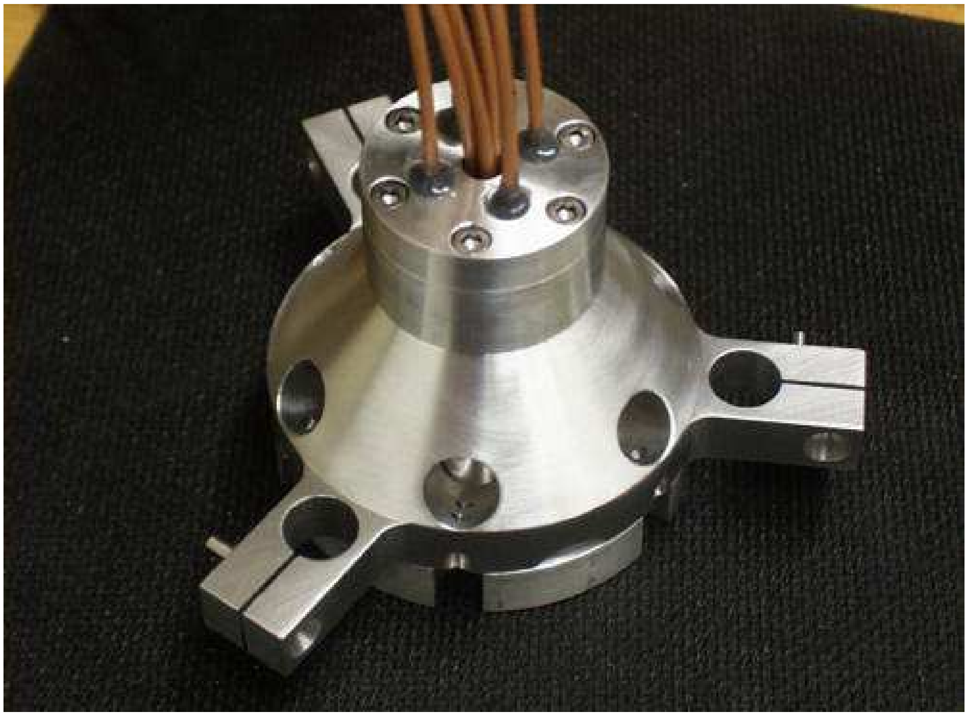

Figure 3-21: The assembly process — waiting for the scanner assembly's epoxy joints to cure.

Tuning Fork Alignment Plate

We also devoted some thought to developing a process for accurately and repeatably mounting the tuning fork sensor in the target endpiece. Figure 3-22 shows one possibility, wherein a pre-assembled fork-fiber unit is positioned inside the target endpiece. Fine alignment of the fiber tip would then be accomplished with the aid of a pair of orthogonally aligned pocket microscopes. This method likely represents the most accurate approach for solving the problem at hand, but would have required too much time to properly develop.

Instead, the simple mechanical solution depicted in Figure 3-23 requires much less time, in terms of development, fabrication, and actual usage. Here, the target endpiece bolts to a flat surface with a shallow groove running along its length. A pair of dowel pins provides angular alignment of the endpiece with respect to the groove. A tuning fork is then dropped through the mating hole in the endpiece,

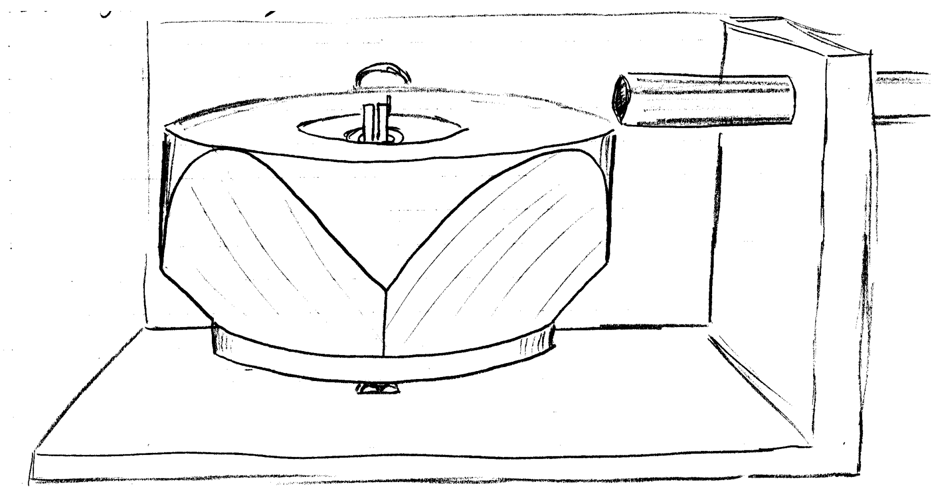

Figure 3-22: Sketch of an early concept for aligning the tuning fork sensor with respect to the target endpiece. In this drawing, the target is based on a corner cube. Two pocket microscopes provide visual feedback during fine positioning of the probe tip.

with the two sides of the groove used to define the position and orientation of the fork's tines (Figure 3-24). With the fork aligned in the endpiece, a couple drops of cyanoacrylate glue are added to bond the can to the endpiece hole, thereby completing the assembly. A mechanical drawing of the fork alignment plate is shown in Figure A-16 of Appendix A.

Probe Assembly

Through our experience with the open-loop AFM prototype, we found that the original procedure for mounting fiber tips to the tuning forks was overly cumbersome and not sufficiently controllable. In designing the fork-fiber alignment fixture for the metrological AFM, we focused on both simplifying the assembly procedure and improving the quality and consistency of the finished probe. As shown in Figure 3-25, the probe assembly fixture consists of a target endpiece — with a tuning fork already glued in place — mounted to a two-axis precision linear stage. The fiber tip is placed near the front edge of an aluminum slab, with angle (in the horizontal plane) and height controlled with a pair of precision stages.

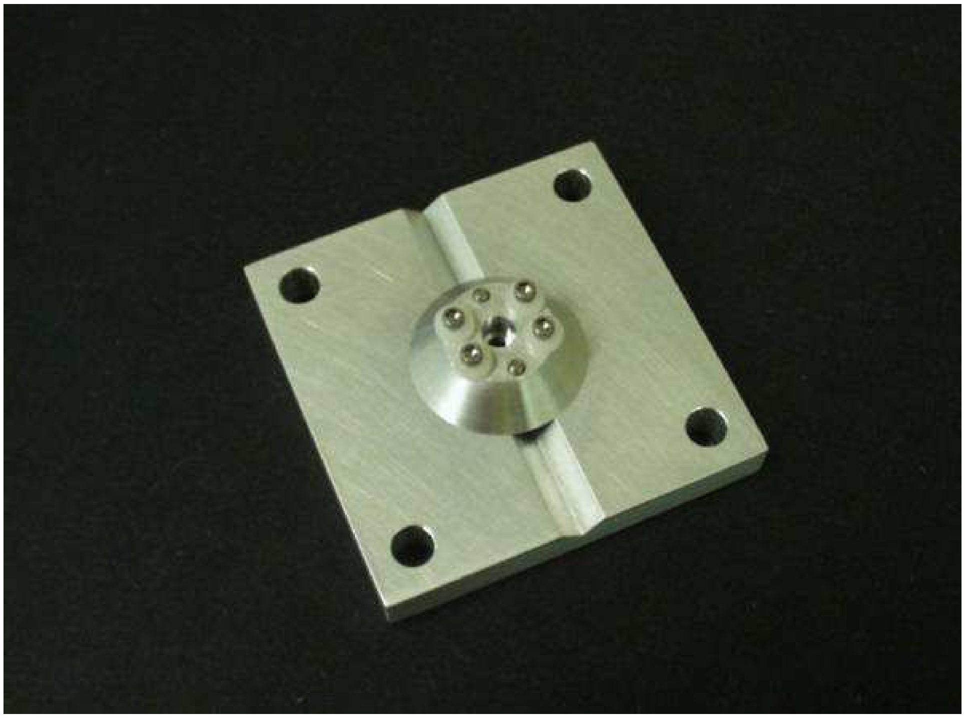

Figure 3-23: The target endpiece mounted to the fork alignment plate. The plate's groove defines the position and orientation of the tuning fork's tines.

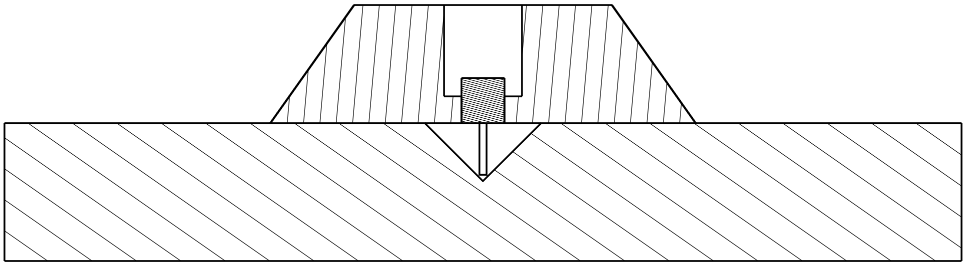

Figure 3-24: A cross-section of the target endpiece mounted to the fork alignment plate, showing the two bottom edges of the fork's tines resting against the two sides of the plate's groove. The tines' thickness is exaggerated in this drawing.

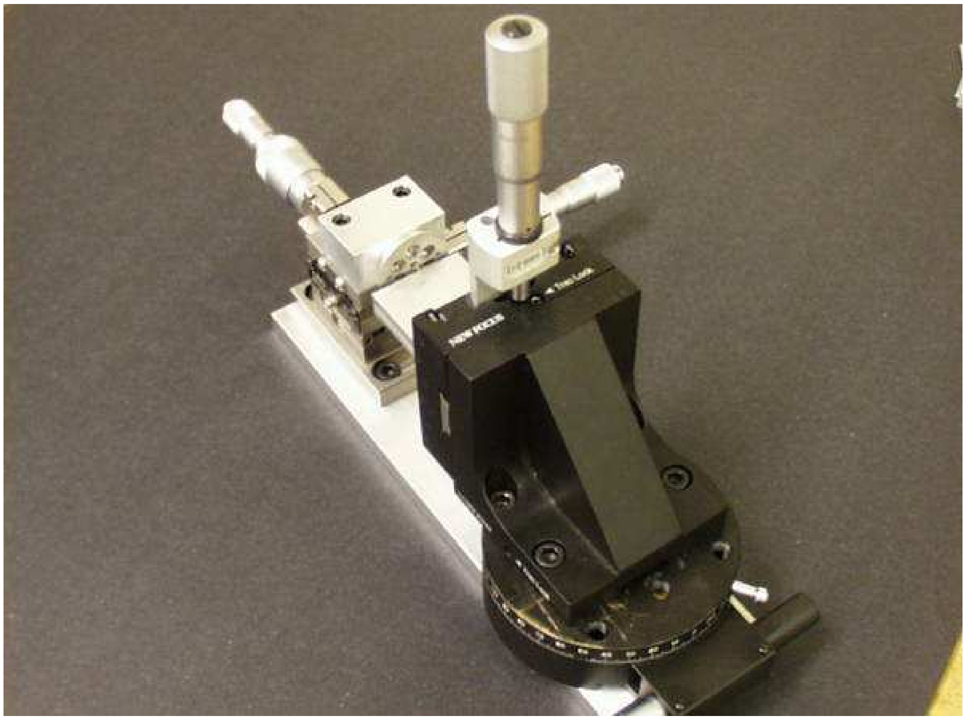

Figure 3-25: The fixture used to mount the fiber tip to the tuning fork.

To reliably transfer a fiber tip from the original fiber to the probe assembly fixture, the uncut fiber is first placed on a piece of double-sided tape, with the tip hanging just beyond the edge of the tape. A knife is then used to cut a line through the tape, slicing off the tip in the process. The resulting strip of tape, with the tip stuck onto it, is placed on the end of the assembly fixture's aluminum slab. A small amount of glue is then wiped onto the edge of the tuning fork's bottom tine, and the slab is raised until the fiber contacts the fork. To control the size of the glue drop, a short length of thin, bare wire is used as a glue wand. For proper positioning of the four adjustable axes, the fiber and fork are viewed under a stereo microscope.

3.3.2 Kinematic Mount

We selected a kinematic mounting scheme for coupling the metrological AFM head to its base plate. Professor Martin Culpepper provided valuable insight during the early phase of this feature's design. The configuration provides the high stiffness and repeatability desired for positioning the probe with respect to the sample [37]. As with the prototype AFM, the coupling is based on a ball-and-vee design, where the balls are located at the ends of the AFM's three height-adjustment micrometer heads and the vees are formed between pairs of hardened steel dowel pins. Three shallow slots were milled into the top surface of the base plate and the pins were epoxied side-by-side in each of the slots.[9] Before placing the pins in the grooves, their surfaces were polished with 600 grit sandpaper, to reduce the height of surface asperities. After setting the pins in place, a few drops of oil were added to prevent cold-welding of the mating surfaces. The assembled grooves can be seen in the photograph of the base plate shown in Figure 3-26. The base plate's five-sheet mechanical drawing is presented in Figures A-17 through A-21 of Appendix A.

With the head sitting in the pin grooves, a set of three extension springs hook between dowel pins in the base plate and dowel pins sticking out of the housing body's micrometer clamps. These springs provide a total preload force of about 24 N, which results in a coupling stiffness of approximately 6×10^9 N/m.

3.3.3 Sample Mount

Figure 3-26 also shows the AFM's sample mount mechanism. The mount consists of a steel gauge block epoxied to the top of the base plate, along with a set of four spring clips. The gauge block provides a flat, hard surface for placing a second plate to which a sample is permanently fixed. Here, it is important that the mounting surface be flat, or the sample plate will make contact at only a few points. This condition could give rise to relatively large stresses in the plate, with resulting large strains, and could potentially distort the sample surface and deteriorate position stability.

We originally planned to use the spring clips to hold the sample plate against the

---

[9] While the epoxy cured, a 20 N preload force was applied evenly among the six groove pins, to insure all epoxy was squeezed out of the pin-on-plate lines of contact.

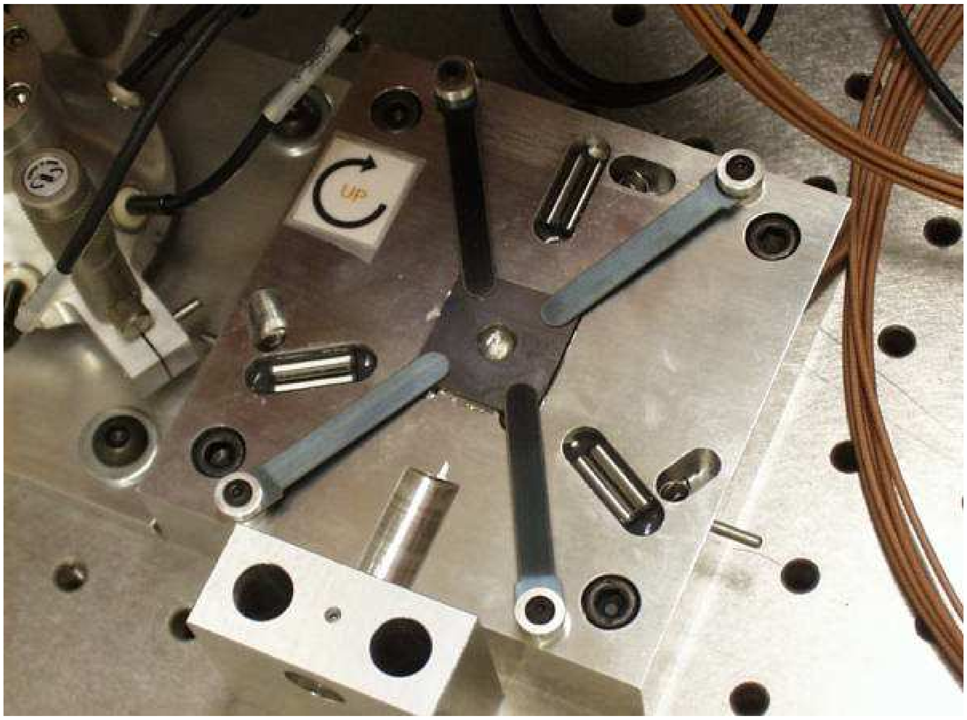

Figure 3-26: The metrological AFM's base plate. Pairs of dowel pins form grooves for the kinematic coupling. Spring clips preload the sample plate (not shown) against a permanently mounted gauge block.

mounting plate. The clips were designed to provide an approximately 1 N preload force at each of the four corners of the sample plate. Unknown to us at the time of ordering, however, the square gauge blocks that we purchased to serve as both the sample and mounting plates are made with large holes through their centers. Whereas we initially planned to glue a sample to the center of each sample plate, we instead have to place the samples offset from this position. As a result, the spring clips cannot reach all four of the sample plate's corners. Instead, we carefully clean the mating surfaces of the two gauge blocks, then wring them together. This approach also results in a simple and effective method for holding the sample firmly against the base plate, and the spring clips are thus not necessary.

3.3.4 Coarse Approach Viewing

Before imaging a sample with the metrological AFM, the probe tip must first be brought into engagement. We use the three micrometers to do this in a controlled fashion, slowly lowering the head into position. As the tip approaches the sample, there must be a reliable means for gauging how close it is. Particular care must be taken to avoid crashing the fiber into the sample, which could potentially break the tip on the tuning fork sensor. For the metrological AFM, a simple 30x-magnification pocket microscope — an Edmund Industrial Optics[10] NT38-427 — serves as the coarse approach viewer (Figure 3-27).[11] A pair of notches are machined into the base plate and AFM housing, so the microscope can fit in the desired location and have an unobstructed view of the probe tip, respectively. A simple aluminum mount holds the microscope in place, using a soft-tipped set screw. The mount can be seen at the bottom of Figure 3-26, and its mechanical drawing is shown in Figures A-22 and A-23 of Appendix A. A 30 Watt light source with adjustable fiber-optic waveguide — a

---

[10] See Appendix B.

[11] This microscope produces an inverted image.

Figure 3-27: The 30x-magnification pocket microscope, used as a coarse approach viewer.

Dolan-Jenner[12] 190-1 — provides a focused beam of light on the sample during the engagement process. In practice, we watch the reflection of the fiber off the top surface of the sample, as the reflected tip gets closer to the real tip. This provides greater sensitivity than just watching the tip motion.

3.4 Summary

This chapter presented the key features of the metrological AFM's mechanical design. The discussion began with a description of several of the concepts considered during the initial stage of the design process. From this conceptualization phase, we decided to 1) align the capacitance sensors such that their measurement axes intersect at the probe tip, thereby minimizing Abbe offset error; 2) use long cylindrical sensors —

---

[12] See Appendix B.

instead of smaller button sensors or home-made circuit board sensors — because of their easy availability and simple mounting scheme; and 3) build a removable cone-shaped endpiece to serve as the sensors' target.

The remainder of the chapter filled in the details of the AFM's hardware, beginning with the housing and endpiece assemblies. The housing gives the AFM head its structure. It contains the holes for the six capacitance sensors and a central bore in which the scanner assembly is located, as well as three clamps for the coarse-approach micrometers. The endpiece assembly mounts to the end of the piezoelectric tube scanner and includes the removable cone-shaped target. In the chapter's third section, the AFM's auxiliary features were explained. This section included discussions of the assembly fixtures (for the AFM's initial assembly, the positioning of the tuning fork in the target endpiece, and the mounting of the fiber tip on the tuning fork sensor), the ball-and-vee kinematic coupling, the sample mount, and the coarse approach viewer.

The next chapter details the integration of the metrological AFM's capacitance sensors. This discussion leads into Chapter 5, which describes the microscope's control system.

Chapter 4

The Metrological AFM — Metrology

This chapter describes the integration of the probe position data from the metrological AFM's capacitance sensors. As noted in section 3.1.2, the AFM head is equipped with six 2805-S capacitance probes made by ADE Technologies.[1] Each sensor provides an analog signal which is assumed to be proportional to the displacement of the target endpiece in the direction of the sensor's measurement axis. The sensor output is sampled by a dSPACE[2] DS1103 controller board, which is described in more detail in section 5.1. For all of the experiments with the metrological AFM, the capacitance sensor signals are converted by 16-bit analog-to-digital (A/D) converters located on the board.

Section 4.1 begins with our definition of the sensor's measurement axis, then briefly describes how we determined its location with respect to the sensor's geometrical axis of symmetry. Knowledge of the relative position of these two axes is important for designing the AFM housing body such that the probe tip lies at the optimal position. Section 4.2 provides details on the linear transformation used to compute the probe's

---

[1] See Appendix B.

[2] See Appendix B.

position with respect to a meaningful coordinate frame, based on the sensor data. Section 4.3 then analyzes the noise in the probe position measurements. For the final system configuration, the measured RMS noise in the transformed X, Y, and Z coordinates within the DS1103 control processor is 1.3 nm, 1.3 nm, and 1.2 nm, respectively. Concluding remarks, with some suggestions for future improvements to the setup of the AFM's metrology, are presented in section 4.4.

4.1 Sensor Measurement Axis

As mentioned in section 3.1.2, the metrological AFM's capacitance sensors are positioned such that Abbe offset error is minimized. This goal requires knowledge of the location of the axis through the sensor which, when aligned with the probe tip, results in zero Abbe offset. We call this preferred axis the 'measurement axis.'

Determining the location of the measurement axis requires some attention, since the probe's sense electrode is relatively large — 5 mm in diameter — and the target surface has significant curvature. If the probe sense electrode diameter were much smaller, we could simply assume that the measurement axis is colinear with the sensor's geometrical axis of symmetry, since the resulting maximum possible error would not be very large. Likewise, if the target surface were flat, we could more safely assume that these two axes are colinear, from symmetry.

As a simple attempt to take account of the target curvature over the finite area of the sensor face, we assume that the measurement axis lies along the intersection of the horizontal and vertical planes shown in Figure 4-1. Here, the vertical plane cuts through the center of the circular sensor face. Both the sensor and the target are symmetric about this plane, so the measurement axis should lie somewhere within it. However, there is no such horizontal plane of symmetry for the conic target surface. Instead, we assume that the preferred horizontal plane is the plane for which the

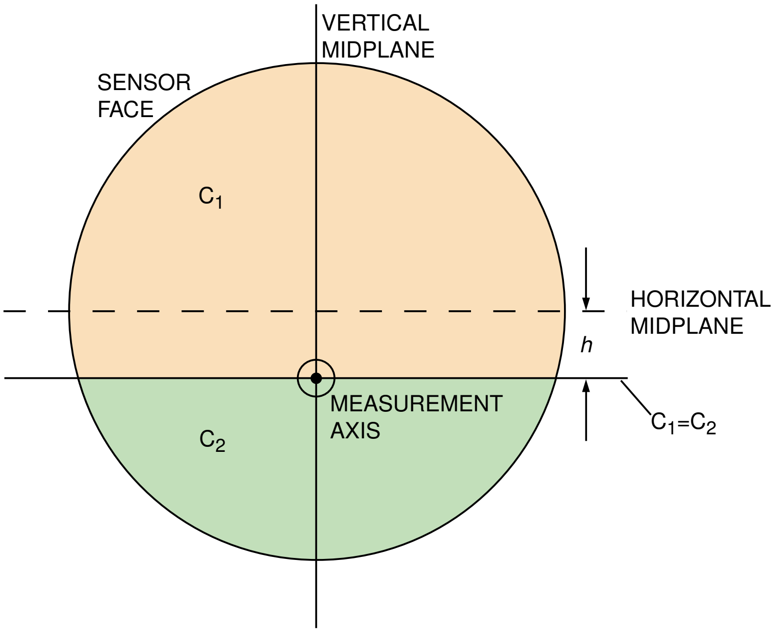

Figure 4-1: Drawing of the capacitance sensor's face, used for the discussion of the sensor's measurement axis. The measurement axis is defined here as the intersection of the vertical midplane with the horizontal plane for which the capacitance above, C_1, equals the capacitance below, C_2.

sensor-target capacitance above equals the sensor-target capacitance below. This problem is solved iteratively to find the position of the preferred horizontal plane, taking into account the elliptical profile of the target face. The elliptical profile is defined by the intersection of the sensor's horizontal plane with the surface of the cone and must be determined in order to calculate the distance between the probe and the target for each point on the surface of the sensor face. This exercise indicates that for our probe and target geometries, the plane lies a distance of $h \approx 20$ μm below the geometrical midplane. This effect is small enough that we neglect it when dimensioning the AFM head and design for the measurement axis to coincide with the geometrical axis of the probe.

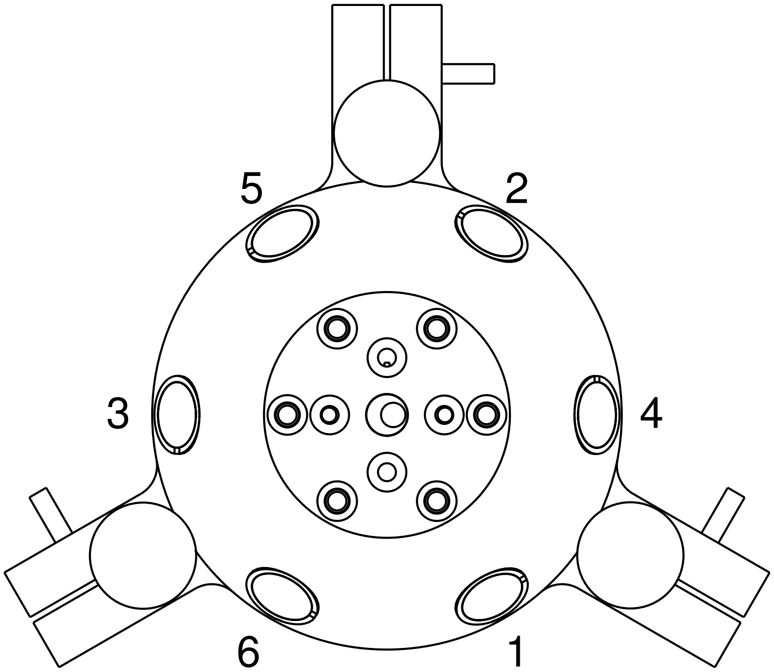

Figure 4-2: Top view of the metrological AFM, with numerical labels assigned to each of the probes. For all of the experiments requiring full three degree-of-freedom position data, we only used the output from sensors 1, 2, and 3.

4.2 Coordinate Transformation

Though the AFM head contains six capacitance probes, we decided to use only three of them for measuring the displacement of the target endpiece. These probes — sensors 1, 2, and 3, as labelled in Figure 4-2 — provide a minimum set of signals for calculating the three degree-of-freedom displacement of the target endpiece. Though we expect future experiments will show improved performance when data is sampled from all six sensors, we decided to work with this slightly simpler configuration to get started more quickly.

The sensors' measurements are converted to position within a coordinate frame referenced to the sample plane, as shown in the schematic drawing in Figure 4-3, for two primary reasons. Firstly, this coordinate transformation makes it easier to compare the imaged sample topography to the actual surface dimensions, when the

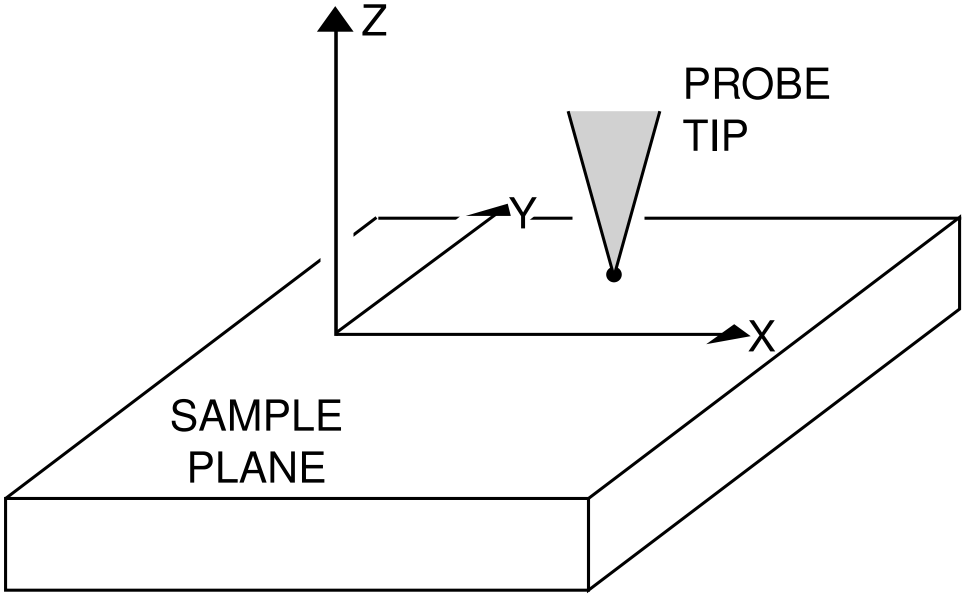

Figure 4-3: The sensor coordinate frame referenced to the sample plane. The X-Y plane lies parallel to the sample plane.

plotted data is properly oriented with respect to the plot's axes. More importantly, for the control of the scanner assembly's lateral motion — which is detailed in section 5.2 — the corresponding controllers must be given measured X and Y position data for comparison with the controller set points.

Figure 4-4 shows the geometry associated with this transformation. In the left drawing, θ is the angle between each sensor's measurement axis and the vertical axis, δ is the displacement of the target endpiece in the direction of the sensor's measurement axis with increasing values as the gap opens, and Z is the component of the endpiece's displacement parallel to the vertical axis. In the equations that follow, each sensor is associated with its own value of δ: δ_1, δ_2, and δ_3, for sensors 1, 2, and 3, respectively. In each case, a positive change in δ corresponds to motion of the target away from the sensor face. Also in this figure, the right drawing shows the projection of the sensor measurement axes into the X-Y plane. The angle between each of the projected axes is 120°.

From basic geometry, the relationship between the values of δ and the probe tip's

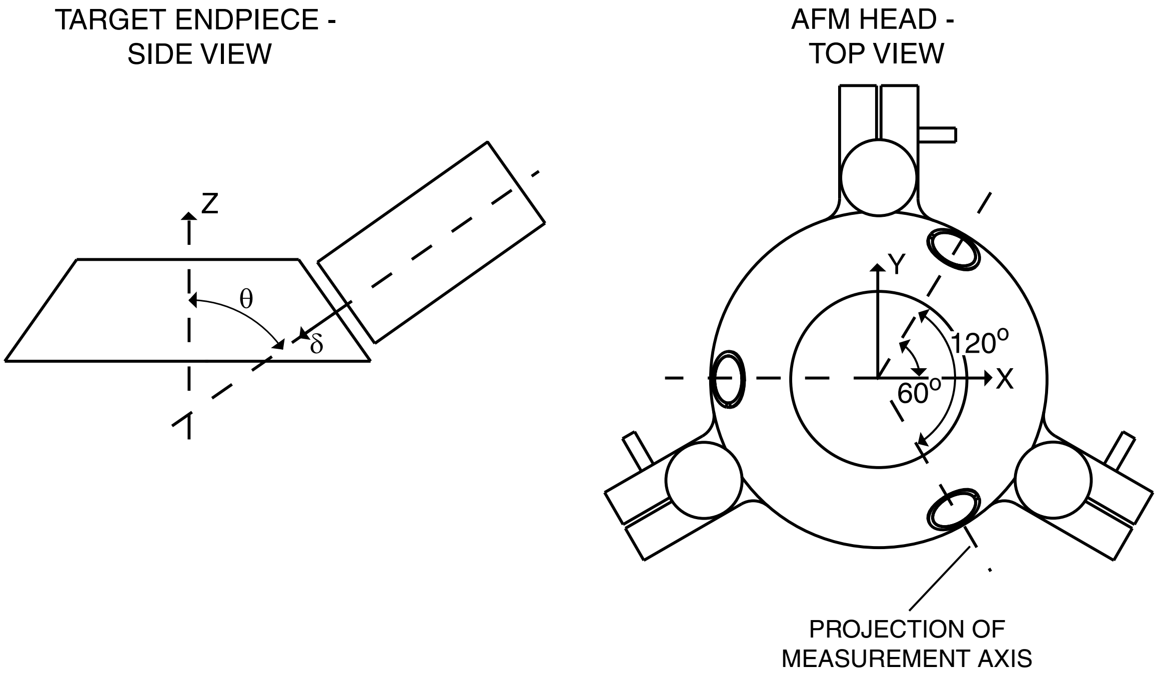

Figure 4-4: Schematic drawing showing the geometry involved in defining the coordinate transformation for the metrological AFM's position data. In the side view of the target endpiece, only one sensor is shown, and the distance from the sensor to the target is exaggerated. In the top view of the AFM head, the unused sensors are not drawn.

(X,Y,Z) position is given by

$$\begin{aligned} \mathrm{X} &= -\delta_1 \sin\theta \cos 60^\circ - \delta_2 \sin\theta \cos 60^\circ + \delta_3 \sin\theta, & (4.1) \\ \mathrm{Y} &= \delta_1 \sin\theta \sin 60^\circ - \delta_2 \sin\theta \sin 60^\circ, & (4.2) \\ \mathrm{Z} &= -\delta_1 \cos\theta - \delta_2 \cos\theta - \delta_3 \cos\theta. & (4.3) \end{aligned}$$

Note that since the measurement axes intersect at the probe tip, we do not need to include the angular deflection of the end of the piezo tube in these calculations.

We assume each sensor's voltage output is directly proportional to the corresponding value of δ, though clearly from the sensors' 'Linearity' specification listed in Table 3.1.2, the relationship is not perfectly linear. From the 'Range' and 'Output Voltage' specs given in the same table, the associated calibration constant is 5 μm/V. Using this value, the probe's (X,Y,Z) position may be computed from the sensor voltage signals — V_1, V_2, and V_3 — using the following matrix equation:

$$\begin{pmatrix} \mathrm{X} \\ \mathrm{Y} \\ \mathrm{Z} \end{pmatrix} = (5\ \mu\mathrm{m/V}) \begin{bmatrix} -\sin\theta\cos 60^\circ & -\sin\theta\cos 60^\circ & \sin\theta \\ \sin\theta\sin 60^\circ & -\sin\theta\sin 60^\circ & 0 \\ -\cos\theta & -\cos\theta & -\cos\theta \end{bmatrix} \cdot \begin{pmatrix} V_1 \\ V_2 \\ V_3 \end{pmatrix}. \qquad (4.4)$$

For this equation, we assume that the sensors are positioned and oriented exactly as specified in the housing drawings and that the housing is perfectly level with respect to the sample plane. As described in section 3.1.2, the housing's sensor holes are aligned such that $\theta = 54.7^\circ$.

However, since the tube scanner is not precisely oriented with respect to the sensor coordinate frame, we pre-multiply this result by a second 'correction' matrix. We prefer to have the measurement system register a displacement strictly in X, when a bipolar change in voltage is applied to the piezoelectric tube scanner's opposing X electrodes. Ideally, the same behavior would also be observed in Y. We originally assumed that the situation could be modelled based on the two planar coordinate frames shown in Figure 4-5. In this figure, X′ and Y′ are parallel to the directions in which the AFM probe moves when differential voltages are applied to the scanner's opposing X and Y electrode pairs, respectively. These axes are assumed to be orthogonal and rotated an angle, α, from the X-Y plane defined in Figure 4-4. To determine the value of α, we commanded a differential voltage to the X electrode pair such that the probe tip moved 2000 nm in X, as calculated using equation (4.4). The corresponding change in the measured Y position was 15 nm. This measurement indicates a rotation angle of $\alpha = 0.43°$. For all of the subsequent experiments which required (X,Y,Z) position data, we simply pre-multiplied equation (4.4) by the transformation matrix

$$R = \begin{bmatrix} \cos\alpha & -\sin\alpha & 0 \\ \sin\alpha & \cos\alpha & 0 \\ 0 & 0 & 1 \end{bmatrix}. \tag{4.5}$$

Then, the final expression for the probe's position, as a function of the capacitance sensor output, is given by

$$\begin{pmatrix} \mathrm{X} \\ \mathrm{Y} \\ \mathrm{Z} \end{pmatrix} = (5\ \mu\mathrm{m/V}) \begin{bmatrix} -.41132 & -.40519 & .81654 \\ .70182 & -.71244 & 0 \\ -.58161 & -.57294 & -.57729 \end{bmatrix} \cdot \begin{pmatrix} V_1 \\ V_2 \\ V_3 \end{pmatrix}. \tag{4.6}$$

After some additional thought, we realized that this approach for aligning the measurement coordinate frame with respect to the scanner assembly's motion is flawed. Specifically, the piezo tube does not move along perfectly orthogonal axes when differential voltages are applied to the two pairs of opposing outer electrodes. In other words, the assumption that the X′ and Y′ axes in Figure 4-5 are orthogonal is false. Also, in open-loop operation, the tube scanner bends significantly in the X-Z plane when a common bias voltage, V_{axial}, is applied to all four outer electrodes — the con-

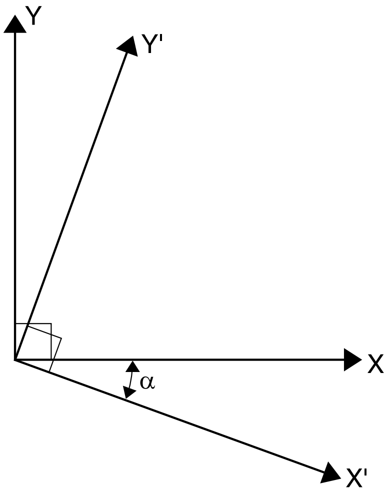

Figure 4-5: Coordinate frames used to determine the 'correction' matrix given in equation (4.5). X′ and Y′ are parallel to the directions in which the AFM probe moves when differential voltages are applied to the scanner's opposing X and Y electrode pairs, respectively. The X-Y plane is as defined in Figure 4-4.

dition used to command vertical displacements, as described in section 2.1.1. Instead of using the matrix in equation (4.5) to rotate the measurement coordinate frame, a better approach would utilize a driving transformation between the controllers' output and the high-voltage amplifier's input. Then, the (X,Y,Z) data would be calculated using equation (4.4) without modification. Figure 4-6 shows the corresponding block diagram. This approach would provide a more effective way of decoupling the commanded motion along the three orthogonal axes of the measurement frame, since it would more directly correct for non-idealities in the relationship between the tube scanner's drive voltage condition and the resulting deflection of the target endpiece. However, this later thought has not been implemented yet, and all the results reported hereafter use the form of equation (4.6) with the coordinate 'correction' included.

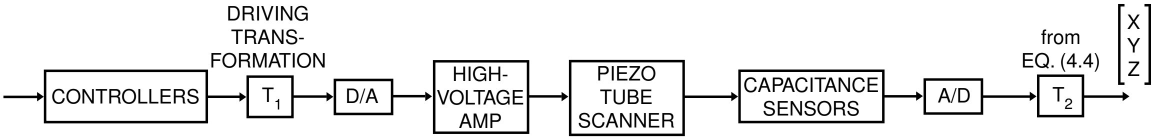

Figure 4-6: Block diagram showing a suggested improvement for aligning the scanner assembly's commanded motion with respect to the sensor coordinate frame. A matrix, T_1, provides a driving transformation between the controllers' output and the high-voltage amplifier's input, so the scanner assembly can more easily be commanded to move parallel to the X, Y, and Z axes in a decoupled manner.

4.3 Sensor Error Budget

The noise in the measurement of the AFM probe's position plays a significant role in the ultimate performance attainable with the imaging system. As such, we have taken some care to minimize the noise. To avoid low-frequency beats from entering the capacitance sensors' output — a problem mentioned in section 2.1.3 in reference to the prototype AFM's inductive sensors — the sensors' electronics are configured such that a single oscillator drives all six capacitance probes, as recommended by the manufacturer, ADE Technologies. Also for optimal noise performance, the relative phases of the sensors' drive signals are set as shown in Figure 4-7, where opposing pairs of sensors are driven 180° apart. This phase configuration results in a net zero current flow through the target.

Among the several alternatives that have been experimentally investigated, the sensor wiring scheme shown in Figure 4-8 demonstrates the lowest electrical noise. Figure 4-9 shows a 1 ms capture of the noise in one of the sensor signals, as measured by an oscilloscope, via a Tektronix[3] AM 502 differential amplifier that was set for a 1 MHz bandwidth. For this experiment, the high-voltage amplifier was turned off. However, since the target was not clamped directly to the sensor body, some of the measured noise may be attributable to mechanical vibration of the scanner assembly. With this consideration, the 1.9 nm RMS noise calculated from the data represents

---

[3] See Appendix B.

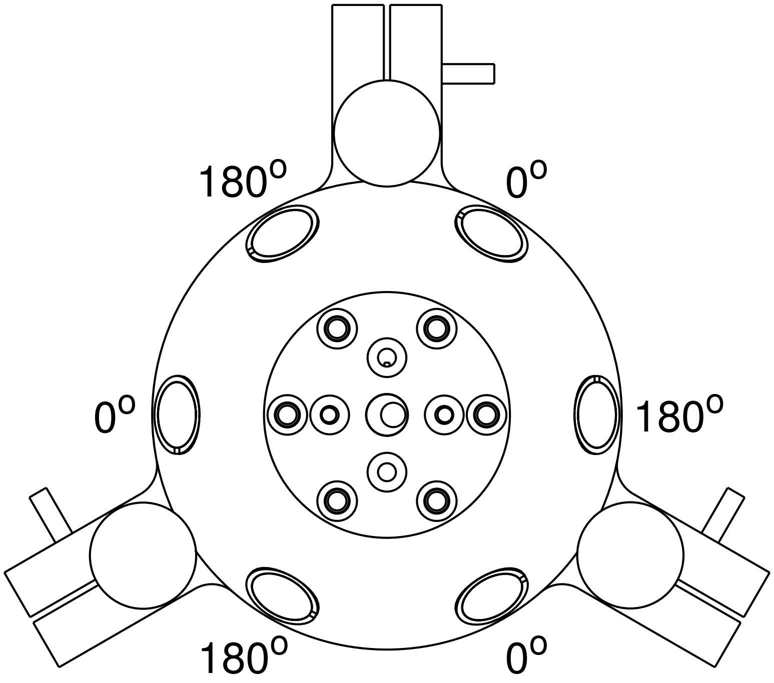

Figure 4-7: Top view of the metrological AFM, with the relative phases of the sensors' drive signals labelled next to the corresponding sensor positions.

only an upper bound on the sensor's electrical noise. As shown in Table 3.1.2, the total sensor travel is 100 μm, which corresponds to ±10 V full-scale output, so the measured RMS noise is approximately one part in 50,000. Also, the data is dominated by a 16 kHz component. This frequency seems too high to be explained by one of the scanner assembly's structural modes. Instead, the observed 16 kHz noise likely originates from the oscillator in the capacitance sensors' electronics, which is believed to run at this frequency.

Figure 4-10 shows data acquired under the same conditions as the data shown in Figure 4-9, except with the high-voltage amplifier turned on. The data indicates a decrease in the noise level for this condition, down to 1.6 nm RMS. The reduction in noise may indicate some change in the electrical configuration — e.g. an altered grounding condition — when the amplifier is switched on.

In converting the sensor output from analog to digital, a significant amount of

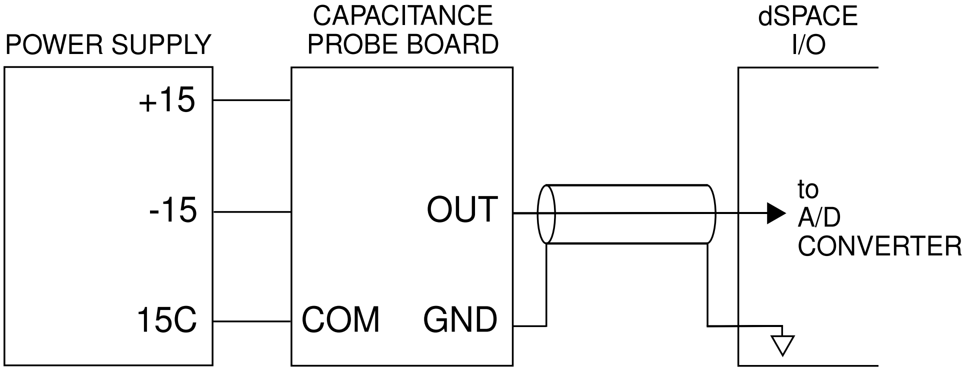

Figure 4-8: Schematic of the capacitance sensor wiring.

random noise is added into the signal. Some of this noise originates in the A/D conversion circuitry, while other portions are likely injected from the other signals in the flat cable connecting the controller's I/O panel to the controller board. A representative 10 ms capture of this noise is presented in Figure 4-11. For this data, a 50 Ω terminator was placed on one of the A/D inputs on the I/O, so — in the absence of noise — the data should equal zero throughout the trace. Instead, the calculated RMS value is 1.4 nm, comparable to the noise measured in the sensor's analog output. Since the signal amplitude is relatively small, the A/D quantization at the 20 kHz sampling rate is clearly visible. The noise corresponds to 5 of the A/D converter's bits, peak-to-peak.

To help reduce the impact of the random A/D noise, we post-filter the A/D conversion with a simple finite impulse response (FIR) filter of the form

$$H_{FIR}(z) = \frac{1 + z^{-1} + z^{-2} + z^{-3} + z^{-4}}{5}. \tag{4.7}$$

The filter's output is the 5-sample moving average of its input. Figure 4-12 presents the continuous-time equivalent Bode plot for this filter, for a 20 kHz sampling frequency. As seen in the data of Figure 4-13, this averager reduces the noise for the

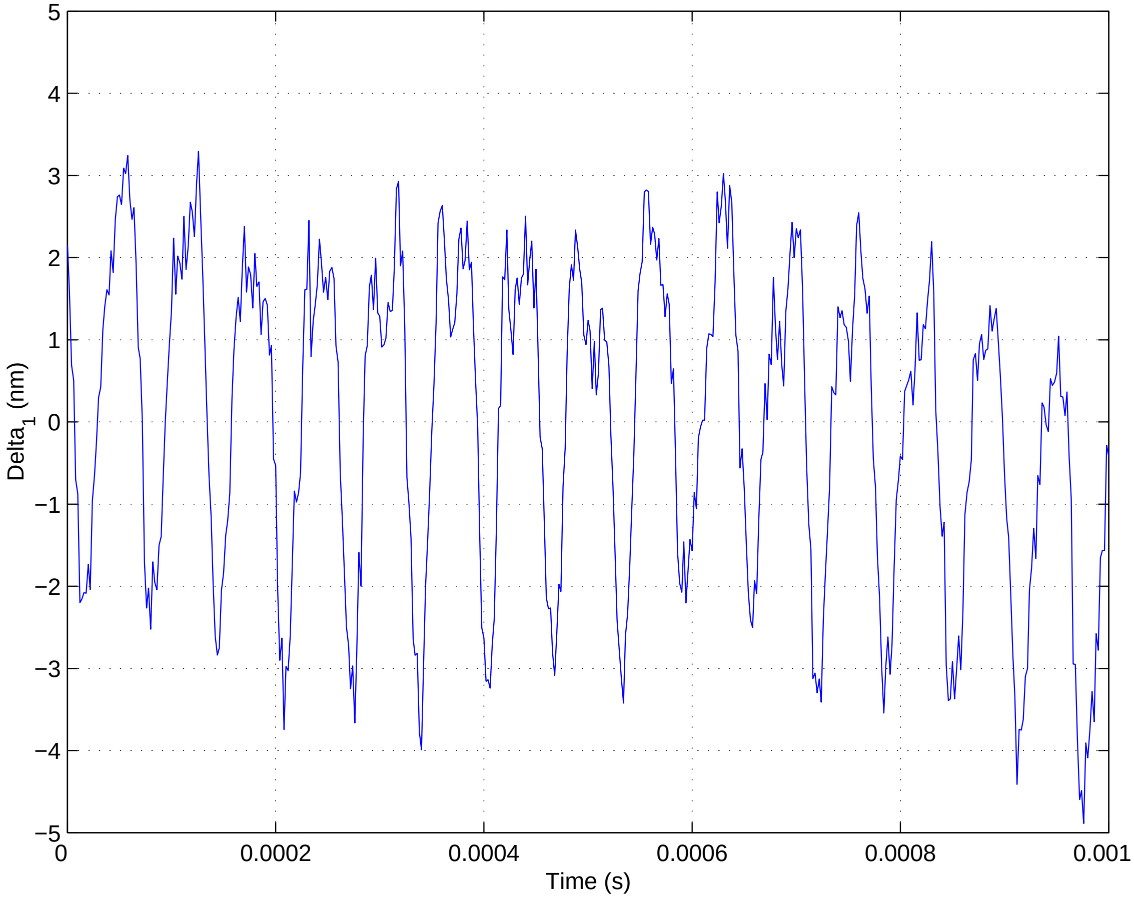

Figure 4-9: High-frequency noise in the output of one of the capacitance sensors, as measured by an oscilloscope, via a Tektronix AM 502 differential amplifier set for a 1 MHz bandwidth. The controller board's A/D converter was not included in the measurement. The piezoelectric tube scanner's high-voltage amplifier was off while the data was acquired. This signal has an RMS value of 1.9 nm, measured over an interval of 1 ms. The 16 kHz contribution to the noise is most likely caused by the sensors' driving oscillator.

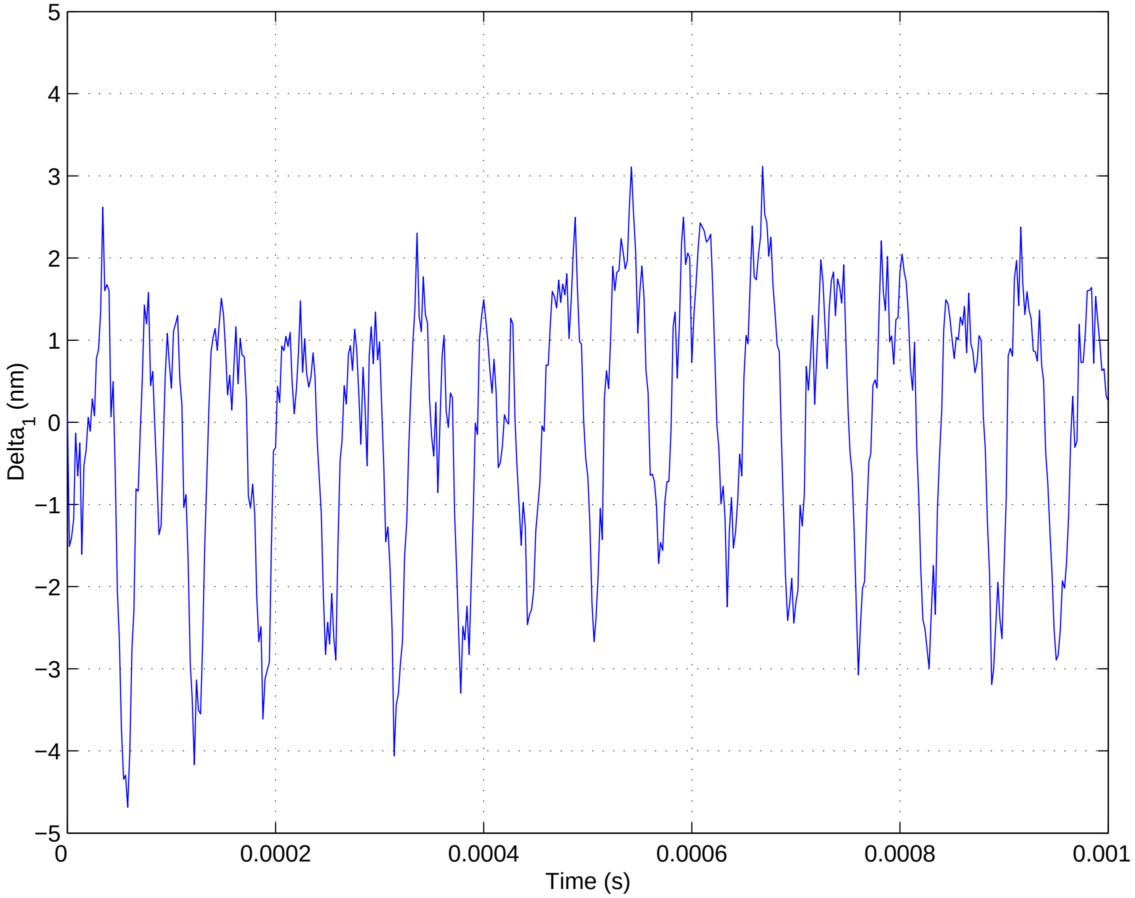

Figure 4-10: High-frequency noise in the output of one of the capacitance sensors, as measured by an oscilloscope, via a Tektronix AM 502 differential amplifier set for a 1 MHz bandwidth. The controller board's A/D converter was not included in the measurement. The piezoelectric tube scanner's high-voltage amplifier was on while this data was acquired. This signal has an RMS value of 1.6 nm, measured over an interval of 1 ms.

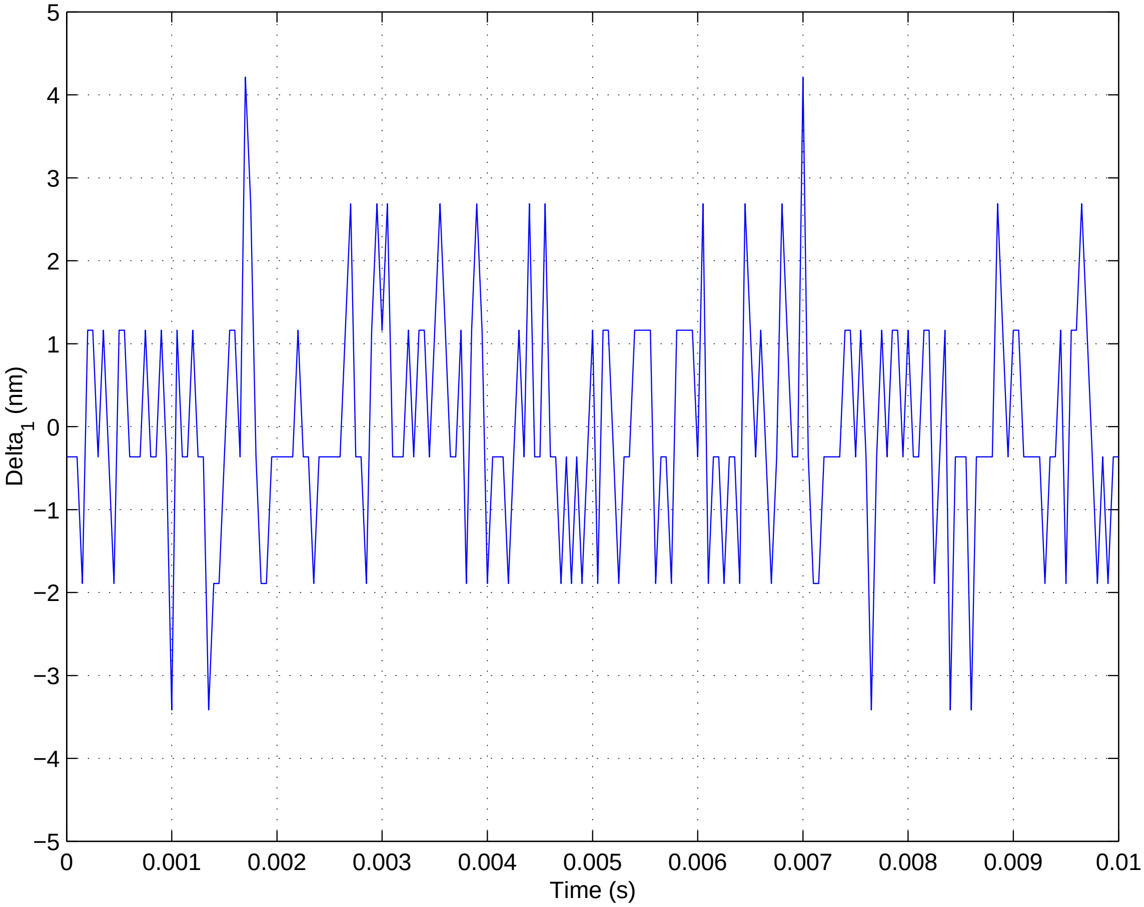

Figure 4-11: Noise measured in one of the controller board's A/D channels, with a 50 Ω terminator placed on the corresponding input on the board's I/O panel. The 10 ms trace has an RMS value of 1.4 nm. The converter quantization levels are apparent in this data.

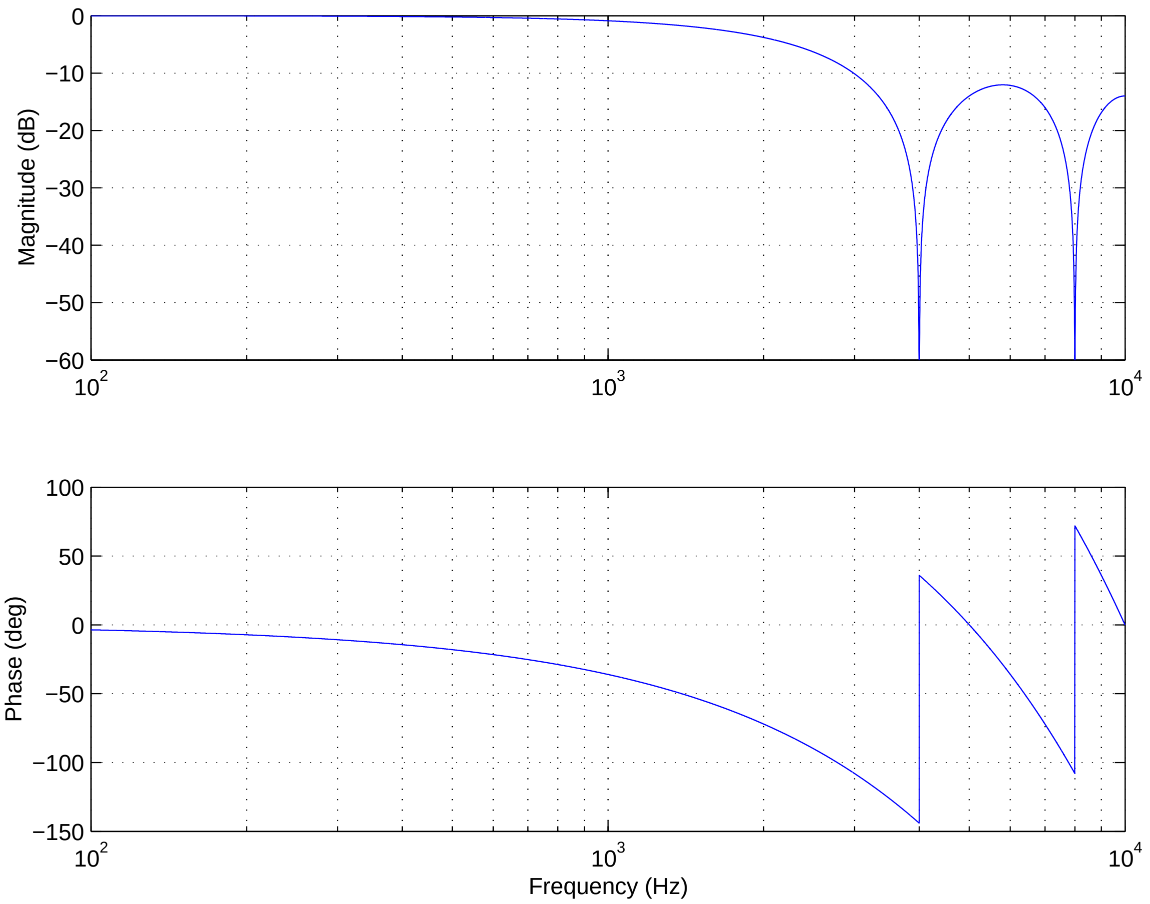

Figure 4-12: Equivalent continuous-time Bode plot of the 5-sample moving average FIR filter. Sampling frequency is 20 kHz.

zero-input condition to 0.7 nm RMS, and also reduces the effect of A/D quantization.

Figure 4-14 shows the noise in one of the sensor signals, sampled at 20 kHz by a 16-bit A/D converter on the controller board. The data was measured using a 5-sample moving average FIR filter and with the high-voltage amplifier turned on. Since the noise in the sensors' analog output (Figures 4-9 and 4-10) has a 16 kHz component, which lies above the 10 kHz Nyquist frequency, the sampled data should have an aliased frequency component at about 4 kHz. However, the FIR filter provides strong attenuation around this frequency, as shown in the magnitude plot in Figure 4-12. As a result, no significant noise is observed at the aliased frequency. The data does have some structure, though, particularly at about 1 kHz. This frequency is

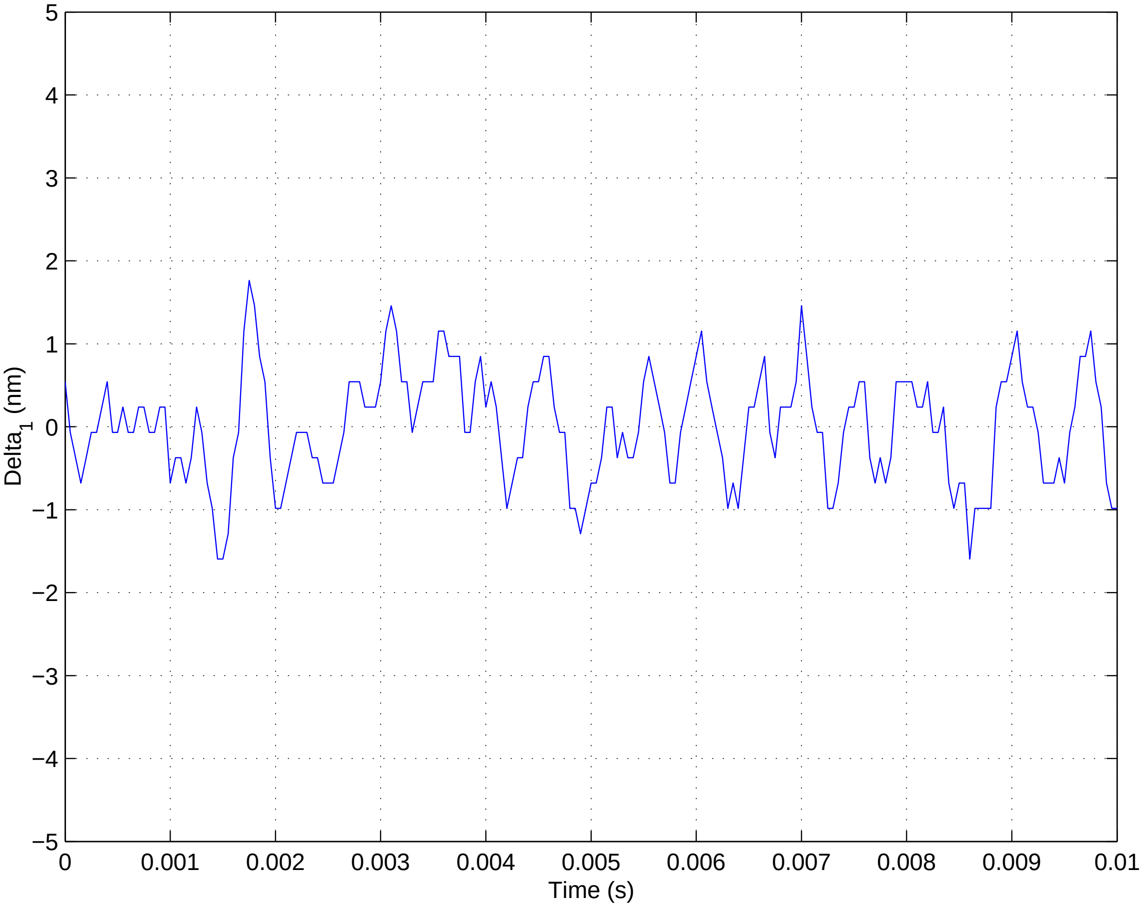

Figure 4-13: Noise measured in one of the dSPACE board's A/D channels, with a 50 Ω terminator connected to the corresponding input on the board's I/O panel. A 5-sample moving averager is used to filter some of the high-frequency noise. The 10 ms trace has an RMS value of 0.7 nm.

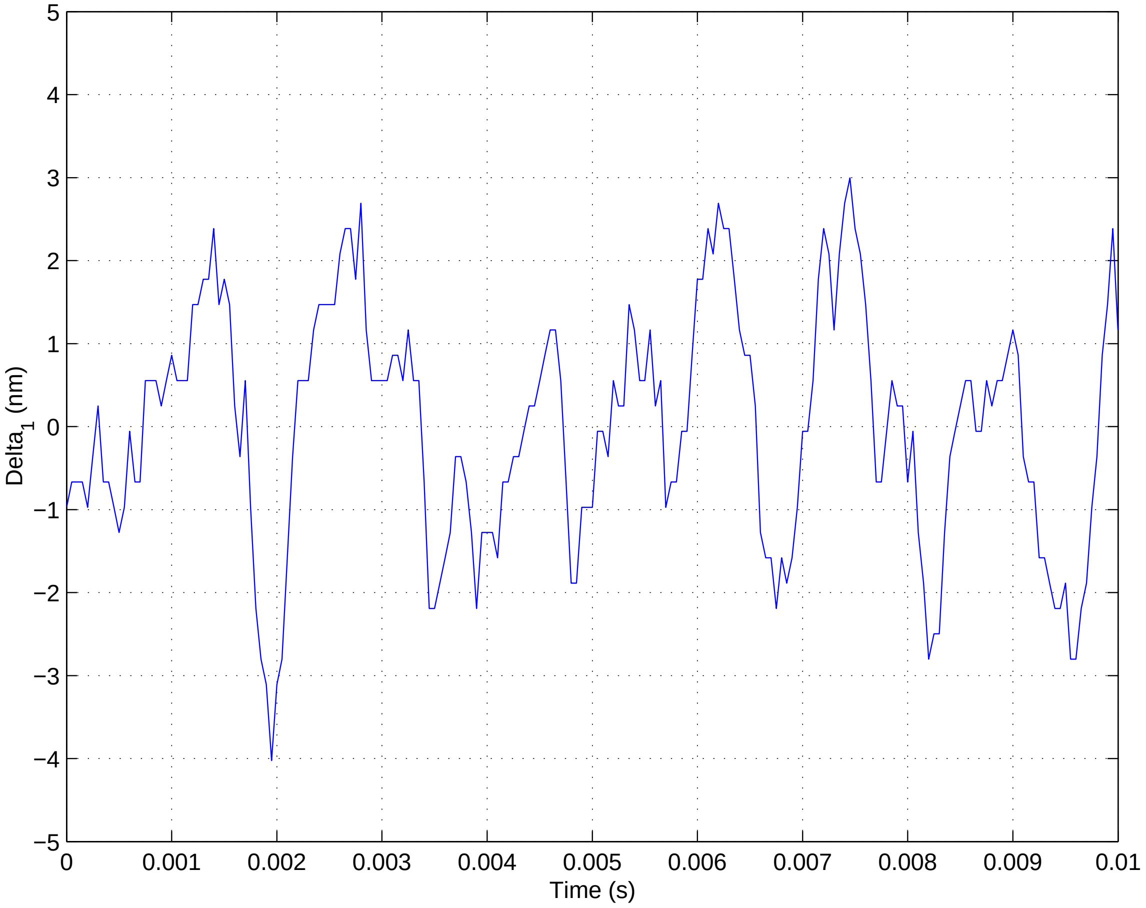

Figure 4-14: Noise data for one of the capacitance sensors, as measured through a 16-bit A/D channel on the controller board. While this data was collected, the high-voltage amplifier was on. Also, a 5-sample moving averager was included in the measurement. The RMS noise calculated over the 10 ms interval is 1.4 nm.

approximately the same as the scanner assembly's bending mode resonance, so the observed oscillations are likely the result of mechanical vibration. The RMS noise for the plotted 10 ms interval is 1.4 nm, slightly less than what was measured for the unfiltered sensor analog output.

Finally, Figure 4-15 shows the total noise in the measurement of the probe's (X,Y,Z) position, again with the high-voltage amplifier turned on and the 5-sample moving averager filtering the sensor data. The probe coordinates are calculated using equation (4.6). The data indicates RMS noise in X, Y, and Z of 1.3 nm, 1.3 nm, and 1.2 nm, respectively.

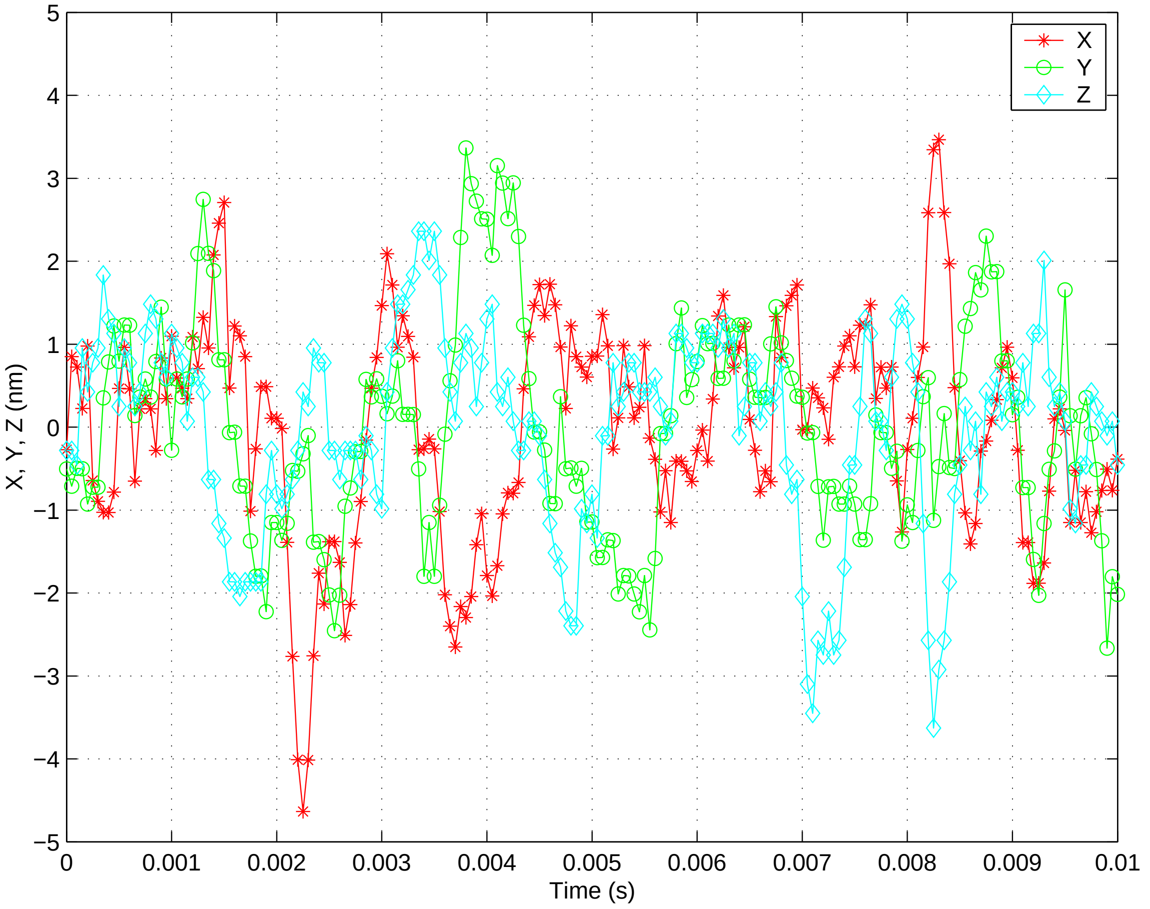

Figure 4-15: Noise data for the computed (X,Y,Z) position of the probe tip. For this measurement, an FIR filter took the 5-sample moving average of the sensor data, and the high-voltage amplifier was on. The RMS noise measured over the 10 ms interval is 1.3 nm, 1.3 nm, and 1.2 nm, for X, Y, and Z, respectively.

4.4 Summary

This chapter described the integration of the metrological AFM's capacitance sensors. The discussion began with a brief analysis of the sensor measurement axis problem. Assuming that the measurement axis lies in the horizontal plane through the sensor face which divides the sensor-target capacitor into two sections of equal capacitance, we found that the measurement axis lies only 20 μm below the sensor's geometrical axis of symmetry. The difference in position was small enough[4] that we assumed the two axes to be collinear, when specifying the dimensions of the sensor head. The analysis described in section 4.1 likely could be refined, by taking account of the full six degree-of-freedom motion — most importantly the rotations — of the target endpiece.

Section 4.2 described the linear transformation used to compute the probe's (X,Y,Z) position, from the data sampled from sensors 1, 2, and 3. We currently use a correction matrix to better align the measurement coordinate frame with the piezo tube's open-loop motion. However, the scanner assembly's three degree-of-freedom motion could be more easily decoupled by replacing this extra measurement transformation with a driving transformation, as shown in Figure 4-6.

Finally, section 4.3 presented the measured noise in the probe position data. Figures 4-9 and 4-10 show the noise in the analog output of one of the capacitance sensors. The data has a large amplitude component at 16 kHz, which is higher than the 10 kHz Nyquist frequency, when the signal is sampled by the controller board. In future tests, better performance may be achieved by including an anti-aliasing filter between the sensor boards' output and the controller board's A/D input. However, the 5-sample moving average FIR filter used in our experiments appears to have attenuated most of the expected 4 kHz aliased frequency component. The final configuration, with (X,Y,Z) computed from the sampled and FIR-filter sensor data using

---

[4] e.g. compared to the tolerance in the assembly of the tuning fork proximity sensor

equation (4.6), indicates RMS noise levels of 1.3 nm, 1.3 nm, and 1.2 nm, in X, Y, and Z, respectively.

The next chapter describes the PC-based digital controller used with the metrological AFM. Once the controller is implemented, the system is ready to take images. The resulting image data is presented in Chapter 6.

Chapter 5

The Metrological AFM — Control System

When imaging samples with the metrological AFM, we use a PC-based digital control system to independently control the microscope's lateral scanning and axial height regulation actions. This chapter provides details of the design and analysis of these two systems.

Figure 5-1 shows a high-level block diagram for the metrological AFM's control system. The desired lateral trajectory of the probe tip is given by (X_{ref},Y_{ref}). These coordinates are fed to the two lateral scanning controllers, which adjust the piezoelectric tube scanner's driving voltage condition to control the probe tip's lateral motion, based on feedback from the capacitance sensors' position measurements. Meanwhile, the axial height regulation system attempts to maintain a constant probe-sample separation at each (X,Y) point in the sample plane through closed-loop control of the tube scanner's voltage condition, using the tuning fork proximity sensor output as its feedback signal. As the probe traces over the contours of the sample surface in this fashion, the control system stores the measured (X,Y,Z) probe position. The resulting set of points, referred to as the image data, is used to construct two- and

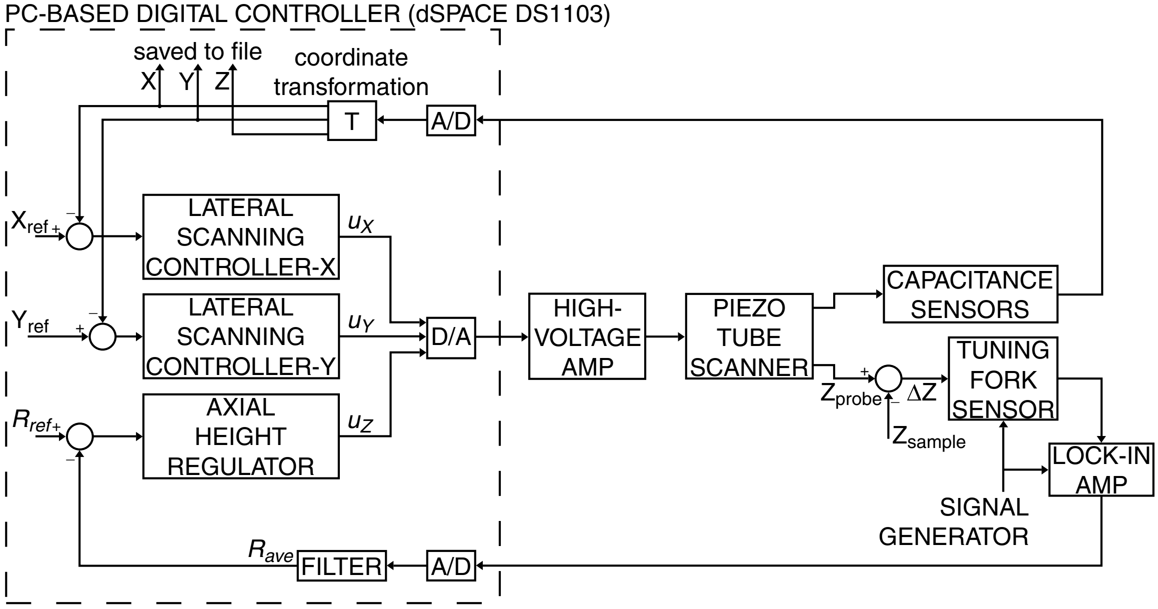

Figure 5-1: High-level block diagram for the metrological AFM. The lateral scanning system controls the probe tip's (X,Y) position, while the axial height regulator tries to maintain a constant probe-sample gap size. The resulting measured (X,Y,Z) coordinates are used to construct an image of the sample topography.

three-dimensional plots of the measured sample topography.

The block diagram in Figure 5-2 shows the superposition of the lateral and axial voltage commands used to produce the desired three degree-of-freedom probe motion. The axial height regulator's output, u_Z, is fed equally to four different D/A channels on the controller board. Before these signals reach the D/A converters, however, they pass through a set of summing junctions, into which the outputs from the two lateral scanning controllers, u_X and u_Y, are differentially added. The superimposed analog command signals are then generated by the D/A converters and input to the high-voltage amplifier. Using this approach, the lateral scanning and axial height regulator controllers may be treated to first order as decoupled systems. Thus, when the lateral scanning system is described in the following text, the behavior of the axial height regulator is ignored, and vice versa.

The chapter begins, in section 5.1, with a brief description of the control system

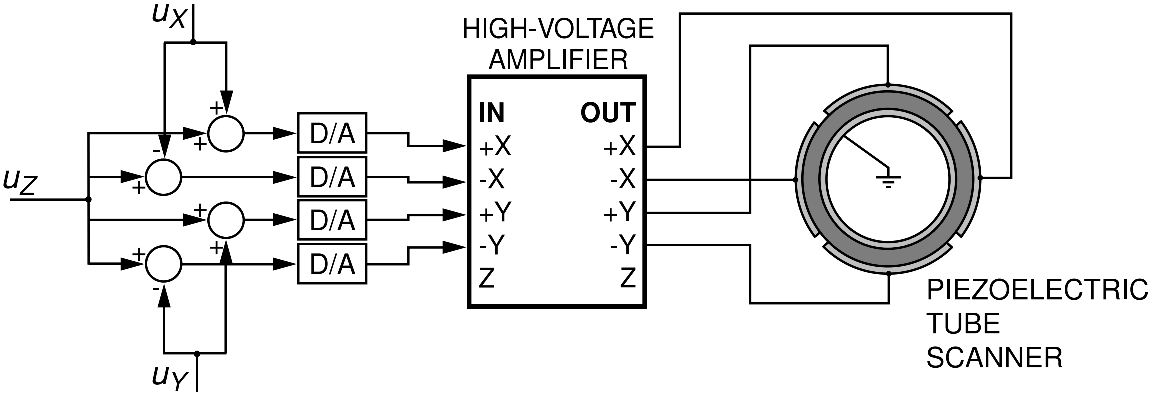

Figure 5-2: Block diagram showing the superposition of the controller outputs, u_X, u_Y, and u_Z, from the X lateral scanning controller, Y lateral scanning controller, and axial height regulator, respectively.

hardware and software. The control system is programmed via block diagrams in Simulink,[1] then the compiled code is executed with a dSPACE[2] controller board that interfaces with the physical world.

Section 5.2 addresses the control of the AFM's lateral scanning system. This discussion starts by developing a physical model of the lateral scanning plant dynamics, then empirically fitting the corresponding transfer function to the measured open-loop frequency response. With a sufficient plant model in hand, we design a controller to achieve the desired closed-loop performance. In this case, the controller consists of an integrator with a pole added beyond cross-over to further attenuate the resonant peak from the tube scanner's bending mode at 1.03 kHz. The resulting lateral scanning loops have measured -3 dB closed-loop bandwidths of 189 Hz and 191 Hz for X and Y, respectively.

Section 5.3 describes the additional set of challenges presented by the axial height regulation system. The most difficult of these is the large degree of variability observed in the system's open-loop dynamics, due to variations in the probe-sample interactions. Even with such difficulties, we have successfully closed the axial follow-

---

[1] See Appendix B.

[2] See Appendix B.

ing loop, achieving a -3 dB closed-loop bandwidth of up to 184 Hz using a lead-lag compensator. However, for reasons that are detailed below, we eventually decided to use a simple proportional controller, which results in a -3 dB closed-loop bandwidth of about 175 Hz.

5.1 Control Implementation

All of the experiments with the metrological AFM are controlled using a dSPACE[3] DS1103 controller board. This hardware includes a 400 MHz PowerPC controller operating on a board in a standard desktop computer. The board has an input/output (I/O) connector panel with access to 20 analog-to-digital (A/D) channels and 8 digital-to-analog (D/A) channels. All of the analog inputs used with the AFM are converted by 16-bit A/D converters,[4] while all of the board's analog outputs are generated by 14-bit D/A converters.

MATLAB's Simulink[5] software package is used to construct the desired system block diagrams, which consist of some combination of continuous- and discrete-time transfer functions, connections to the controller board's I/O, and standard block diagram elements. An example block diagram is shown in Figure 5-3. MATLAB's Real-Time Workshop translates the specified model to the C programming language, then additional software provided by dSPACE compiles and links this code for execution on the controller board.

We also use dSPACE's ControlDesk software, which provides a user-configurable graphical interface to the running controller. The interface allows for real-time adjustment of system parameters and viewing of various signals of interest.

---

[3] See Appendix B.

[4] The board also provides four channels for 12-bit analog-to-digital conversion, but we do not use any of these, since we are more concerned with the resolution of the conversion, rather than its speed.

[5] See Appendix B.

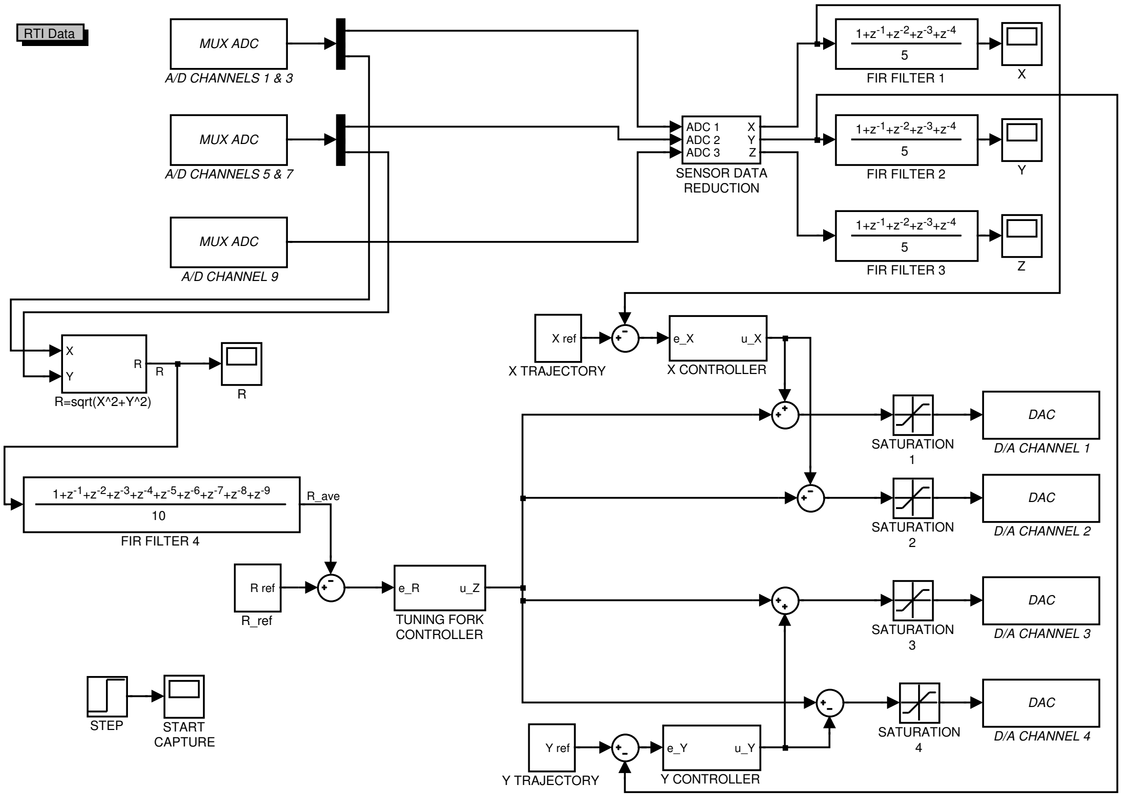

Figure 5-3: An example of one of the block diagrams that was implemented in Simulink for controlling the metrological AFM.

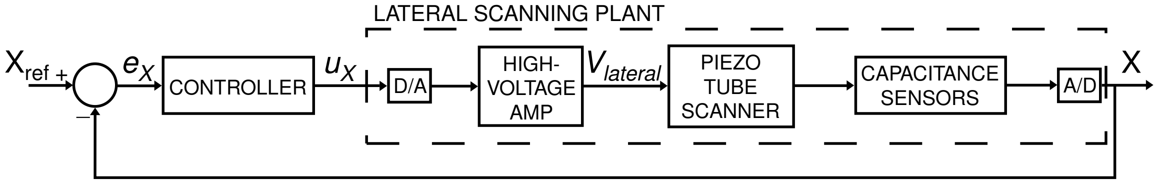

Figure 5-4: A simplified block diagram for the X scanning controller. The Y controller is virtually identical.

5.2 Lateral Scanning

The lateral scanning system provides closed-loop control of the probe tip's position in X and Y. The coordinate transformation expressed in equation (4.6) is used to compute these coordinates, based on the capacitance sensors' output. As shown in the simplified block diagram of the X scanning controller of Figure 5-4, the measured X position is compared with the controller's set point, X_{ref}, to produce an error signal, e_X. The controller then acts on the error to produce a drive signal, u_X, which is converted to an analog voltage and fed to the piezoelectric tube scanner's high-voltage amplifier. The resulting differential voltage condition, $V_{lateral}$, dictates the degree to which the tube scanner is bent in the X direction, as described in section 2.1.1. After the capacitance sensor signals are converted back to the digital domain, they are used to calculate the probe's X position, completing the loop. The Y controller is virtually identical to what is described here for X.

5.2.1 Plant Dynamics

Before designing the controller for the lateral scanning system, we developed a model for the system's plant dynamics, based partly on a physical model of the scanner assembly and the measurement electronics, then fitted to the measured open-loop frequency response. The final model is represented by the block diagram shown in Figure 5-5. The actual plant dynamics were measured with a dSPACE-based dynamic

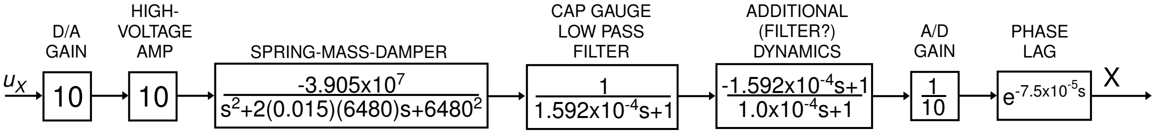

Figure 5-5: Block diagram for the plant model fitted to the lateral scanning system's open-loop frequency response.

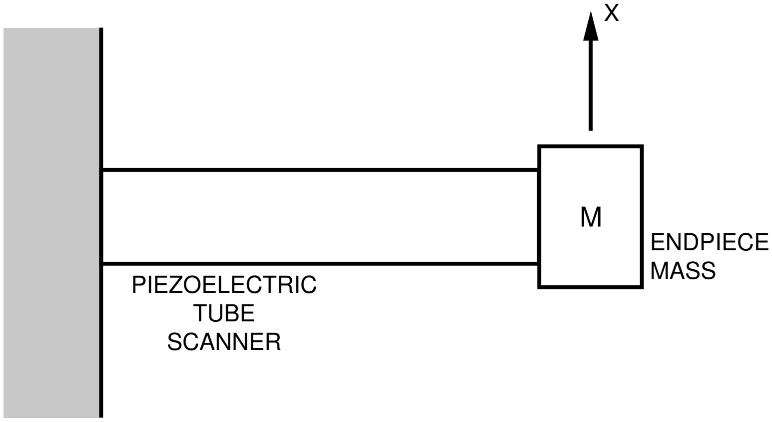

Figure 5-6: Model of the piezoelectric tube scanner plus the endpiece mass as a spring-mass-damper system.

signal analyzer (DSA) that was developed by Katherine Lilienkamp, another graduate student in our lab [31].[6]

The scanner assembly may be modelled mechanically as a spring-mass-damper system, shown schematically in Figure 5-6. Here, the tube scanner is represented as a cantilevered beam, with a lumped mass at its free end, which oscillates transversely with respect to the tube's axis. The dynamics for this system — with resonant frequency, ω_n, and damping ratio, ζ — are described by the transfer function

$$\frac{\mathrm{X}(s)}{V(s)} = \frac{A}{s^2 + 2\zeta\omega_n s + \omega_n^2}. \tag{5.1}$$

From equation (3.3), we anticipate this mode will have $\omega_n \approx 870$ Hz.

---

[6] The DSA runs from a MATLAB script and uses dSPACE I/O to excite the plant and measure its response. The associated software is available for download from the Precision Motion Control Laboratory's website, http://web.mit.edu/pmc/www/Links/download/download.html.

Additional plant dynamics originate from the capacitance probes' electronics. Each of the sensors includes a 3800 gaging module, which is manufactured by ADE Technologies.[7] The modules are configured with a 1 kHz bandwidth. We initially modelled the associated low-pass filter as a single pole with a break frequency of 1 kHz, i.e.,

$$H_{sensor}(s) = \frac{1}{1.592 \times 10^{-4}s + 1}. \tag{5.2}$$

To complete a simple model for the lateral scanning system, we include the phase lag, ϕ_{lag}, from the controller board's discrete-time processing. Here, we assume that the processing introduces a pure time delay, T_d, as an effect of both the controller's computation time and the D/A converters' zero-order hold. In the frequency domain, the delay corresponds to

$$H_{delay}(s) = e^{-sT_d}. \tag{5.3}$$

As a function of frequency, ω, the resulting phase lag is

$$\phi_{lag} = -\omega T_d. \tag{5.4}$$

We assume that the controller requires approximately a full sampling period for its computations, and that the zero-order hold results in a half-sample delay. As a result, for a 20 kHz sampling frequency, $T_d \approx 7.5 \times 10^{-5}$ s. As seen in Figure 5-7, the resulting phase lag becomes significant for frequencies greater than about 100 Hz.

Figure 5-8 shows the measured open-loop lateral scanning Bode plots for motion in the X axis,[8] compared to the combined spring-mass-damper/low-pass filter/phase lag system described above. The plant has 180° of phase at low frequencies, since a positive change in u_X cause motion in the negative X direction. Adjusting the model parameters to fit this data, we find that ω_n = 1.03 kHz and ζ = 0.015 result in a

---

[7] See Appendix B.

[8] All of the data presented for the lateral scanning system was measured for commanded motion in X. Data measured for motion in the Y axis is essentially identical, as expected from symmetry.

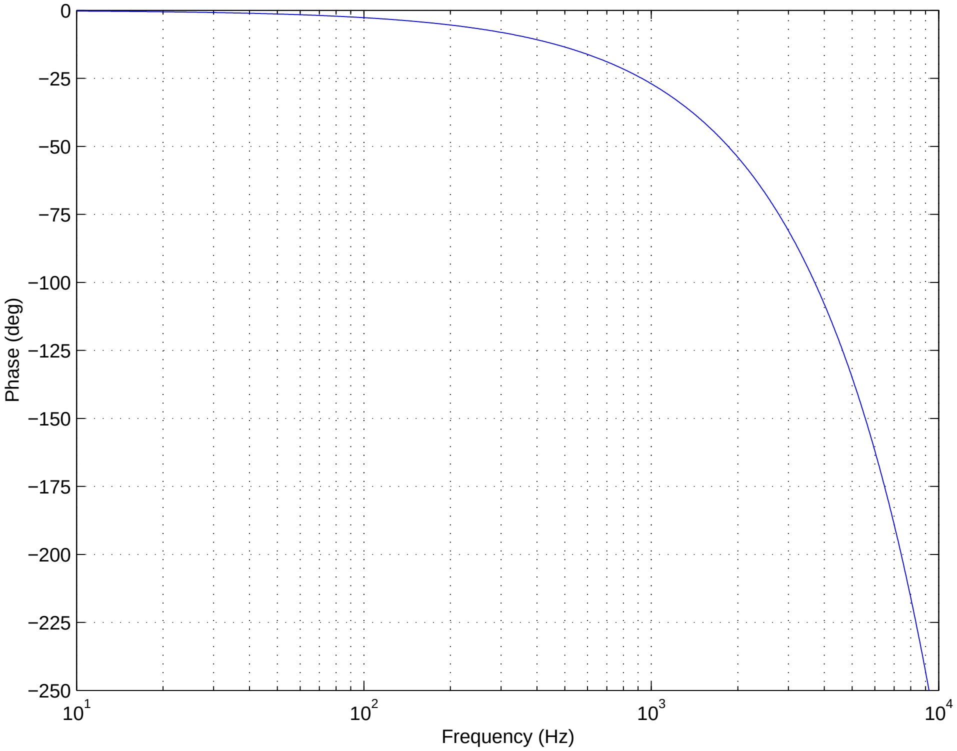

Figure 5-7: Phase lag, ϕ_{lag}, resulting from a representative time delay of 7.5×10^{-5} s, for a 20 kHz sampling frequency.

good approximation of the plant's resonant peak. The measured resonance occurs at a higher frequency than what was predicted, most likely because an overly conservative estimate of the lumped mass on the prototype AFM's scanner assembly was used with equation (3.3). This simple model approximates the shape of the measured system gain fairly well, except for very high frequencies, where precise agreement is not important. However, there is an unacceptably large discrepancy between the modelled and observed phase response over the frequency range of interest, which cannot be accounted for by simply adjusting the estimate of the time delay from the controller's discrete-time processing.

At this point, we attempt to achieve better agreement in the model by simply adding poles and zeros. We believe the additional dynamics may originate from a higher-order low-pass filter used for the capacitance gauge electronics, though we are not certain this is the true cause. By adding one more pole with an associated break frequency at 1.6 kHz and a non-minimum phase zero with an associated break frequency at 1.0 kHz, the frequency response of the approximate plant model becomes sufficiently close to the measured response, as shown in Figure 5-9. The corresponding fitted transfer function is given by

$$P_L(s) = \frac{-(3.905 \times 10^{8})(-1.592 \times 10^{-4} s + 1)e^{-7.5 \times 10^{-5} s}}{(1.592 \times 10^{-4} s + 1)(1.0 \times 10^{-4} s + 1)(s^2 + 2(0.015)(6480)s + 6480^2)}. \quad (5.5)$$

5.2.2 Controller Design

Having sufficiently developed the model of the lateral scanning plant dynamics, we next design a controller. We aim for a closed-loop bandwidth of over 100 Hz, with a phase margin of about 45°. As is evident from Figure 5-9, the resonant peak from the tube scanner's bending mode is fairly sharp. The lateral controller is designed to strongly attenuate this resonance, such that the peak of the resulting negative of

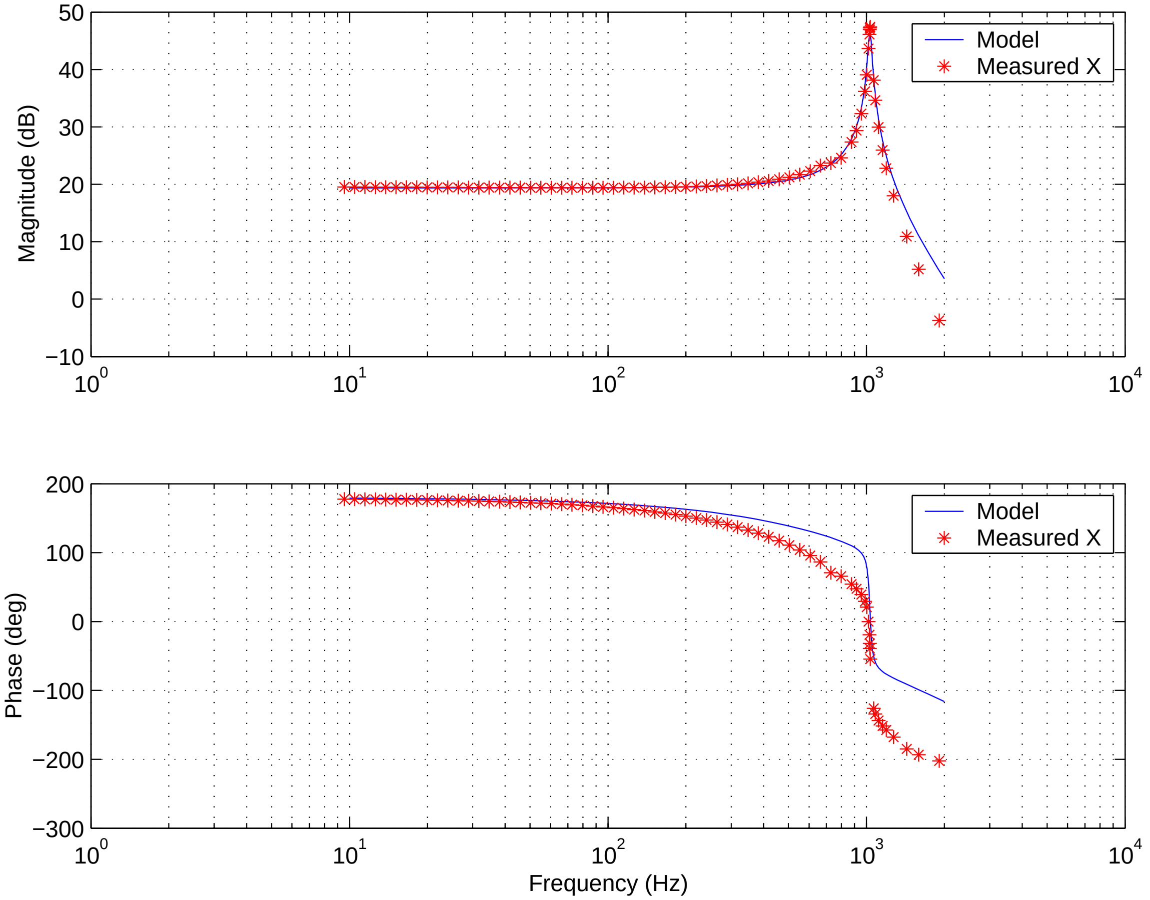

Figure 5-8: The measured open-loop frequency response for the lateral scanning system, compared to a simple model composed of a spring-mass-damper in series with a single-pole low-pass filter, and with additional phase lag from the time delay of discrete-time processing in the controller board. The spring-mass-damper models the cantilevered tube scanner with the lumped endpiece mass on its free end. The low-pass filter is intended to model the capacitance gauges' 1 kHz bandwidth. Note that the plant phase begins at 180°, since a positive change in u_X results in a negative change in lateral position. A sign inversion in the processing electronics could be used to remove this extra minus sign, so it is of no significance.

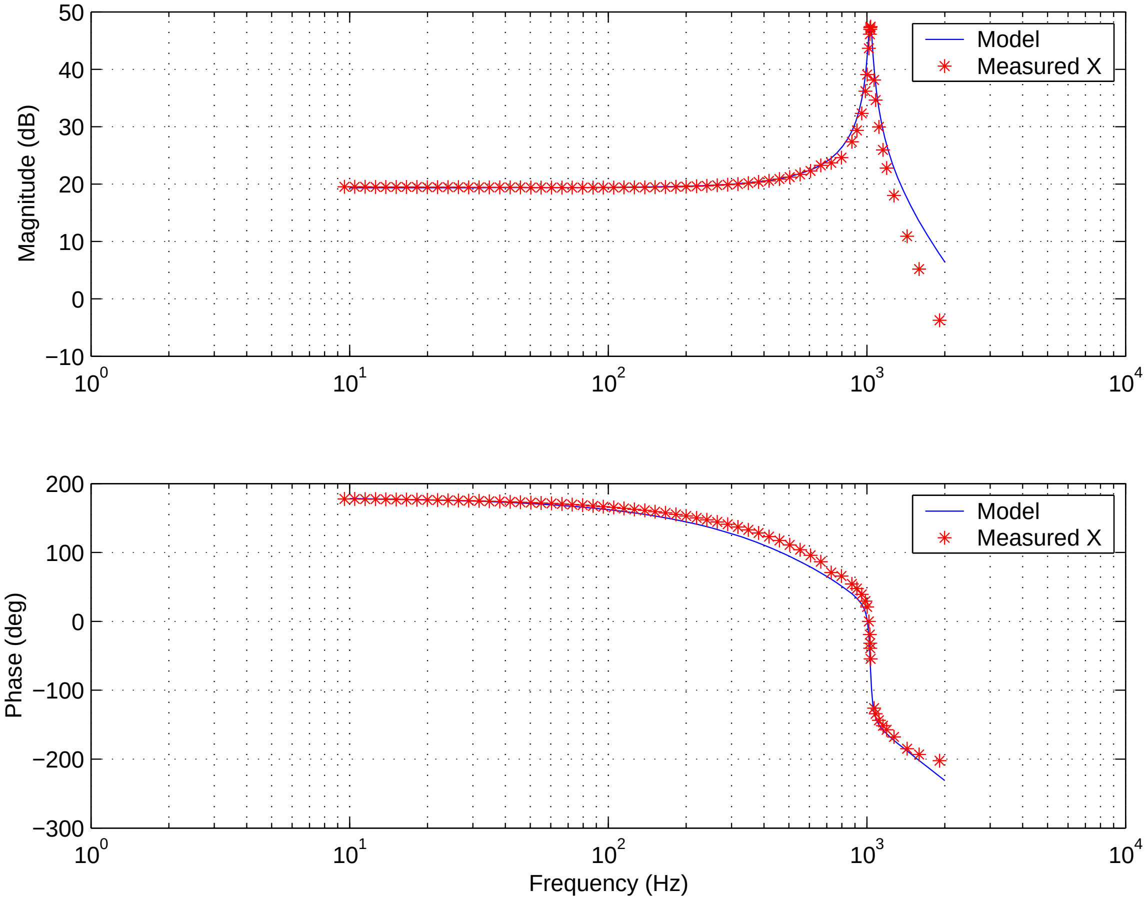

Figure 5-9: The measured open-loop lateral scanning frequency response compared to a higher-order model. The model includes an extra pole and a non-minimum phase zero, which result in much better agreement with the measured plant phase than the model used for Figure 5-8.

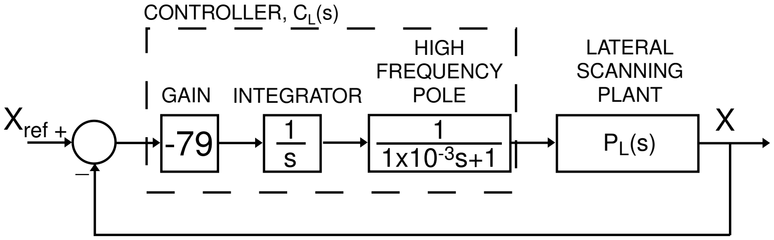

Figure 5-10: Block diagram for the X lateral scanning controller, which consists of an integrator in series with a pole.

the loop transmission stays completely below the 0 dB line. We have implemented the controller shown in Figure 5-10 — an integrator in series with a pole. The integrator provides large low-frequency gain, as well as a -20 dB/decade slope in the magnitude of the negative of the loop transmission through the chosen 100 Hz cross-over. This slope allows us to pick a relatively stable cross-over frequency, assuming the plant dynamics do not change significantly over time, by appropriately setting the controller gain. In determining the break frequency associated with the controller's pole, we balance the desire for strong attenuation of the scanner assembly's 1.03 kHz resonant peak against the desire for a large phase margin. Lower break frequencies result in stronger attenuation, while higher break frequencies result in a larger phase margin. The final controller design uses a pole at 160 Hz, which pushes the resonant peak safely below 0 dB, while leaving a theoretical phase margin of 42°. The resulting controller is described by the transfer function

$$C_L(s) = -79\left(\frac{1}{s}\right)\left(\frac{1}{1\times 10^{-3}s+1}\right). \tag{5.6}$$

Figure 5-11 presents the modelled and measured negative of the loop transmission for this system. The system crosses over at 97 Hz, with a measured phase margin of 44°.

We could achieve a significantly higher bandwidth through relaxing the gain margin specification and requiring only phase stabilization of the bending mode resonance, using the Nyquist criterion to determine stability. However, considering the project's

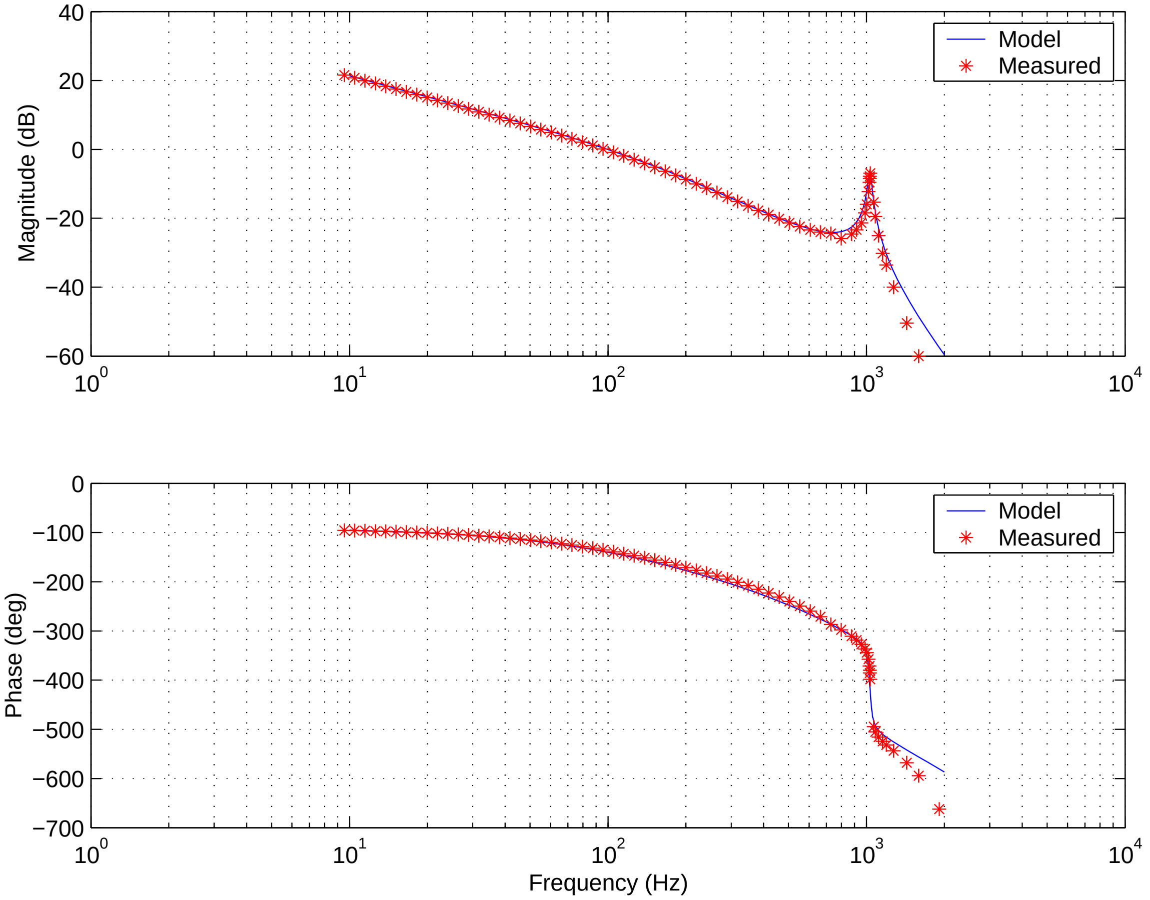

Figure 5-11: Bode plots of the negative of the loop transmission for the X loop of the lateral scanning system. The resonant peak remains safely below the 0 dB line. The system crosses over at 97 Hz and has a measured phase margin of 44°.

time constraints and the relatively good performance measured for the controller described by equation (5.6), we have decided to forego the extra design effort.

5.2.3 Performance

Figure 5-12 provides a comparison of the actual closed-loop frequency response measured for the X loop of the lateral scanning system with the theoretical closed-loop response calculated from the approximate plant model given in equation (5.5). For ease of computation, the model's time delay is neglected in the calculation of the expected response. Excellent agreement is observed between the two sets of data, for the frequencies of interest. The measured response indicates a -3 dB closed-loop bandwidth of 189 Hz, which is fast enough to meet the needs of the imaging system. Likewise, the measured -3 dB closed-loop bandwidth for the Y loop is 191 Hz.

Figure 5-13 shows the step response measured for the X loop, as compared to the predicted response. Again, the time delay is left out of the model, for easier computation. From this data, the system has a 33% maximum overshoot and a 2% settling time of 13.6 ms. Note the lightly damped scanner resonant mode present in this response. No step response data was measured for Y, but we expect the performance would be essentially the same.

Figure 5-14 shows the measured closed-loop positioning noise in X, sampled over a 50 ms interval. The data is filtered through the 5-sample moving average FIR filter mentioned in section 4.3. Based on this data, the closed-loop lateral positioning noise is 1.3 nm RMS. The same RMS noise is also measured for the Y loop.

5.3 Axial Height Regulation

This section details the design and analysis of the metrological AFM's axial height regulation system, which controls axial motion of the tube scanner on the basis of

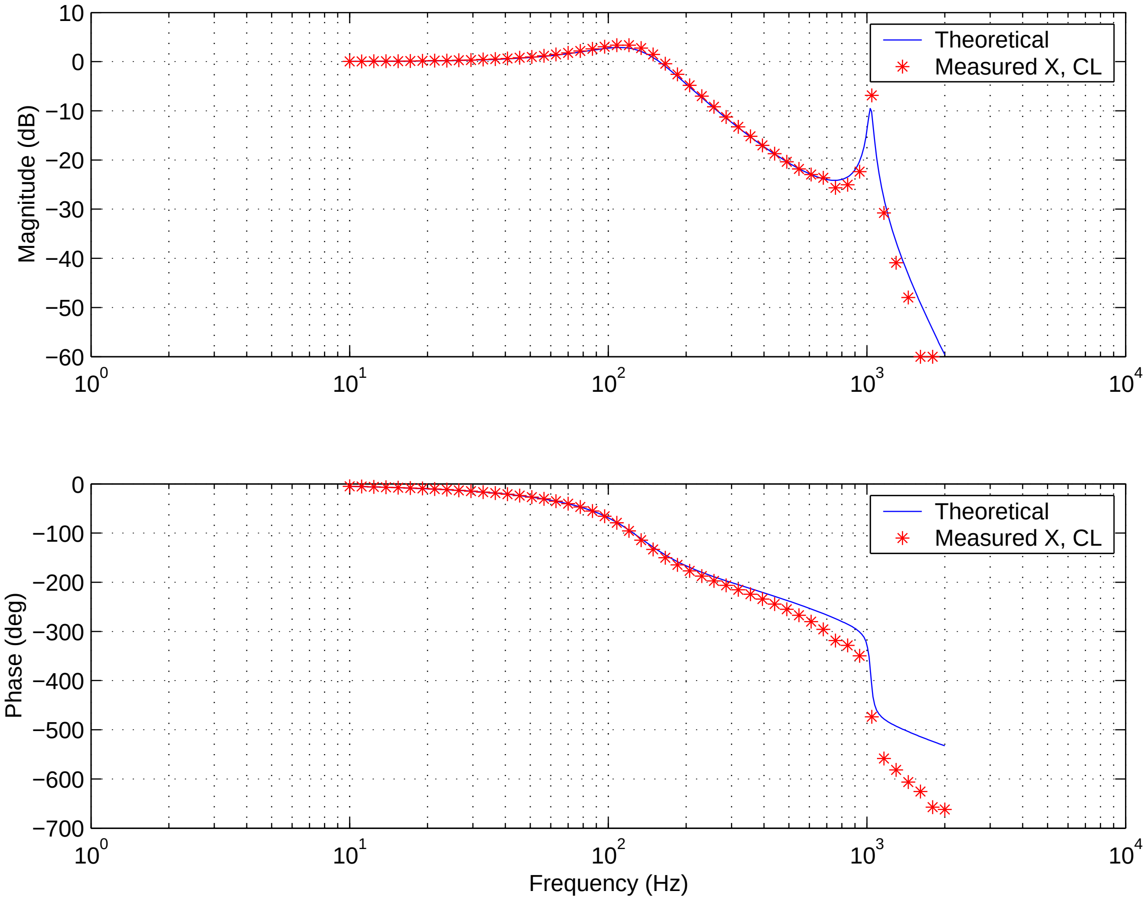

Figure 5-12: Closed-loop frequency response of the lateral scanning system, for the X loop. The measured data is compared to the theoretical response. The plant's time delay is neglected, for easier computation. The measured -3 dB closed-loop bandwidths for the X and Y loops are 189 Hz and 191 Hz, respectively. The data for the Y lateral scanning loop is not shown here, since it is essentially identical to what is shown for X.

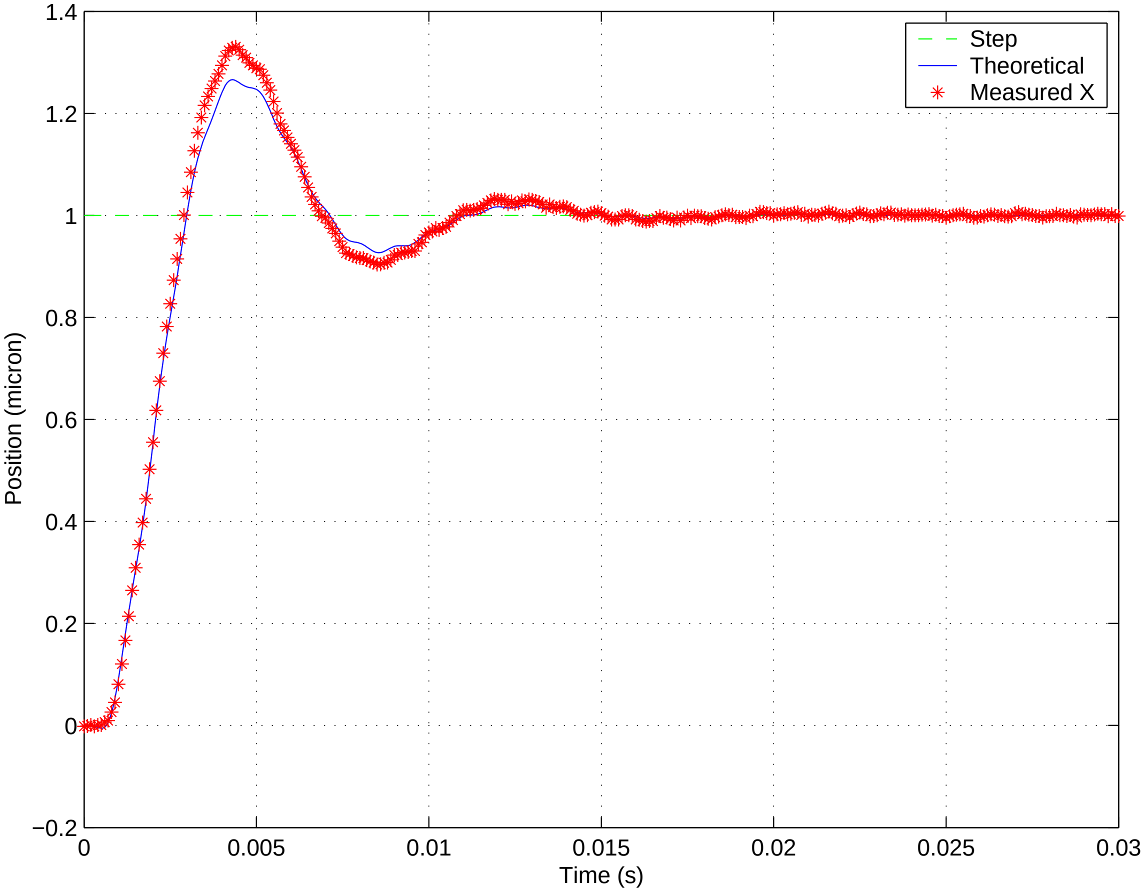

Figure 5-13: Closed-loop step response for the X loop of the lateral scanning system. Time delay is left out of the plant model used to compute the theoretical response. The measured maximum overshoot is 33%, and the 2% settling time is 13.6 ms. The data clearly shows the scanner assembly's lightly damped 1.03 kHz resonant mode.

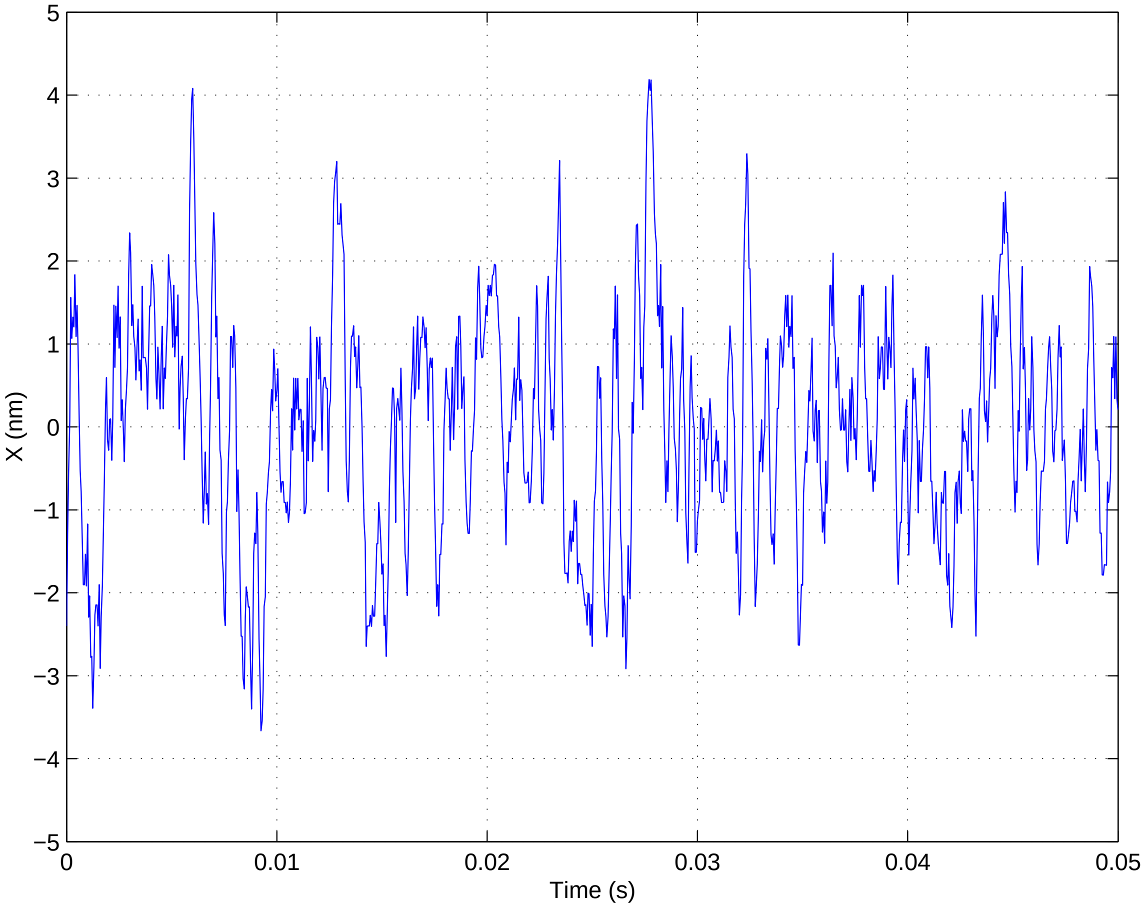

Figure 5-14: Measured closed-loop positioning noise in X, for a 50 ms interval. The position data is filtered through a 5-sample moving averager, and the sampling frequency is 20 kHz. The RMS noise for both the X and Y loops is 1.3 nm.

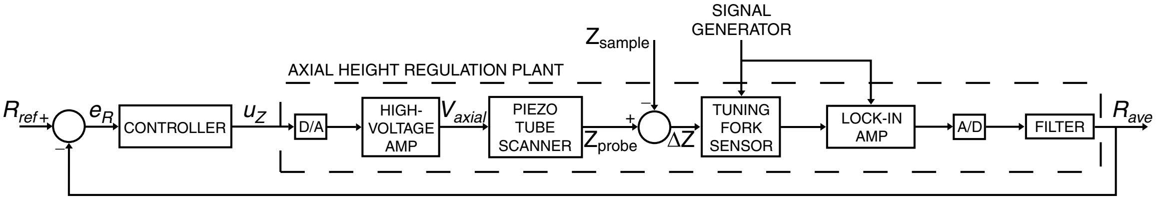

Figure 5-15: A simplified block diagram for the axial height regulation system. The controller commands a common control voltage, V_{axial}, to the piezoelectric tube scanner's four outer electrodes. The common control voltage adjusts the height of probe tip, Z_{probe}. The loop attempts to maintain a constant probe-sample gap size, ΔZ, while the probe scans laterally over the sample surface.

proximity sensing from the tuning fork probe, in an effort to maintain a constant probe-sample gap size. A simplified block diagram for this system is shown in Figure 5-15. Here, the controller acts on an error signal, e_R, to command a common voltage, V_{axial}, to the piezoelectric tube scanner's four outer electrodes, via the high-voltage amplifier. As described in section 2.1.1, this common driving voltage is used to adjust the tube scanner's length, which dictates the probe tip's vertical position, Z_{probe}. The probe-sample separation, ΔZ, is the difference of Z_{probe} and Z_{sample}, the Z-direction position of the sample directly beneath the probe. With the fork driven by a signal generator, the current flowing through the tuning fork proximity sensor is a function of ΔZ, as described in section 2.1.2. A lock-in amplifier measures the proximity sensor's output signal. For this block diagram, the sensor's output is the magnitude of the current, R, though other measures of the current may also be used. The measured R is digitally filtered, to produce a cleaner signal, R_{ave}. To complete the loop, R_{ave} is compared to the set point, R_{ref}, to produce the error signal.

As in the open-loop prototype AFM, the metrological AFM's tuning fork sensor is electrically driven with a sinusoidal voltage at a frequency just below its resonance, using the circuit shown in Figure 5-16. The fork's drive signal, V_{fork}, has an amplitude of about 1 mV, which produces an oscillation of the fork's tips with an amplitude of approximately 0.1 nm, based on equation (2.8). This drive level is set lower than what

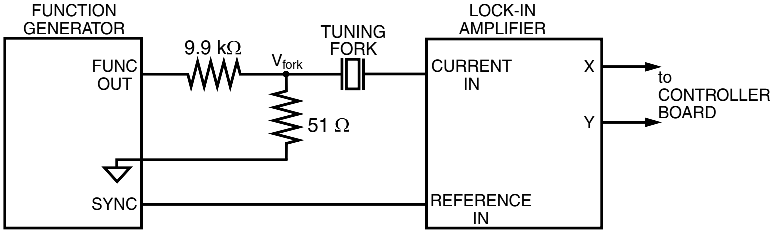

Figure 5-16: The circuit used to excite the tuning fork oscillations and synchronously detect the resulting current through the tuning fork, which is on the order of 1 nA. The resistive attenuator reduces the signal generator output while maintaining a 50 Ω driving impedance.

was used with the open-loop prototype AFM, to provide greater probe resolution, but at the cost of diminished signal-to-noise ratio. The same lock-in amplifier described in section 2.2.2 is used to synchronously detect the current drawn by the fork at the driving frequency, which is on the order of 1 nA. The lock-in provides in-phase (X) and quadrature-phase (Y) measurements, which are converted to digital signals via a pair of 16-bit A/D converters. These signals are then used to calculate the current's magnitude, R, and phase, ϕ, within the dSPACE controller, based on the equations

$$R = \sqrt{X^2 + Y^2}, \tag{5.7}$$

and

$$\phi = \tan^{-1}\left(\frac{Y}{X}\right). \tag{5.8}$$

5.3.1 Plant Dynamics

With the fork driven in the fashion described above, the probe tip is manually lowered into engagement with the sample, using the head's coarse-approach micrometers. Again, the region of engagement is defined as the length above the sample for which the lock-in's electrical output changes as a function of gap size (i.e., $\frac{dR}{d\Delta Z} \neq 0$). When the tip is engaged on the sample in this manner, the axial height regulation system's

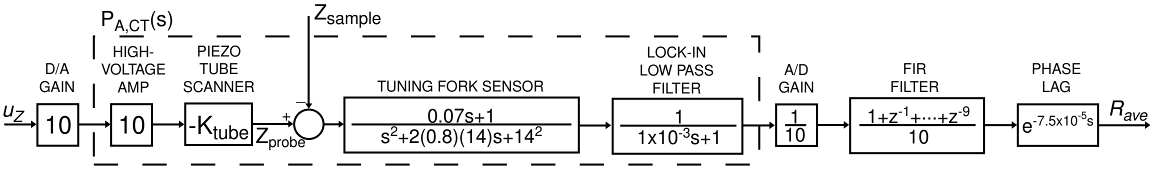

Figure 5-17: Block diagram showing a representative model used to approximate the axial height regulator's plant dynamics. This model was fitted to one set of measured open-loop frequency response data.

open-loop frequency response can be measured, from which a model of the plant dynamics may be constructed. The open-loop response is measured from u_Z to R_{ave}. A representative plant model, which was fitted to one set of measured frequency response data, is shown in the block diagram in Figure 5-17. As described below, we have observed significant variability in the measured plant dynamics, so this block diagram represents only one of a series of models we have used to approximate the system's open-loop behavior.

Before the open-loop frequency response can be measured, however, a low-bandwidth controller must be implemented to compensate for the system's thermal drift. Without this compensator, the tip can wander in and out of engagement over the course of a single frequency sweep. A simple low-gain integral controller is used to provide the desired function, with a closed-loop bandwidth of approximately 1 Hz or less. Figure 5-18 shows a block diagram for the corresponding low-bandwidth closed-loop system. The system is given a fixed set point which corresponds approximately to the center of the engagement region. A sinusoidal disturbance signal, u_d, is added to the integrator's output, to force the probe to move vertically about the nominal position commanded by the compensator. The integrator's gain is set low enough that it provides almost no rejection of this disturbance over the frequency range of interest. Further, the piezoelectric tube scanner's dynamic response remains essentially constant for frequencies up to 1 kHz or more. As a result, the amplitude of the probe's vertical motion can be directly controlled by simply adjusting the amplitude of u_d.

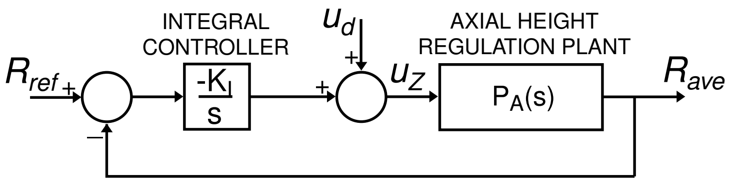

Figure 5-18: Block diagram of the low-bandwidth closed-loop system used to measure the axial height regulator's open-loop frequency response.

We generally set the amplitude such that the probe moves through almost the entire extent of the engagement region, to maximize the signal-to-noise ratio. Then, the DSA measures the response in R_{ave}, as a function of the frequency of u_d, to produce the plant frequency response data.

As described in section 4.3 in reference to the capacitance sensors, we use a finite impulse response (FIR) filter to clean up some of the noise in the lock-in signal. Here a 10-sample moving averager is used:

$$H_{FIR}(z) = \frac{1 + z^{-1} + z^{-2} + \ldots + z^{-9}}{10}. \tag{5.9}$$

The filter's continuous-time equivalent frequency response is plotted in Figure 5-19, for a 20 kHz sampling frequency.

Figure 5-20 shows a comparison of the plant frequency response data, for four different output variables. In each case, one of the lock-in variables — X, Y, R, or ϕ — was passed through the 10-sample moving averager to produce a filtered output — X_{ave}, Y_{ave}, R_{ave}, or ϕ_{ave}, respectively. The data indicates that Y_{ave} is much less sensitive to changes in gap size than any of the other three signals, since the corresponding magnitude of the ratio of the lock-in output to the disturbance input is considerably smaller than for any of the other variables. Among the remaining choices, the data shows that R_{ave} results in a slightly higher sensitivity than either X_{ave} or ϕ_{ave}. Since the phase characteristics for these variables are essentially identical

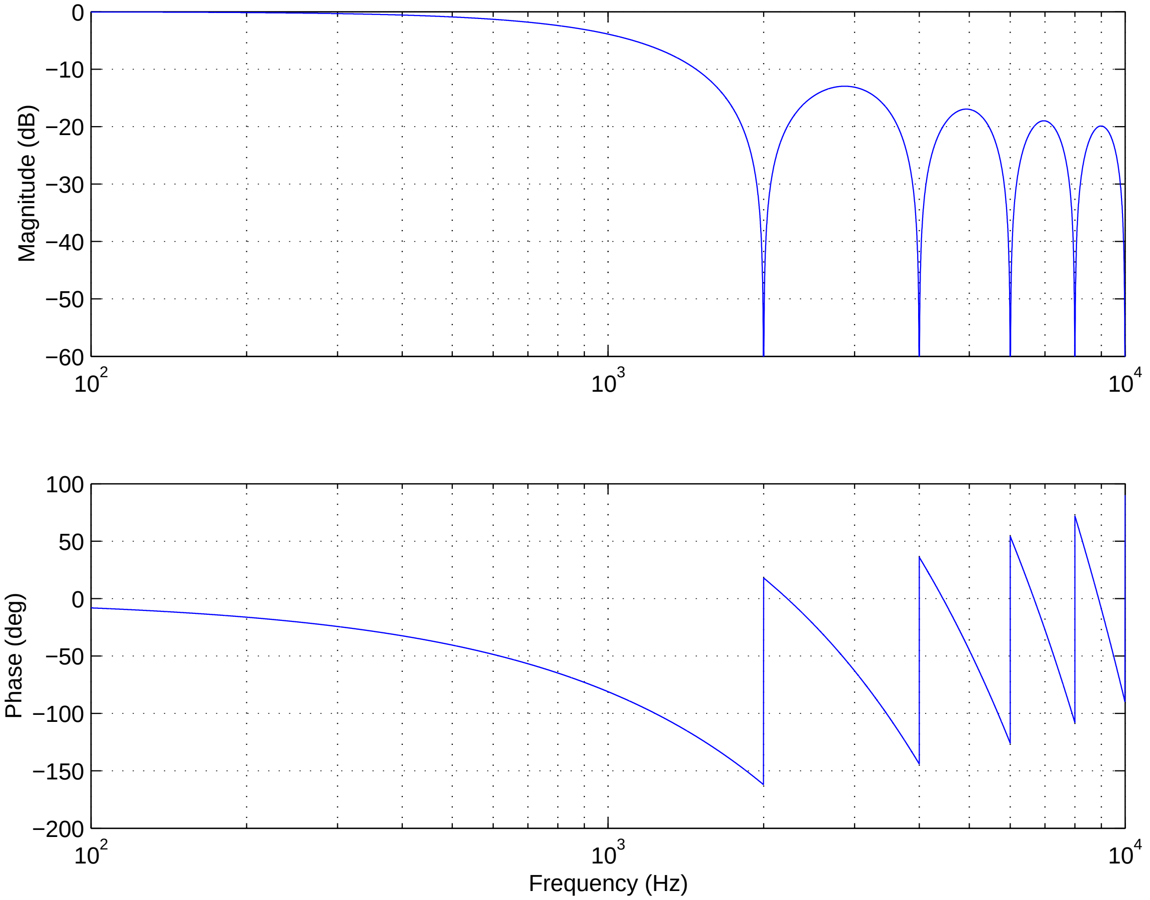

Figure 5-19: Equivalent continuous-time Bode plot of the 10-sample moving average FIR filter used to attenuate some of the noise in the lock-in signal. Sampling frequency is 20 kHz.

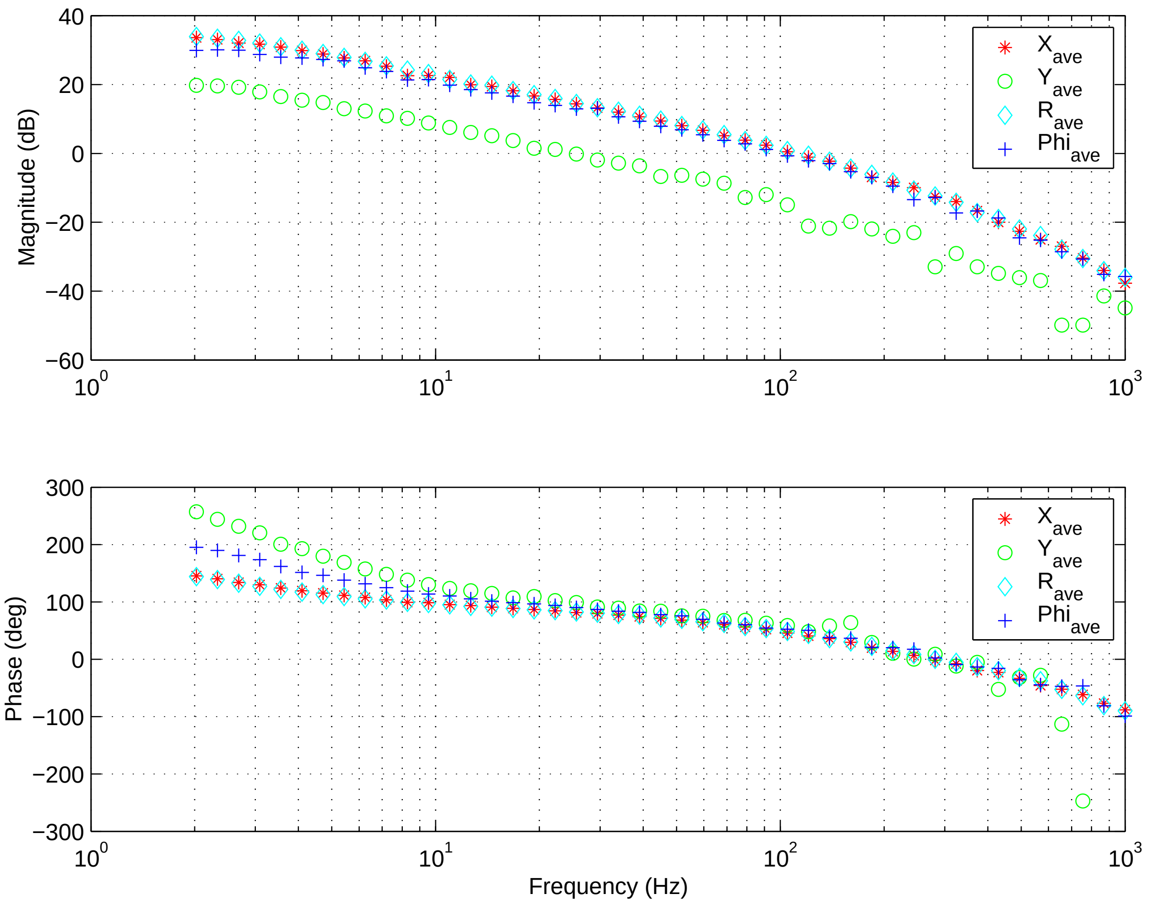

Figure 5-20: Comparison of the open-loop frequency responses of the axial height regulation plant, for four different output variables: X_{ave}, Y_{ave}, R_{ave}, and ϕ_{ave}. These variables are filtered versions of the in-phase component, quadrature-phase component, magnitude, and phase, respectively, of the tuning fork current measured by the lock-in.

over the frequencies we care about — approximately between 10 Hz and 1000 Hz — the better sensitivity suggests using R_{ave} for the axial height regulator's feedback signal.

Based on the data in Figure 5-20, the system should be easily controllable to bandwidths of greater than 100 Hz, since the plant phase changes by only about -130° at this frequency.[9] However, we run into some complications in our attempt to characterize the plant dynamics. As shown in Figure 5-21, significant variability

---

[9] As with the lateral scanning system, there is a sign inversion between DC input and DC output for the axial height regulation plant, resulting in 180° of system phase at low frequencies.

has been observed in the plant's behavior as a function of time. This data shows the axial height regulator's open-loop frequency response measured on four separate occasions — the first three sets of data were taken over the course of a single day, the fourth was collected on the following morning. The measured magnitude and phase change by as much as 8 dB and 30°, respectively. Clearly, these variations must somehow be addressed when attempting to close the loop. For our experiments, we simply remeasured the plant dynamics and adjusted the controller accordingly, if a long period of time had elapsed since the plant had last been characterized. We believe that much of the observed variability results from the poor environmental controls in our laboratory. In particular, the large swings in the lab's temperature — on the order of several degrees — likely have a dramatic effect on the tuning fork sensor's behavior. During a single day's worth of experiments, for example, we occasionally needed to adjust the tuning fork's drive frequency — usually by 1 Hz or less — to track the fork's changing resonant frequency. The change in resonance is almost certainly caused by temperature changes.

Another issue is illuminated by the data shown in Figure 5-22. Here, variations are observed in the open-loop behavior of the height regulation system for different tuning fork probes. Over the course of our experiments, a total of four probes were tested. The plot shows the plant dynamics for three of these probes. We believe the observed variability is most likely related to changes in the mass of the fiber tip and glue, though differences in the tip's geometry may also play a role.

Data for probe #2 is not included in Figure 5-22, because of a defect observed during testing of this probe. When the probe's tip was brought into engagement and the axial height regulator was activated, the controller tended to saturate, such that the probe was positioned too close to the sample. When this happened, we could see the fiber buckle, when looking through the coarse-approach viewer. We believe that the fiber mounted to the probe was too long and thin. This geometry apparently

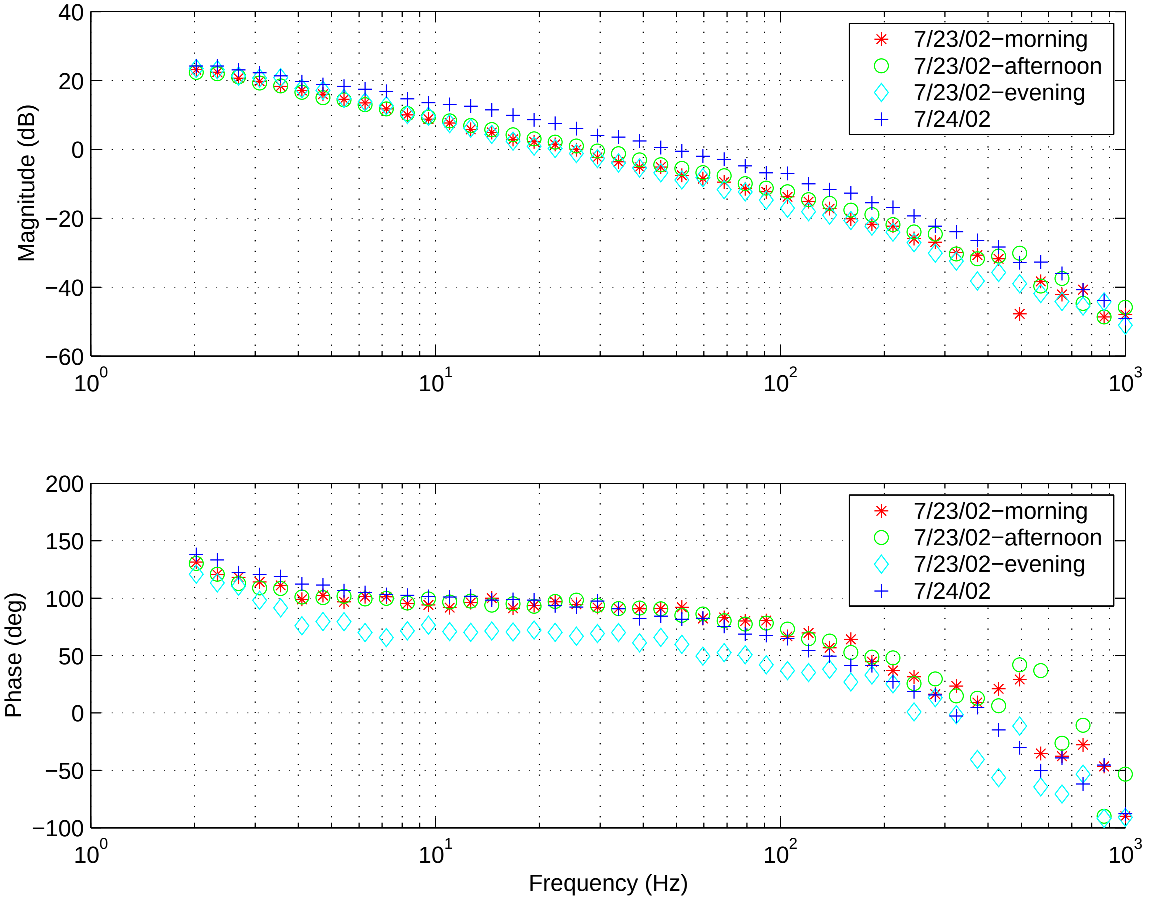

Figure 5-21: Comparison of the open-loop frequency responses of the axial height regulation plant, taken with the same probe and measuring the same output variable, but acquired at four different times. The data suggests significant variation in the plant's behavior as a function of time.

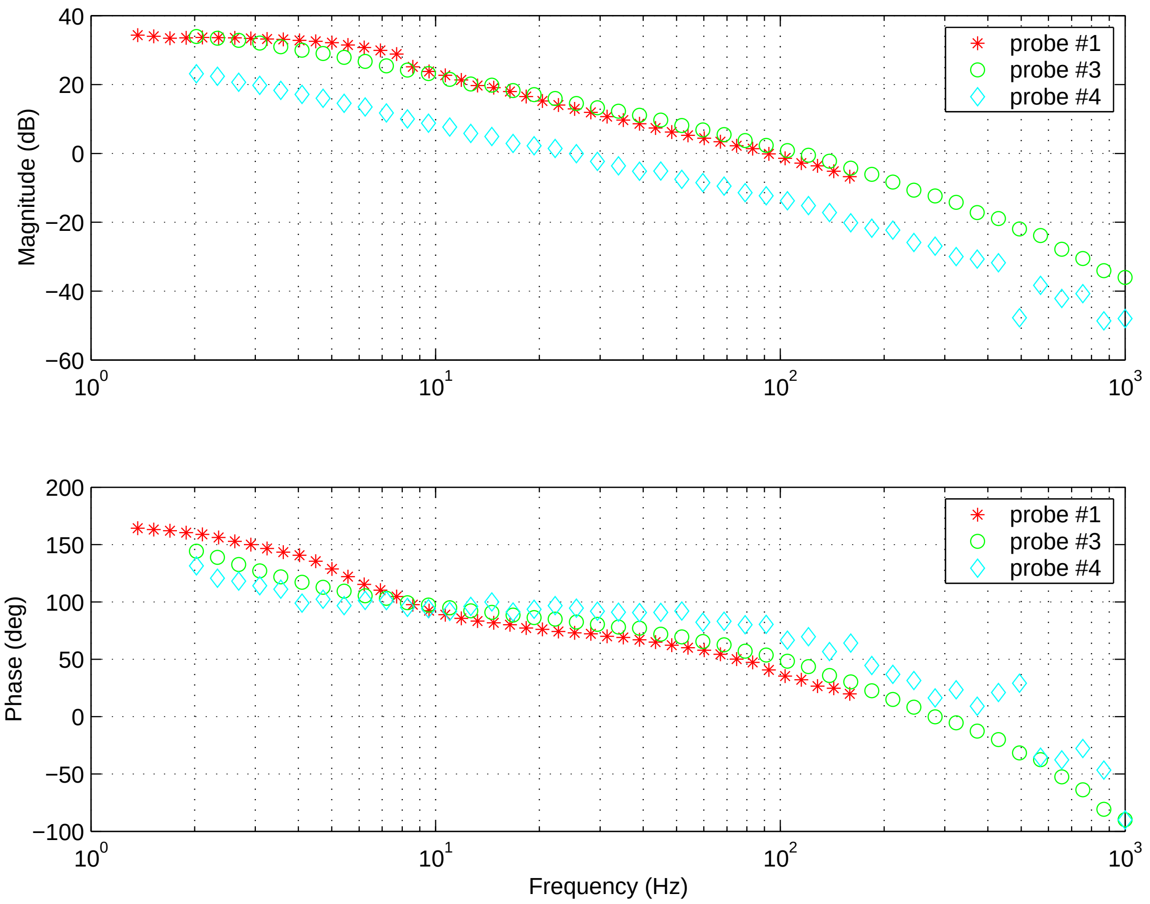

Figure 5-22: Comparison of the open-loop frequency responses of the axial height regulation plant, for three different tuning fork probes. The plant dynamics change significantly in switching from one probe to another.

caused an inversion in the tuning fork's behavior when the fiber touched the sample surface. While the fiber was in its buckled state, the lock-in's output indicated a relatively large current flowing through the proximity sensor, which would normally indicate that the probe was too far from the sample. With this inversion, the axial height regulator could not be reliably stabilized.

The metrological AFM was tested on two different samples — a silicon calibration grating and a steel gauge block. As shown in Figure 5-23, a significant reduction in system gain — with corresponding reduction in probe sensitivity — is observed in moving from the silicon surface to the steel surface. Besides the drop in magnitude, the two system responses appear to be quite similar. The reduction in gain corresponds to a larger region of engagement for the steel surface — with depth of approximately 1 μm — compared to the silicon's region of engagement — with depth closer to 25 nm. These values were approximated by increasing the amplitude of u_d until the upper and lower portions of the tuning fork sensor's output curve flattened noticeably. We assume that the flat sections correspond to the proximity sensor having been moved 'out of range,' where the tip either is in contact with the sample surface or has been moved far enough above the surface that it no longer interacts with the sample. By taking the difference of the measured probe Z positions at the times when the R_{ave} curve begins to flatten, we find a reasonable estimate for the engagement region's depth. The dramatic increase in the depth for the gauge block might well be explained as the result of a thin layer of oil covering the block's surface, as the block was not thoroughly cleaned before the measurement.

Even with the observed system variability, we are able to fit a model to the measured data that requires only minimal adjustment on a day-to-day, probe-to-probe, and sample-to-sample basis. For the majority of measured open-loop response curves, fairly good agreement is achieved by multiplying the discrete-time equivalent of

$$P_{A,CT}(s) = \frac{-(0.07s+1)}{(1\times 10^{-3}s+1)(s^2+2(0.8)(14)s+14^2)} \tag{5.10}$$

by the FIR filter given in equation (5.9), then subtracting the phase lag that results from the digital controller's time delay. As noted in section 2.3, the low-frequency resonance seems to be related to the tuning fork dynamics. The lock-in amplifier's low-pass filter provides the 160 Hz pole. Finally, equation (5.10) includes a zero with a break frequency of about 2 Hz, which is added to the model to force the theoretical curve into better agreement with the measured data. Considering the very low frequency at which this zero occurs, it seems most likely to originate from the tuning fork dynamics, of which we have an incomplete understanding.

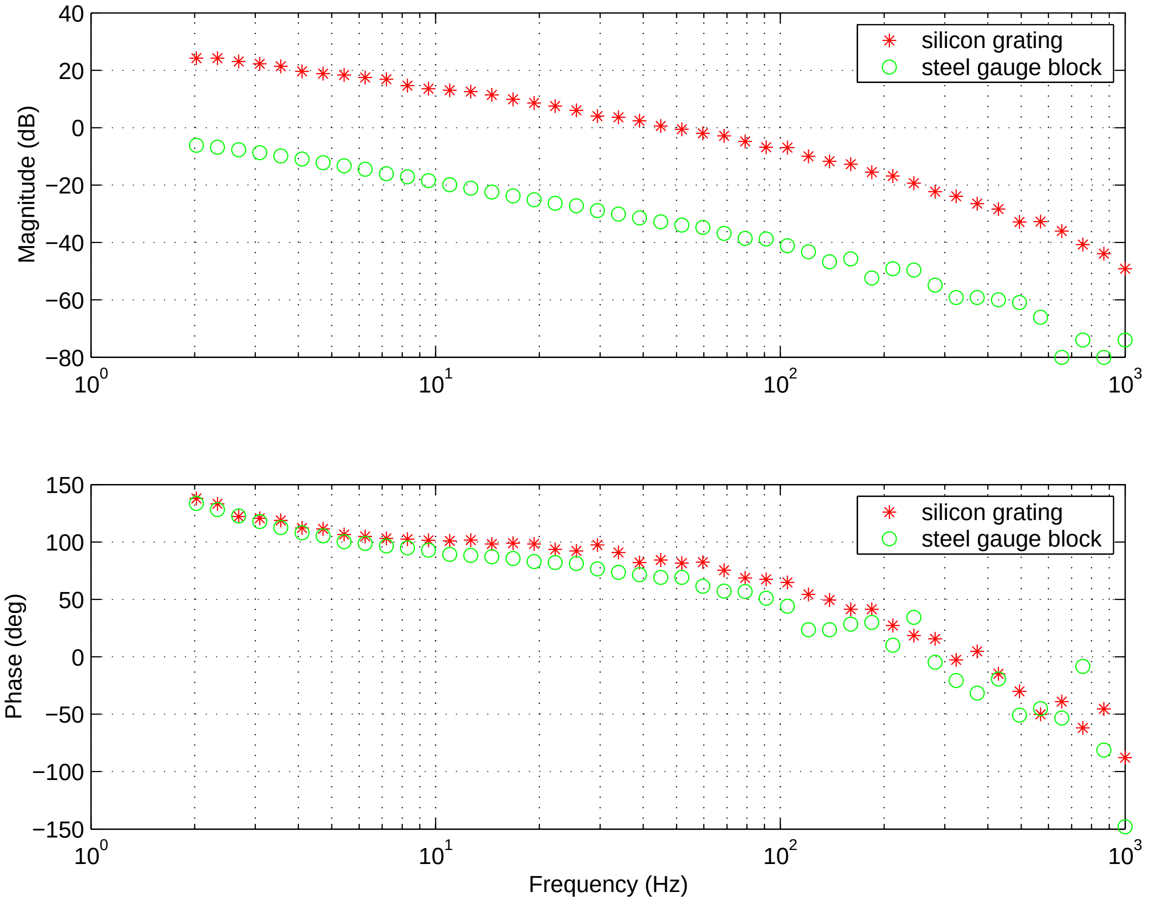

Figure 5-23: Comparison of the open-loop frequency responses of the axial height regulation plant, for two different samples. The data was measured using probe #4, with R_{ave} as the output variable. A significant reduction in gain is observed in moving from the silicon grating to the steel gauge block.

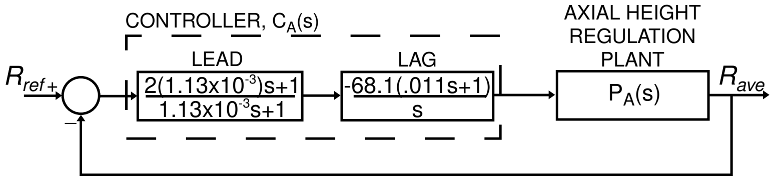

Figure 5-24: Block diagram for the axial height regulation loop, with lead-lag control.

5.3.2 Controller Design

We implemented several different control strategies for the axial height regulation loop. In general, we sought a closed-loop bandwidth of about 100 Hz, with a relatively large phase margin — 50° or more — to accommodate the uncertainty in the plant model. The block diagram in Figure 5-24 represents one attempt at closing the loop, using a standard lead-lag compensator. The lag element provides large low-frequency gain and the lead element increases the system phase at cross-over. Frequency response data for the resulting negative of the loop transmission is presented in Figure 5-25, along with the response predicted by the approximate plant model. The data indicates a measured phase margin of 60°, at a 110 Hz cross-over.

Though we had some success with the lead-lag controller in achieving a high bandwidth, as well as in imaging the test grating, we found the closed-loop system too prone to instability. The lag's free integrator likely plays a key role in this unwanted behavior. When the system becomes unstable, the probe crashes into the sample surface, potentially damaging the tip. To address this issue, we changed to the simple proportional control strategy shown in Figure 5-26. Here, the gain is adjusted to achieve a cross-over frequency of about 100 Hz, which results in a phase margin of approximately 47°. The corresponding theoretical negative of the loop transmission Bode plot is shown in Figure 5-27. Due to time constraints, we did not measure the actual loop transmission response for this controller.

Finally, a slightly different controller was employed when imaging the steel gauge

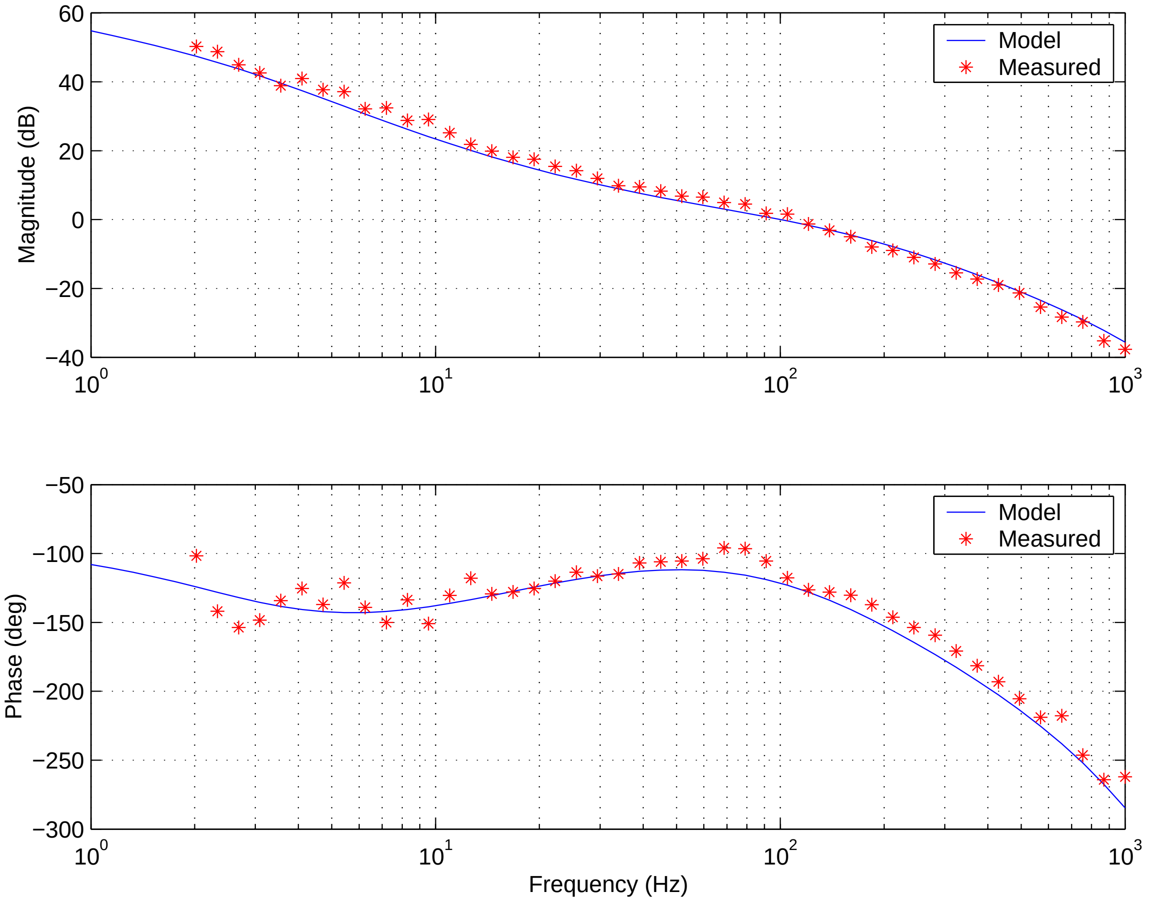

Figure 5-25: Negative of the loop transmission Bode plots for the axial height regulator, using a lead-lag controller. The system crosses over at 110 Hz and has a phase margin of 60°.

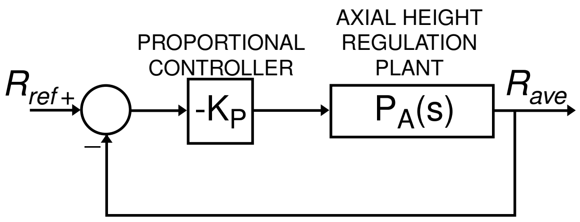

Figure 5-26: Block diagram for the axial height regulation loop, with proportional control.

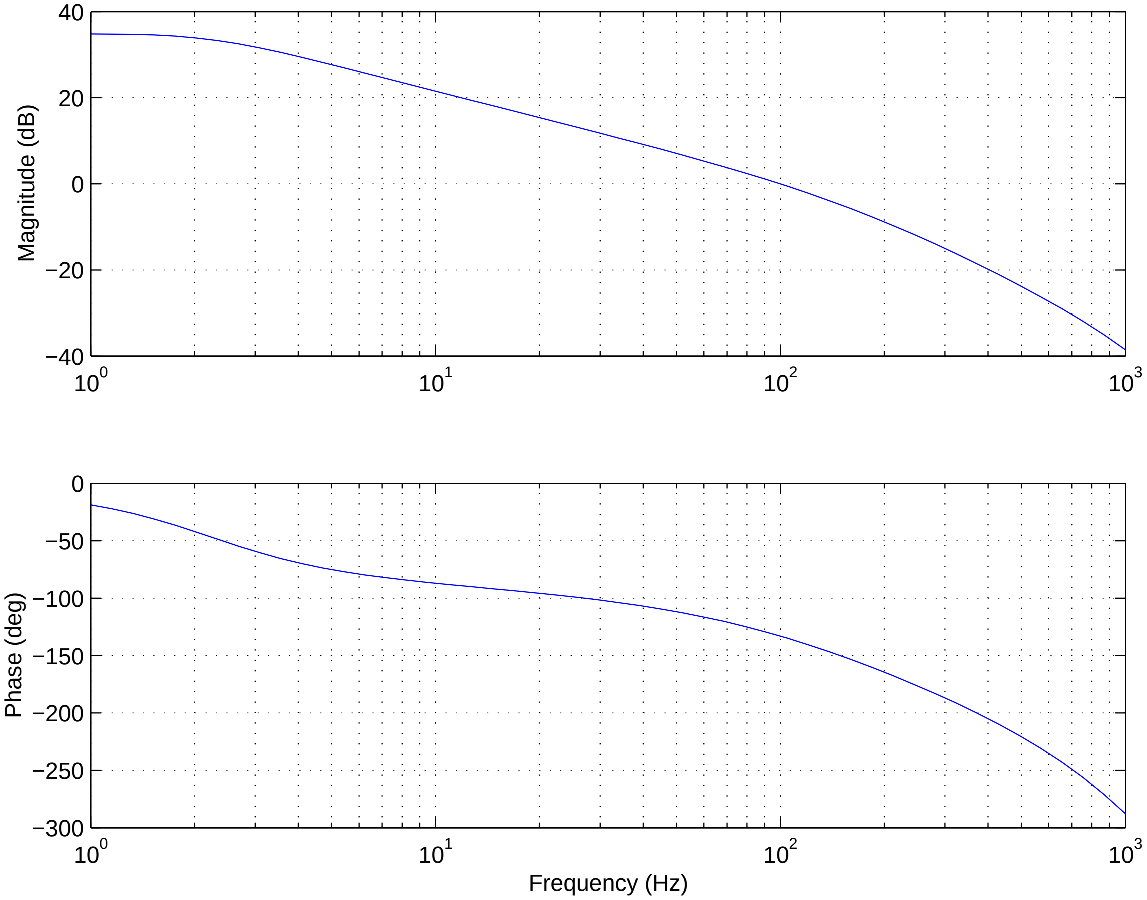

Figure 5-27: Theoretical negative of the loop transmission Bode plots for the axial height regulator, using a proportional controller. The predicted cross-over frequency is 100 Hz, with a 47° phase margin. We did not measure the actual loop transmission frequency response for this controller.

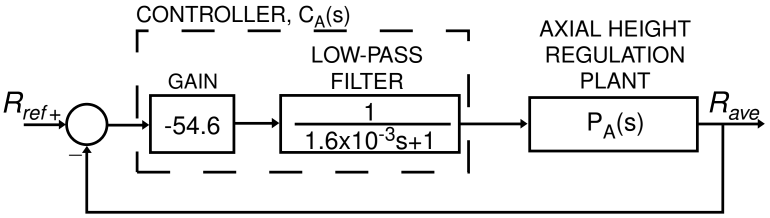

Figure 5-28: Block diagram for the axial height regulation loop implemented for the gauge block sample. A single-pole low-pass filter is added to attenuate the high-frequency noise in the system.

block. As previously mentioned, the tuning fork sensor is much less sensitive to changes in gap size when engaged on this sample. We originally attempted to close the loop using essentially the same proportional controller shown in Figure 5-26. However, when running this controller, the AFM emitted an audible buzz. We conjecture that this noise resulted from the rather large gain needed to produce the desired 100 Hz cross-over. This gain amplifies electrical noise in the lock-in signal, which then drives the tube scanner at relatively large amplitudes. To reduce the closed-loop system's noise, we added a pole beyond cross-over, as shown in Figure 5-28. The inclusion of this low-pass filter in the loop eliminated the buzzing altogether, presumably because the high frequency noise in the error signal was sufficiently attenuated. The corresponding frequency response for the negative of the loop transmission is presented in Figure 5-29. For this data, the controller's gain was set relatively low, to further reduce the closed-loop positioning noise. As a result, the cross-over frequency moves down to about 50 Hz. The measured phase margin is approximately 40°.

5.3.3 Performance

This section presents performance data for the three closed-loop systems described above. For the lead-lag controller (Figure 5-24), we have measured the corresponding closed-loop frequency response, as shown in Figure 5-30. The data indicates a

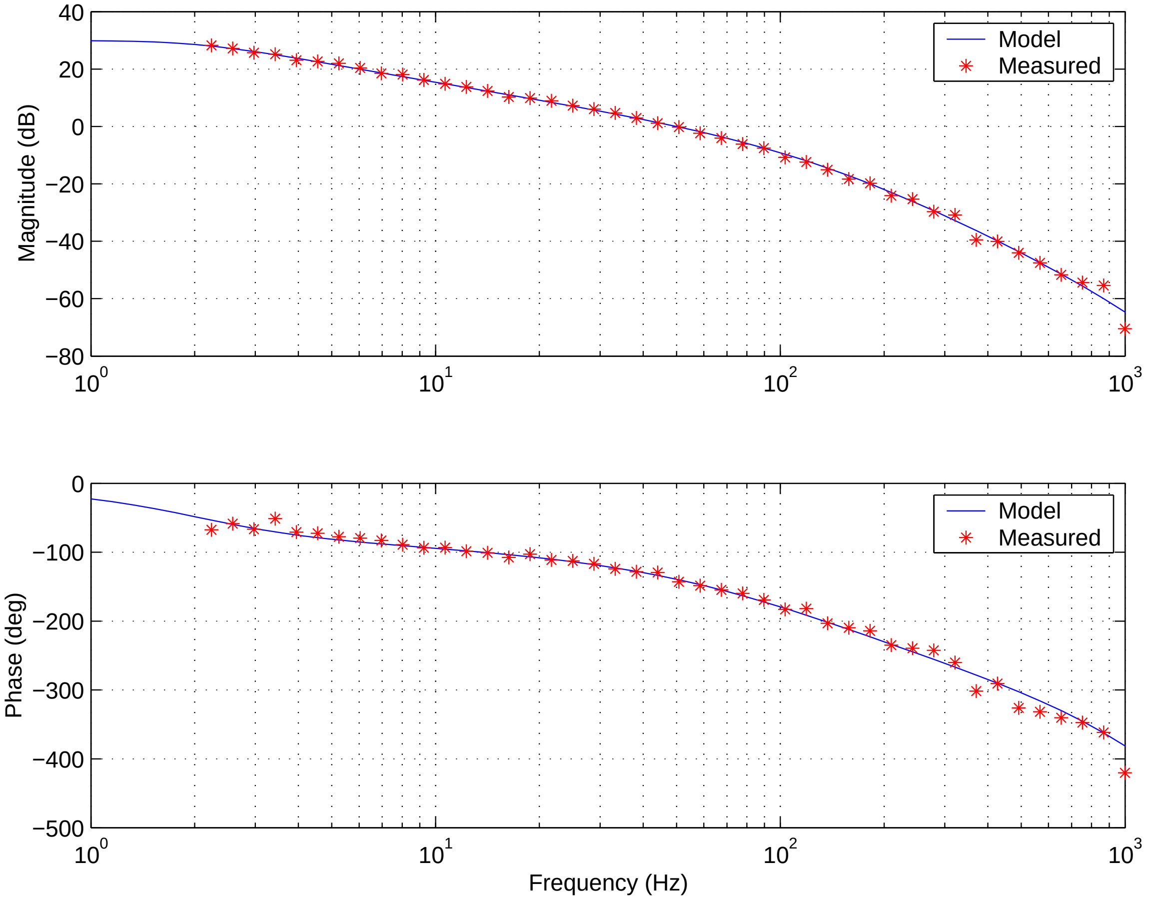

Figure 5-29: Negative of the loop transmission Bode plots for the axial height regulator used with the steel gauge block sample. The measured cross-over frequency and phase margin are approximately 50 Hz and 40°, respectively.

-3 dB closed-loop bandwidth of about 160 Hz.[10] The system's theoretical closed-loop response is not included in this plot, due to computational difficulties. Figure 5-31 presents the step response for the closed-loop system. The data is averaged over 10 triggers, to remove some of the random noise in the measured signal. From this data, the system's 2% settling time is approximately 40 ms. The step response contains significant noise at approximately 200 Hz, which seems to originate within the tuning fork proximity sensor's measurement circuit. Finally, the closed-loop positioning noise in Z is shown in Figure 5-32, for a 0.05 s interval. This data indicates an RMS noise level of 2.0 nm.

Figures 5-33 and 5-34 contain the theoretical closed-loop frequency response and step response, respectively, for the proportionally controlled system of Figure 5-26. Because of time constraints, we did not collect the associated performance data for this system. Based on the fitted model, however, we expect a -3 dB closed-loop bandwidth of about 175 Hz and a 2% settling time of approximately 11 ms.

Finally, Figures 5-35, 5-36, and 5-37 present the closed-loop frequency response, step response, and axial positioning noise, respectively, as measured on the steel gauge block sample, using the single-pole controller shown in Figure 5-28. This data demonstrates a -3 dB closed-loop bandwidth of 90 Hz, a 20 ms settling time, and a Z positioning noise of 54 nm RMS.

5.4 Summary

This chapter described the PC-based digital control system implemented with the metrological AFM. When imaging a sample, three control loops are utilized to produce the desired three degree-of-freedom motion of the probe tip. The two controllers in the lateral scanning system each use an integrator and a high-frequency pole, to

---

[10] Prior to acquiring this data, we measured a 184 Hz -3 dB closed-loop bandwidth using a nearly identical controller.

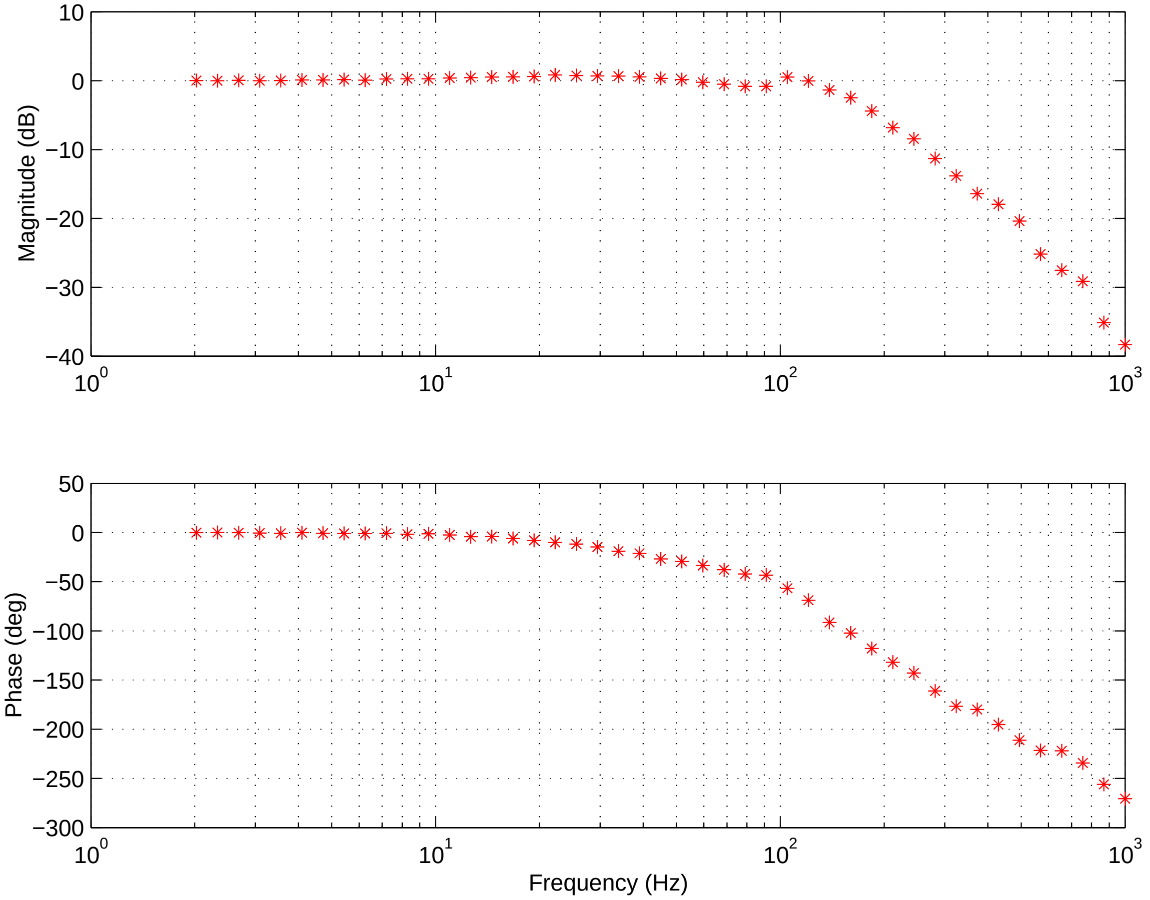

Figure 5-30: Closed-loop Bode plots for the axial height regulator, using lead-lag control. The measured -3 dB closed-loop bandwidth is approximately 160 Hz.

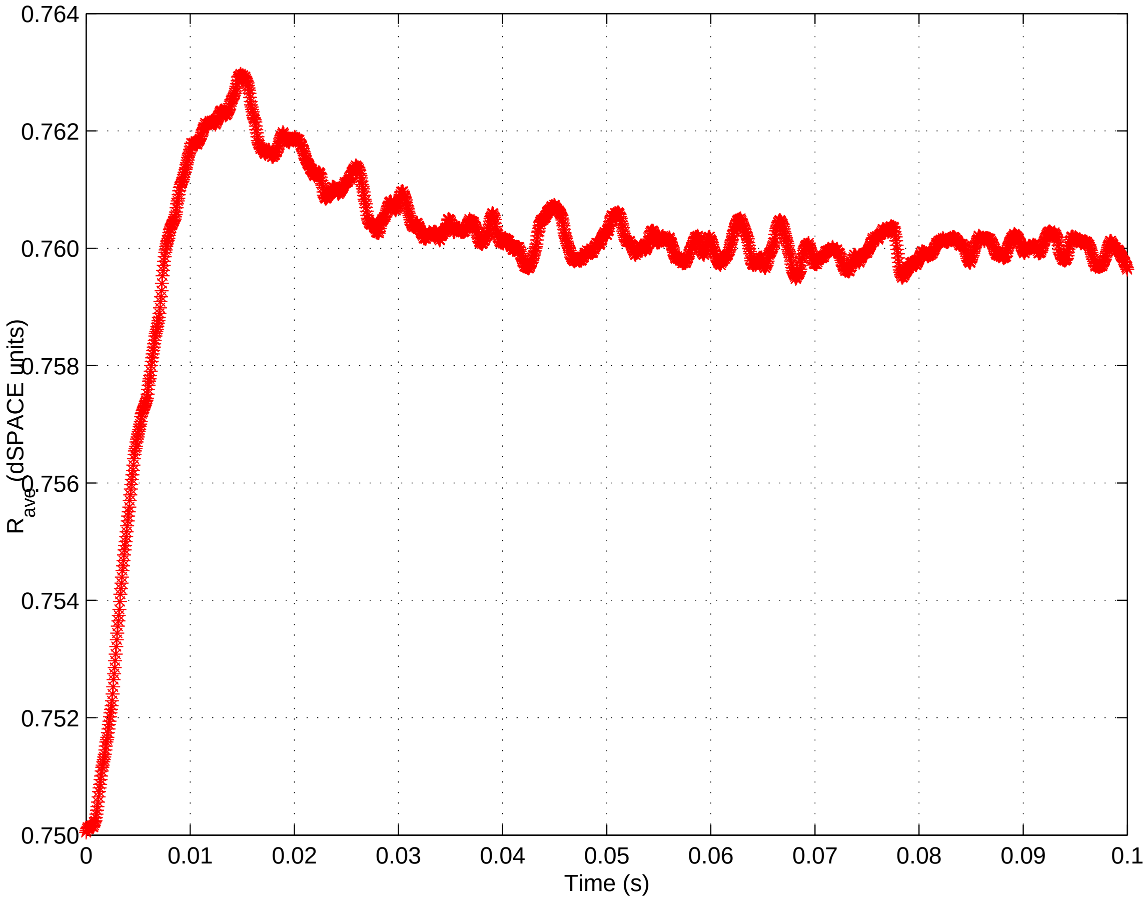

Figure 5-31: Step response for the axial height regulator, using lead-lag control. The plotted data is the average of 10 sets of captured data. The observed 200 Hz noise appears to originate within the tuning fork proximity sensor's measurement circuit.

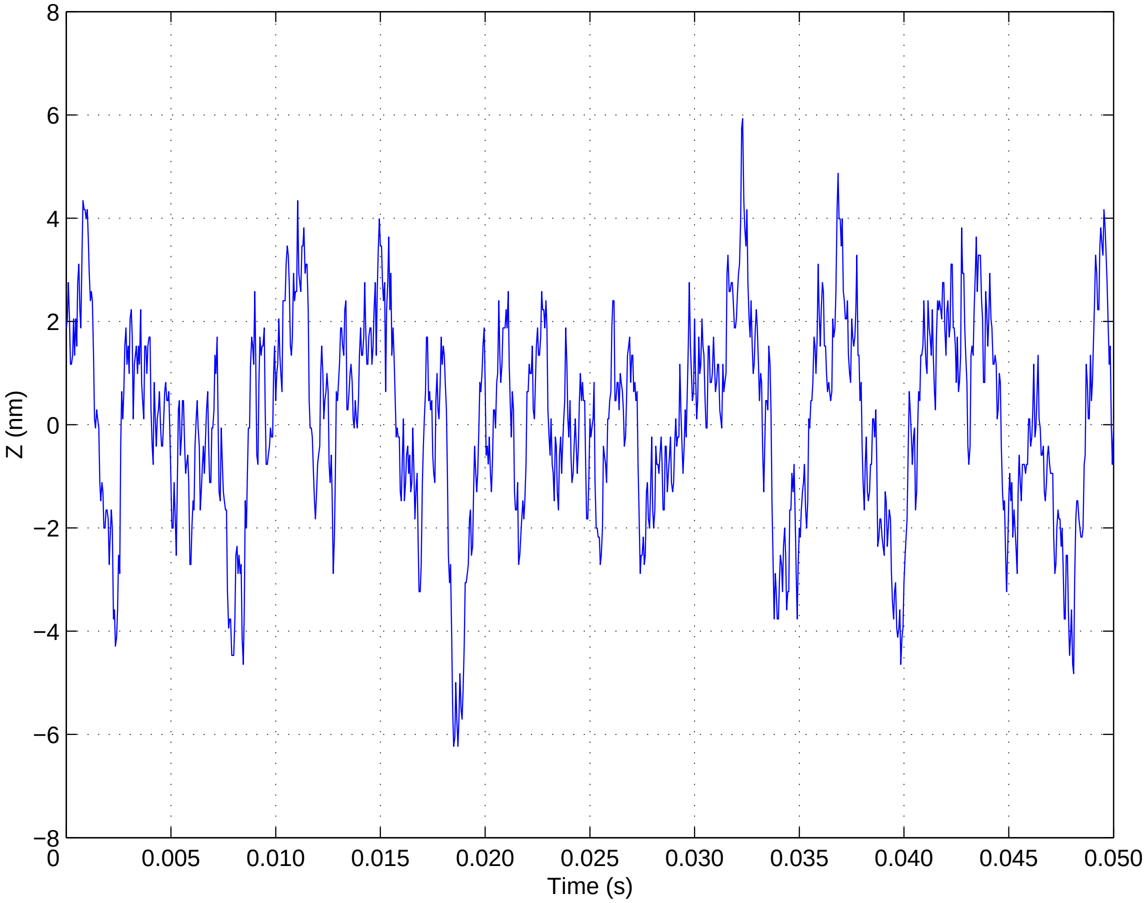

Figure 5-32: The measured positioning noise in Z over a 0.05 s interval, with a lead-lag controller in the axial height regulation loop. The data indicates 2.0 nm RMS noise. The Z value is filtered through a 5-sample moving averager, and the sampling frequency is 20 kHz.

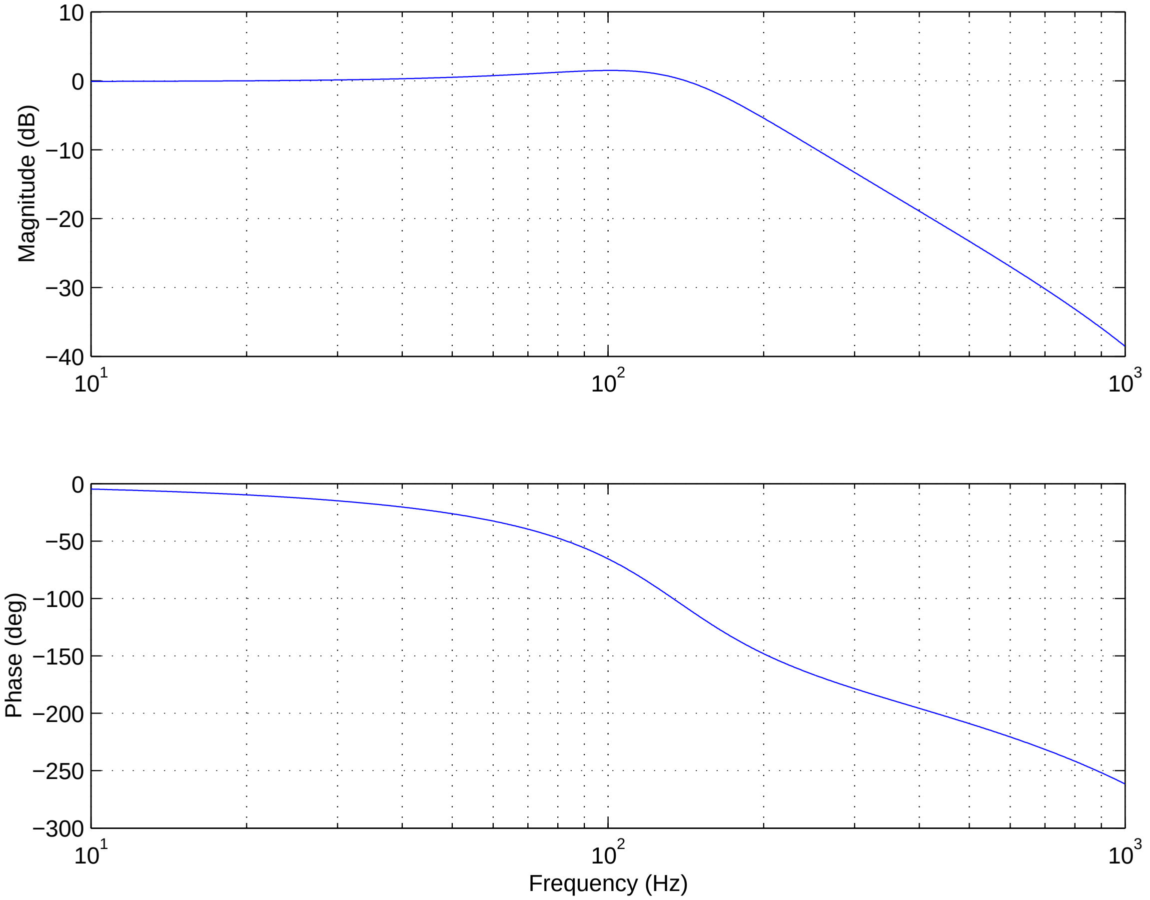

Figure 5-33: Theoretical closed-loop Bode plots for the axial height regulator, using proportional control. The phase lag from the controller board's discrete-time processing is left out of the model, for ease of computation. The theoretical -3 dB closed-loop bandwidth is 175 Hz.

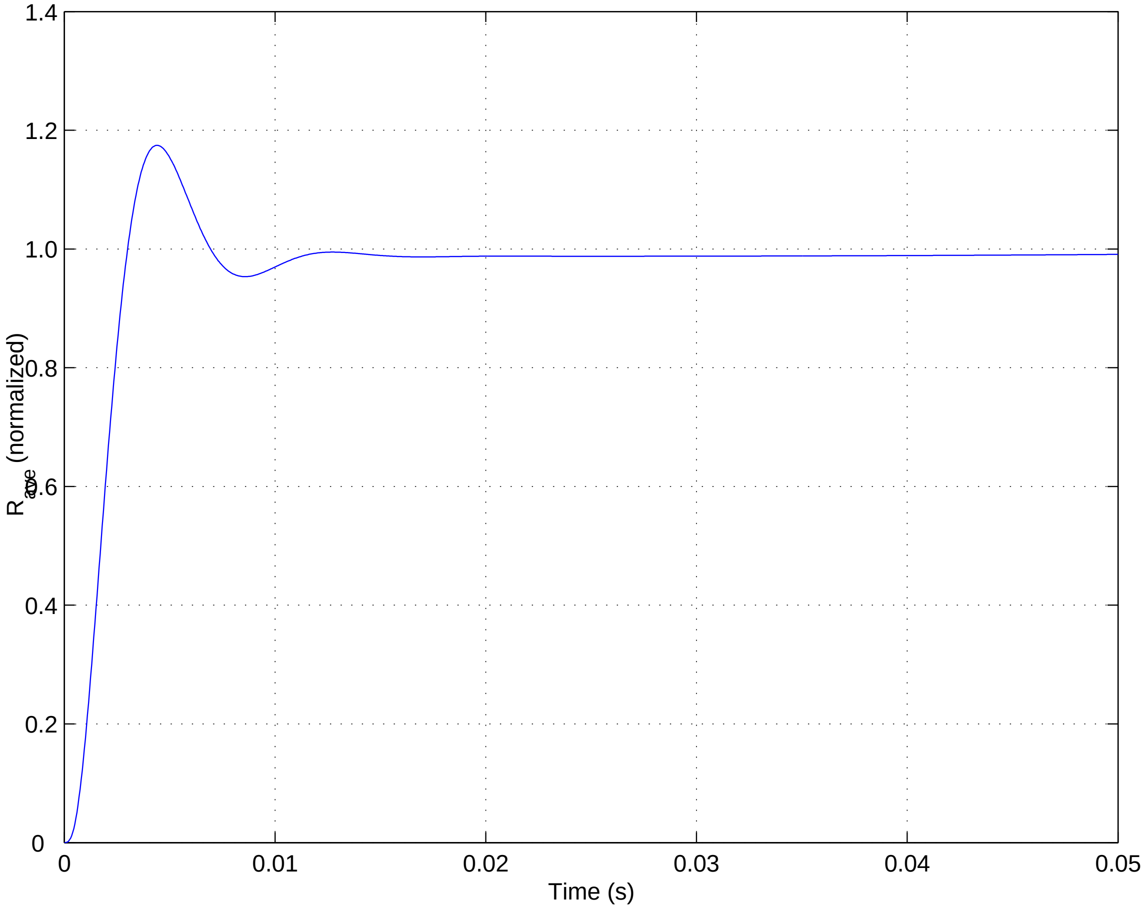

Figure 5-34: Theoretical step response for the axial height regulator, using proportional control. The estimated 2% settling time is 11 ms.

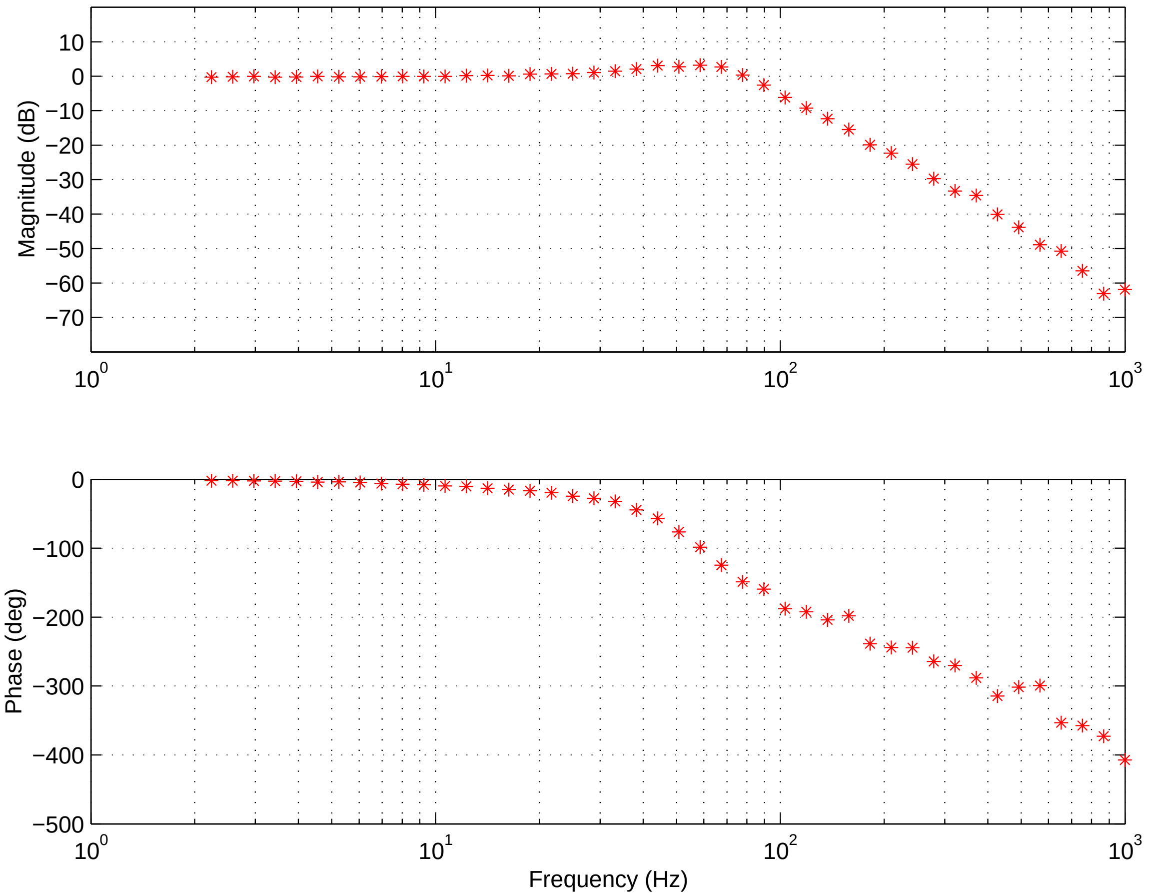

Figure 5-35: Closed-loop Bode plots for the axial height regulator used for the steel gauge block sample. The measured -3 dB closed-loop bandwidth is approximately 90 Hz.

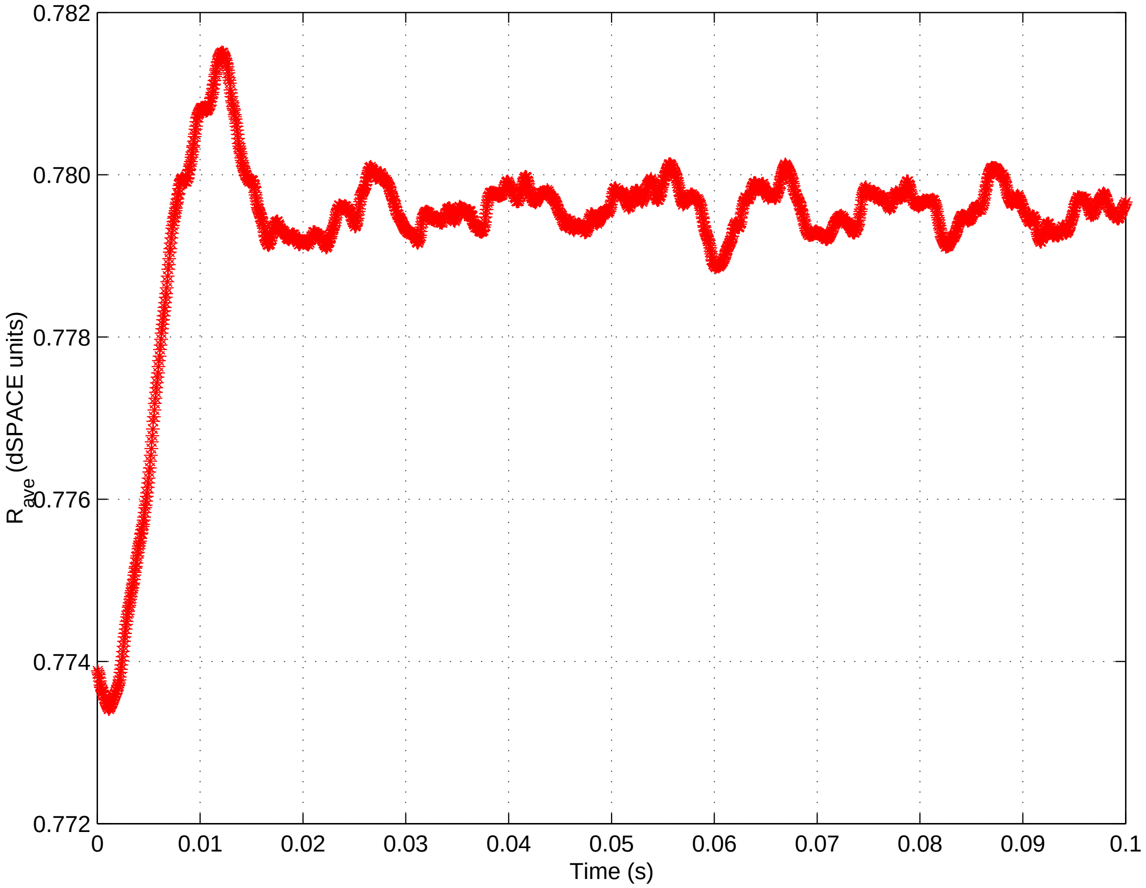

Figure 5-36: Step response for the closed-loop axial height regulation system, with the probe engaged on the steel gauge block sample. The data indicates a 2% settling time of approximately 20 ms. The observed 100 Hz noise component apparently originates in the tuning fork proximity sensor's measurement circuit.

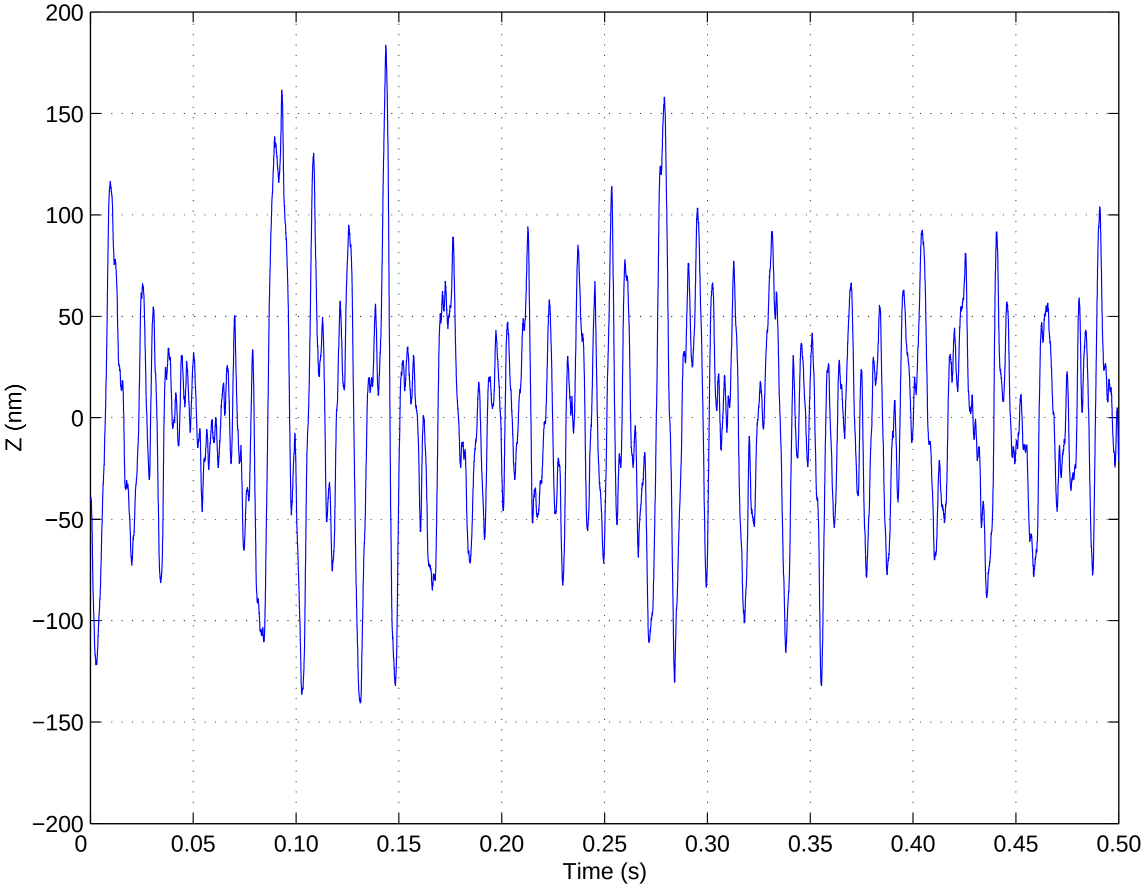

Figure 5-37: Measured positioning noise in Z for a 0.5 s interval, using a single-pole controller with the steel gauge block sample. The RMS noise is approximately 54 nm. The Z value is filtered through a 5-sample moving averager, and the sampling frequency is 20 kHz.

control the probe's position in the X-Y plane. The X and Y loops have measured -3 dB closed-loop bandwidths of 189 Hz and 191 Hz, respectively, and both have demonstrated closed-loop positioning noise of 1.3 nm RMS. These bandwidths are high enough for the scan speeds we require. Likewise, the positioning noise is essentially no higher than what was measured for the open-loop system. Based on these two performance measures, the lateral scanning system works quite well. If we had wanted to increase the bandwidths, however, we could have done so through phase stabilization of the scanner assembly's 1.03 kHz bending mode, using the Nyquist stability criterion as an additional design tool.

We encountered more difficulty when designing the controller for the axial height regulation system. For this system, we tried several different control strategies. A lead-lag controller provided relatively good closed-loop performance, but had a tendency to go unstable, perhaps because of the lag's free integrator. A simple proportional controller seemed to be more easily stabilized, without sacrificing much performance. However, one drawback of using the proportional control strategy for the axial height regulator is that the gain must be set relatively low to stabilize the loop with a reasonable phase margin. For example, we commonly used a gain of approximately $K_P = 1$ when testing with this system. Then, considering that the averaged magnitude of the tuning fork current, R_{ave},[11] has a range of about $0.5 \leq R_{ave} \leq 1.0$, and that we generally use a set point of $R_{ref} = 0.75$, the range of values output by the controller is approximately

$$\begin{aligned} -K_P(R_{ref} - R_{ave,min}) \quad &\leq u_Z \leq \quad -K_P(R_{ref} - R_{ave,max}), \\ -0.25 \quad &\leq u_Z \leq \quad +0.25, \end{aligned} \tag{5.11}$$

where $-1.0 \leq u_Z \leq +1.0$ corresponds to the controller board D/As' ±10 V full-scale

---

[11] This variable is computed within the controller processor and is expressed as a unit-less quantity.

range. As a result, the range of the common control voltage, V_{axial}, is limited to approximately one quarter of what it would be if the full range of the D/As were used. Therefore, the maximum change in sample height that the probe can track without saturating the controller is significantly reduced when using this controller.

When testing with the steel gauge block sample, we found that the tuning fork proximity sensor's engagement region was significantly larger than what was measured for the silicon calibration grating. The increased size corresponds to a reduction in the proximity sensor's sensitivity. As a result, the closed-loop system used with the gauge block exhibited large positioning noise, even when the controller's gain was set relatively low. The reason for the increase in the engagement region's size seems most likely related to an oil film covering the steel surface.

In the next chapter, images of the grating and gauge block are presented. The grating data provides strong evidence that the imaging system performs properly. As expected, the gauge block images contain significant noise, which obscures the actual surface topography.

Chapter 6

The Metrological AFM — Results

This chapter presents image data collected with the metrological AFM head. Two different samples were imaged — a silicon calibration grating and a steel gauge block. The calibration grating — a TGZ02 grating, made by MikroMasch[1] and distributed by K-TEK International, Inc.[2] — has a squarewave cross-section with a calibrated 104.5 nm step height and a 3000 nm pitch. A schematic view of the grating surface is shown in Figure 6-1. The manufacturer quotes an accuracy on the step height of ±1.5 nm over the entire active area. The grating is made of SiO_2 steps on a Si wafer and is coated with Si_3N_4 to prevent the Si from oxidizing. The gauge block has a flat steel surface, which is used to provide reference image data.

Two sets of data are shown for each sample — linescans and three-dimensional images. The images of the calibration grating demonstrate that the metrological AFM is readily capable of resolving 100 nm-scale features. However, the image data also contain a number of errors, which we attempt to explain below. The images of the steel gauge block are more than an order of magnitude noisier than the corresponding grating images. This behavior is directly related to the lower sensitivity observed for this sample material, as discussed in section 5.3, and hampers our ability to make

---

[1] See Appendix B.

[2] See Appendix B.

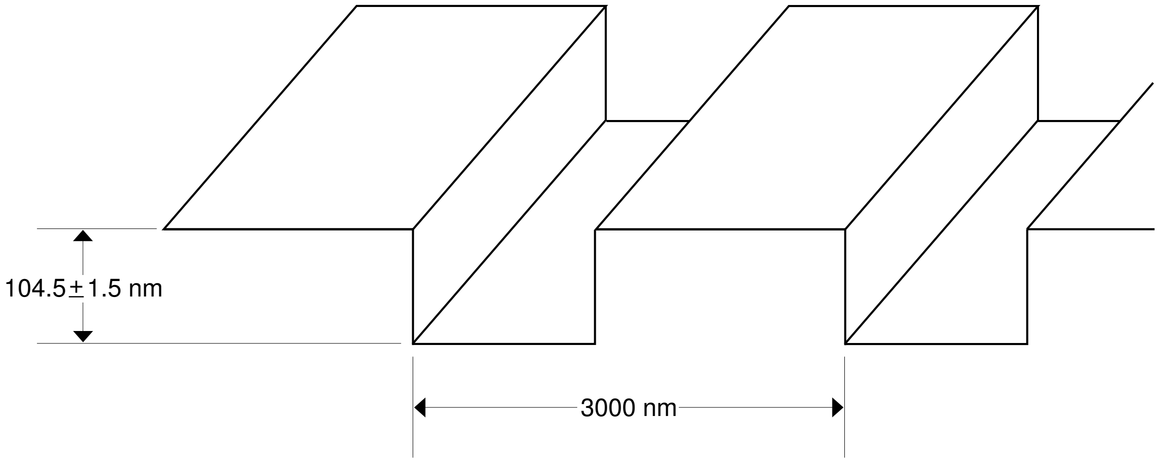

Figure 6-1: Schematic drawing of the squarewave calibration grating used as a test sample for the metrological AFM. The grating has a calibrated 104.5±1.5 nm step height and a 3000 nm pitch.

additional judgements on the AFM's performance.

6.1 Linescans

To produce a linescan, we engage the probe tip on a point above the sample surface, then command the probe to scan in a line parallel to either the X or Y axis while the axial height regulator attempts to maintain a fixed probe-sample separation. The measured probe position data is collected for the duration of the scan, then the resulting two-dimensional probe trajectory is plotted in MATLAB.

6.1.1 Silicon Calibration Grating

Figure 6-2 presents a linescan of the calibration grating measured using the same lead-lag controller for height regulation as shown in the block diagram of Figure 5-24. A 15 μm sweep was commanded in X, moving from left-to-right. The commanded X trajectory is shown in Figure 6-3. The scan lasted 45 seconds.

This data provides strong evidence that the metrological AFM functions properly.

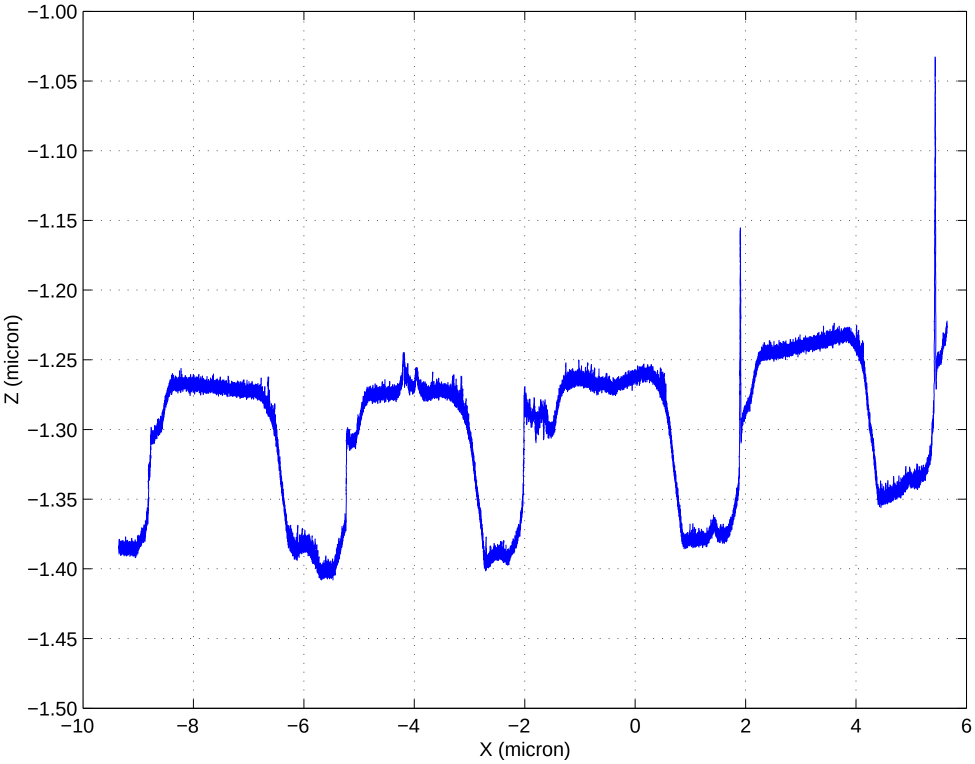

Figure 6-2: Linescan of the calibration grating, measured using lead-lag control of the axial height regulation system. The grating's periodic structure is clearly visible. A number of errors are also observed in the image data, including: a discrepancy between the measured and actual grating dimensions, jumps in the probe's vertical position at the rising edges, bumps in the flat sections of the grating, rounding of the corners, and concave-up curvature.

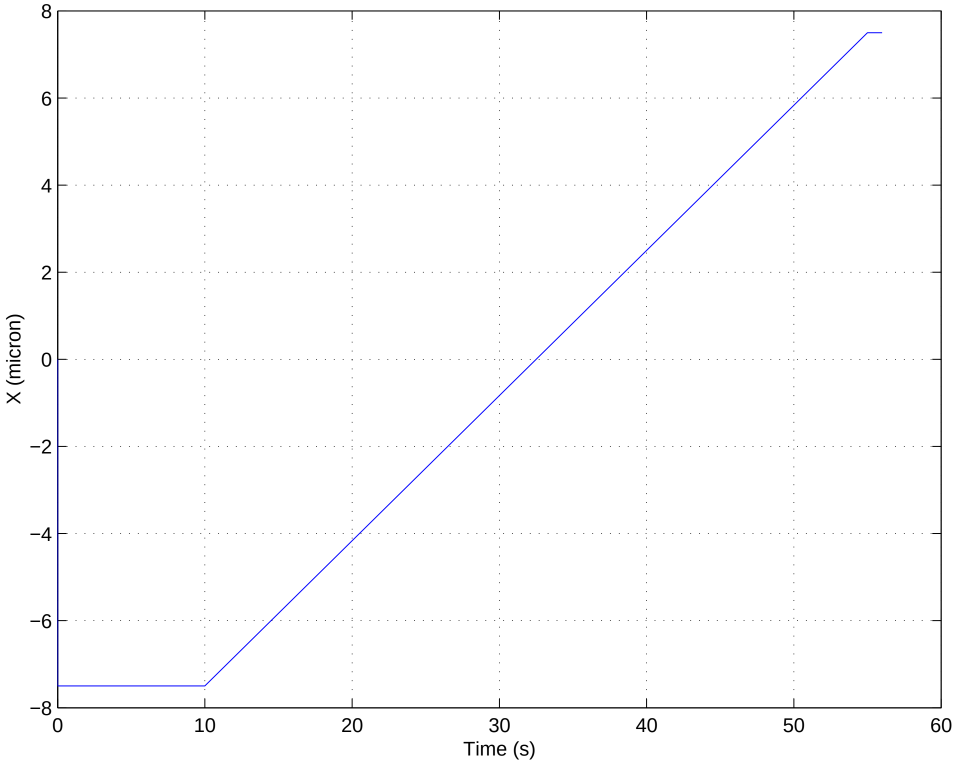

Figure 6-3: Commanded X trajectory used for the linescan in Figure 6-2. The probe moves 15 μm in X during the 45 s scan.

The scan contains a periodic structure with feature size on the order of the grating dimensions. The AFM has clearly resolved the 100 nm-scale grating ridges. However, there also appear to be several imaging errors in the scan. Firstly, the measured 120 nm step height and 3500 nm pitch are both significantly larger than the actual grating dimensions. The manufacturer of the AFM's capacitance probes calibrated each probe on a large, flat conductive surface. Since the AFM's conical target geometry is considerably different — small and curved, rather than large and flat — we believe the actual relationship between the displacement of the target and the sensor's output likely differs from the quoted 5 μm/V calibration constant. This difference is likely the primary reason for the discrepancy in the measured grating size.

A number of other errors can be detected in the scan. For example, the data contains some rounding of the corners of the ridges. This effect may be explained by the convolution of the tip and the sample topography, which is a common image artifact in atomic force microscopy.

On all five rising edges, the probe tip abruptly jumps in the positive Z direction. Also, the flat sections of the grating do not always get imaged as flat in the scan, particularly in the sections between the ridges. For these errors, we believe the unexpected probe trajectory may be caused by either poor tip sharpness or dirt buildup on the tip and/or the sample surface. The geometry of the tips used for these experiments was never rigorously checked, beyond looking at the fibers through a low-magnifcation optical microscope. We suspect that some of the tips were not particularly sharp and were perhaps irregularly shaped. No special precautions were taken to keep the probe or grating surface clean, either. All of the experiments were run in open-air in a non-clean room laboratory environment, so there was ample opportunity for dirt to collect in the scan region.

Finally, the scan appears to have some unexpected concave-up curvature. This behavior has been observed in a number of other scans as well, but we have not yet developed a detailed model to explain it. Perhaps the small, curved surface of the cone-shaped target results in nonlinearities in the sensors' measurements. Another possible explanation relates to the piezoelectric tube scanner's bent geometry, when the probe is laterally displaced. The AFM's metrology does not directly account for the resulting rotation of the cone-shaped target, which can become significant for large scans, as is evident from the discussion of Abbe offset error in section 3.1.2. Ideally, the target endpiece would simply translate in three degrees of freedom, without any rotation. Clearly, the accuracy of the sensor measurements should deteriorate somewhat when the tube scanner rotates the target endpiece through an angle, though the zero-Abbe offset sensor alignment should minimize this effect. We also suspect that the tilt of the target surface for large lateral scans results in nonlinearities in the sensors' output, which again could contribute to the observed image curvature.

Several other linescans were acquired, including the one shown in Figure 6-4. For this scan, the axial height regulator used a proportional controller similar to the one shown in Figure 5-26, but with a lower cross-over frequency — 80 Hz instead of 100 Hz. We also implemented a modified scanning strategy to remove discontinuities from the scanner's lateral trajectory (Figure 6-5). This smoothing of the commanded X motion lessens the danger of unwanted image artifacts being introduced from abrupt changes in the scanner's lateral motion.

Again, the metrological AFM clearly detects the grating's ridges. This data also indicates a relatively small RMS noise of about 3 nm, which was calculated for a flat section on the top of the ridge on the right side of the plot. However, the linescan contains more evidence of imaging errors. Unlike the data in Figure 6-2, the rising edges in this scan look rather clean, while the falling edges contain large vertical spikes. Also, two unexpected bumps are observed between the ridges. As mentioned above, we believe both types of error may be related to either a blunt tip or dirt buildup. This image lacks the curvature of Figure 6-2, for reasons that are, as yet,

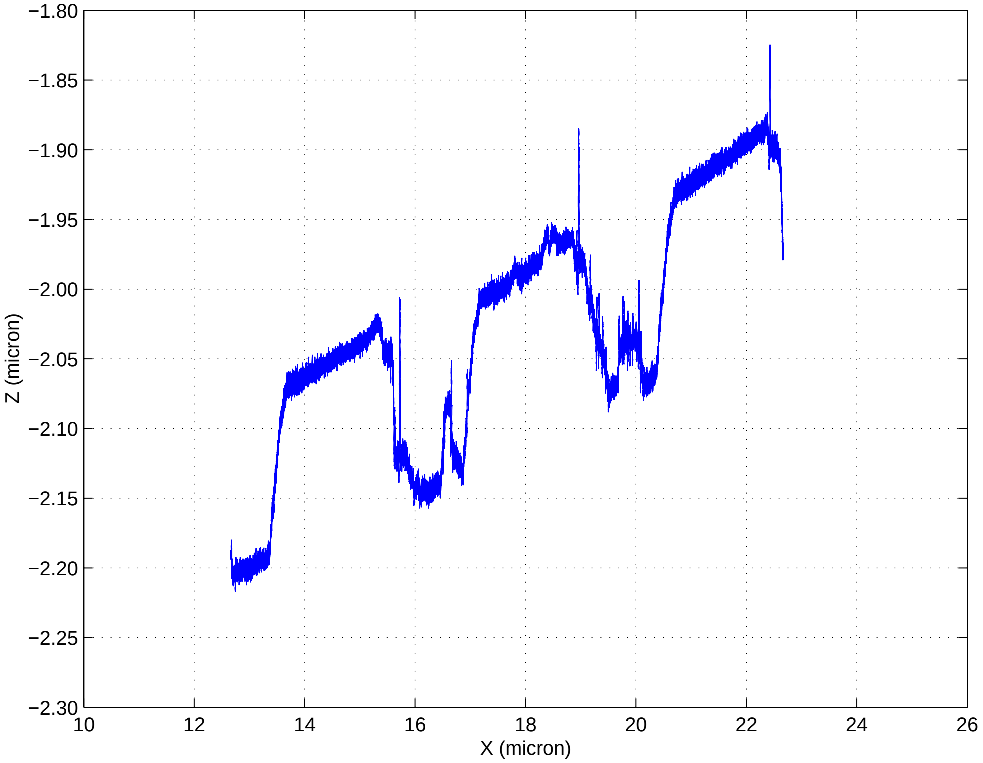

Figure 6-4: Linescan of the calibration grating, measured using proportional control of the axial height regulation system. The grating features are again clearly resolved, though some errors are still present in the image data. Specifically, there are sharp spikes at the falling edges and two large bumps between the ridges. This data indicates a Z positioning noise of approximately 3 nm RMS.

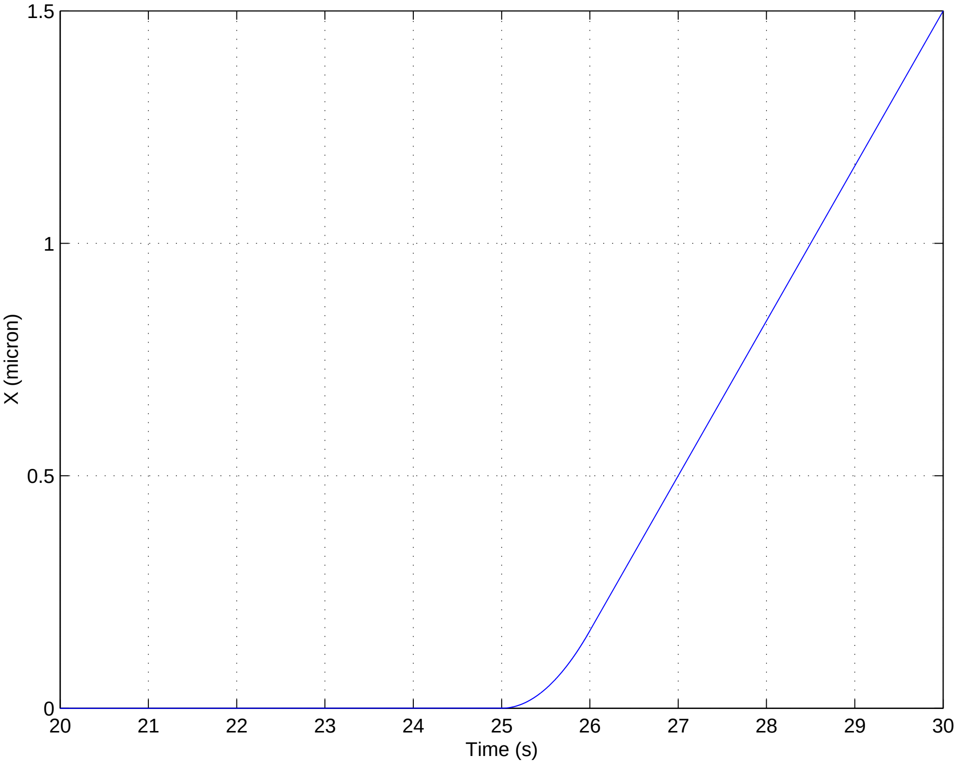

Figure 6-5: A section of the commanded X trajectory used in taking the linescan of Figure 6-4. The transition from the initial scanner location to the constant-speed scanning section is shaped with a parabolic curve, to remove discontinuities from the commanded X velocity.

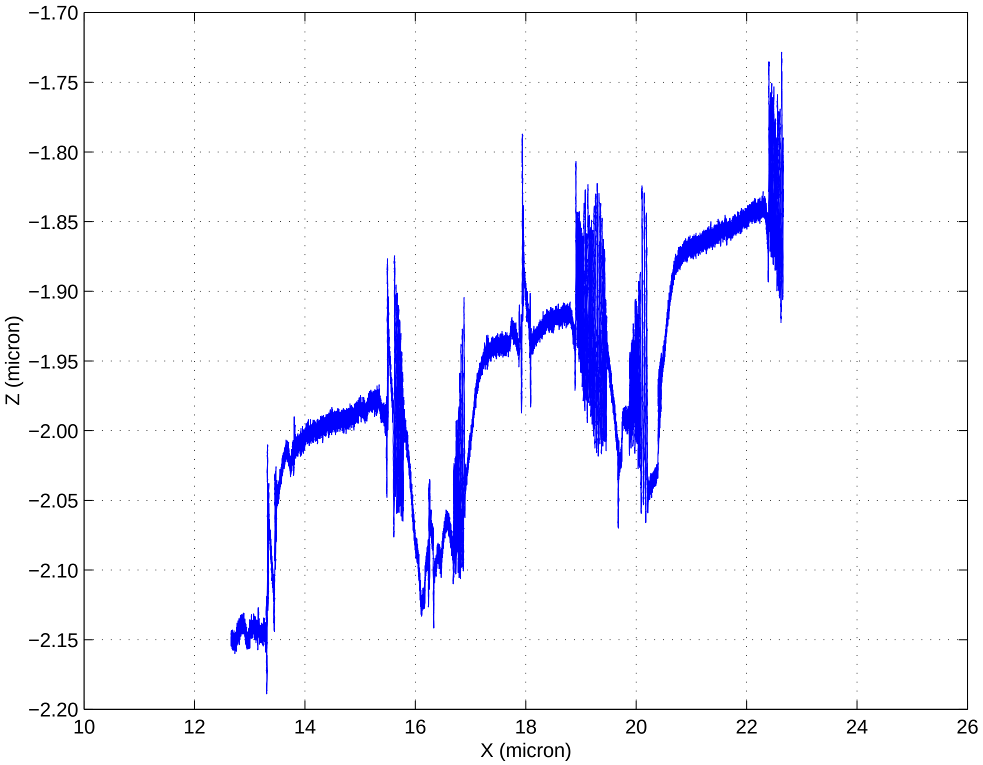

Figure 6-6: Linescan of the calibration grating, taken a few minutes after the scan in Figure 6-4. Significant deterioration is observed in the image data, possibly as a result of dirt on the probe tip and/or the sample surface.

unclear. Finally note that, while the scan appears to be heavily tilted because of the unequal scaling of the plot's axes, the actual tilt is only about 1°. Further, such tilts can readily be removed mathematically.

Within several minutes of acquiring the data for Figure 6-4, the same region was scanned again using the same controller, with the results presented in Figure 6-6. The scan data has deteriorated significantly in the image. Our best guess at the reason for this scan's poor quality again returns to the issue of dirt buildup. Perhaps the tip transferred dirt to the sample during the previous scan — or vice versa — which then interfered with the tip-sample force interaction, occasionally destabilizing the axial height regulator. The reasons for this behavior bear further investigation.

6.1.2 Steel Gauge Block

When the gauge block experiments were planned, they were designed to help characterize the metrological AFM's performance when imaging a nominally flat surface. This data would have been helpful for debugging some of the errors observed in the grating images — e.g. the apparent curvature of Figure 6-2 — and generally would have provided a more complete characterization of the AFM's imaging capabilities. However, as discussed in section 5.3, the tuning fork sensor is much less sensitive when engaged on this sample, as compared to the silicon grating, which results in considerably larger positioning noise in Z. This observation is borne out in the X linescan presented in Figure 6-7. In this scan, significant noise is also apparent in the lateral dimension, which agrees with an earlier observation that the piezoelectric tube scanner's X and Z degrees of freedom are coupled. More specifically, when the high-voltage amplifier supplies a common voltage, V_{axial}, to the tube scanner's four outer electrodes, the tube extends (or contracts), but also bends slightly in the X direction when the X scanning controller is disabled. As a result, during closed-loop scans, the X controller sees a disturbance from the axial height regulator's control signal. This unwanted behavior results in the observed coupling in the noise of the probe's measured X and Z coordinates. This problem likely could have been avoided by changing the scaling of the amplifier command signals in the Simulink controller model, as discussed in section 4.2.

The X linescan may be compared with the Y linescan shown in Figure 6-8, where significant noise is again observed in Z, but with a fairly clean trajectory in Y. This behavior is understandable, since essentially no coupling was observed between Y and Z during previous open-loop experiments. The Z positioning noise for this image has been calculated at approximately 50 nm RMS, far more than the 3 nm RMS value computed from the grating scan plotted in Figure 6-4. Unfortunately, the gauge block results can provide little additional insight into the AFM's performance, as a result

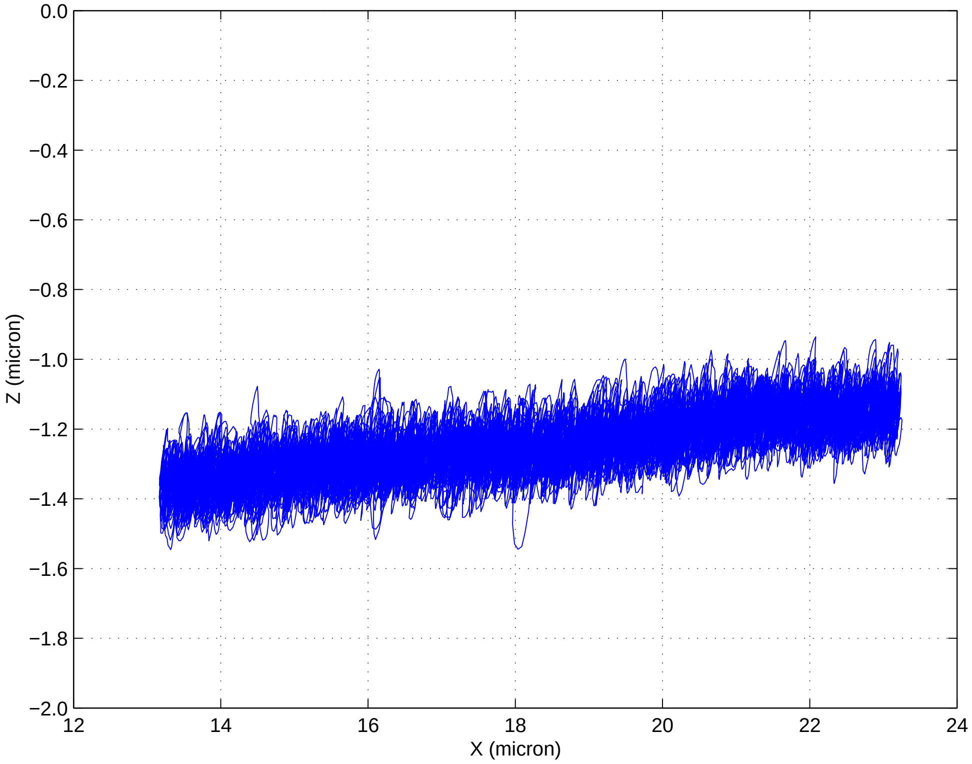

Figure 6-7: Linescan of the steel gauge block, for a scan parallel to the X axis. Significant noise is observed in both dimensions, which results from the coupling of the piezoelectric tube scanner's X and Z degrees of freedom.

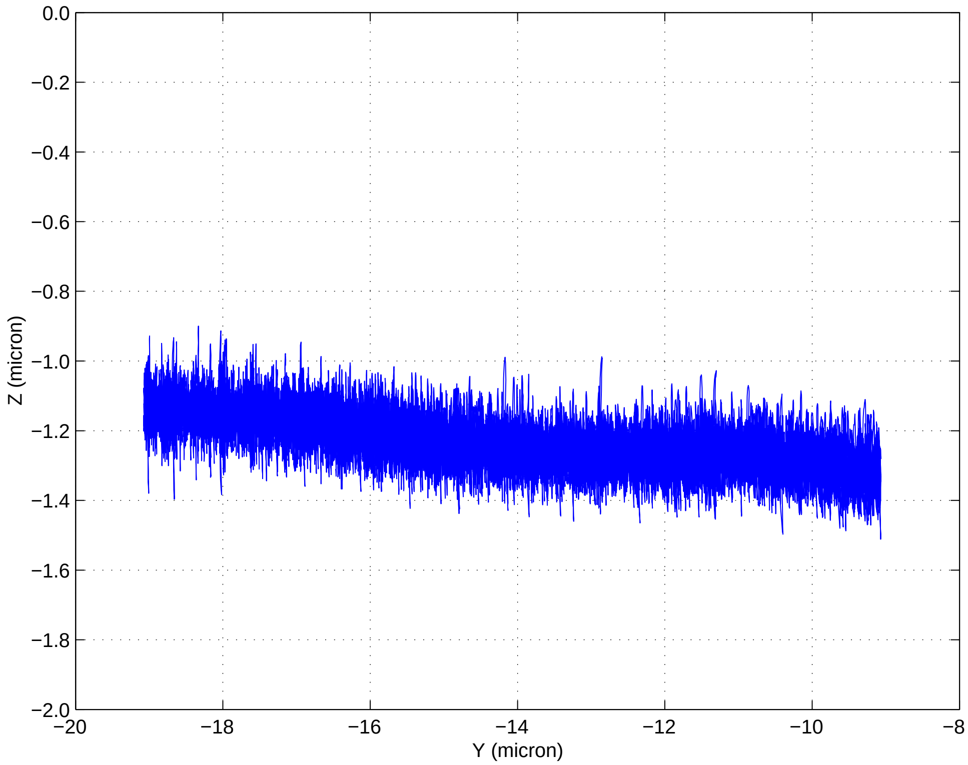

Figure 6-8: Linescan of the steel gauge block, for a scan parallel to the Y axis. The lateral trajectory looks much cleaner here than in Figure 6-7, since there is essentially no coupling between the piezoelectric tube scanner's Y and Z degrees of freedom. This data indicates an RMS positioning noise in Z of approximately 50 nm.

of the heavy noise.

6.2 Three-Dimensional Images

The three-dimensional image data is collected in much the same way as described above for a linescan, except with a commanded lateral trajectory in both X and Y. When taking images of the silicon calibration grating, the sample is oriented such that the steps occur in X, while the surface is essentially flat in Y. To optimize the trade-off between scan speed and lateral resolution, fast periodic motion is commanded in Y, while the probe makes a single slow sweep in X. Since there is no preferred direction for the nominally flat gauge block, we simply employ the same scanning strategy when taking images of its surface. While the AFM performs a scan, the probe position data is saved to a file, which is then used to create a three-dimensional plot of the tip trajectory in MATLAB.

6.2.1 Silicon Calibration Grating

We have captured several three-dimensional images of the silicon calibration grating with the metrological AFM. Figure 6-9 shows the result of one of the earliest attempts, for which a lag controller was used to maintain a constant value of ϕ_{ave}.[3] This image clearly contains a pair of ridges, but again with a few imaging errors. Notably, the scan data deteriorates significantly toward the right extreme in X, perhaps as the result of a mechanical disturbance or the presence of dirt. Also, some unexpected surface details are observed along the right edges of the two ridges. These features may simply be related to tip convolution, though the apparent bumps in the image seem to indicate some type of surface contamination.

Figure 6-11 shows the results of another attempt at imaging the grating, using the same lag controller as used for the image in Figure 6-9, but with a different scanning strategy. A squarewave step-and-hold trajectory is commanded in X and Y — as shown in Figure 6-10 — where the lateral scanning controllers are fed a list of coordinates which result in point-to-point motion with intermittent rests. The original goal was to acquire cleaner data with this strategy, by waiting for the axial height regulator to settle at each point before sampling the probe's position. This method could also have provided greater flexibility for defining complex trajectories, whereas before the X and Y controllers were simply fed ramp and sinusoidal reference trajectories, respectively (Figure 6-12). As seen in the grating image, the initial results using this strategy were not promising. Large spikes are observed at each stop along the X-Y trajectory, since many data points were collected and plotted at each point in

---

[3] This controller is not detailed in section 5.3, since it was not used extensively during our experiments.

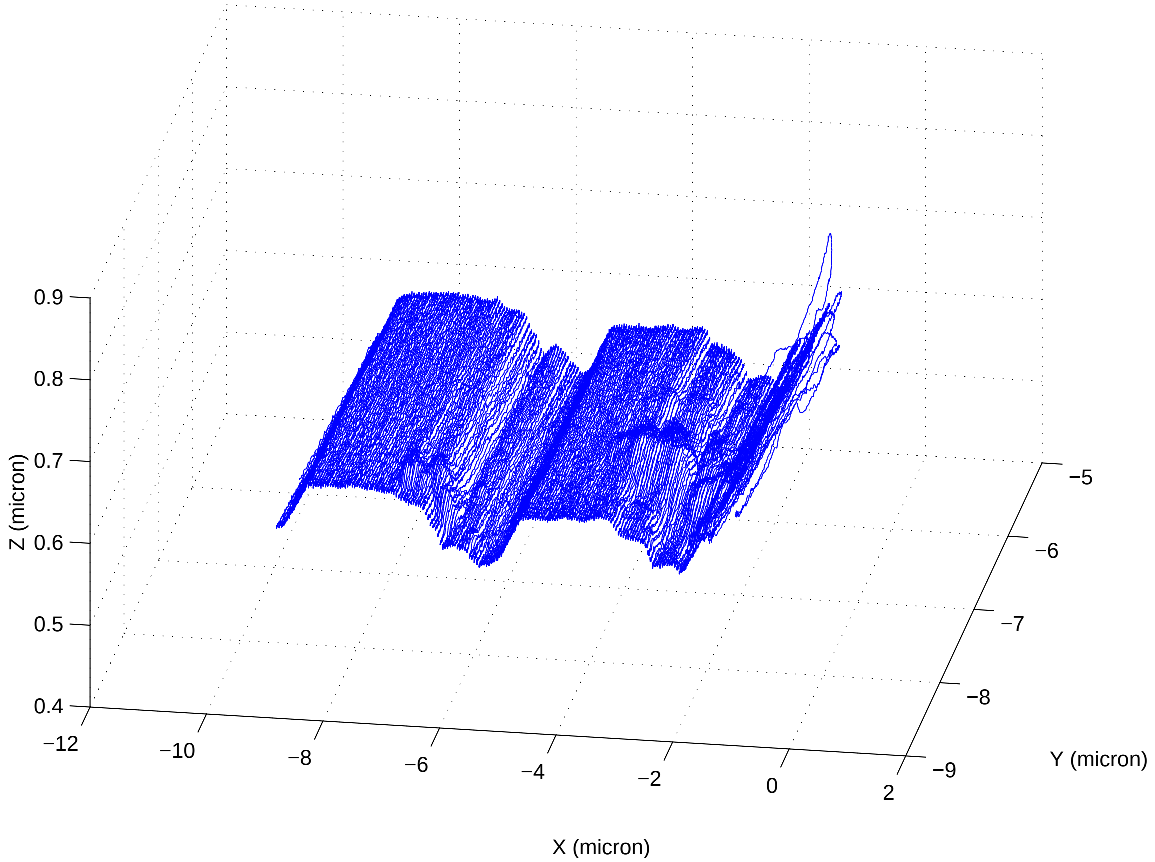

Figure 6-9: One of the first three-dimensional images of the silicon calibration grating taken with the metrological AFM. A pair of ridges are clearly shown. The image also contains several errors, particularly at the right extreme in X. The bumps on the right edges of the ridges may be caused by surface contamination.

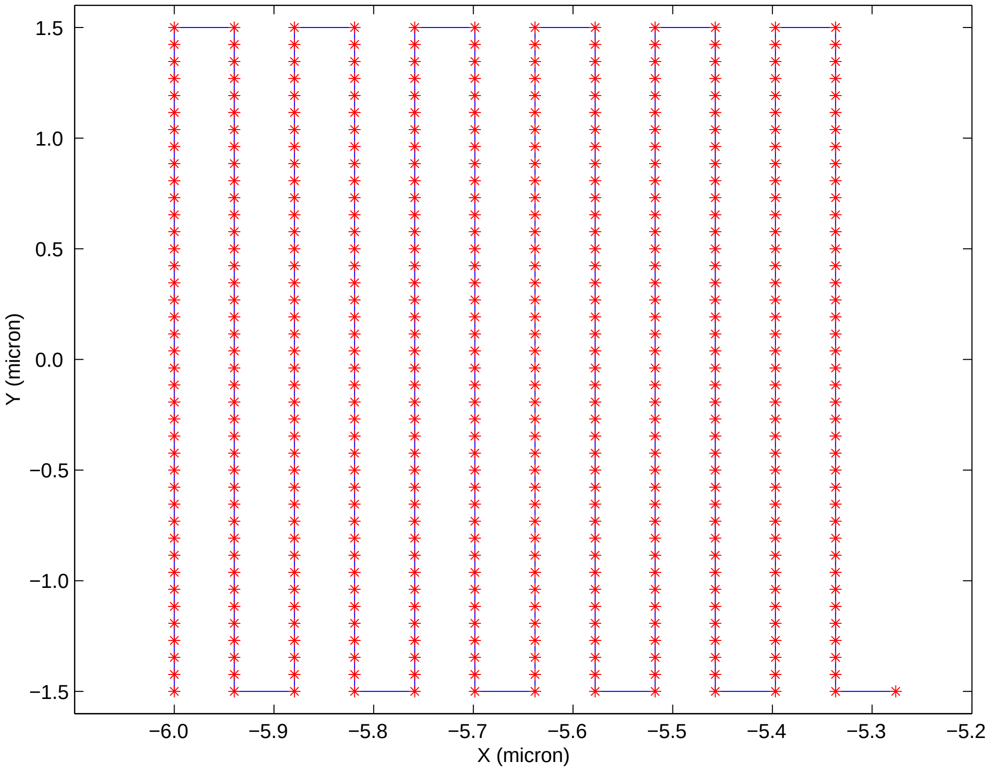

Figure 6-10: Part of the step-and-hold scanning trajectory used for the image in Figure 6-11. The stars indicate the commanded coordinates, while the solid line shows the path taken by the probe.

the lateral plane. These peaks could be smoothed out by averaging the measurement data at each X-Y position, but we decided that the extra effort would come with little benefit. Instead, we decided to use a smooth trajectory similar to the one in Figure 6-12 for all of the remaining three-dimensional scans.

Figure 6-13 presents one of the best three-dimensional grating images we have acquired with the metrological AFM to date. For this image, a lead-lag controller was used for axial height regulation, similar to the one specified in the block diagram in Figure 5-24, but with X_{ave} as the feedback signal. Here, X_{ave} was chosen based on earlier data that indicated that this signal was the most sensitive measure of probe-sample separation. The majority of the image is characterized by sharp edge detection and good flatness. However, the image also contains a couple of apparent flaws.

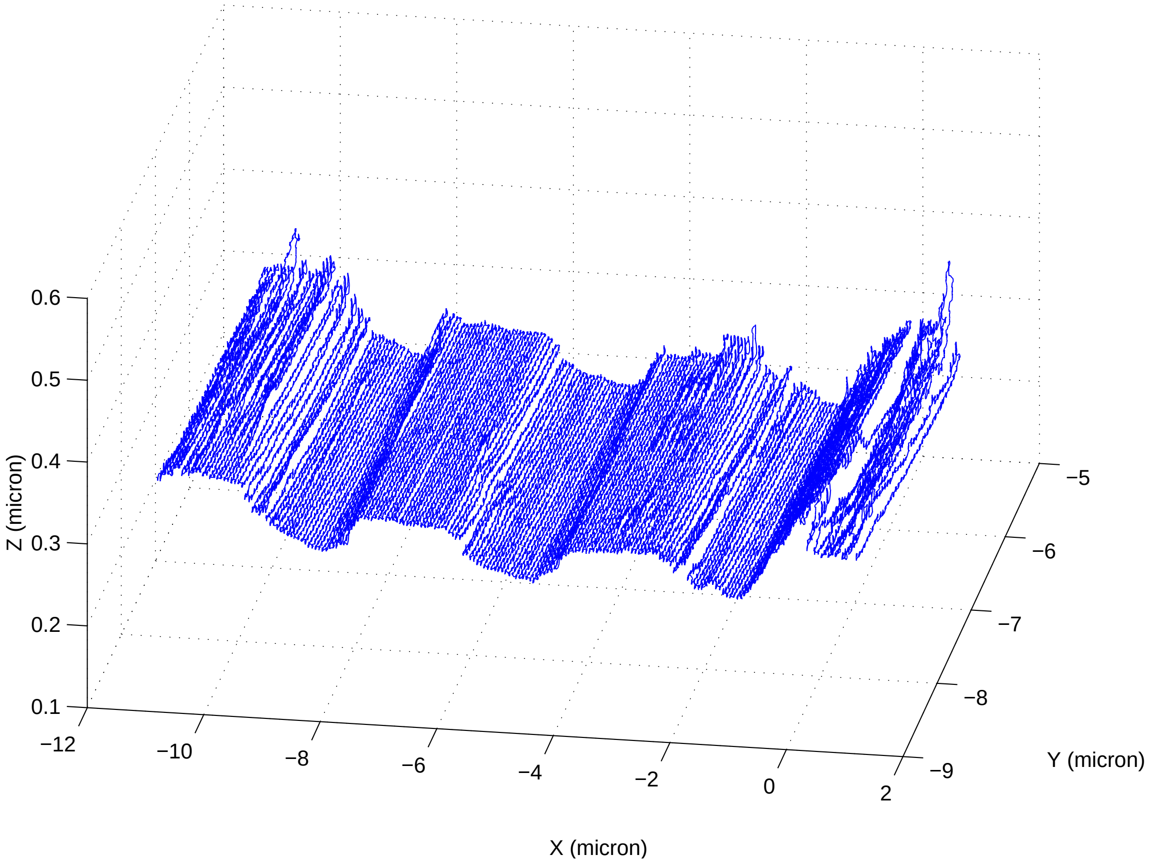

Figure 6-11: Three-dimensional image of the silicon calibration grating, for a commanded step-and-hold scanning trajectory. Spikes are observed at each point along the trajectory, since many data points were collected at each X-Y position, then plotted without averaging.

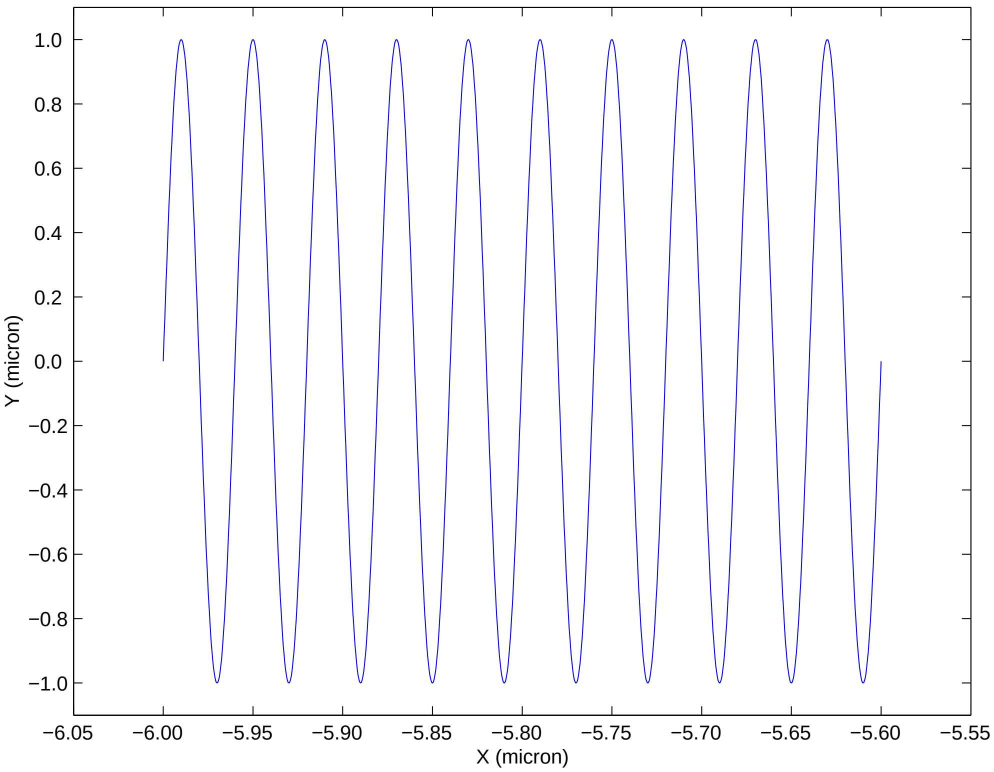

Figure 6-12: Part of a smooth scanning trajectory, with sinusoidal motion commanded in Y and a constant-speed sweep in X. This scanning strategy was used for the images in Figures 6-9, 6-13, 6-14, and 6-18.

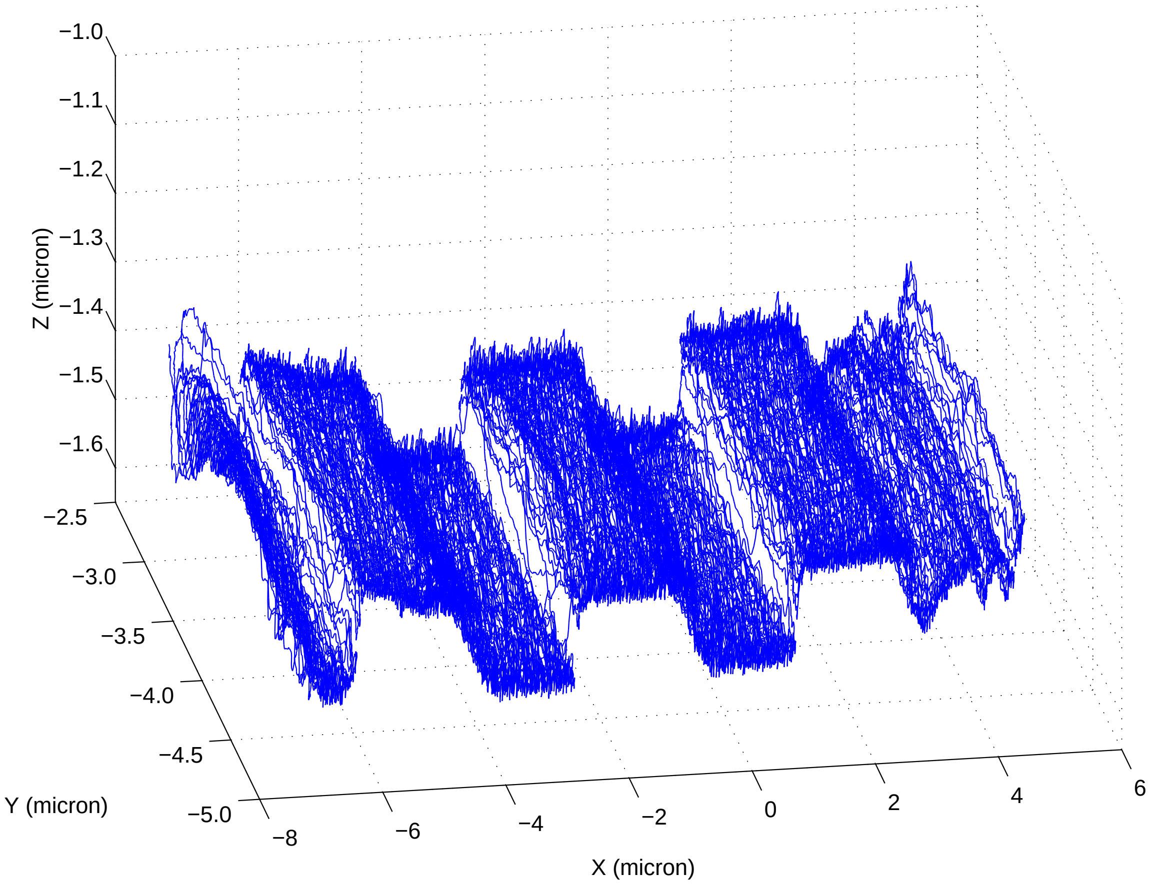

Figure 6-13: Three-dimensional image of the silicon calibration grating. In this image, three of the grating's ridges are clearly resolved.

Firstly, the two extremes in X are noisy. Again, this behavior may be related to the presence of dirt in the scan region or some kind of mechanical disturbance. Another possible explanation is the discontinuous velocity commanded to the X controller — where the commanded trajectory has the same shape as the one shown in Figure 6-3 — though this would only affect the beginning portion of the scan. Finally, this image contains the same concave-up curvature previously noted for the linescan in Figure 6-2, with possible reasons for this behavior mentioned above.

Since the completion of the bulk of the research described in this thesis, the metrological AFM project has been handed over to David Otten, a research engineer at MIT. During his work with the microscope, he has successfully acquired several clean

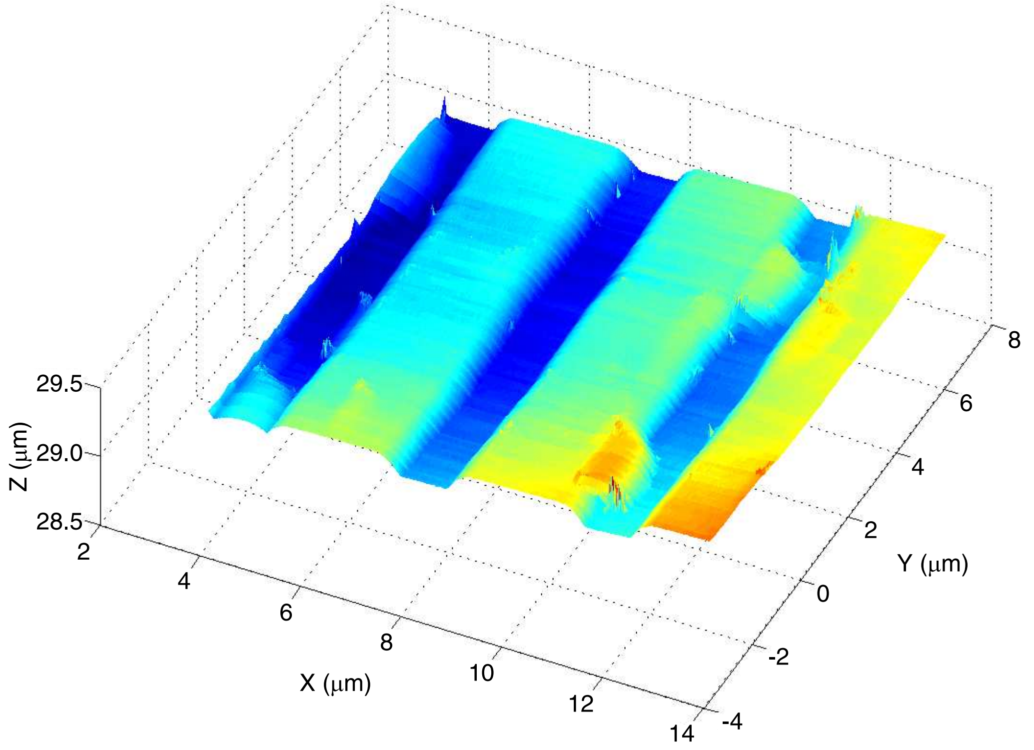

Figure 6-14: Three-dimensional image of the silicon calibration grating, shown with a continuous surface. The image data was acquired by David Otten, and the plot was generated with a MATLAB script written by Katherine Lilienkamp.

sets of image data for the calibration grating sample. The plot shown in Figure 6-14 represents the best three-dimensional image of the grating yet taken with the microscope. For this plot, we received help from Katherine Lilienkamp, another graduate student in our lab, who wrote a MATLAB script to construct a continuous surface from the AFM's position data. A plan view of the same data is shown in Figure 6-15. The image contains several bumps, which apparently are real features of the sample surface. We suspect these bumps represent specks of dirt that have accumulated on the grating surface over time.

Figures 6-14 and 6-15 may be compared to the images shown in Figures 6-16 and 6-17, respectively. These images were taken using MIT's Analytical Shared Ex-

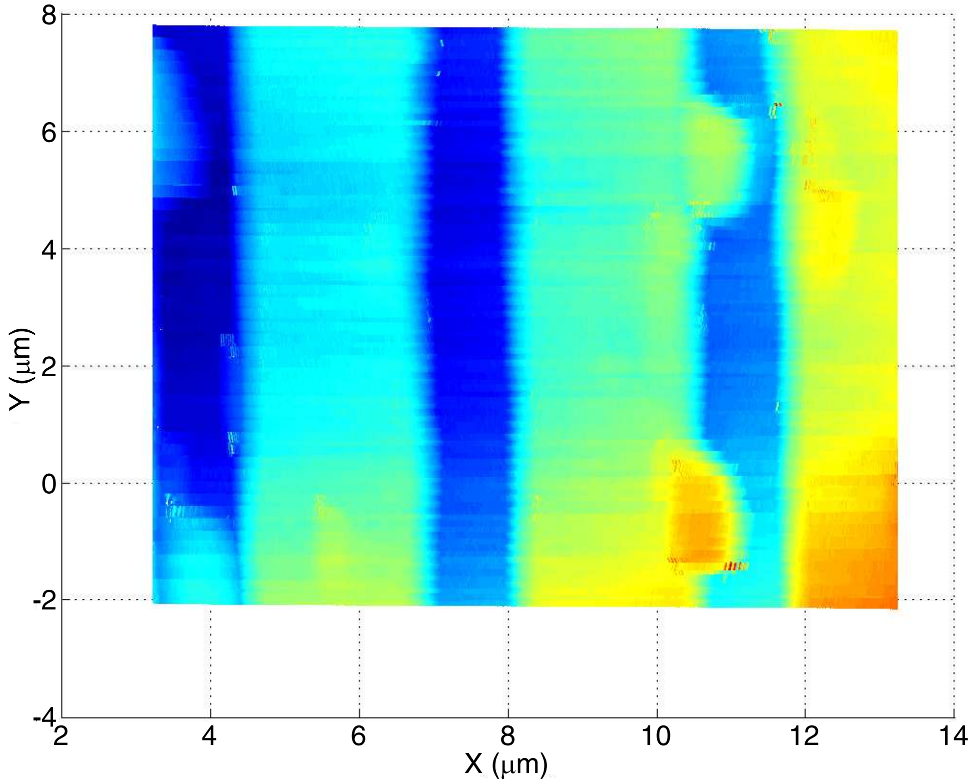

Figure 6-15: A plan view of the grating image shown in Figure 6-14.

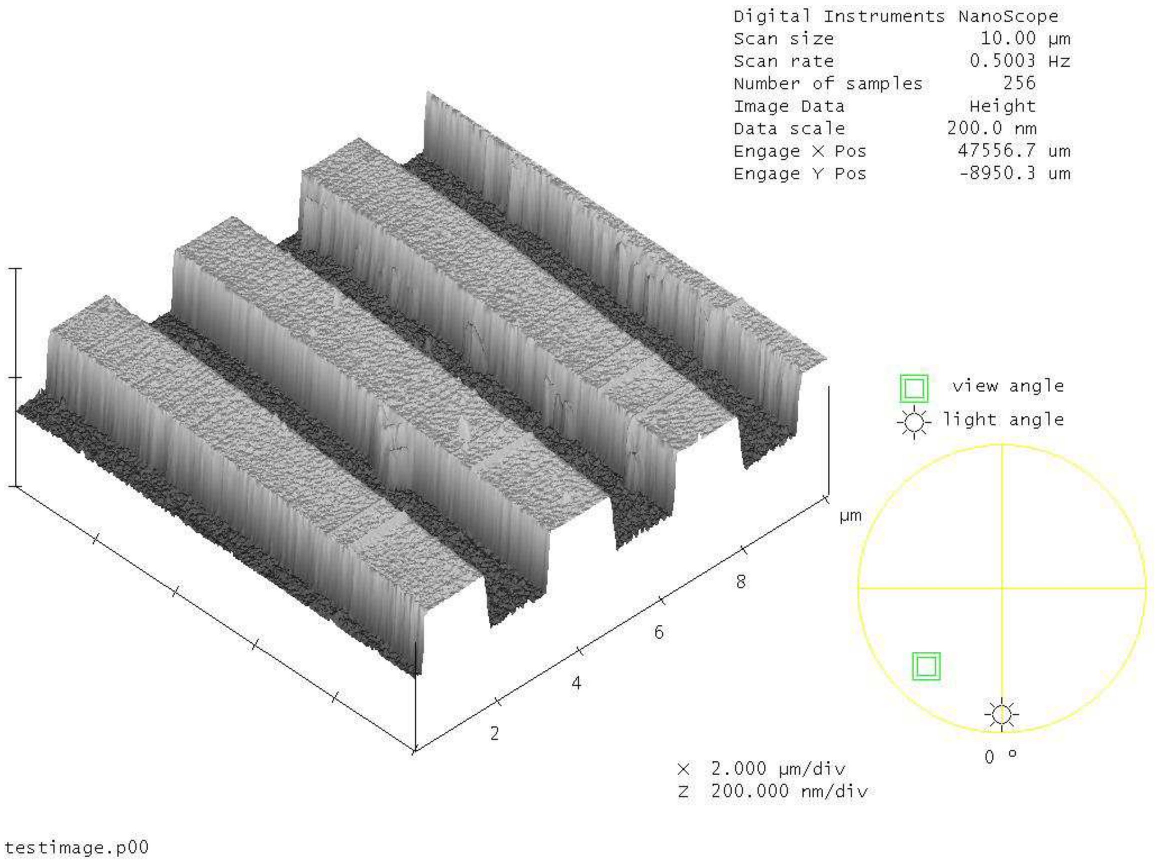

Figure 6-16: Image of the silicon grating surface, taken with a Digital Instruments/Veeco FEI Dimension 3000 SPM head — isometric view.

perimental Facilities, with assistance from Elisabeth Shaw. She used a Digital Instruments/Veeco FEI Dimension 3000 SPM head, which was operated in the tapping mode AFM configuration, to image the TGZ02 silicon grating. The image data indicates a 103.3 nm peak-to-peak amplitude, which is within the range specified by the grating's manufacturer. These measurements were conducted in a non-temperature controlled and non-clean room environment, but with the head surrounded by an enclosure. Based on these images, our metrological AFM clearly does not yet perform to the level of a commercial system, but the similarities between the two sets of data are still quite promising.

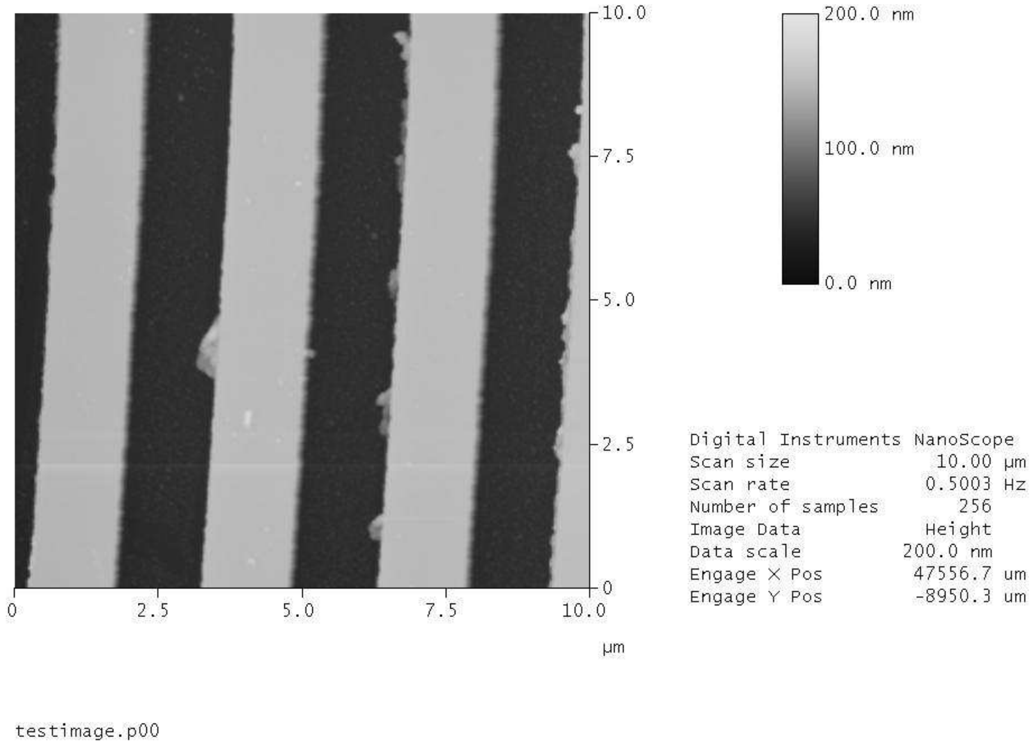

```
Digital Instruments NanoScope
Scan size                  10.00 µm
Scan rate                 0.5003 Hz
Number of samples            256
Image Data                Height
Data scale               200.0 nm
Engage X Pos           47556.7 um
Engage Y Pos           -8950.3 um
```

Figure 6-17: Image of the silicon grating surface, taken with a Digital Instruments/Veeco FEI Dimension 3000 SPM head — plan view.

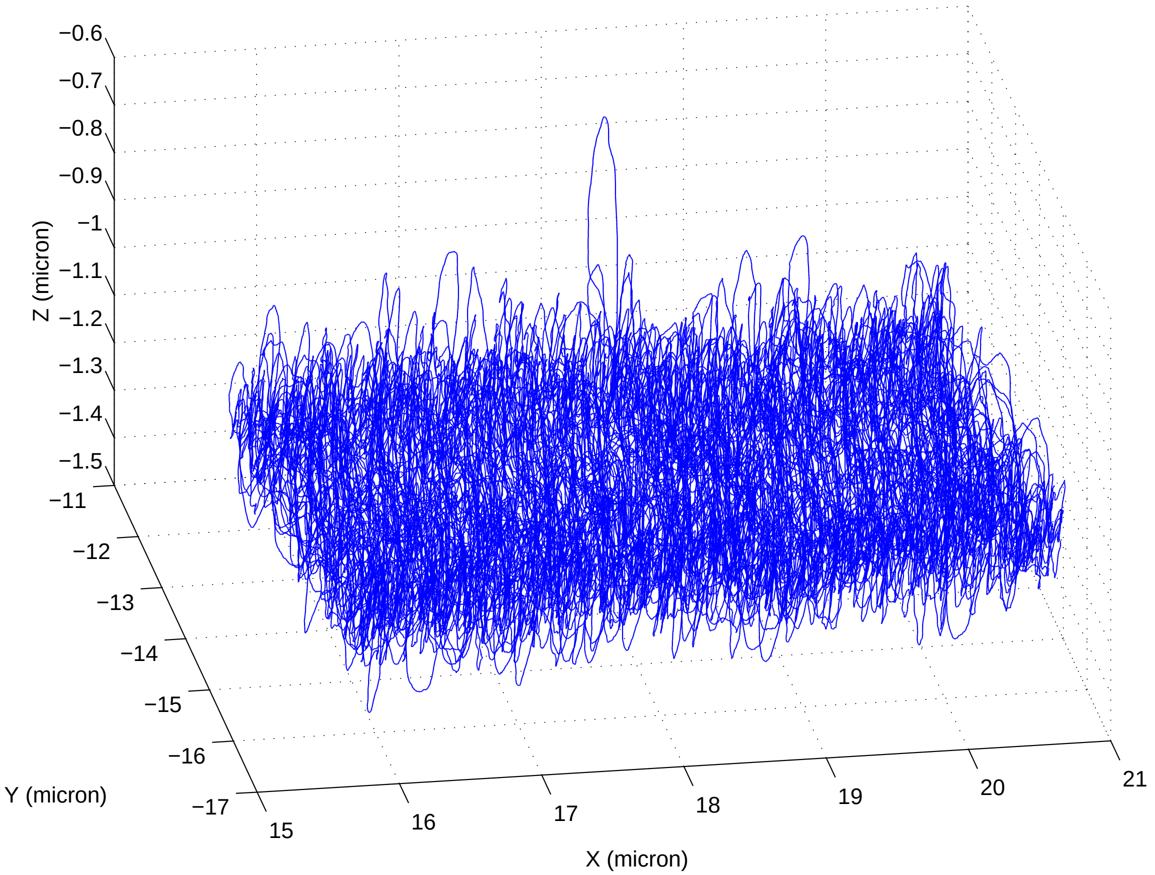

Figure 6-18: Three-dimensional image of the steel gauge block, taken with the metrological AFM. The sample topography is buried in noise, as expected.

6.2.2 Steel Gauge Block

Figure 6-18 shows a three-dimensional image of the steel gauge block, taken with the metrological AFM. Significant noise is again observed in Z because of the relatively low sensitivity of the tuning fork proximity sensor when engaged on this sample. As expected, based on the behavior observed in the X linescan of Figure 6-7, the three-dimensional image data is also fairly noisy in X, again since the tube scanner's motion along this axis is coupled to the common control voltage commanded by the axial height regulator. The noise prevents us from making conclusive statements about the AFM's performance, beyond what has already been deduced from the images of the silicon calibration grating.

6.3 Summary

This chapter detailed the metrological AFM's experimental results. Data from three linescans of a squarewave silicon calibration grating were presented. In each of these images, the grating's 100 nm-scale ridges are clearly resolved. However, several image errors are also observed in each of these plots. For example, the measured grating dimensions are significantly larger than the values quoted by the manufacturer. This problem most likely indicates that the AFM's probe position sensors are poorly calibrated for the microscope's cone-shaped target. The data also includes several examples of imaged surface details that do not appear to be a real part of the sample topography, such as the bumps between the ridges in Figure 6-4. Generally, we believe these errors may be attributed to either poor sharpness of the fiber tip or dirt buildup in the scan region. The curvature observed in Figure 6-2 is another significant error, though we are presently unsure of its origin. We have conjectured that the curvature either results from nonlinearities in the sensors' measurements due to the target's curved surface or from measurement errors related to the tube scanner's finite radius of curvature for non-zero lateral displacements. All of these image errors will be addressed in future work with the metrological AFM.

Two linescans taken of the flat surface of a steel gauge block were presented, as well. We are unable to extract much useful information about the AFM's imaging capabilities from this data, since the measured Z positioning noise is more than an order of magnitude larger than the noise measured in the grating linescan data.

This chapter also included several three-dimensional images captured with the metrological AFM. As with the linescans, the three-dimensional grating images indicate that the system can readily detect the sample's 100 nm-scale steps, though again some errors are observed in the data. The metrological AFM's images were also compared to those acquired by a commercial AFM system. This comparison clearly shows that our AFM is not yet capable of reaching the performance standards set by commercial systems, though the similarities in the two sets of data are promising for the future success of our system. Finally, one of the metrological AFM's images of the gauge block was shown, but this data can provide no useful insight, since the sample topography is obscured by noise.

The next chapter provides a summary of the metrological AFM project and points toward possible follow-on work.

Chapter 7

Conclusions and Suggestions

7.1 Summary

This thesis described a metrological atomic force microscope that we designed, built, and tested, as a prototype for a similar microscope that will later be integrated with the Sub-Atomic Measuring Machine. We began this project by developing an open-loop prototype AFM, to gain practical experience with some of its mechanical and electrical components. After some successful experimentation with this hardware, we started work on the mechanical design of the metrological AFM. The resulting design utilizes a set of capacitance sensors aimed at a cone-shaped target at the base of a piezoelectric tube scanner. The sensors are aligned with their measurement axes intersecting at the probe tip — a tapered optical fiber glued to one side of a quartz tuning fork. This novel sensor configuration nominally results in zero Abbe offset error, an important consideration for optimizing the ultimate accuracy achievable with this AFM design.

After the design, fabrication, and assembly of the metrological AFM's hardware, we focused on developing a strategy for controlling the probe's motion. For the AFM's lateral scanning system — which dictates the motion of the probe tip parallel to the sample plane — we implemented integral control with a high-frequency pole. This system has measured -3 dB closed-loop bandwidths of 189 Hz and 191 Hz in X and Y, respectively. We also closed the loop on the microscope's axial height regulation system, which adjusts the length of the tube scanner to maintain a fixed probe-sample separation as the probe scans over the surface. Several control strategies were tried for the height regulator, which resulted in a -3 dB closed-loop bandwidth as high as 184 Hz. However, the measured plant dynamics contained significant variability, which complicated our attempts to characterize and control the system.

The AFM has acquired image data — both linescans and three-dimensional images — for a silicon calibration grating and a steel gauge block. The grating images demonstrate that the AFM can readily resolve the grating's 100 nm-scale rectangular ridges. From the grating data, we have measured Z positioning noise of approximately 3 nm RMS. The gauge block data contains much more noise — about 50 nm RMS in one scan — which results from the considerable reduction in the tuning fork proximity sensor's sensitivity when engaged on this surface.

7.2 Conclusions

Overall, we believe the design of our metrological AFM provides a solid framework for the development of a high-accuracy SAMM AFM. The novel configuration of the microscope's capacitance sensors provides a distinct advantage over alternative designs where large Abbe offsets are introduced. Given the preliminary images of the calibration grating taken with this system, we feel that the project has shown good initial success.

However, we did experience some difficulties while testing the AFM, particularly in our experience with the tuning fork proximity sensor. Its dynamic behavior varied significantly on a day-to-day, probe-to-probe, and sample-to-sample basis, requiring large amounts of time be devoted to the repetitive tasks of system identification and controller adjustment. In the future development of this microscope, some effort should be expended on finding and eliminating the sources of this variability. Perhaps the proximity sensor system would be more stable if operated in a self-excited mode, rather than with the fixed frequency signal generator excitation currently used.

While the AFM has produced some clean images of the calibration grating, the system has demonstrated a relatively low degree of repeatability. Much of the data contains unexpected image artifacts, which in many cases seem likely to be related to poor sharpness of the tip or dirt buildup on the tip and/or the sample. However, we do not believe that these artifacts result from any fundamental flaws in the microscope's design, so we expect that follow-on work will succeed in eliminating them from future images taken with the system.

The gauge block images contain far too much noise to provide significant insight into the AFM's performance. The noise is a direct result of the tuning fork probe's poor sensitivity when engaged on this sample, where the reduced sensitivity is likely caused by a thin oil film covering the surface. In a future experiment, one could simply clean the top of the block with a solvent, then try to re-image the sample. Alternatively, one could image an optical flat, which can be purchased having the desired surface flatness. A low-noise image of such a surface could provide valuable information on several aspects of the AFM — total system noise, image curvature, and drift, for example — so this experiment is certainly worth pursuing.

Also, while the probe assembly technique used for the metrological AFM is easier to use and more reliable than the one employed for the open-loop prototype AFM, it still leaves much to be desired. Most importantly, the present setup does not provide any direct means for measuring the distance from the fiber probe to the cone-shaped endpiece, so the probe tip cannot be reliably located at the zero-Abbe offset position. Any future probe assembly fixture should provide a clear reference for mounting the tip at the desired point.

7.3 Suggestions for Future Work

While we are generally pleased with the metrological AFM's demonstrated performance, we undoubtedly have not yet realized the microscope's full potential. This section provides some ideas for improving various aspects of the imaging system. Also, since this research is part of a long-term effort to equip the SAMM with a similar AFM, we offer a few suggestions for the next-generation microscope's design.

7.3.1 Minimizing Environmental Variability and Disturbances

Much of the variability and noise in the system likely could be reduced simply by providing better environmental control of the air in the immediate vicinity of the microscope. For the best control of the imaging conditions, future experiments with the AFM head should take place in a clean room with a tightly controlled temperature. However, in the short term, it may be more feasible to add a small enclosure around the AFM head, such as the one used with the Digital Instruments/Veeco FEI SPM head mentioned in section 6.2.1. This structure would provide thermal insulation, prevent air currents from entering the scan region, and reduce the opportunity for contamination of the probe tip and the sample surface.

The imaging system might also benefit from better vibration isolation than what is currently employed. At present, the AFM's base plate is bolted to a small optical table, whose three pressurized legs rest on the top of a workbench. This setup is clearly not optimal for protecting the AFM head from mechanical disturbances. We would prefer to have the head mounted on a more massive table with a set of vibration isolators coupled directly to the floor.

7.3.2 Changes to the Probe Tip

The microscope's performance could also be improved through a more thorough investigation of the options available for the probe tip. For all of the metrological AFM experiments described in this thesis, the tips were taken from a set of optical fibers provided to us by Dr. Chunhai Wang, who at the time was at UNCC conducting post-doctoral research on the SAMM. He used the heating-and-pulling method mentioned in section 2.1.2 to produce these tips. While we had some success with these fibers, they likely are not as sharp as we would prefer. Also, we made no attempt to characterize the ideal tip geometry, beyond noting a tendency for long, thin fibers to buckle, as mentioned in section 5.3.1. Since the shape and size of the probe tip clearly play a major role in an AFM's resolution, some additional thought should probably be devoted to this issue.

Likewise, the heating-and-pulling method represents a relatively old approach for making SPM fiber tips. The chemical etching technique detailed in [17] likely would prove a more dependable, simpler method for producing tips in the future, though with the added risk associated with handling hydrofluoric acid. Better control of the tip geometry — as well as of the tip mounting process — would help greatly in making the metrological AFM a more reliable imaging device in the future.

Taking a broader view, the fiber tip may well be an inferior solution for this microscope for probing sample surfaces. In fact, much of the motivation for adopting this approach stems from our early thoughts of developing a near-field scanning optical microscope (NSOM), rather than an AFM, to install on the SAMM. If we had built an NSOM, the optical fiber would have provided a convenient light path, as well as a sub-wavelength aperture, but these concerns are not relevant in atomic force microscopy. Other groups have employed alternative tip materials and form factors for quartz tuning fork sensors used in AFMs [14, 30, 35, 13]. Another intriguing approach was briefly investigated by the Grober lab at Yale: etching a tip directly into the tine of the quartz tuning fork.

7.3.3 New Cone-Shaped Endpiece

We have also discussed the possibility of building a new cone-shaped target for the metrological AFM, which would likely involve new methods for mounting the quartz tuning fork and for aligning and mounting the probe tips. Based on a suggestion from Dr. Hans Danzebrink — from the Physikalisch-Technische Bundesanstalt in Germany — the tuning fork probe would likely be operated in the tapping mode in this design. This mode apparently results in better behavior of the proximity sensor, as compared to the shear mode that was used for all of the experiments mentioned in this thesis.

Improvements might also be made in the way that the tuning fork probes are mounted in the conic endpiece. For example, one could remove the tuning fork from its can, then mount the base or side of the fork in some type of receptacle underneath the endpiece. Other groups have demonstrated success with similar direct mounting schemes [14, 30]. This approach potentially allows a more compact probe design, while eliminating possible alignment errors caused by the relatively loose tolerance on the tuning fork's position in its can.

7.3.4 Sensing, Actuation, and Control

A number of non-mechanical aspects of the metrological AFM could also be improved. For example, one could examine ways for reducing noise in the tuning fork circuit, a subject to which we did not devote much energy but which directly affects the overall performance of the imaging system. Also, as discussed with Dr. Danzebrink, the tuning fork sensor may perform better in its 'self-excited' mode, where its output signal is phase-shifted by 90°, then fed back to the fork to excite its first mechanical resonance. With this technique, the tuning fork automatically tracks its resonance, resulting in reduced sensitivity to temperature fluctuations. This mode would likely

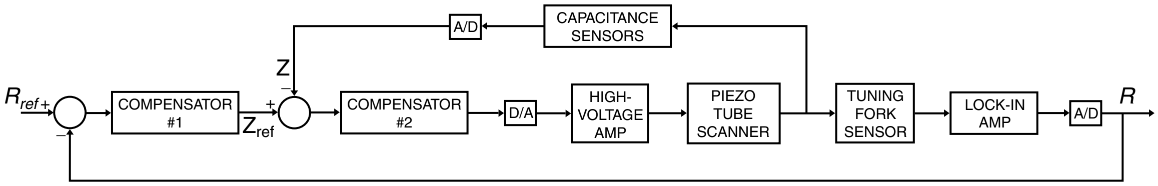

Figure 7-1: Block diagram of the axial height regulator, with inner-loop compensation.

be implemented with a phase-locked loop — a control strategy that several other research groups in this field have already employed [13, 1].

Other improvements could be made to the AFM's control strategy. With reference to the block diagram in Figure 7-1, one could implement inner-loop compensation within the axial height regulator, feeding back the capacitance sensors' Z measurement to more directly compensate for the piezoelectric tube scanner's nonlinearities. Also, the bandwidth of the lateral scanning system could be increased, with phase stabilization of the scanner assembly's 1.03 kHz bending mode resonance.

Our piezoelectric tube scanner can withstand higher drive voltages than were supplied during our experiments. Simply by increasing the gain of the high-voltage amplifier, one could improve the probe's range of motion considerably. However, increasing the range in this way might lead to larger positioning noise, as well.

Finally, we expect that the AFM's noise level and accuracy would both benefit from including all six capacitance sensor signals in the calculation of the probe's position. Presently, only three of the signals are used.

7.3.5 The SAMM AFM

The work described in this thesis will ultimately lead to the development of a metrological AFM for the SAMM stage. We can foresee several changes that should be made to the microscope's design to help achieve the best performance from this next-generation imaging system. As mentioned in section 3.1.1, we selected aluminum for most of the parts in our AFM head, primarily because of its low cost and ease of machining. However, this material has a high coefficient of thermal expansion, which can contribute to relatively large measurement errors when subjected to temperature fluctuations. Significant portions of the SAMM AFM likely should be made from a material with a much lower expansion coefficient — such as Invar or Zerodur — to reduce the effect of this error source. Also, the microscope will benefit from the relatively well-controlled environment of the UNCC metrology laboratory where the SAMM stage is located. This lab maintains temperature control of about ±0.1°C.

The SAMM AFM head will need to be significantly smaller than the one we have built, to fit within the relatively tight packaging constraints of both the SPM mounting hole in the stage's metrology head and the recessed sample holder in the reference block. The capacitance sensor geometry represents the limiting factor on how small the microscope can be built. We investigated using small 'button sensors' for the prototype metrological AFM, and these may prove to be the final solution for the SAMM AFM. However, the circuit board sensor idea discussed briefly in section 3.1.2 — where a set of sensor electrodes are cut into a thin sheet of circuit board — may provide a more elegant solution to this problem.

The capacitance sensors in our metrological AFM are not properly calibrated for the scanner assembly's target endpiece, as shown by the scale-factor errors in the microscope's grating images. The SAMM stage provides the means for in situ calibration of the sensors in the next-generation AFM. This calibration could be accomplished by first having the AFM find a feature on a sample mounted on the stage. The stage could then translate the sample to a new position, after which the AFM would again locate the feature. One could then adjust the sensors' calibration constants so the translation of the feature measured by the AFM equals the value provided by the SAMM stage's metrology.

We have also considered a new strategy for measuring calibration crosses with the SAMM AFM, using what we term a 'synthetic slit' scanning mode. A schematic

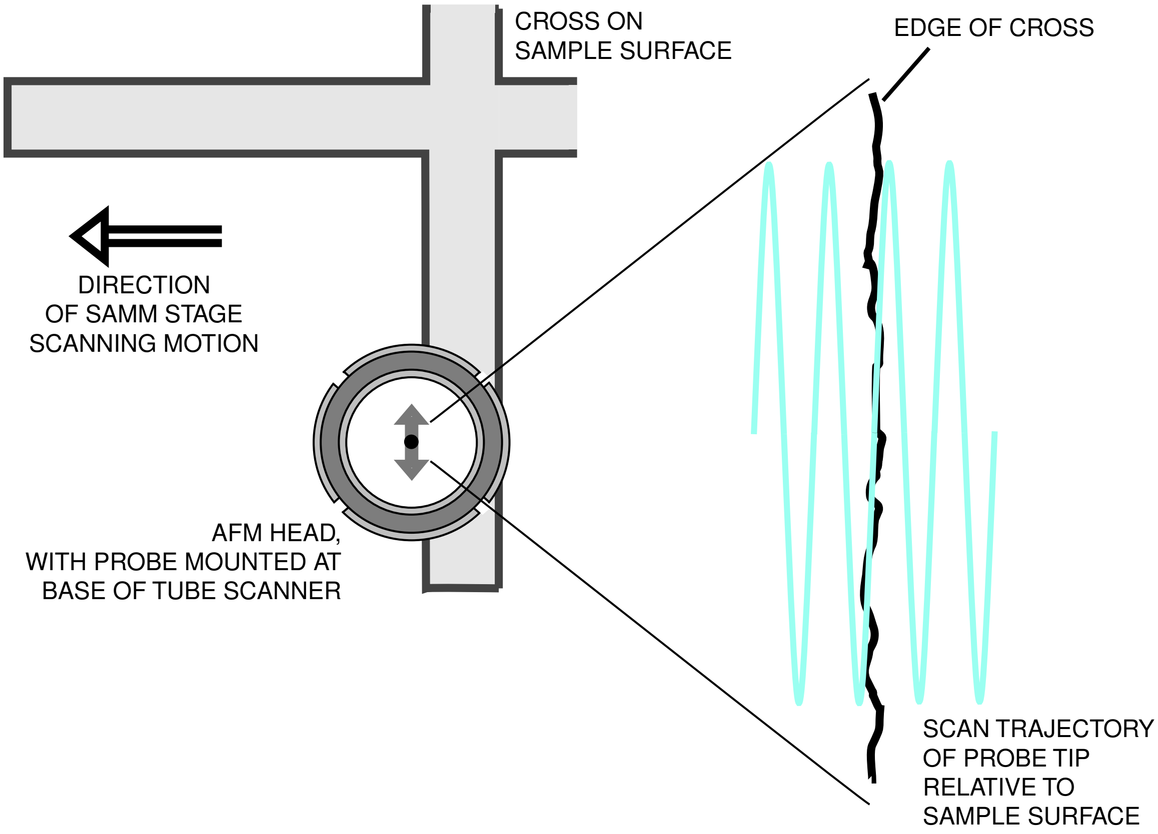

Figure 7-2: Schematic drawing of the proposed synthetic slit scanning mode. The probe oscillates rapidly in the direction perpendicular to the SAMM stage's slow scanning motion, to provide spatial filtering of the cross features.

drawing of this mode is shown in Figure 7-2. In this configuration, the SAMM stage would slowly scan the cross-pattern sample laterally, while the AFM probe would oscillate at a relatively high frequency along the lateral direction normal to the stage's direction of motion. We envision this scanning mode as a form of AFM spatial filtering, functionally similar to the slit-based optical microscope that was developed by Wang and Hocken and used in the SAMM stage to measure the locations of crosses to a repeatability on the order of 1 nm.

Overall, we are happy with the outcome of the research described in this thesis. We are encouraged by the metrological AFM's initial results and believe that planned follow-on work will succeed in demonstrating the utility of this microscope's novel metrology configuration.

Appendix A

Mechanical Drawings

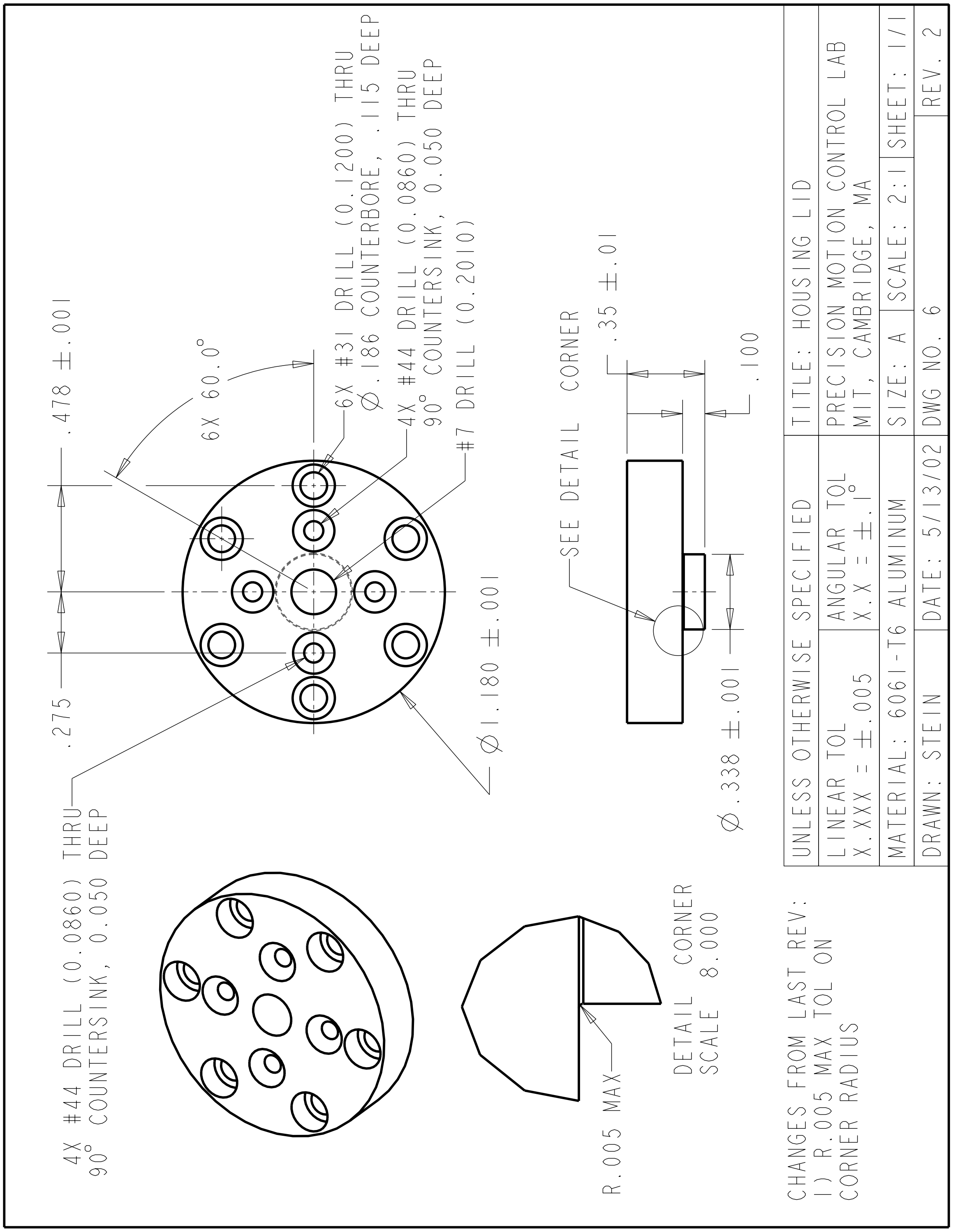

Figure A-1: Housing cap mechanical drawing.

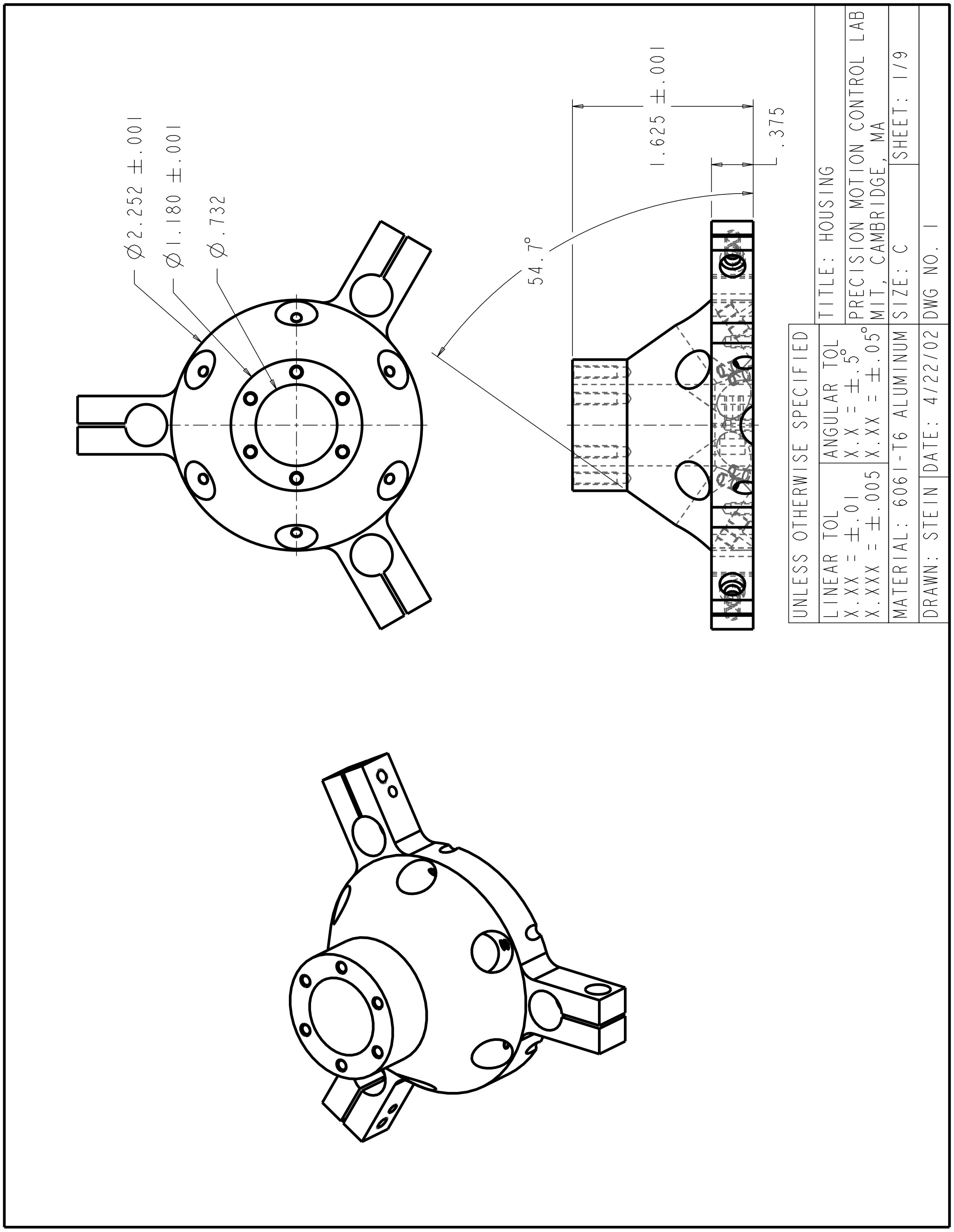

Figure A-2: Housing body mechanical drawing, sheet 1.

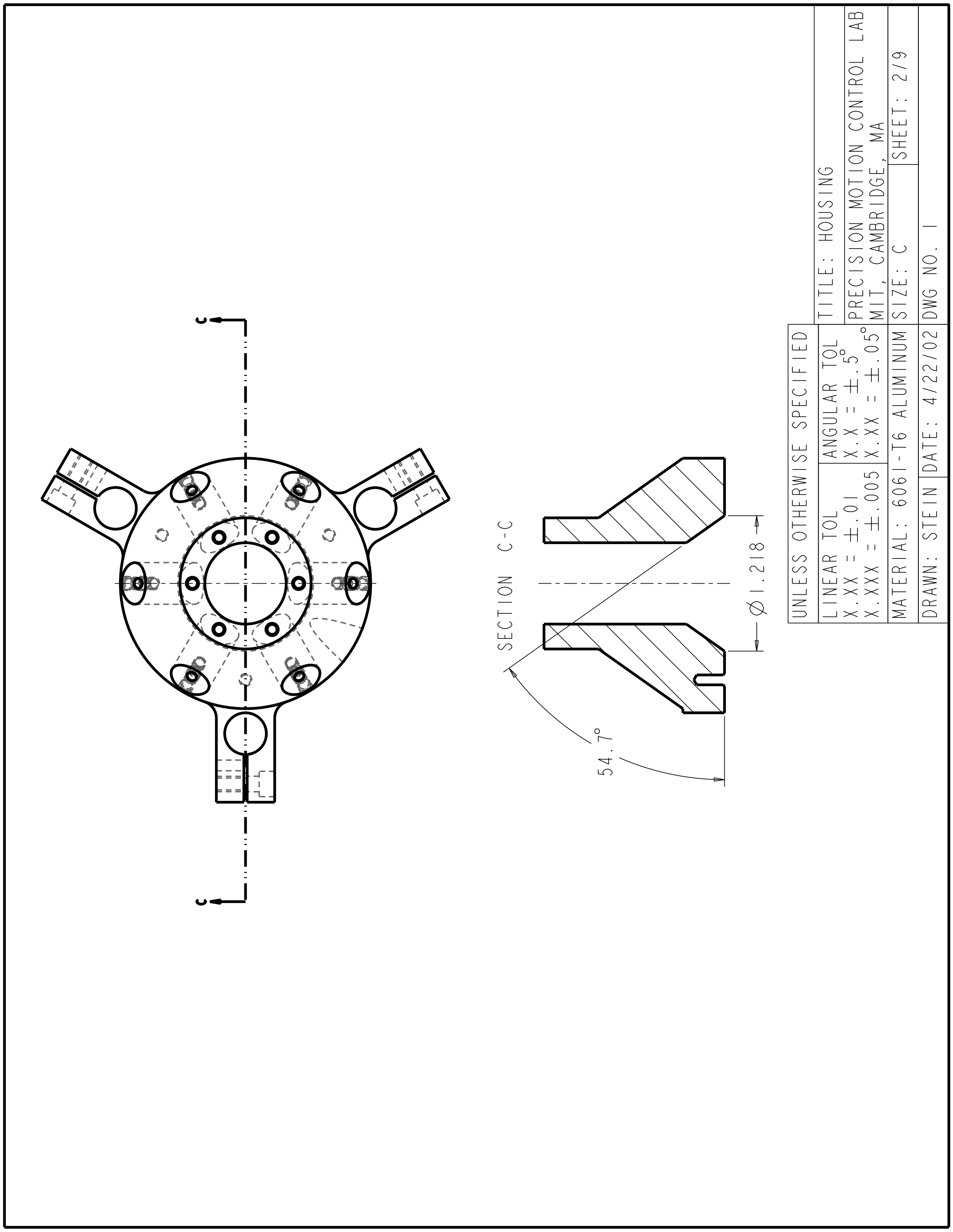

Figure A-3: Housing body mechanical drawing, sheet 2.

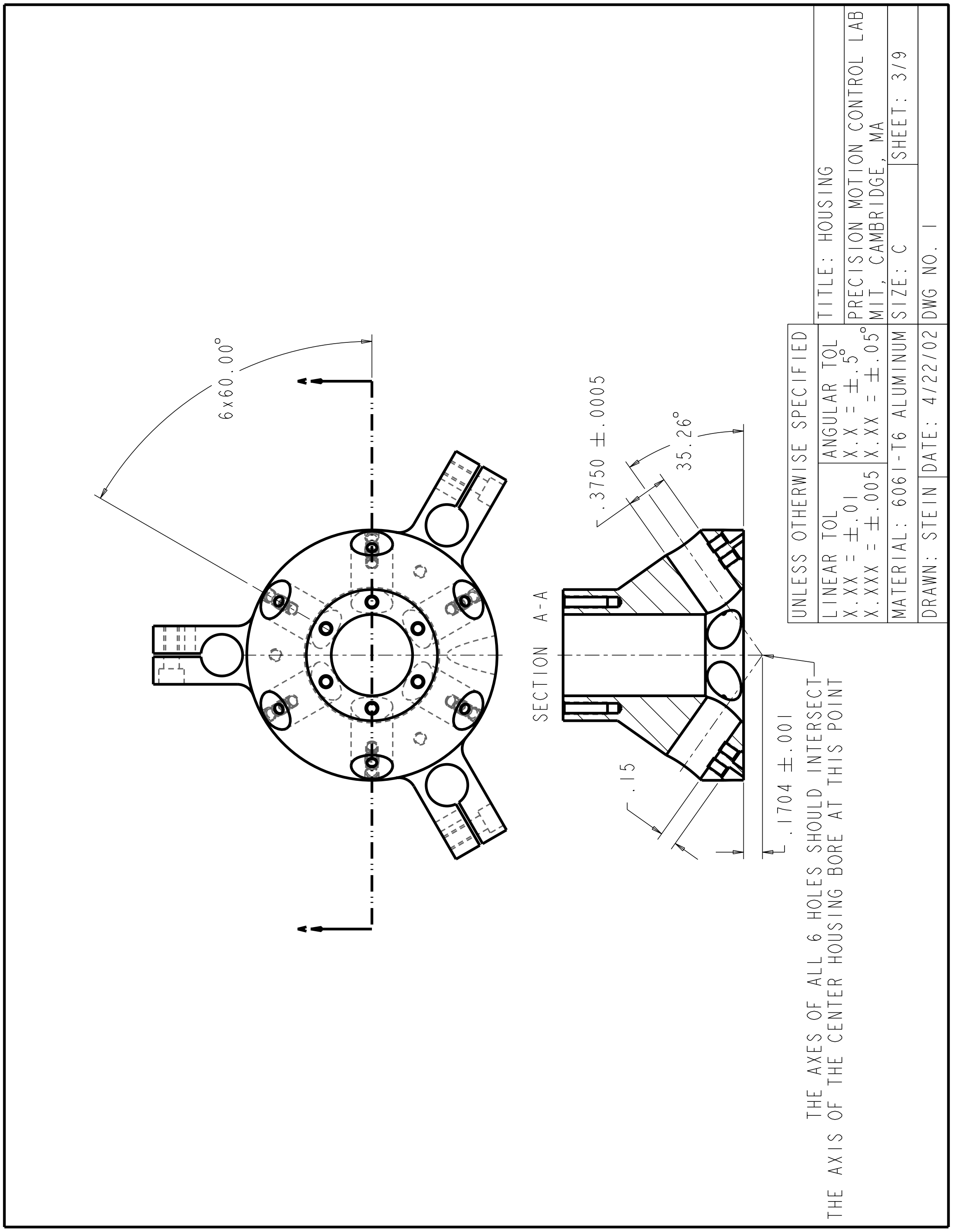

Figure A-4: Housing body mechanical drawing, sheet 3.

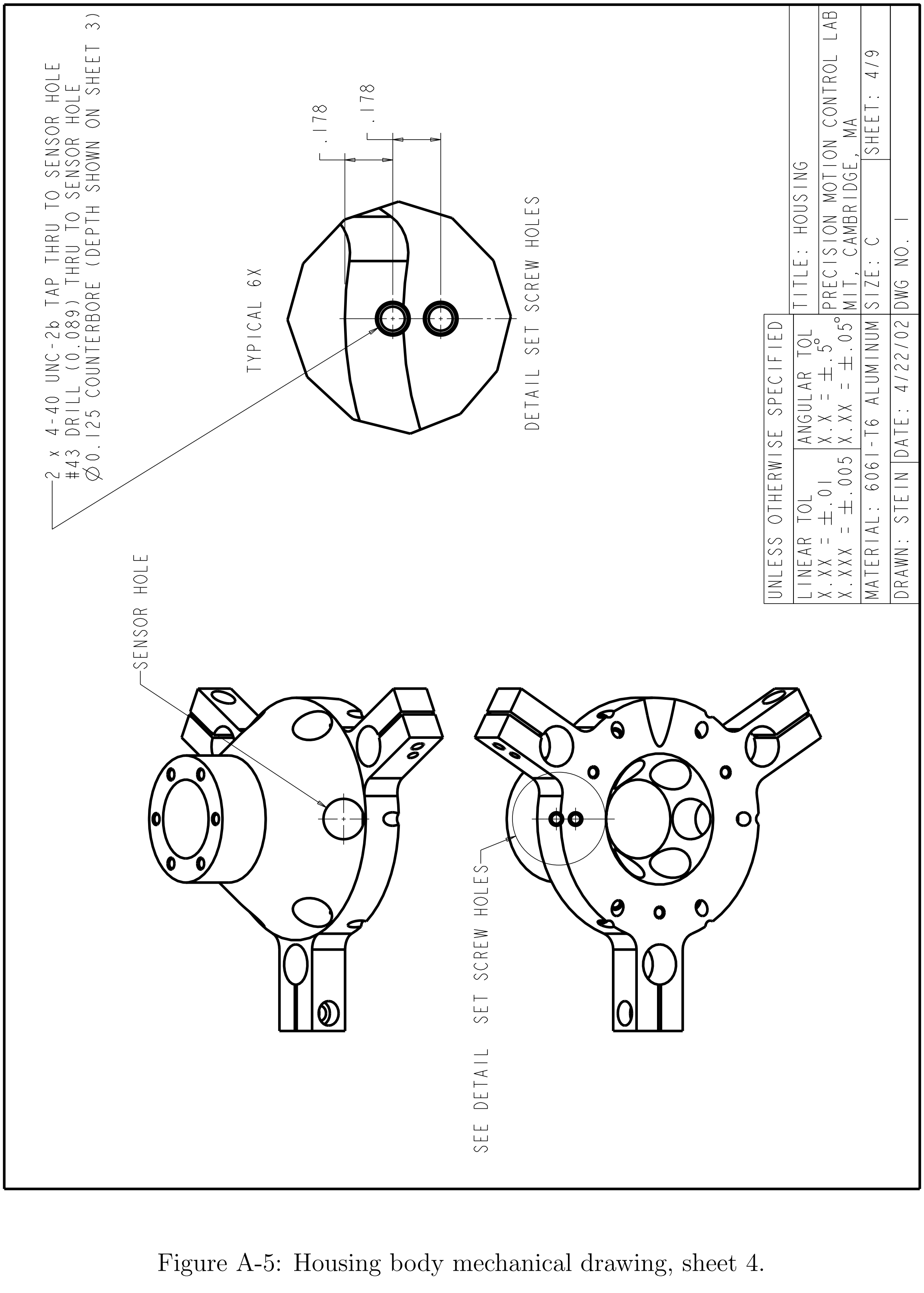

Figure A-5: Housing body mechanical drawing, sheet 4.

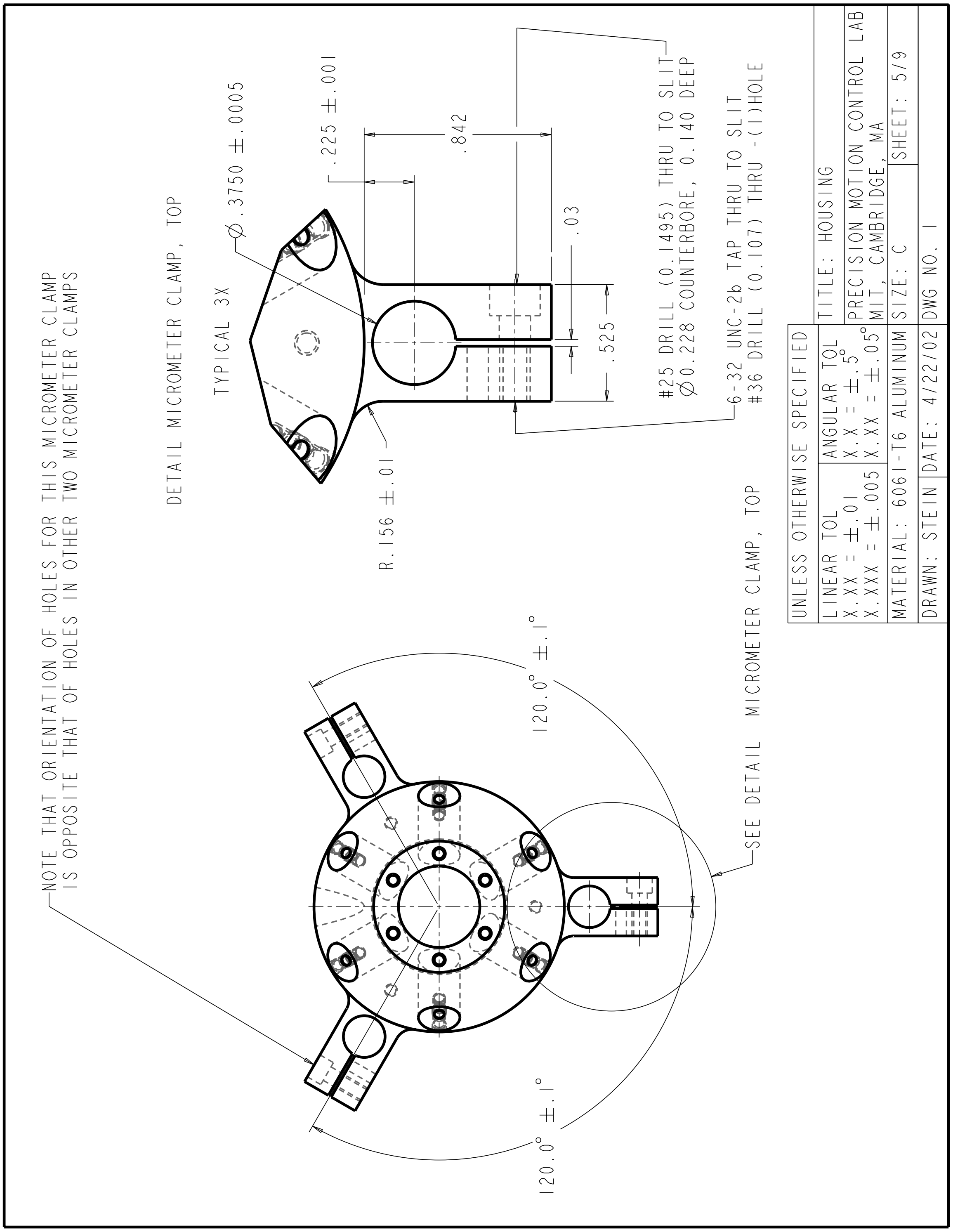

Figure A-6: Housing body mechanical drawing, sheet 5.

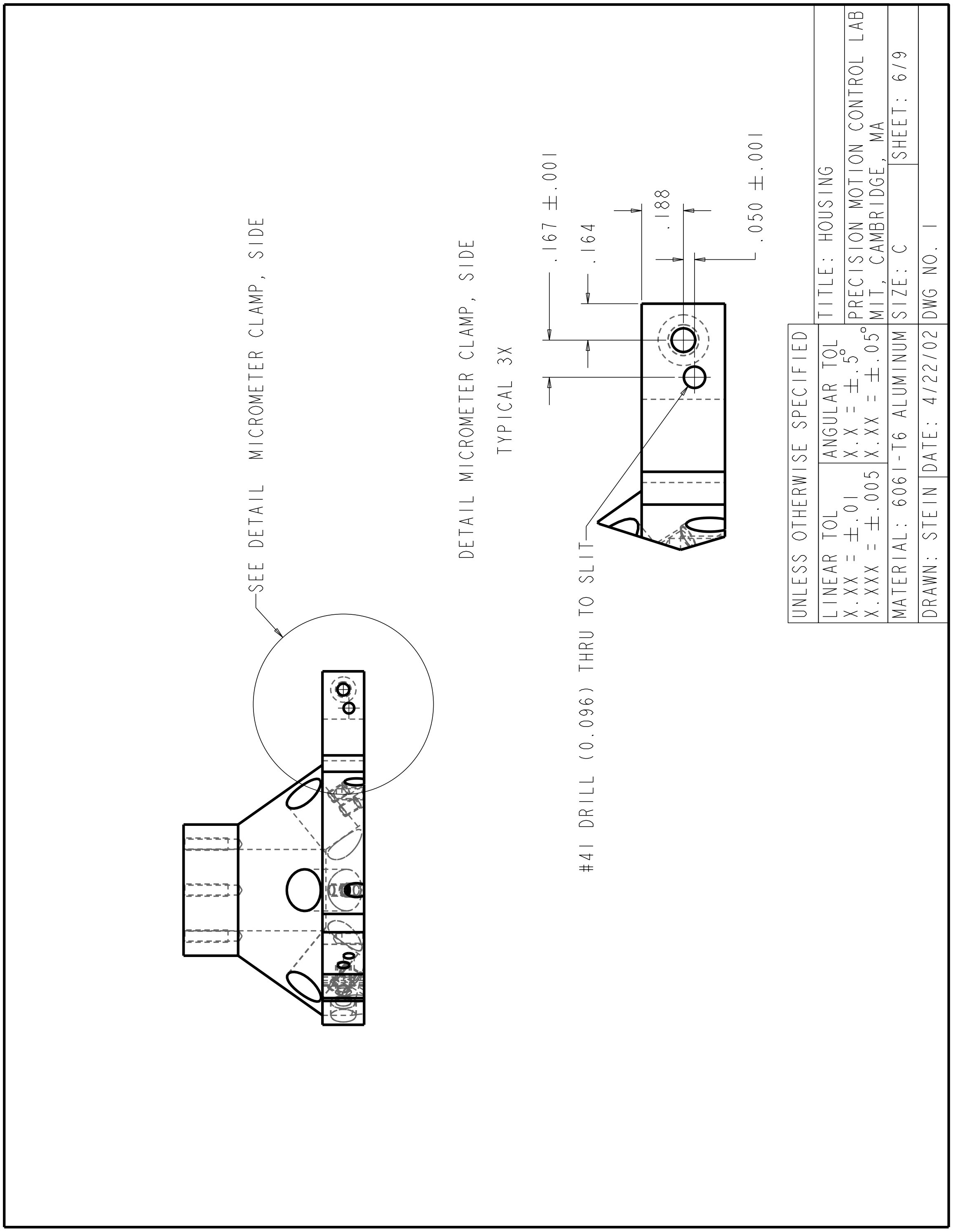

Figure A-7: Housing body mechanical drawing, sheet 6.

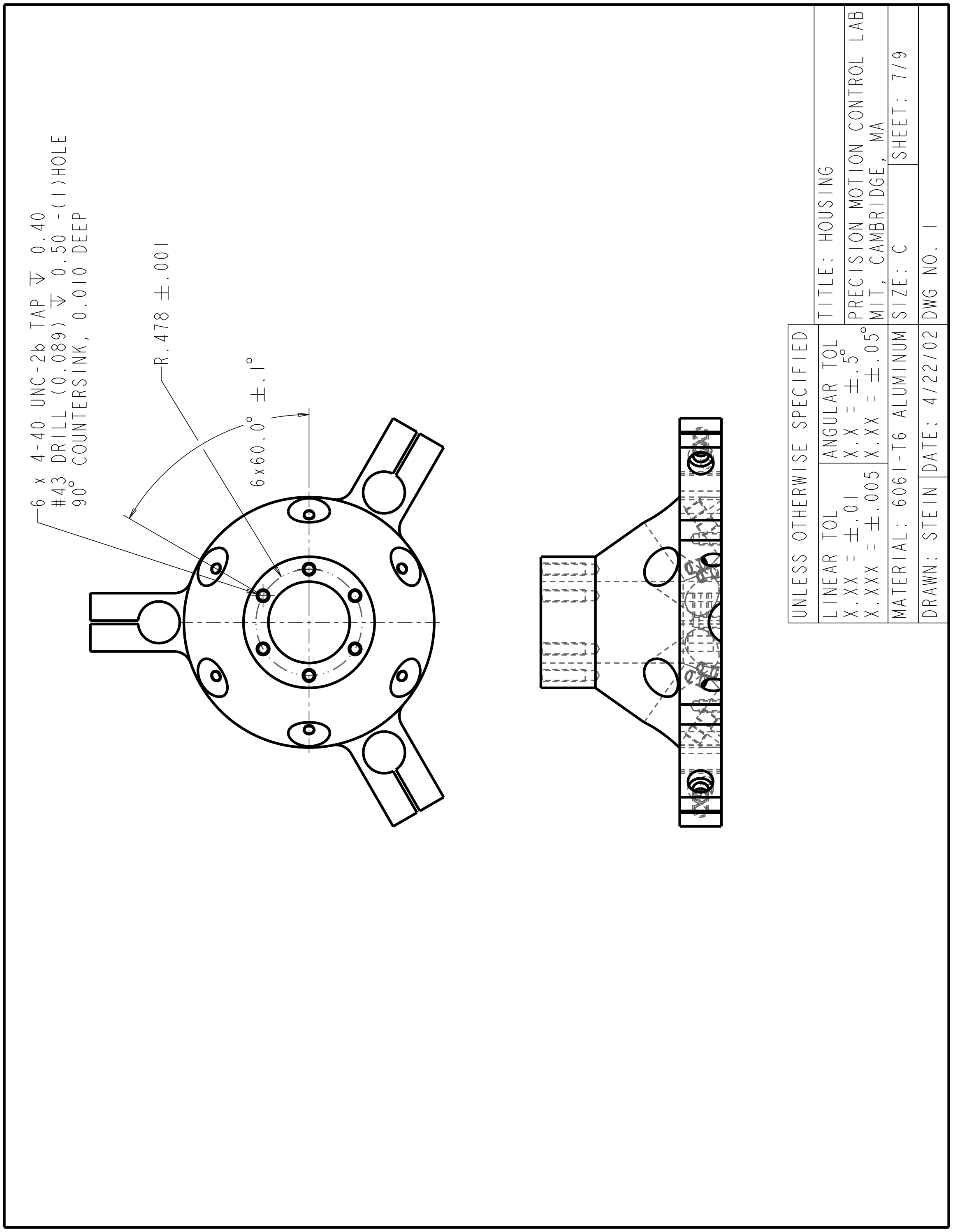

Figure A-8: Housing body mechanical drawing, sheet 7.

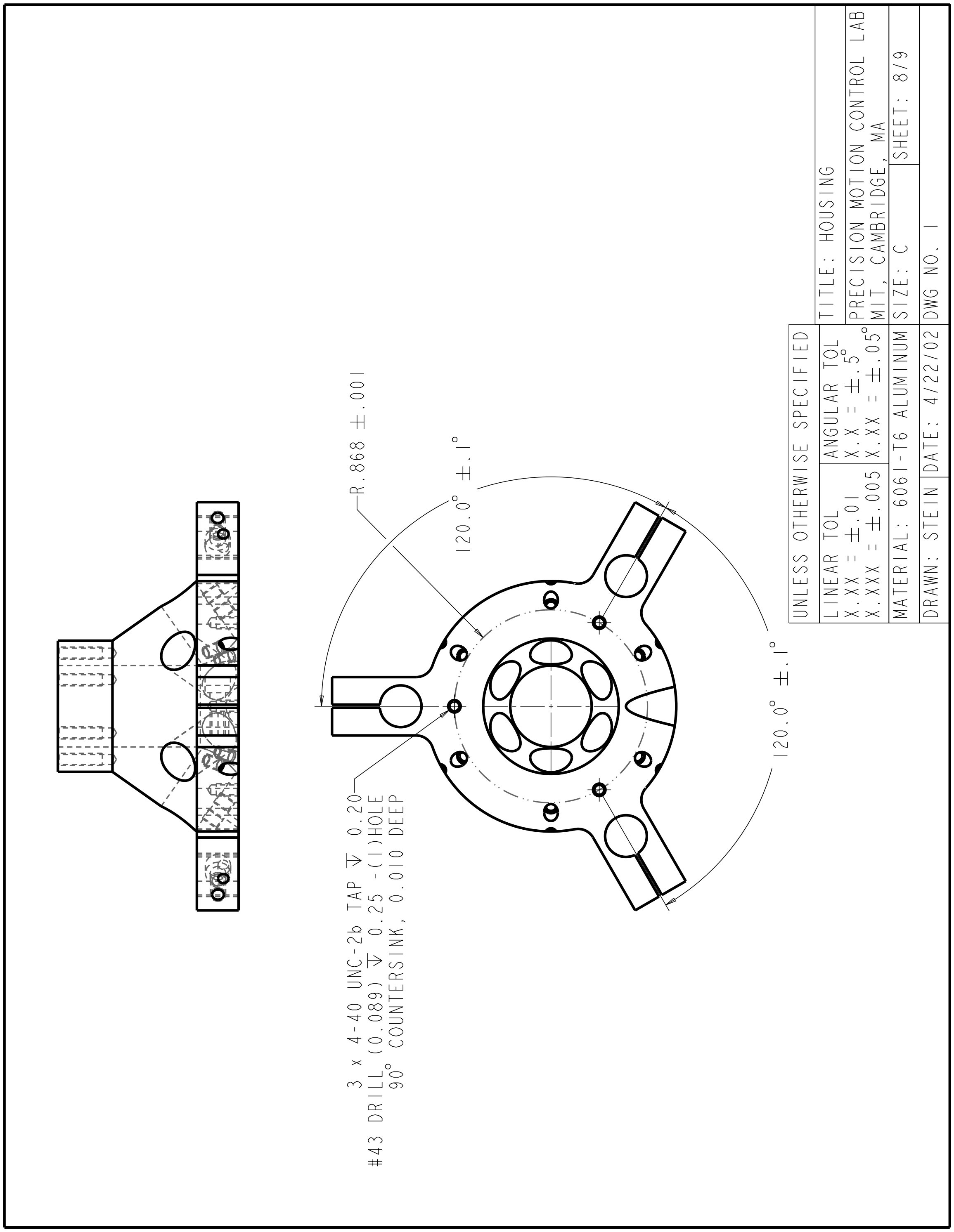

Figure A-9: Housing body mechanical drawing, sheet 8.

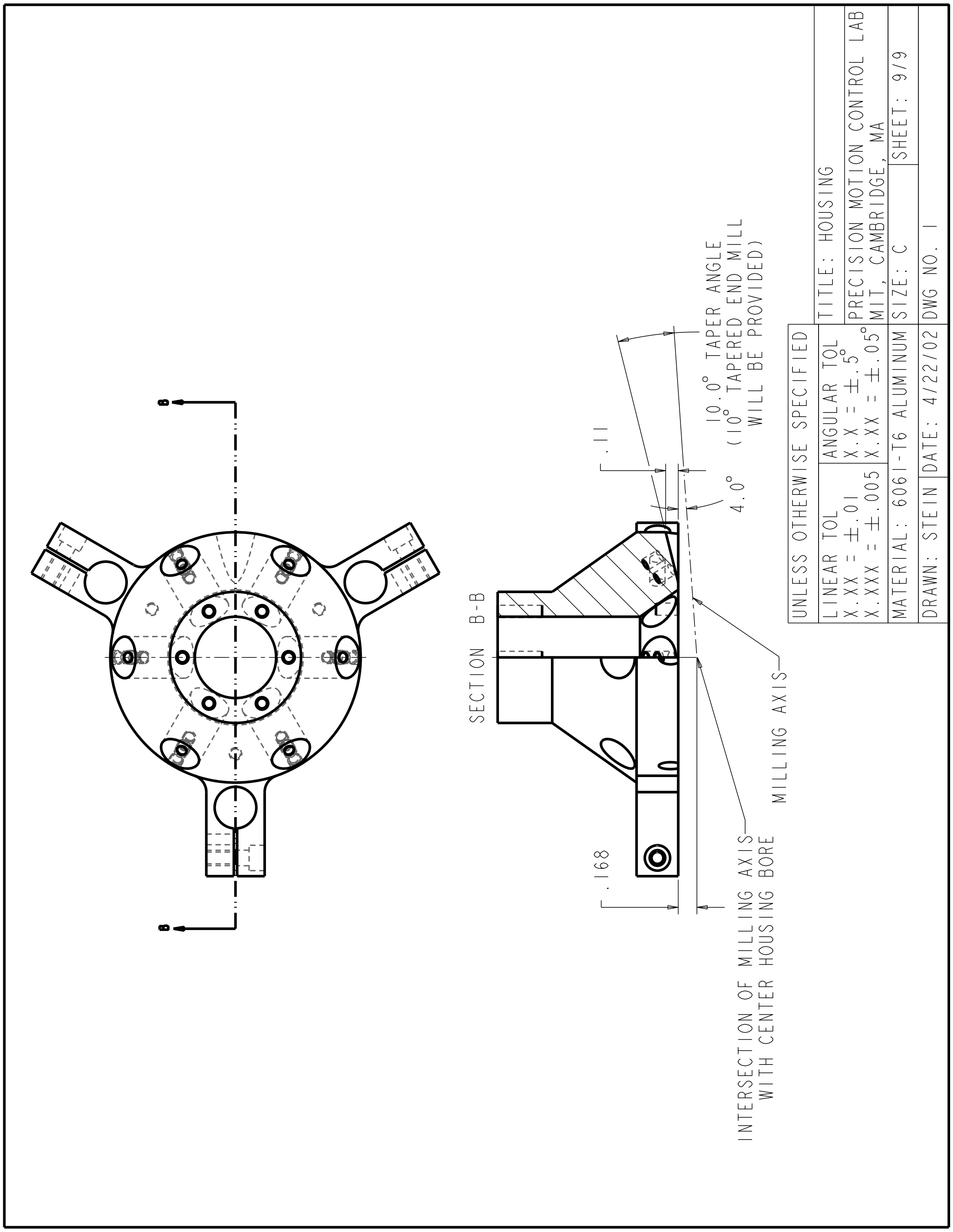

Figure A-10: Housing body mechanical drawing, sheet 9.

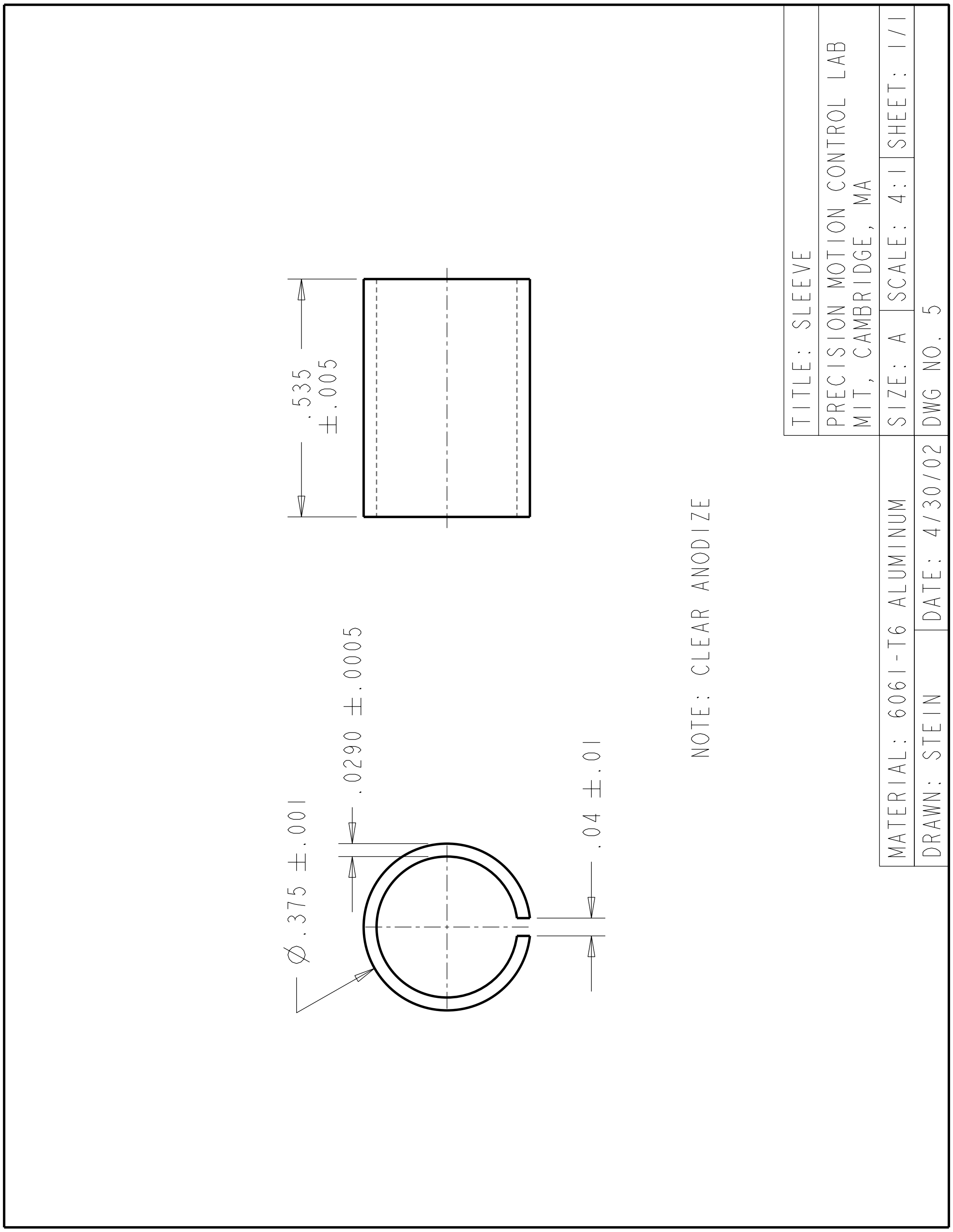

Figure A-11: Sensor sleeve mechanical drawing.

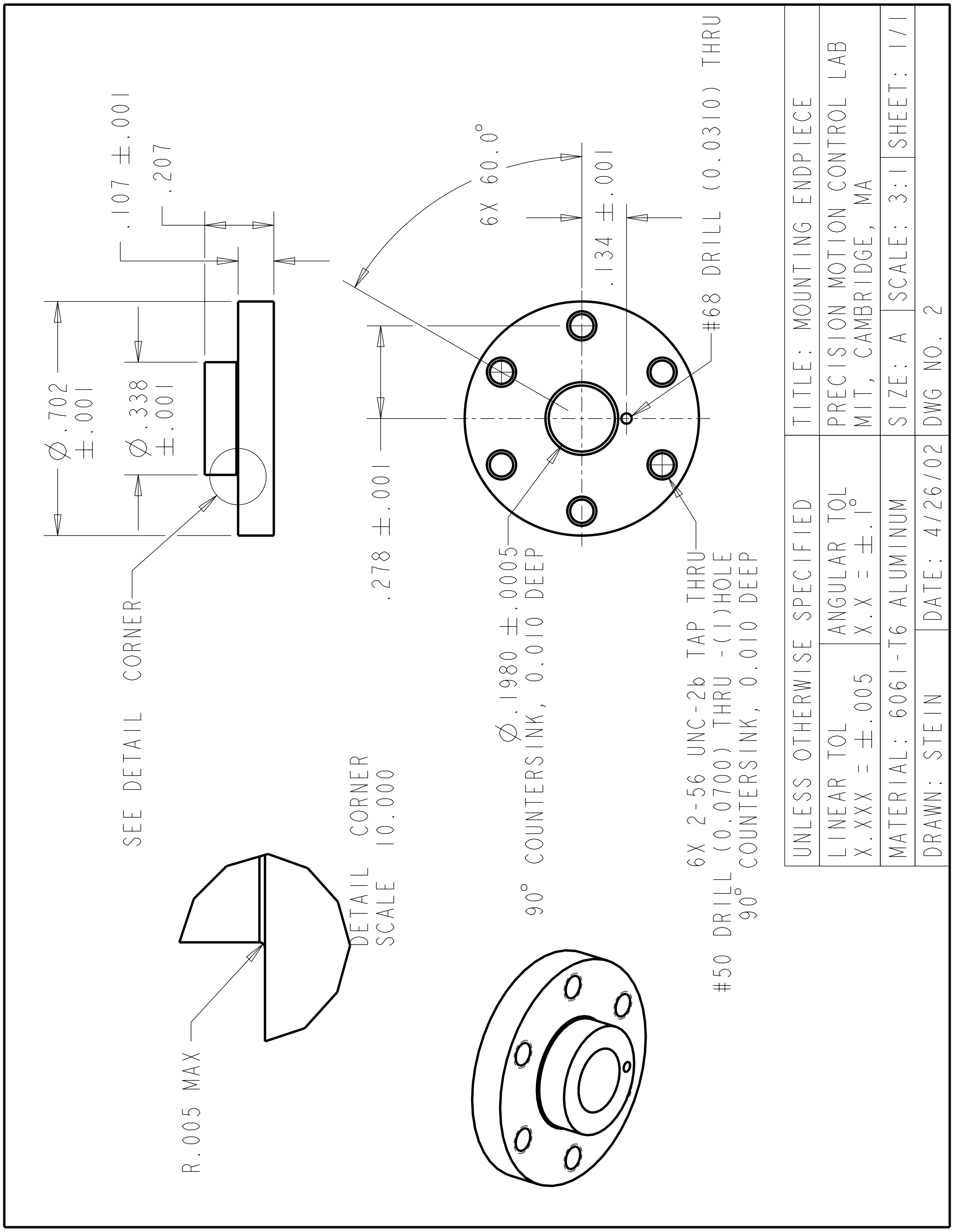

Figure A-12: Mounting endpiece mechanical drawing.

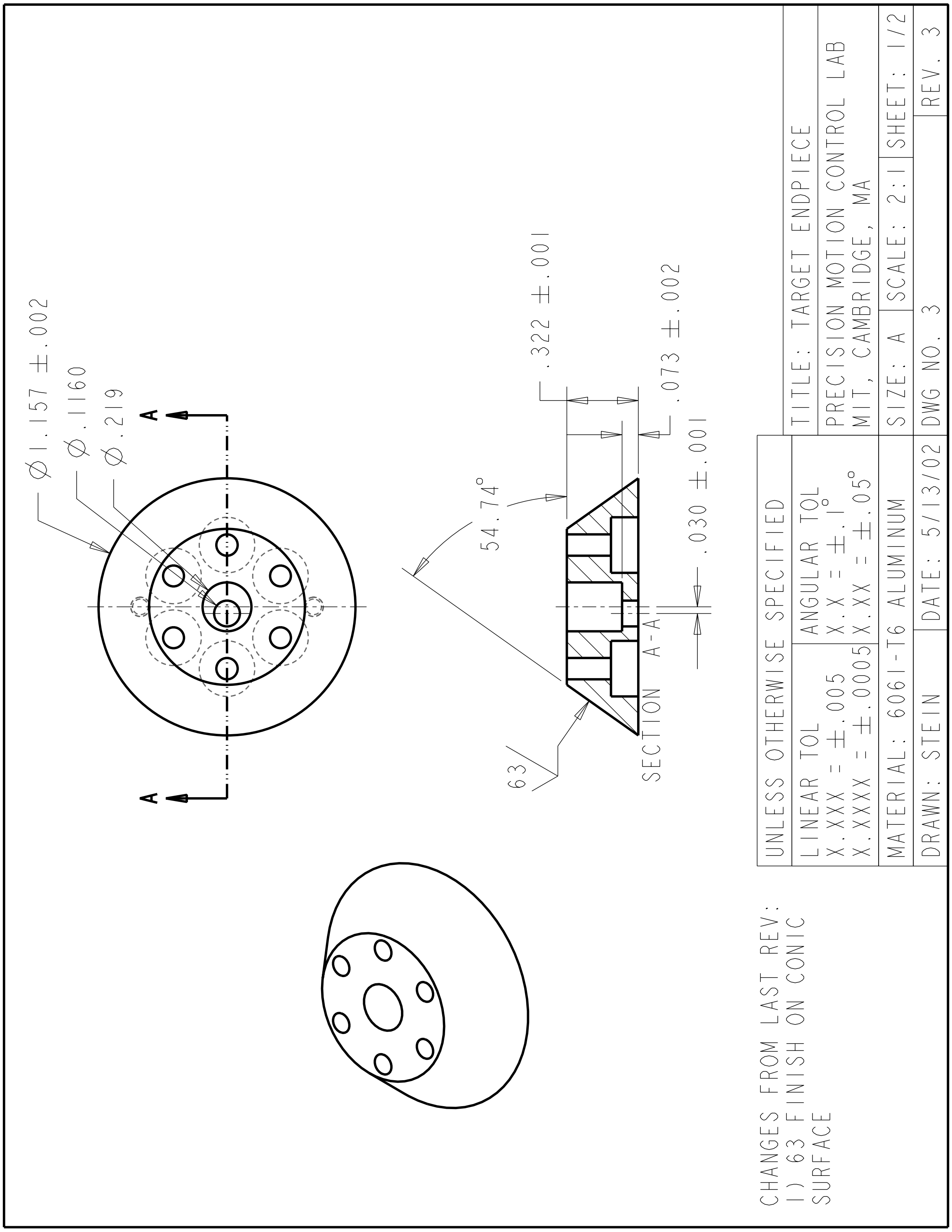

Figure A-13: Target endpiece mechanical drawing, sheet 1.

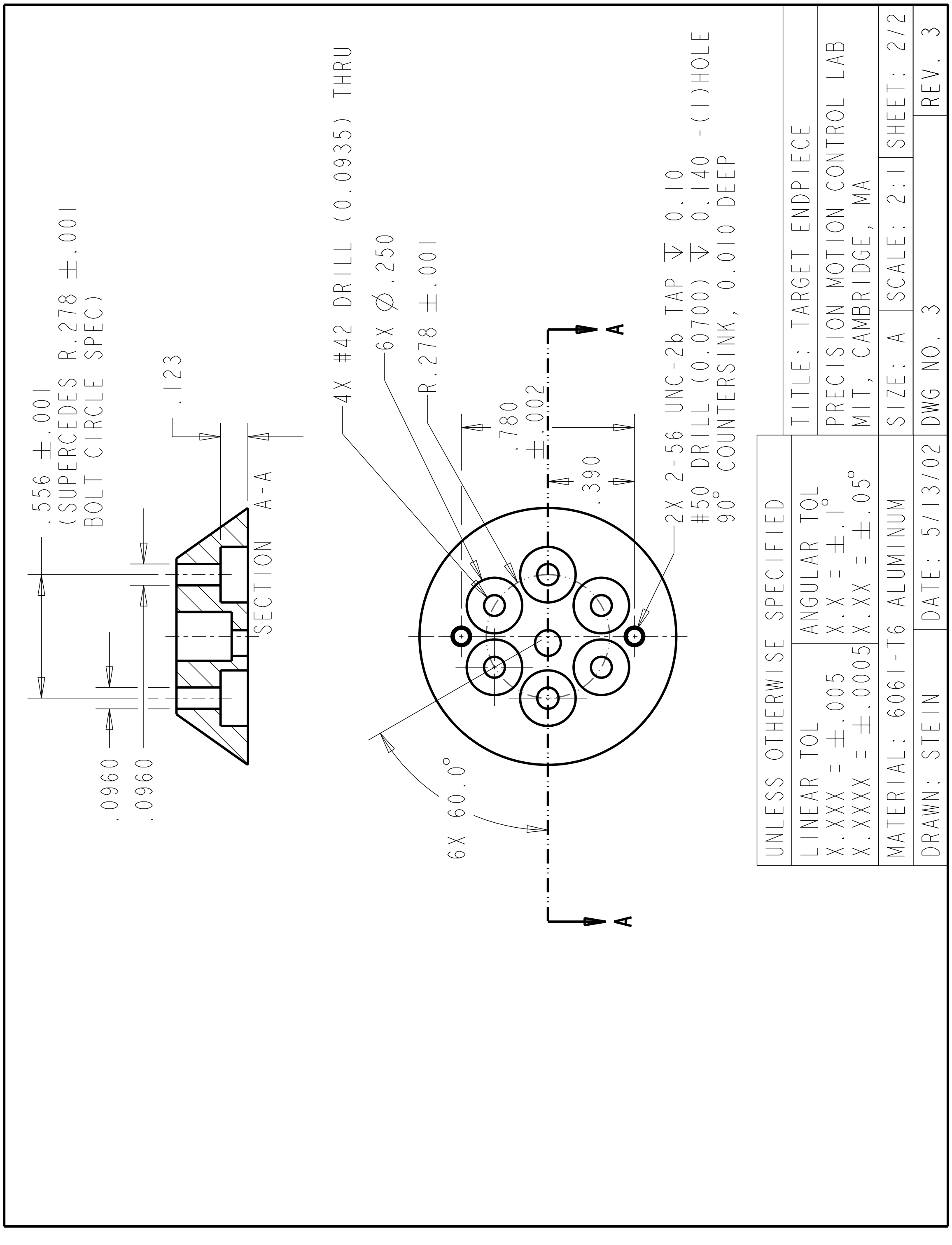

Figure A-14: Target endpiece mechanical drawing, sheet 2.

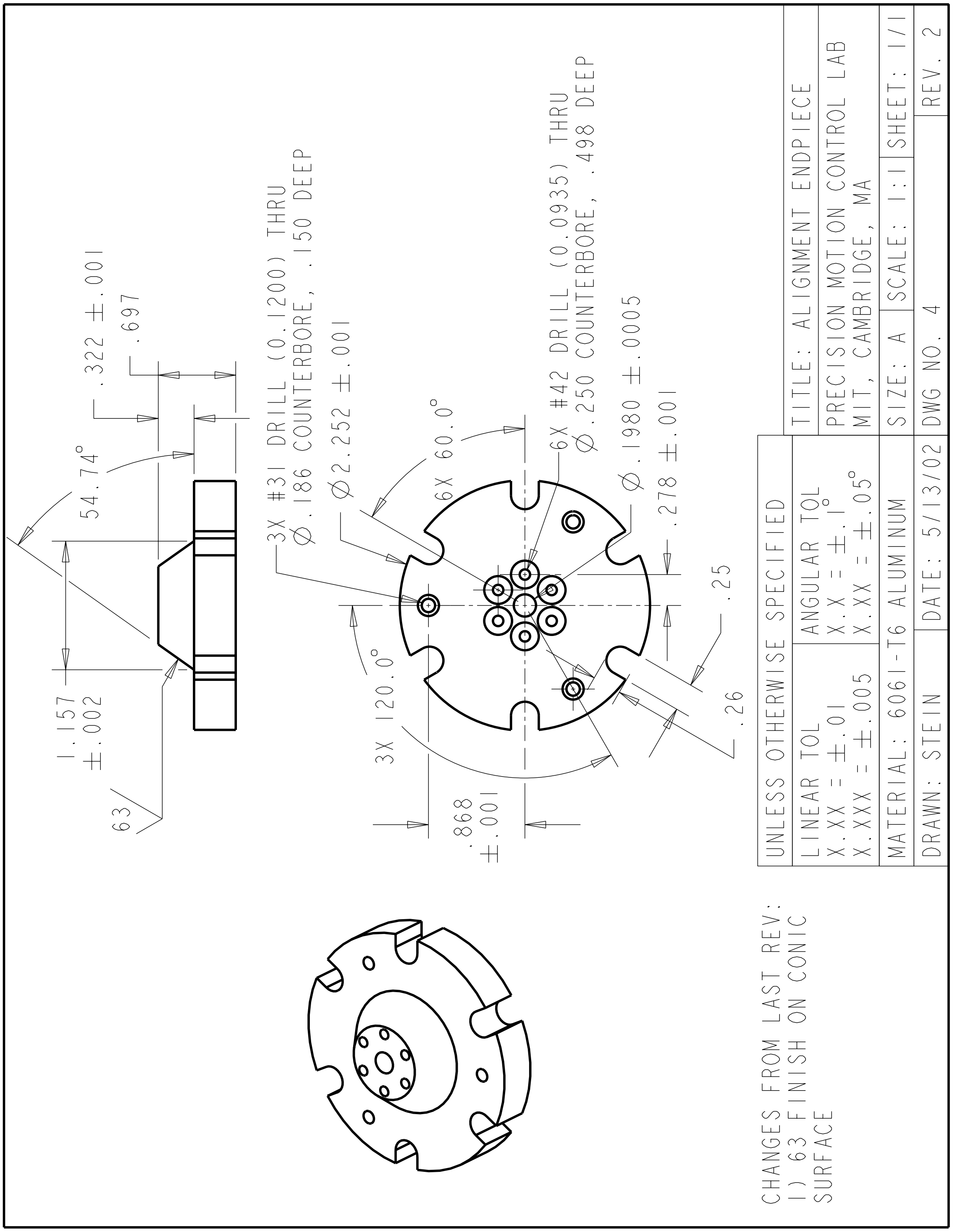

Figure A-15: Alignment endpiece mechanical drawing.

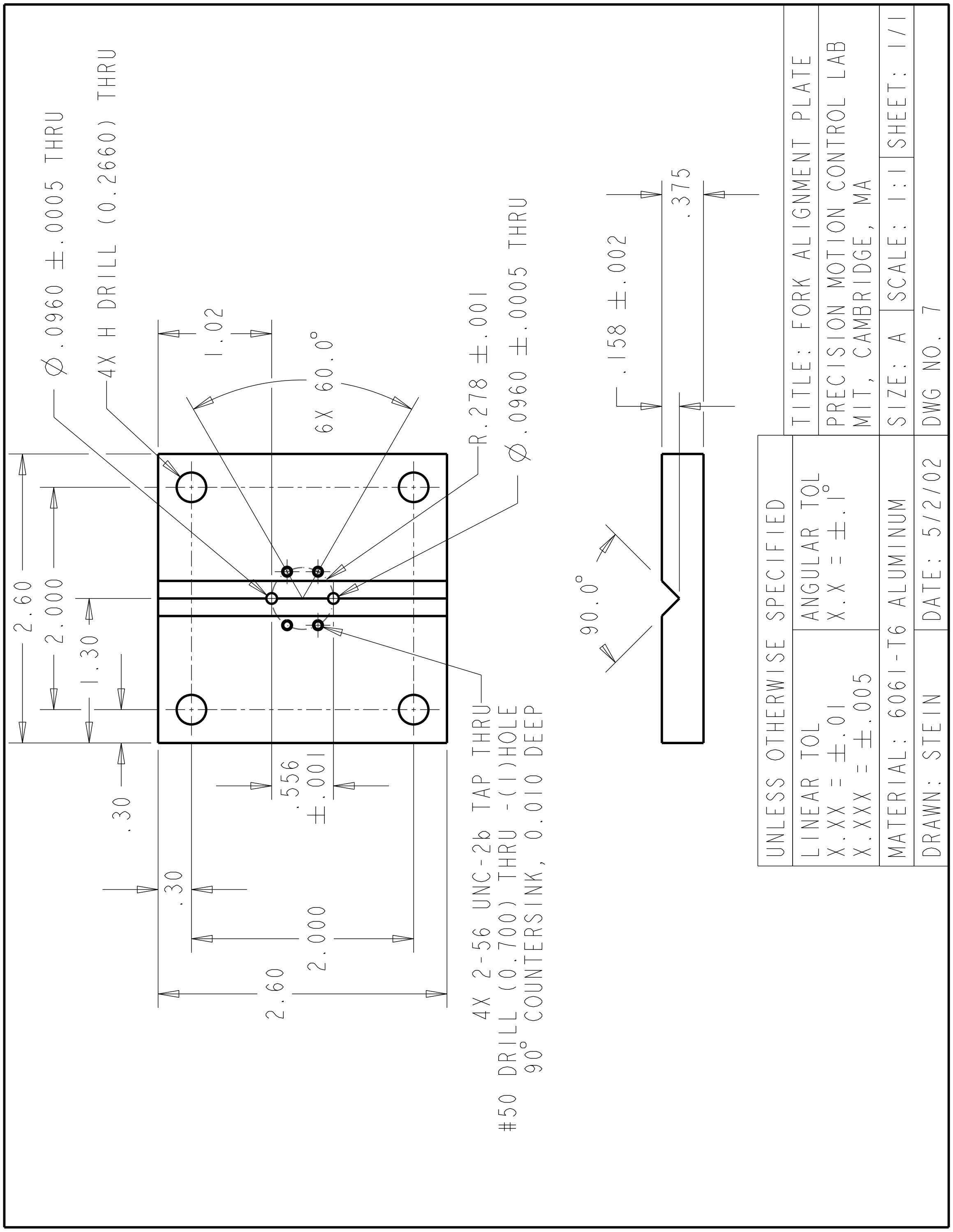

Figure A-16: Fork alignment plate mechanical drawing.

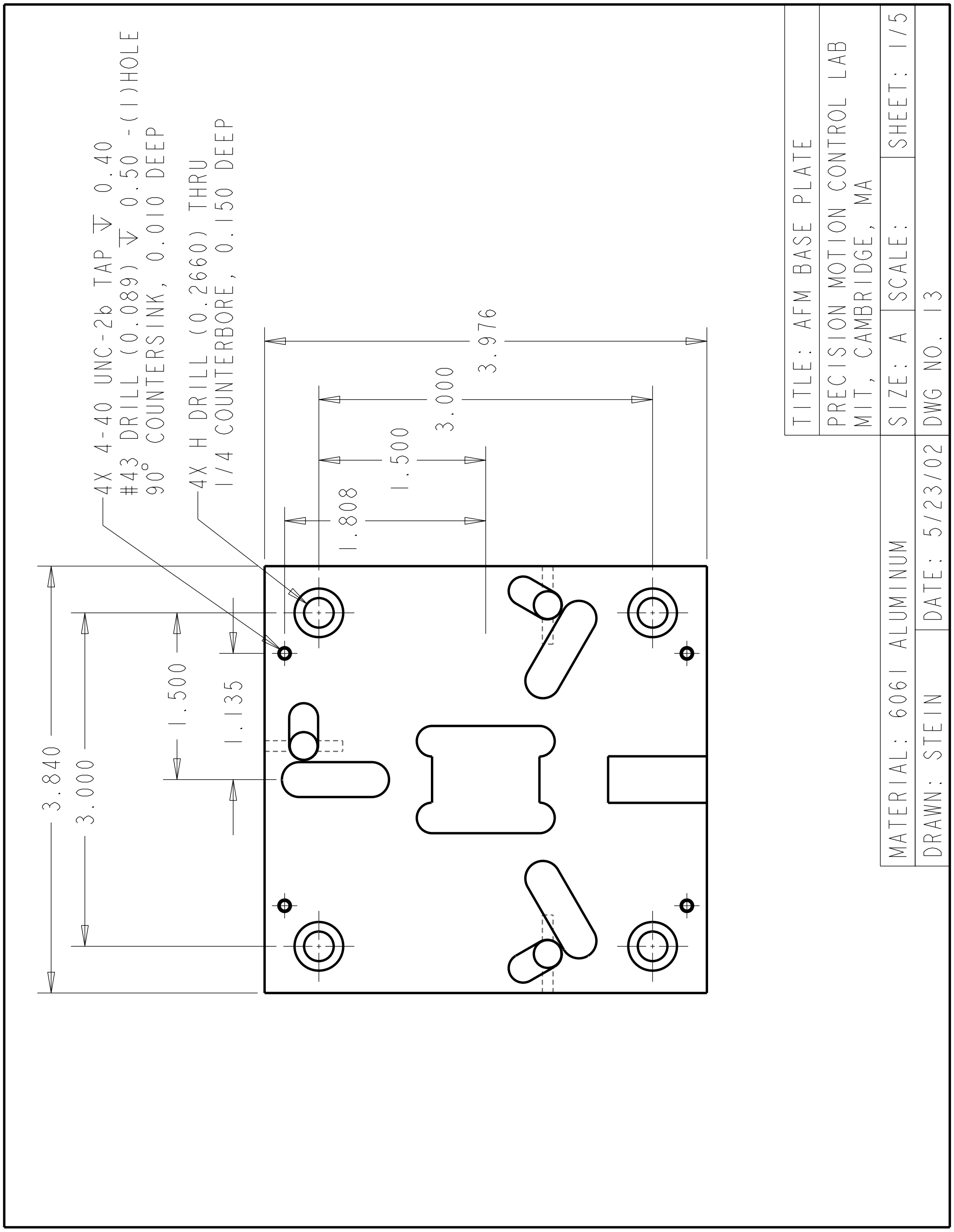

Figure A-17: Base plate mechanical drawing, sheet 1.

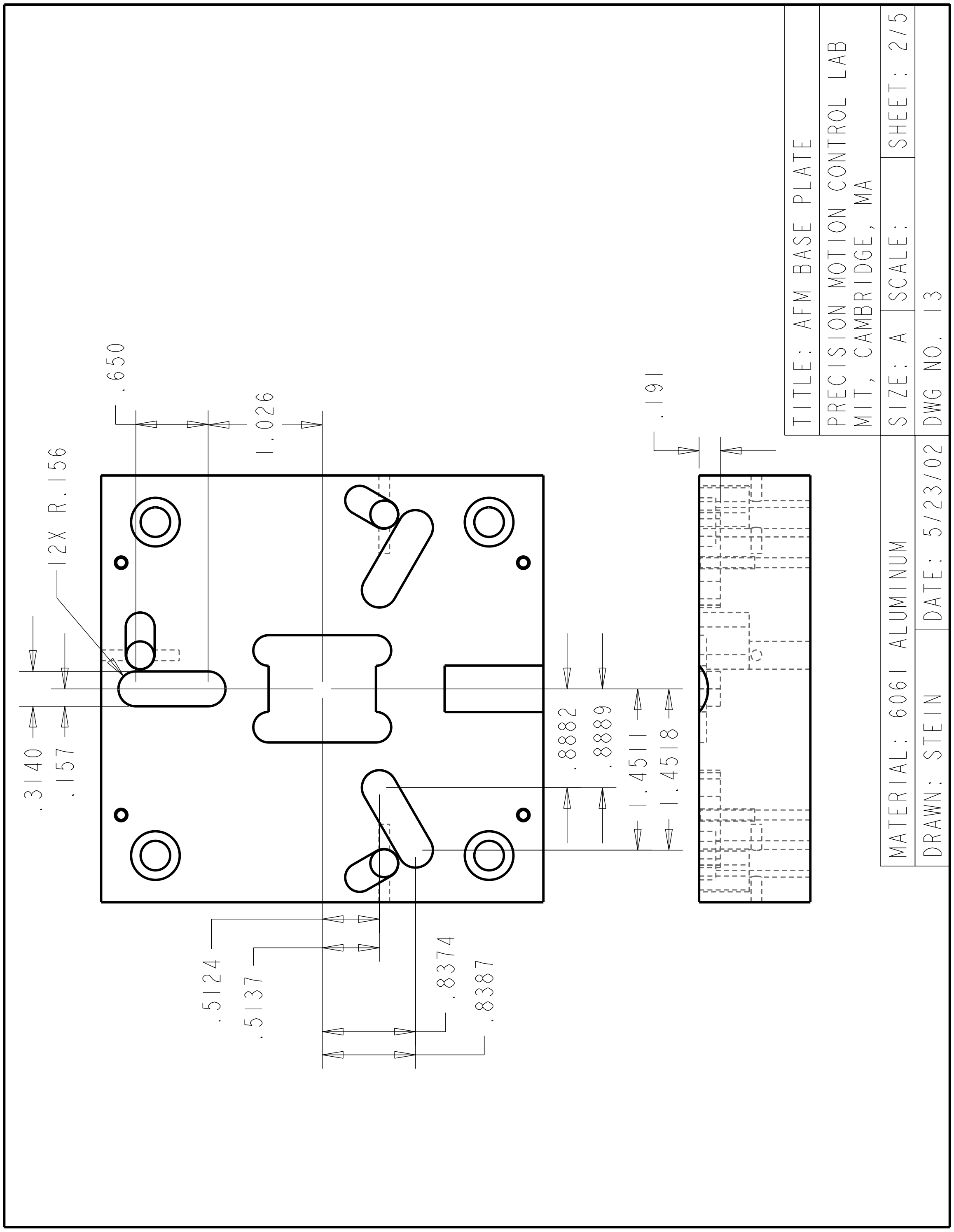

Figure A-18: Base plate mechanical drawing, sheet 2.

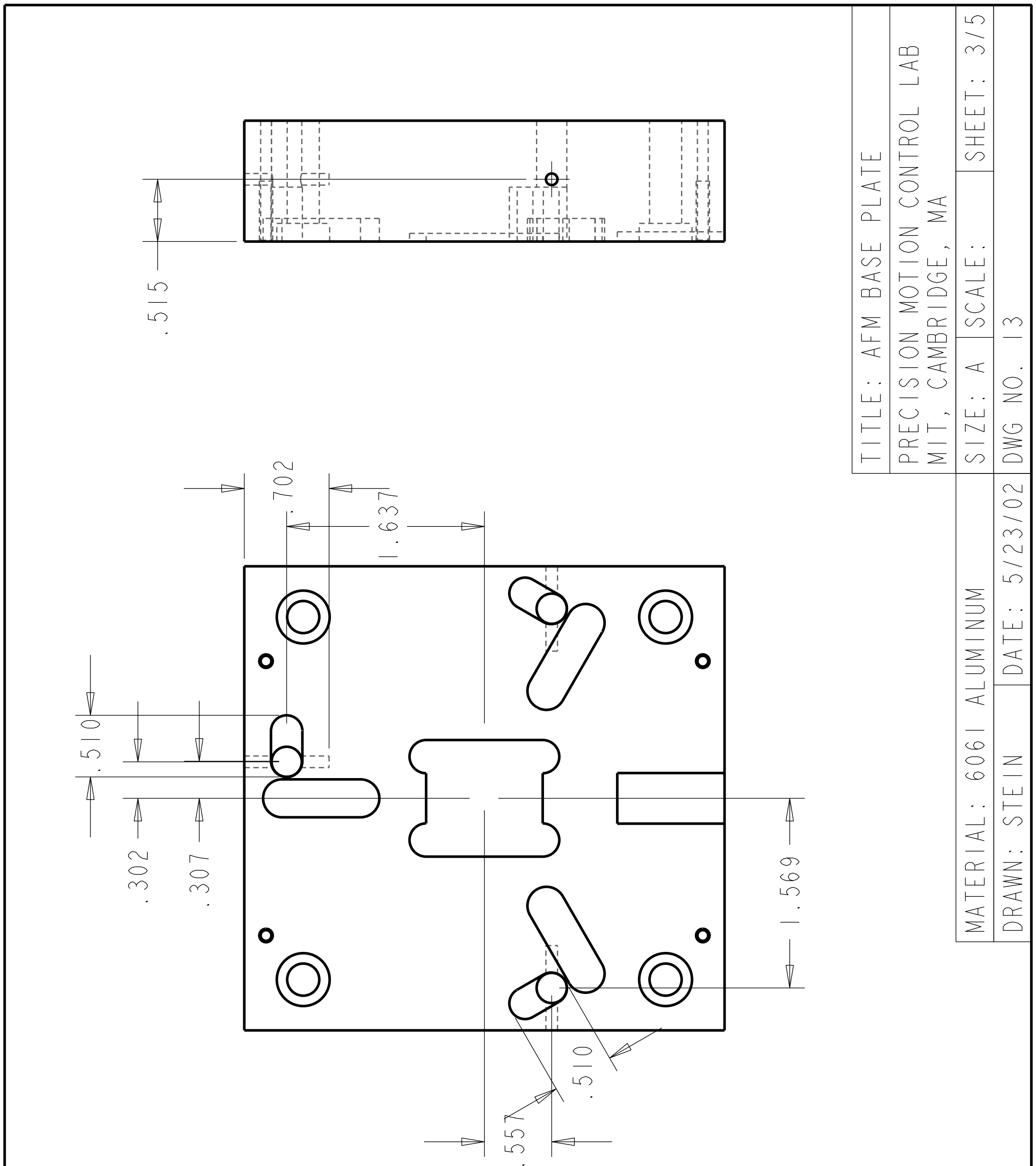

Figure A-19: Base plate mechanical drawing, sheet 3.

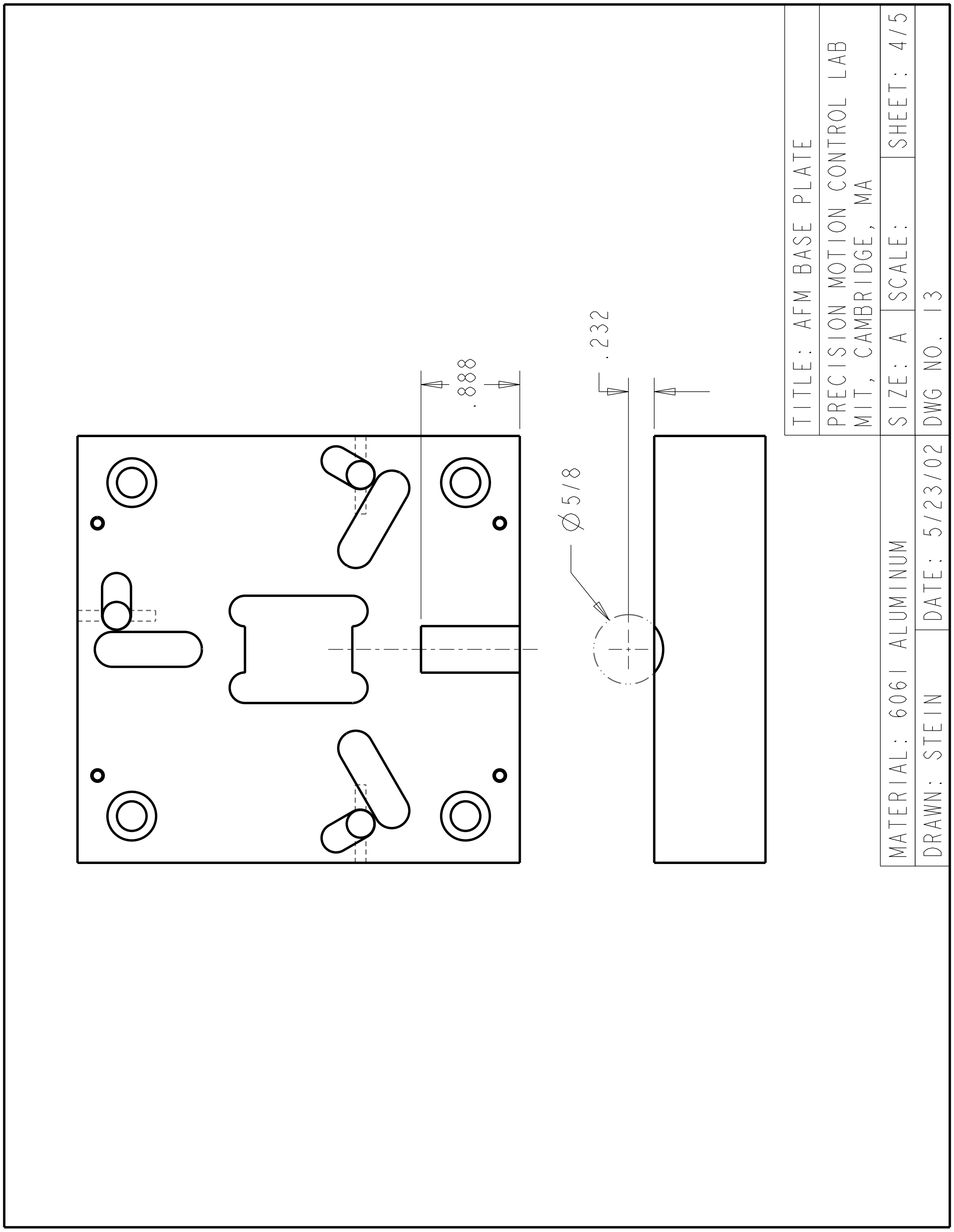

Figure A-20: Base plate mechanical drawing, sheet 4.

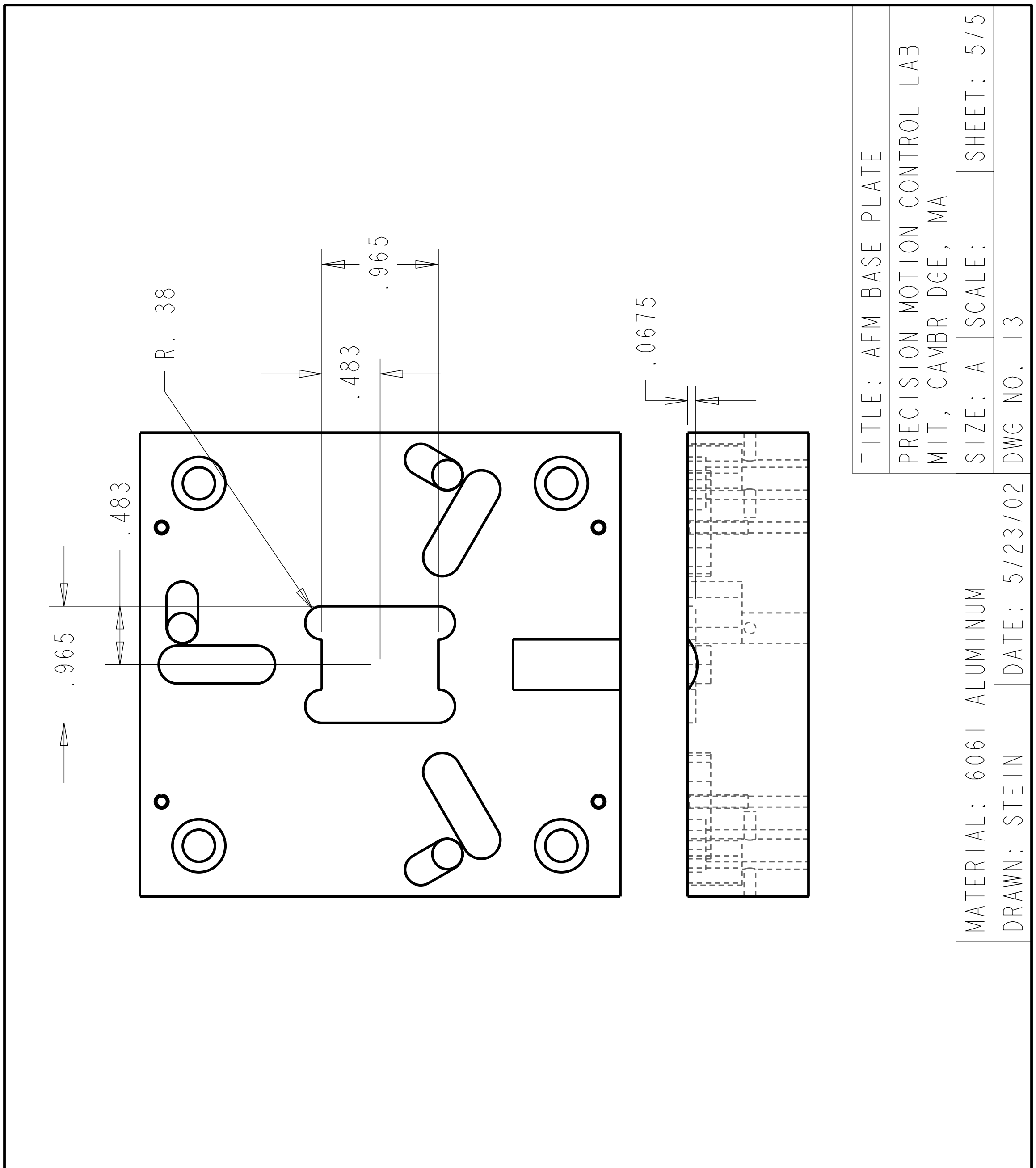

Figure A-21: Base plate mechanical drawing, sheet 5.

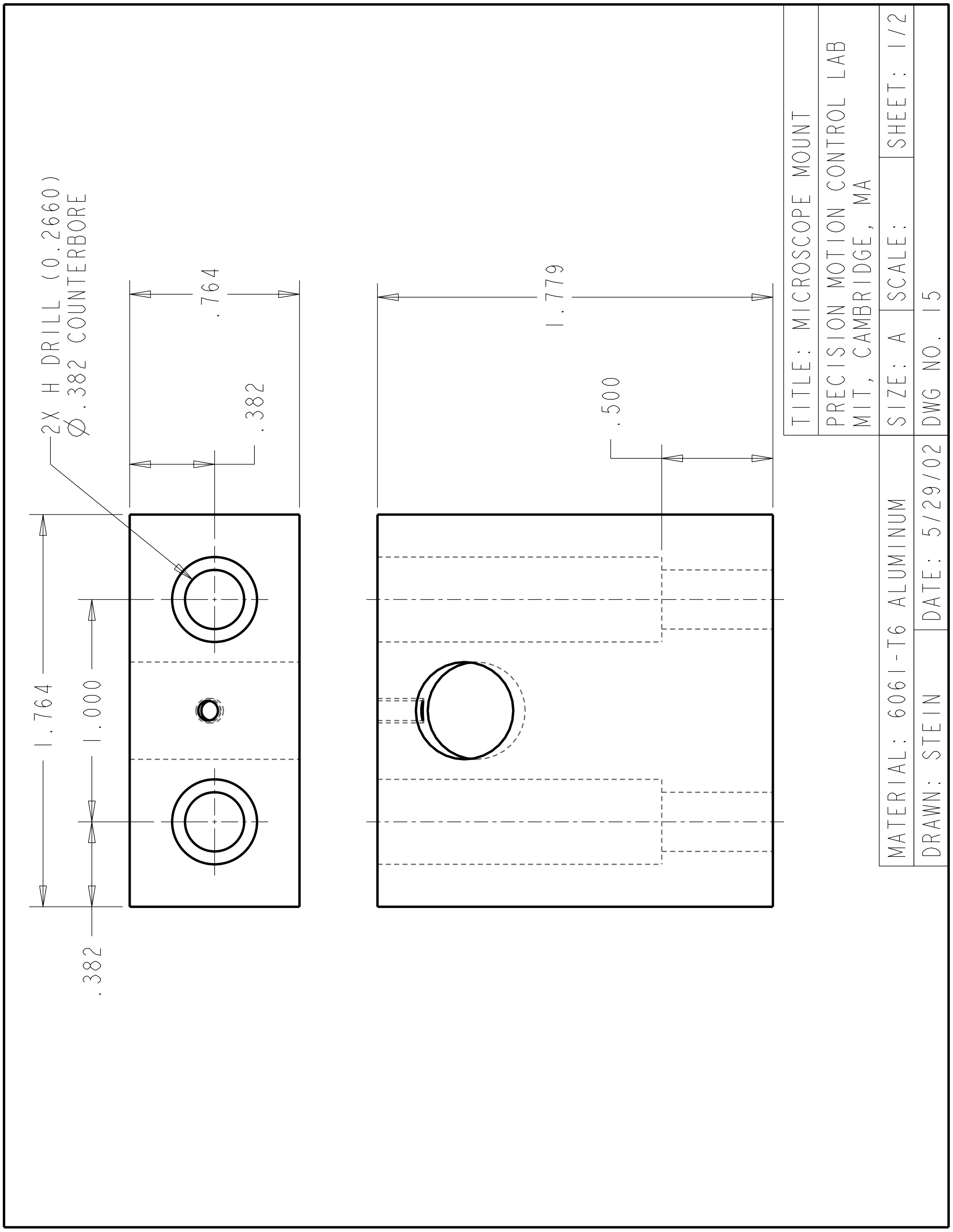

Figure A-22: Coarse approach viewer mount mechanical drawing, sheet 1.

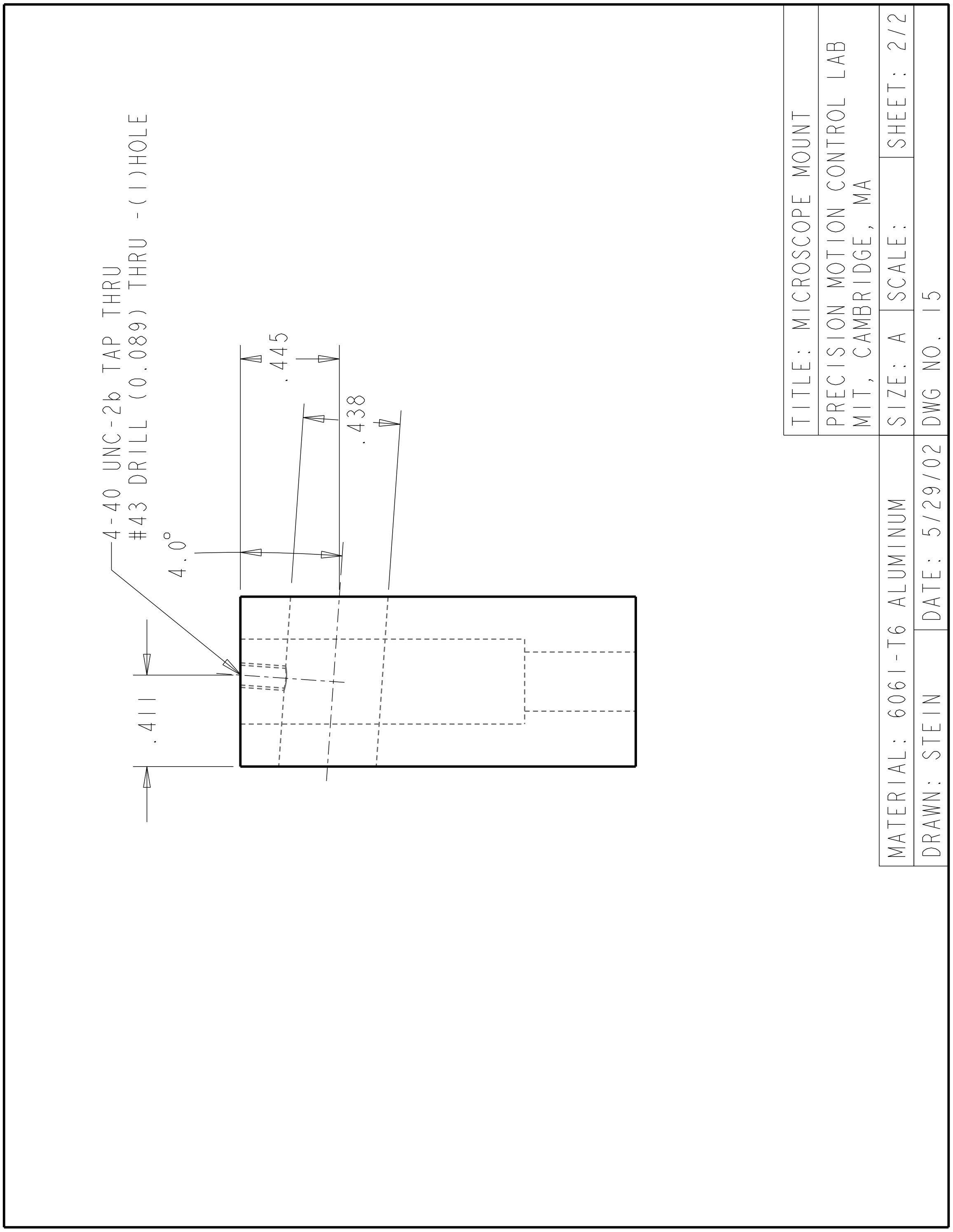

Figure A-23: Coarse approach viewer mount mechanical drawing, sheet 2.

Appendix B

Vendors

ADE Technologies, Inc.
77 Rowe St.
Newton, MA 02466
Telephone — (617) 831-8000
Web address — http://www.ade.com/
Products used: 2805-S Passive Probes, 3800 Gaging Modules

Dolan-Jenner Industries, Inc.
678 Andover St.
Lawrence, MA 01843
Telephone — (800) 833-4237
Web address — http://12.31.52.97/jenner/mikesindxr.htm
Product used: 190-1 Fiber-Lite Fiber Optic Illuminator

Dremel
4915 21st St.
Racine, WI 53406
Telephone — (800) 437-3635
Web address — http://www.dremel.com
Product used: #4485 Collet Nut Kit

dSPACE Inc.
28700 Cabot Drive – Suite 1100
Novi, MI 48377
Telephone — (248) 567-1300
Web address — http://www.dspaceinc.com/index.htm
Product used: ACE Kit DS1103

ECS, Inc. International
1105 S. Ridgeview
Olathe, KS 66062
Telephone — (913) 782-7787
Web address — http://www.ecsxtal.com/
Product used: ECS-3X8 32.768 kHz Tuning Fork Crystals

Edmund Industrial Optics
101 E. Gloucester Pike
Barrington, NJ 08007
Telephone — (800) 363-1992
Web address — http://www.edmundoptics.com/
Product used: NT38-427 30x Deluxe Direct Measuring Pocket Microscope

Kaman Instrumentation
3450 N. Nevada Ave.
Colorado Springs, CO 80907
Telephone — (800) 552-6267
Web address — http://www.kamansensors.com/html/core.htm
Product used: SMU 9000-15N Sensor Systems

K-TEK International, Inc.
7086 S.W. Beveland St.
Portland, OR 97223
Telephone — (503) 624-0315
Web address — http://www.ktekintl.com/
Product used: MikroMasch TGZ02 Silicon Grating

The MathWorks, Inc.
3 Apple Hill Dr.
Natick, MA 01760-2098
Telephone — (508) 647-7000
Web address — http://www.mathworks.com
Products used: MATLAB, Simulink

MikroMasch
Narva mnt. 13, 10151 Tallinn, Estonia
Telephone — +372 614 31 17
Web address — http://www.spmtips.com/
Product used: TGZ02 Silicon Grating
Distributor: K-TEK International, Inc. (see separate listing)

Polytec PI, Inc.
16 Albert St.
Auburn, MA 01501
Telephone — (508) 832-3456
Web address — http://www.physikinstrumente.com/
Product used: PT-130.24 Piezoceramic Tube

Stanford Research Systems
1290-D Reamwood Ave.
Sunnyvale, CA 94089
Telephone — (408) 744-9040
Web address — http://www.srsys.com/
Product used: SR530 Lock-In Amplifier

Tektronix, Inc.
14200 S.W. Karl Braun Drive
P. O. Box 500
Beaverton, OR 97077
Telephone — (800) 835-9433
Web address — http://www.tektronix.com/
Product used: AM 502 Differential Amplifier

Thorlabs, Inc.
435 Route 206 North
Newton, NJ 07860
Telephone — (973) 579-7227
Web address — http://www.thorlabs.com
Product used: WR1 Laser Diode Can Opener

Bibliography

[1] Walid A. Atia and Christopher C. Davis. A phase-locked shear-force microscope for distance regulation in near-field optical microscopy. *Applied Physics Letters*, 70(4):405–407, January 1997.

[2] Robert E. Betzig. *Non-Destructive Optical Imaging of Surfaces with 500 Ångstrom Resolution*. PhD thesis, Cornell University, August 1988.

[3] G. Binnig, C. F. Quate, and Ch. Gerber. Atomic force microscope. *Physical Review Letters*, 56(9):930–934, March 1986.

[4] G. Binnig, H. Rohrer, Ch. Gerber, and E. Weibel. Surface studies by scanning tunneling microscopy. *Physical Review Letters*, 49(1):57–61, July 1982.

[5] G. Binnig and D. P. E. Smith. Single-tube three-dimensional scanner for scanning tunneling microscopy. *Review of Scientific Instruments*, 57(8):1688–1689, August 1986.

[6] Robert H. Bishop, editor. *The Mechatronics Handbook*. CRC Press, Boca Raton, FL, 2002.

[7] Dawn A. Bonnell, editor. *Scanning Tunneling Microscopy and Spectroscopy: Theory, Techniques, and Applications*. VCH, New York, 1993.

[8] Brian D. Boudreau. *Near-Field Thermal Imaging of Surfaces below the Diffraction Limit*. PhD thesis, Michigan Technological University, July 1997.

[9] C. Julian Chen. Electromechanical deflections of piezoelectric tubes with quartered electrodes. *Applied Physics Letters*, 60(1):132–134, January 1992.

[10] Digital Instruments, Veeco Metrology Group. *Scanning Probe Microscopy Training Notebook*, 2000. Version 3.0.

[11] R. G. Dixson, R. Köning, J. Fu, T. V. Vorburger, and T. B. Renegar. Accurate dimensional metrology with atomic force microscopy. In *Proceedings of SPIE*, volume 3998, pages 362–368, 2000.

[12] Urs Dürig, Dieter Pohl, and Flavio Rohner. Near-field optical scanning microscopy with tunnel-distance regulation. *IBM Journal of Research and Development*, 30(5):478–483, September 1986.

[13] Hal Edwards, Larry Taylor, Walter Duncan, and Allan J. Melmed. Fast, high-resolution atomic force microscopy using a quartz tuning fork as actuator and sensor. *Journal of Applied Physics*, 82(3):980–984, August 1997.

[14] Franz J. Giessibl. Atomic resolution on Si(111)-(7x7) by noncontact atomic force microscopy with a force sensor based on a quartz tuning fork. *Applied Physics Letters*, 76(11):1470–1472, March 2000.

[15] R. D. Grober, J. Acimovic, J. Schuck, D. Hessman, P. J. Kindlemann, J. Hespanha, A. S. Morse, K. Karrai, I. Tiemann, and S. Manus. Fundamental limits to force detection using quartz tuning forks. *Review of Scientific Instruments*, 71(7):2776–2780, July 2000.

[16] Robert J. Hocken, David L. Trumper, and Chunhai Wang. Dynamics and control of the UNCC/MIT sub-atomic measuring machine. *CIRP Annals*, 50(1):373–376, 2001.

[17] Patrik Hoffmann, Bertrand Dutoit, and René-Paul Salathé. Comparison of mechanically drawn and protection layer chemically etched optical fiber tips. *Ultramicroscopy*, 61:165–170, December 1995.

[18] Michael L. Holmes. *Analysis and Design of a Long Range Scanning Stage.* PhD thesis, University of North Carolina at Charlotte, 1998.

[19] Michael L. Holmes, Robert J. Hocken, and David L. Trumper. The long-range scanning stage: a novel platform for scanned-probe microscopy. *Precision Engineering*, 24(3):191–209, July 2000.

[20] Michael L. Holmes and David L. Trumper. Magnetic/fluid-bearing stage for atomic-scale motion control (the angstrom stage). *Precision Engineering*, 18(1):38–49, January 1996.

[21] Paul Horowitz and Winfield Hill. *The Art of Electronics.* Cambridge University Press, Cambridge, UK, second edition, 1989.

[22] Takurō Ikeda. *Fundamentals of Piezoelectricity.* Oxford University Press, Oxford, 1996.

[23] M. Isaacson, E. Betzig, A. Harootunian, and A. Lewis. Scanning optical microscopy at tenth wavelength resolution using near-field imaging methods. In A. P. Somlyo, editor, *Recent Advances in Electron and Light Optical Imaging in Biology and Medicine*, pages 448–456. New York Academy of Sciences, New York, 1986.

[24] Albert Jansen, Nick Rosielle, and Piet Schellekens. A fully elastically guided 3-D CMM with a measuring volume of 1 cm^3. In *Proceedings of 1999 ASPE Annual Conference*, volume 20, pages 452–455.

[25] J. F. Jørgensen, K. Carneiro, L. L. Madsen, and Knut Conradsen. Hysteresis correction of scanning tunneling microscope images. *Journal of Vacuum Science & Technology B*, 12(3):1702–1704, May 1994.

[26] O. Jusko, X. Zhao, H. Wolff, and G. Wilkening. Design and three dimensional calibration of a measuring scanning tunneling microscope for metrological applications. *Review of Scientific Instruments*, 65(8):2514–2518, August 1994.

[27] Hiroshi Kaizuka. Application of capacitor insertion method to scanning tunneling microscopes. *Review of Scientific Instruments*, 60(10):3119–3122, October 1989.

[28] Khaled Karrai and Robert D. Grober. Piezoelectric tip-sample distance control for near field optical microscopes. *Applied Physics Letters*, 66(14):1842–1844, April 1995.

[29] Khaled Karrai and Robert D. Grober. Tip-sample distance control for near-field scanning optical microscopes. In *Proceedings of SPIE*, volume 2535, pages 69–81, July 1995.

[30] G. M. King, J. S. Lamb, and G. Nunes, Jr. Quartz tuning forks as sensors for attractive-mode force microscopy under ambient conditions. *Applied Physics Letters*, 79(11):1712–1714, September 2001.

[31] Katherine A. Lilienkamp and David L. Trumper. Dynamic signal analyzer for dSPACE. In *Proceedings of the dSPACE User's Conference*, May 2000.

[32] V. J. Morris, A. R. Kirby, and A. P. Gunning. *Atomic Force Microscopy for Biologists*. Imperial College Press, London, 1999.

[33] C.V. Newcomb and I. Flinn. Improving the linearity of piezoelectric ceramic actuators. *Electronics Letters*, 18(11):442–444, May 1982.

[34] Michael A. Paesler and Patrick J. Moyer. *Near-Field Optics: Theory, Instrumentation, and Applications*. Wiley, New York, 1996.

[35] W. H. J. Rensen, N. F. van Hulst, A. G. T. Ruiter, and P. E. West. Atomic steps with tuning-fork-based noncontact atomic force microscopy. *Applied Physics Letters*, 75(11):1640–1642, September 1999.

[36] T. A. M. Ruijl. *Ultra Precision Coordinate Measuring Machine*. PhD thesis, Delft University of Technology, 2001.

[37] Alexander H. Slocum. *Precision Machine Design*. Prentice-Hall, Englewood Cliffs, NJ, 1992.

[38] M. E. Taylor. Dynamics of piezoelectric tube scanners for scanning probe microscopy. *Review of Scientific Instruments*, 64(1):154–158, January 1993.

[39] T. V. Vorburger, J. A. Dagata, G. Wilkening, and K. Iizuka. Industrial uses of STM and AFM. *CIRP Annals*, 46(2):597–620, 1997.

[40] R. Wiesendanger and H.-J. Güntherodt, editors. *Scanning Tunneling Microscopy III: Theory of STM and Related Scanning Probe Methods.* Springer, Berlin, second edition, 1996.

[41] Masaki Yamamoto, Keisaku Yamaguchi, and Shinichiro Aoki. Application of vibroscanning method to nonconductive sample's micro profile measurement using a quartz tuning fork. *Journal of the Japan Society for Precision Engineering*, 67(6):992–996, June 2001.

[42] Russell D. Young. Field emission ultramicrometer. *Review of Scientific Instruments*, 37(3):275–278, March 1966.

[43] Russell D. Young, John Ward, and Fredric Scire. The topografiner: an instrument for measuring surface microtopography. *Review of Scientific Instruments*, 43(7):999–1011, July 1972.